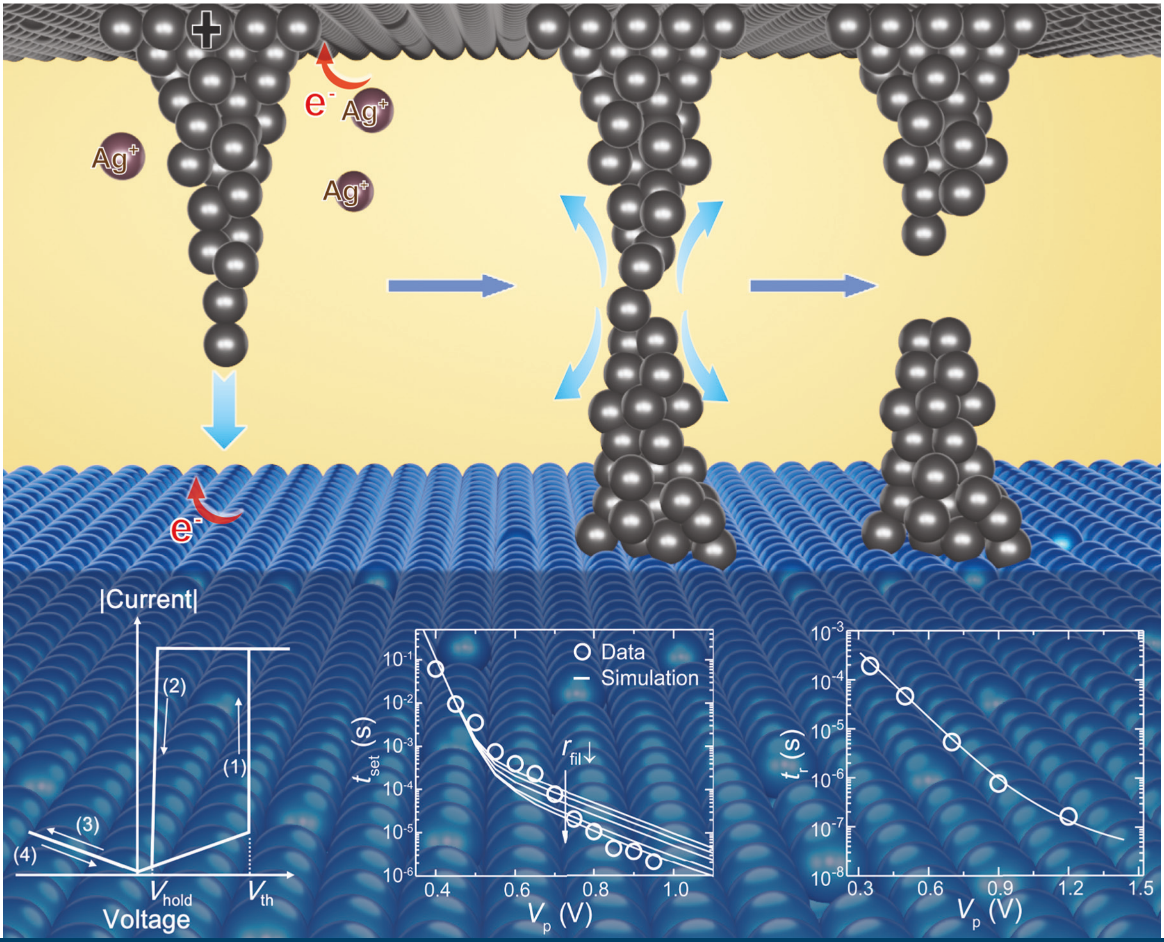
Ag$^+$
e$^-$
+
|Current|
(1)
(2)
(3)
(4)
V_{hold}
V_{th}
Voltage
Data
Simulation
t_{set} (s)
r_{fil}↓
V_p (V)
t_r (s)
0.4
0.6
0.8
1.0
0.3
0.9
1.2
1.5
10^{-1}
10^{-2}
10^{-3}
10^{-4}
10^{-5}
10^{-6}
10^{-7}
10^{-8}

Unveiling the relaxation dynamics of Ag/HfO$_2$ based diffusive memristors for use in neuromorphic computing

Solomon Amsalu Chekol

Information
Band / Volume 101
ISBN 978-3-95806-729-5

Mitglied der Helmholtz-Gemeinschaft

JÜLICH
Forschungszentrum

Schriften des Forschungszentrums Jülich
Reihe Information / Information Band / Volume 101

Forschungszentrum Jülich GmbH
Peter Grünberg Institut (PGI)
Elektronische Materialien (PGI-7)

Unveiling the relaxation dynamics of Ag/HfO_2 based diffusive memristors for use in neuromorphic computing

Solomon Amsalu Chekol

Schriften des Forschungszentrums Jülich
Reihe Information / Information Band / Volume 101

ISSN 1866-1777 ISBN 978-3-95806-729-5

Bibliografische Information der Deutschen Nationalbibliothek.
Die Deutsche Nationalbibliothek verzeichnet diese Publikation in der Deutschen Nationalbibliografie; detaillierte Bibliografische Daten sind im Internet über http://dnb.d-nb.de abrufbar.

Herausgeber und Vertrieb: Forschungszentrum Jülich GmbH
Zentralbibliothek, Verlag
52425 Jülich
Tel.: +49 2461 61-5368
Fax: +49 2461 61-6103
zb-publikation@fz-juelich.de
www.fz-juelich.de/zb

Umschlaggestaltung: Grafische Medien, Forschungszentrum Jülich GmbH

Druck: Grafische Medien, Forschungszentrum Jülich GmbH

Copyright: Forschungszentrum Jülich 2023

Schriften des Forschungszentrums Jülich
Reihe Information / Information, Band / Volume 101

D 82 (Diss. RWTH Aachen University, 2023)

ISSN 1866-1777
ISBN 978-3-95806-729-5

Vollständig frei verfügbar über das Publikationsportal des Forschungszentrums Jülich (JuSER) unter www.fz-juelich.de/zb/openaccess.

This is an Open Access publication distributed under the terms of the Creative Commons Attribution License 4.0, which permits unrestricted use, distribution, and reproduction in any medium, provided the original work is properly cited.

Abstract

The rapid growth in volume and complexity of data and transfer, driven by advancements in information technologies such as artificial intelligence (AI), cloud computing, big data, and machine learning, is placing significant demands on computation power and speed. Traditional computing architectures are facing challenges in meeting these demands due to the Von Neumann bottleneck, which limits the data transfer rate between the memory and the central processing unit and causes high energy consumption. Today, neuromorphic computing (NC) concepts that mimic the structure and function of the biological brain are gaining popularity as they promise energy-efficient and scalable computing solutions. Currently, neuronal functionality is often performed using a transistor-based neuron, which is area- and energy-inefficient. Therefore, research in the "beyond von Neumann" area is aimed at novel volatile switching components with adjustable switching times, low power consumption, and high scalability, which could potentially be used as artificial neurons in NC circuits. These include threshold-switching devices that switch abruptly from the high-resistance state (HRS) to the low-resistance state (LRS) at a defined voltage. As soon as the applied voltage falls below a certain value, the cell relaxes back to the initial HRS state. In particular, diffusive memristors built from volatile electrochemical metallization (ECM) cells are attracting attention in emerging NC areas such as temporal encoding. These diffusive memristors consist of switching layers made from oxides or chalcogenides sandwiched between an electrochemically active electrode (e.g., Ag or Cu) and an inert electrode (e.g., Pt metal). The cells can be miniaturized down to the sub-micrometer range and the switching itself relies on the formation and dissolution of a metallic filament. Since the temporal behavior of diffusive memristors is their main characteristic, it is of crucial importance to understand the relaxation dynamics of these devices from a physical perspective. This is a prerequisite for optimizing and modulating the performance of diffusive memristors, especially for applications requiring precise control of switching times. Previous approaches mainly describe the relaxation time as a function of the given filament diameter while the filament growth process is not considered.

In contrast, the present work takes a comprehensive approach based on the physical description of filament formation and relaxation and a possible dependence between the two. The goal is to develop a deeper understanding of the relaxation dynamics of diffusive memristors, with particular emphasis on the influence of SET parameters on the structure and diameter of the filament formed in each case. To this end, devices were fabricated from an amorphous HfO_2 layer of a few nanometers thickness sandwiched between electrode layers of Ag and Pt. For material influence studies, SiO_2 as an electrolyte layer and two other metals (TiN and W) as alternative counter electrodes (CEs) were also investigated. By evaluating the transient current response to applied voltage pulses, the SET kinetics and relaxation dynamics of the cells were comprehensively analyzed. This allowed the identification of different mechanisms as rate-limiting steps for filament formation. In particular, three processes, namely nucleation, electron-transfer, and mixed processes (electron-transfer and ion-migration), were identified as rate-limiting steps during the SET process. It was shown that the relaxation time strongly depends on the selected SET parameters. This is explained by the different mechanisms of filament formation during the SET event. A slow SET process at low voltage results in a relatively thick filament that takes long to self-rupture. In contrast, fast SET processes at high voltage lead to dendritic filaments with short relaxation times. This assertion is consistent with previous Monte Carlo simulations for similar ECM cells and is further supported by physics-based simulations using the "JART ECM" model developed in collaboration with IWE 2/RWTH. Furthermore, it has been demonstrated that applying a higher voltage pulse amplitude or longer duration leads to a substantial increase in relaxation time. This could be due to a small residual voltage drop across the diffusive memristor in the LRS, which causes further growth of the filament after closure. The new findings resulting from the combined analysis of SET kinetics and relaxation dynamics underline the importance of filament formation for relaxation behavior and provide important information for optimal operating conditions of these threshold switches in NC circuits. In addition, the work addresses the influence of CE material on the SET kinetics of diffusive memristors. For example, both TiN and W CEs slow down the switching speed compared to the Pt electrode. This is attributed to the different electrocatalytic activity of the different metals in the redox reaction. Oxide formation at the interface of non-noble metals (i.e., TiN and W) is also included in the discussion. An important effect for use in NC circuits is the significant influence of a series resistor on the relaxation behavior. It has been shown that the magnitude of the series resistance can strongly influence the relationship between relaxation time and pulse voltage amplitude. This can be attributed to the highly non-linear nature of the SET kinetics and the role that a residual voltage drop across the device in the ON-state plays in promoting continued growth and strengthening of the conductive filament.

In summary, this work shows that diffusive memristors based on volatile ECM cells have a high potential for use as artificial neurons and further applications in the field of NC. The obtained results contribute to a deeper physical understanding of the interplay between filament formation and relaxation and can be directly transferred to the optimization of the operational conditions of diffusive memristors in neuromorphic circuits. This represents an important step towards the realization of energy-efficient NC solutions. In addition, the work classifies volatile devices in terms of different adjustable relaxation times against the background of various NC applications.

Kurzfassung

Die starke Zunahme der Menge und Komplexität zu verarbeitender Daten, die durch Fortschritte in der Informationstechnologie wie künstliche Intelligenz (KI), Cloud Computing, Big Data und maschinelles Lernen vorangetrieben wird, erfordert hohe Bearbeitungsgeschwindigkeiten und Rechenleistungen. Herkömmliche Rechner mit getrennten Speicher- und Prozessor-Einheiten können diese Anforderungen kaum noch erfüllen. Ursache ist das sogenannte "Von-Neumann-Bottleneck", welches die limitierte Datenübertragungsrate zwischen Speicher und Prozessor bezeichnet und maßgeblich den Energieverbrauch beeinflusst. Dies begründet das große Interesse an neuartigen, skalierbaren, energieeffizienten Rechenkonzepten wie dem neuromorphen Computing (NC), welches die Struktur und Funktion des biologischen Gehirns nachahmt. Aktuell werden künstliche neuronale Funktionen noch mit Transistor-Schaltungen realisiert, die einen hohen Flächen- und Energiebedarf besitzen. Daher zielt die Forschung im Bereich "Beyond-von Neumann" auf neuartige flüchtig-schaltende Bauelemente mit einstellbaren Schaltzeiten, geringem Leistungsverbrauch und hoher Skalierbarkeit, die die Funktion künstlicher Neuronen in NC-Schaltungen übernehmen. Dazu zählen schwellenwertschaltende Bauelemente, die bei einer definierten Spannung sprunghaft vom hochohmigen (HRS: high resistance state) in den niederohmigen (LRS: low resistance state) Widerstandszustand schalten. Sobald die angelegte Spannung den Schwellenwert unterschreitet, relaxiert die Zelle in den HRS. Insbesondere diffusive Memristoren aus flüchtigen elektrochemischen Metallisierungszellen (ECM) scheinen interessant für neue NC-Anwendungen wie die zeitliche Kodierung. Diffusive Memristoren bestehen meist aus einer Oxid- oder Chalkogenid-Schicht eingebettet zwischen eine elektrochemisch aktive Elektrode (z.B. Ag oder Cu) und eine inerte Elektrode (z.B. Pt). Die Zellen können bis in den sub-Mikrometerbereich miniaturisiert werden. Das Schalten selbst beruht auf der Bildung und dem Auflösen eines metallischen Filaments. Von besonderem Interesse sind die Zeit- und Spannungsabhängigkeit des Schalt- und Relaxationsverhaltens, da diese Kenngrößen über die Eignung als künstliche Neuronen entscheiden. Daher ist das physikalische Verständnis der Schaltkinetik und der Relaxationsdynamik diffusiver Memristoren entscheidend für die Entwicklung anwendungsoptimierter energieeffizienter Bauelemente. Jedoch setzen bisherige physikalische Beschreibungen der Relaxationszeit erst bei einem gegebenen Filamentdurchmesser an, während der Prozess des Filamentwachstums weitgehend unberücksichtigt bleibt.

Im Unterschied dazu verfolgt die vorliegende Arbeit einen umfassenden Ansatz basierend auf der physikalischen Beschreibung der der Filament-Bildung und -Relaxation sowie einer mögliche Abhängigkeit. Ziel ist es, ein tieferes Verständnis der Relaxationsdynamik diffusiver Memristoren zu entwickeln unter besonderer Berücksichtigung des Einflusses der SET-Parameter auf die Struktur und den Durchmesser des jeweils gebildeten Filaments. Dazu wurden Bauelemente hergestellt aus einer amorphen HfO_2 Schicht von wenigen Nanometern Dicke eingebettet zwischen Elektrodenschichten aus Ag und Pt. Für Studien zum Materialeinfluss wurden zusätzlich SiO_2 als Elektrolytschicht und zwei weitere Metalle (TiN und W) als alternative Gegenelektroden (CE: counter electrode) untersucht. Durch die Auswertung der transienten Stromantwort auf angelegte Spannungspulse wurden die SET-Kinetik und die Relaxationsdynamik der Zellen umfassend analysiert. Für die SET-Kinetik konnten entsprechend physikalischer Modelle ("JART ECM", IWE 2/RWTH) drei Bereiche mit unterschiedlichem ratenbegrenzenden Mechanismus identifiziert werden: Nukleation, Elektronentransfer und gemischte Prozesse (Elektronentransfer und Ionenwanderung). Es wurde gezeigt, dass die Relaxationszeit bis zur Auflösung des Filaments von den gewählten SET-Parametern abhängt. Durch Vergleich mit Monte-Carlo-Simulationen für ähnliche ECM-Zellen konnte die Struktur des Filaments als primäre Ursache identifiziert werden. Ein langsamer SET-Prozess bei geringer Spannung resultiert in einem massiven Filament, welches sich nur langsam selbst auflöst. Dem gegenüber resultieren schnelle SET-Prozesse bei hoher Spannung in dendritischen Filamenten mit kurzer Relaxationszeit. Darüber hinaus wurde gezeigt, dass das Einschreiben des Filaments mit einem Spannungspuls höherer Amplitude oder längerer Dauer zu einer signifikanten Verlängerung der Relaxationszeit führt. Hierfür konnte ein geringer verbleibender Spannungsabfall über dem diffusen Memristor im LRS verantwortlich gemacht werden, der fortgesetztes Filamentwachstum bewirkt. Die gewonnen neuen Erkenntnisse unterstreichen die Bedeutung der Filamentbildung auf das Relaxationsverhalten und liefern wichtige Hinweise für optimale Operationsbedingungen dieser Schwellenwertschalter in NC-Schaltungen. Zusätzlich behandelt die Arbeit den Einfluss des CE-Materials auf die SET-Kinetik. Im Vergleich zu Pt wurde sowohl für TiN als auch für W eine geringere Schaltgeschwindigkeit der Ag/HfO_2-Zellen gefunden. Als Ursachen werden die unterschiedliche elektrokatalytische Aktivität der Metalle sowie eine Oxidation der Nichtedelmetalle an der Grenzfläche diskutiert. Ein für den Einsatz in NC-Schaltungen wichtiger Effekt ist der deutliche Einfluss eines Serienwiderstands auf das Relaxationsverhalten. Dies konnte auf die hochgradig nicht-lineare SET-Kinetik und ihren Einfluss auf die Filament-Struktur und -Größe zurückgeführt werden.

Zusammenfassend zeigt diese Arbeit, dass diffusive Memristoren auf Basis flüchtiger ECM-Zellen ein hohes Potenzial für den Einsatz als künstliche Neuronen und in NC-Anwendungen allgemein besitzen. Die erzielten Ergebnisse tragen zu einem tieferen physikalischen Verständnis des Einflusses der Filamentbildung auf die erzielbare Relaxationszeit bei und können direkt auf die Optimierung der Operationsparameter der diffusiven Memristoren in NC-Schaltungen übertragen werden.

Acknowledgments

This dissertation was written during my doctoral research at the Peter Grünberg Institute 7 (PGI-7) at the Forschungszentrum Jülich GmbH. At this point, I would like to express my sincere gratitude to the following individuals for their invaluable support and contribution to the successful completion of my thesis.

First and foremost, I would like to thank Prof. Rainer Waser for allowing me to pursue my doctoral research in his group and for serving as the first examiner of my thesis. I would also like to thank Prof. Matthias Wuttig who kindly agreed to co-examine the thesis.

I am deeply grateful to Dr. Susanne Hoffmann-Eifert for her diligent supervision and unwavering support during my research. Her scientific expertise and personal guidance have been instrumental in shaping the course of my research and professional growth.

I would like to thank Dr. Stephan Menzel for his fruitful discussions and collaborations regarding the simulation model. Special thanks go to Rana Walied Ahmad for performing and providing the simulation data. Furthermore, I thank Dr. Stefan Wiefels, Dr. Moritz Witzleben, and Stephan Außen for the insightful discussions that helped shape my papers.

Also, a lot of thanks to my colleagues Felix Cüppers, Tobias Ziegler, and Dr. Alexander Hardtdegen for their invaluable assistance in helping me navigate the logistics of living in Germany and settling into the institute at the start of my PhD. Their support and guidance were essential in ensuring a smooth and successful transition to this new environment. Special thanks to Tobias for generously providing me with probe tips that have resistor pockets, as they have been a huge help for my measurements.

I would also like to thank the ALD group members Zhaodong Wang, Hassan Sultani, Oliver Solfronk, Yonas Assefa Eshete, and Bojian Zhang as well as my colleagues from PGI-7: Niclas Schmidt, Alexander Gutsche, Judith Knabe, Luisa Bayer, Tim Kempen, Johannes Hellwig, Hsin-Yu Chen, Lisa Heymann, Anton Kaus, Marcus Wohlgemuth, Max Buczek, and numerous others for all the fun we shared inside and outside of work. Furthermore, I thank the entire PGI-7 staff for creating a positive work environment and supporting scientific growth.

I thank my student Richard Nacke for his hard work and contribution to the project.

I would like to thank the technical staff at our institute: René Borowski, Grigory Potemkin, Clemens Wiedenhöft, Dr. Stefan Trellenkamp, and Dr. Florian Lentz, who have provided invaluable assistance in lithography technologies, Jochen Friedrich for the support with the SEM, and Benjamin Bennemann for the support and maintenance of the ALD tool. Marcel Gerst for taking care of computer-related issues. Thanks Maria Garcia for always being pleasantly willing to help with administrative tasks.

I would like thank the DAAD (Deutscher Akademischer Austauschdienst) for the financial support.

Finally, I would like to thank my whole family for their unwavering love, support, and encouragement throughout my academic journey.

Declaration on publications

The presented thesis is based on the publications below.

Effect of the Threshold Kinetics on the Filament Relaxation Behavior of Ag-Based Diffusive Memristors
by S. A. Chekol, S. Menzel, R. W. Ahmad, R. Waser, and S. Hoffmann-Eifert
Published in Advanced Functional Materials, 32, 2111242, 2022, DOI: 10.1002/adfm.202111242 [1]

Strategies to Control the Relaxation Kinetics of Ag-Based Diffusive Memristors and Implications for Device Operation
by S. A. Chekol, S. Menzel, R. Waser, and S. Hoffmann-Eifert
Published in Advanced Electron Materials, 8, 2200549, 2022, DOI: 10.1002/aelm.202200549 [2]

SET Kinetics of Ag/$\mathbf{HfO_2}$-Based Diffusive Memristors under Various Counter-Electrode Materials
by S. A. Chekol, R. Nacke, S. Aussen, and S. Hoffmann-Eifert
Published in Micromachines, 14(3), 571, 2023, DOI: 10.3390/mi14030571 [3]

An Ag/$\mathbf{HfO_2}$/Pt Threshold Switching Device with an Ultra-Low Leakage ($<$ 10 fA), High On/Off Ratio ($>$ 10^{11}), and Low Threshold Voltage ($<$ 0.2 V) for Energy-Efficient Neuromorphic Computing
by *S. A. Chekol, F. Cüppers, R. Waser, and S. Hoffmann-Eifert*
Published in Proc. 2021 IEEE 13th International Memory Workshop, 2021, DOI: 10.1109/IMW51353.2021.9439601 [4]

Contents

1 Introduction 1

2 Fundamentals 7
- 2.1 Fundamentals of Memristive Devices . . . 7
- 2.2 Principle of Electrochemical Metallization (ECM) Cells . . . 9
- 2.3 Charge Carrier Transport Mechanisms and SET Kinetics of ECM Cells 14
- 2.4 Diffusive Memristors . . . 17
- 2.5 Material Properties . . . 22
  - 2.5.1 Metals . . . 22
  - 2.5.2 Oxides . . . 23

3 Experimental methods 25
- 3.1 Thin Film Deposition . . . 25
  - 3.1.1 Atomic Layer Deposition (ALD) . . . 25
  - 3.1.2 Physical Vapor Deposition (PVD) . . . 31
- 3.2 Thin Film Analysis . . . 35
- 3.3 Device Fabrication . . . 36
  - 3.3.1 Crossbar Devices . . . 36
  - 3.3.2 Nano Plug Devices . . . 38
  - 3.3.3 Samples Used in This Work . . . 39
- 3.4 Electrical Measurements . . . 40

4 Threshold Switching in Diffusive Memristors 45
- 4.1 Threshold Switching in Ag/HfO_2/Pt Cells . . . 45
  - 4.1.1 Initial Forming Behavior . . . 45
  - 4.1.2 Threshold Switching . . . 48
  - 4.1.3 Device Scalability . . . 56
  - 4.1.4 Influence of the Sweep Rate on Threshold Voltage . . . 57
  - 4.1.5 Influence of Counter Electrode on Device Performance . . . 60
- 4.2 Threshold Switching in Ag/SiO_2/Pt Cell . . . 67
  - 4.2.1 Initial Forming Behavior . . . 67
  - 4.2.2 Threshold Switching . . . 68
- 4.3 Comparison and Summary . . . 69

5 SET Kinetics of Diffusive Memristors 71
5.1 SET Kinetics of HfO_2-based Diffusive Memristor 71
5.1.1 Impact of Voltage on the SET Kinetics 72
5.1.2 Impact of a Series Resistor on the SET Kinetics 75
5.1.3 Influence of Counter Electrode on the SET Kinetics 80
5.2 SET Kinetics of SiO_2-based Diffusive Memristor 84
5.3 Comparison and Summary 86

6 Relaxation Behavior of Diffusive Memristors 89
6.1 Relaxation Dynamics of HfO_2-based Cells 89
6.1.1 Impact of Programming Scheme on Relaxation Behavior . . . 89
6.1.2 Origin of the Relaxation Time Dependence on Programming Pulse Width 91
6.1.3 Impact of Series Resistor on the Relaxation Dynamics 93
6.1.4 Impact of Sweep Rate on the Relaxation Dynamics 100
6.2 Relaxation Dynamics of Ag/SiO_2-based Cells 105
6.2.1 Impact of Programming Scheme on Relaxation Behavior . . . 105
6.3 Comparison and Summary 106

7 Correlation between the SET Kinetics and Relaxation Behavior 109
7.1 Interdependence of SET and Relaxation Processes 109
7.2 Filament Evolution During SET Process and Relaxation Behavior . . 111
7.3 Series Resistor and its Implications in Device Operation 116

8 Applications of Diffusive Memristors 119
8.1 Design Rule of Diffusive Memristors for Emerging Applications 119
8.2 Diffusive Memristors as Synaptic Emulators 121
8.3 Diffusive Memristors as Artificial Neuronal Elements 124

9 Summary and Outlook 129

Appendix A Numerical and Analytical JART ECM Models 133

Appendix B Device Fabrication Protocols 135
B.1 Micro-crossbar structure fabrication | AZ 5214E resist 135
B.2 Micro-crossbar structure fabrication | AZ MIR 701 and AZ nLOF 2020 resists 137
B.3 Nanoplug structure fabrication 139

List of Abbreviations 141

List of Publications 159

Bibliography 161

Chapter 1

Introduction

Since the invention of the transistor in 1947, electronic technologies have had a profound impact on our daily lives. Computers have made significant progress over the past few decades, thanks to the miniaturization, optimization, and integration of semiconductor electronics. Today's computer design is based on the von Neumann architecture, which involves a physically separated Central Processing Unit (CPU) and Memory Unit connected by a data bus [5]. Nevertheless, the emergence of future technologies such as artificial intelligence and machine learning has led to an enormous increase in the size and complexity of data. As a result, the limitations of the von Neumann architecture have become relevant, as a significant amount of energy is expended in shuttling data back and forth [6, 7]. It has been predicted that by 2050, the amount of energy needed to process all data will be equivalent to the total energy produced worldwide [8]. This is a significant challenge that current research must address.

One of the potential contenders for future computing is neuromorphic architecture. This computer architecture mimics the structure and function of the biological brain using networks of simple processing units called "neurons" that interact with each other through connections called "synapses" to form what is commonly referred to as neural networks. These systems are optimized for cognition tasks and, here, they provide significant advantages over the classical computing architectures in terms of power consumption by leveraging in-memory computation and massive parallelism. (Figure 1.1a) [9–11].

For optimal use of neuromorphic computing (NC), efficient, fast, and scalable synapses and neurons are essential. Artificial synapses need to be non-volatile for permanent information storage and exhibit plasticity. While some aspects of plasticity have been

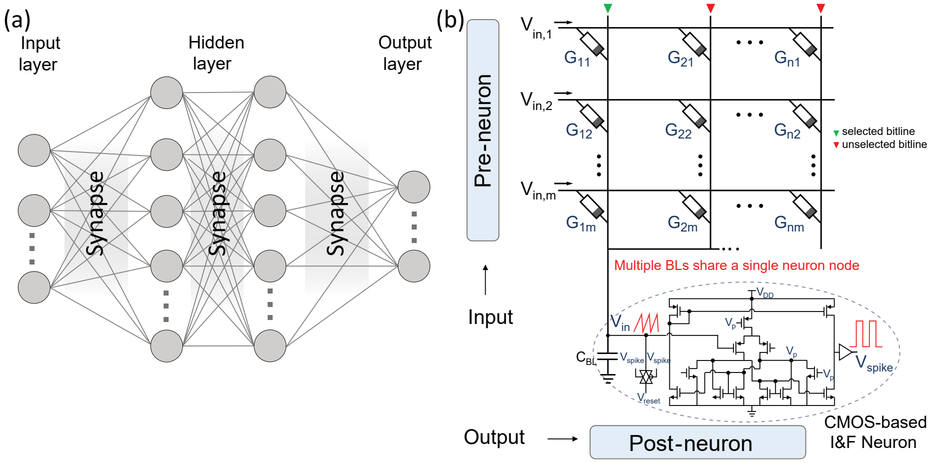
(a)
Input layer
Hidden layer
Output layer
Synapse
Synapse
Synapse
(b)
Pre-neuron
Input
Output
$V_{in,1}$
$V_{in,2}$
$V_{in,m}$
G_{11}
G_{21}
G_{n1}
G_{12}
G_{22}
G_{n2}
G_{1m}
G_{2m}
G_{nm}
selected bitline
unselected bitline
Multiple BLs share a single neuron node
V_{DD}
V_{in}
V_p
C_{BL}
V_{spike}
V_{reset}
V_{spike}
CMOS-based I&F Neuron
Post-neuron

Figure 1.1: (a) Illustration of a neural network consisting of an input layer, hidden layers, and an output layer. (b) Equivalent circuit representation of one layer with a CMOS-based neuron connected to the output side of the layer. (b) is redrawn with permission from [4]. Copyright © 2021 IEEE.

achieved with silicon semiconductor technology, scalability, and energy consumption problems prevent large-scale implementation. In this context, efforts are underway to explore the use of non-volatile and more energy-efficient memristive (short for 'memory and resistor') technologies, such as phase change RAM (PCRAM) [12–14], magnetic RAM (MRAM) [15, 16], redox-based resistive RAM (ReRAM) [17, 18], and ferroelectric RAM (FRAM) [19, 20]. A recent example of this is the NeuRRAM chip from Stanford University, which uses ReRAM and has demonstrated exceptional energy efficiency while achieving accuracy comparable to software realizations on complementary metal oxide semiconductor (CMOS) systems [21].

On the other hand, the neuronal component needs to possess volatility to reset itself after each output signal. Currently, CMOS-based analog-to-digital (ADC) and digital-to-analog (DAC) converters are widely used to compute and interpret information in modern computing systems [22–24]. However, these converters are made up of several transistors, which results in a large footprint, leading to an area and power bottleneck. The large space requirement forces a single artificial neuron to be shared with multiple artificial synapses, resulting in sequential readout and loss of the massive parallelism, which is one of the key features of NC (Figure 1.1b). Even with the best optimized neuromorphic chips, a substantial amount of power is consumed by the ADC and

DAC converter modules. Therefore, there is a real need to find more energy-efficient and scalable artificial neuron elements for the realization of future neuromorphic chips.

Threshold switching (TS)-based devices are emerging as a potential candidate for artificial neurons thanks to their promising scalability and energy efficiency. Some of the main types of TS devices are of technological interest: Ovonic threshold switches (OTS), insulator-to-metal-transition (IMT) devices, Mott-devices, and diffusive memristors. OTS operates by trapping and detrapping of charge carriers in chalcogenide-based (Te- or Se-based) systems [25–28]. On the other hand, IMT is observed in metal oxide systems, where an electro-thermal-induced phase transition triggers threshold switching. Examples are VO_2 [29] and NbO_2 [30, 31]. The purely electric field-driven transition via an electronic avalanche breakdown mechanism is referred to as Mott transition seen, for example, in Cr-doped V_2O_3 [29]. Diffusive memristors, based on volatile electrochemical metallization memory (ECM) cells lose their programmed low resistance state (LRS) as soon as the voltage bias is removed [1, 32–35]. This is achieved by the formation of a small, unstable metallic filament (Cu or Ag) that spontaneously breaks after a period of time, returning the resistance of the cell to its original high resistance state (HRS).

Among the different types of TS devices, diffusive memristors have a significant advantage in terms of power consumption thanks to their extremely low leakage current and low threshold voltages, as illustrated in Figure 1.2a. This makes them ideal candidates for applications in emerging NC areas. Among others, diffusive memristors have been proposed for use as selectors [36, 37], artificial neurons [33, 34, 38], true random number generators (TRNG) [39, 40], and short-term synapses [33]. The volatile nature and simple structure of diffusive memristors make them particularly suitable for use as artificial neurons (e.g., in spiking neural networks (SNNs)). In addition, their small size allows them to be placed directly at the end of each bit-line, enabling parallel calculations, as shown in Figure 1.2b.

Information encoding in neural networks using artificial neurons can be accomplished in a variety of ways, including spike frequency, spike amplitude and shape, and spike timing. Most of these coding techniques leverage the temporal behavior of the neuron, thus the time constants of the SET and relaxation processes become very important. In diffusive memristors both the SET (t_{set}) and relaxation (t_{r}) times can be modulated over several orders of magnitude depending on the programming condition, which provides a unique advantage of designing a system with a specific combination of t_{set} and t_{r} [1]. Despite these interesting aspects of diffusive memristors, their use in the

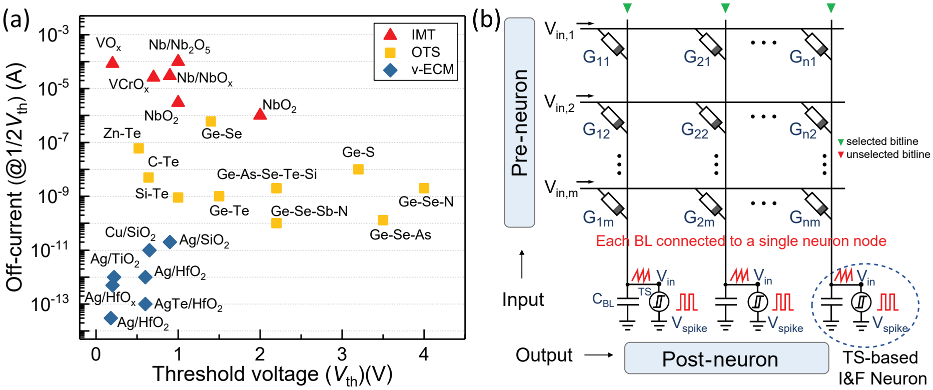

Figure 1.2: (a) Equivalent circuit illustration of memristive arrays connected to a threshold switching based neuron. (b) Leakage current and threshold voltage of various types of threshold switching devices. Data in (a) are collected from [25–30, 36, 41–54]. (b) is redrawn with permission from [4]. Copyright © 2021 IEEE.

emerging field of NC is hampered by limited knowledge of the mechanism behind the volatile properties of diffusive memristor cells, which include the self-dissolution of the conducting filament.

Efforts have been made to understand the filament's nature through electrical and physical analyses. The formation of a chain-like filament consisting of Ag nanoparticles in a $Pt/TiO_2/Ag$ cell at a low compliance current of 1 nA was reported by Hsiung et al. [55]. They explained their findings using the Rayleigh instability theorem. Sun et al. observed a similar discontinuous chain-like filament in a $Pt/SiO_2/Ag$ cell at lower compliance currents of 5 and 10 nA [56]. However, for a higher compliance current of 100 µA, a continuous conductive filament was observed, leading to the suggestion that the switching occurs due to the modulation of the tunneling barrier caused by ion migration between neighboring nanoparticles or charge trapping/detrapping. Wang et al. explained the relaxation process of diffusive memristors based on a thermodynamic approach utilizing the surface diffusion mechanism [57]. Taking a defined filament shape and size as input parameters, good agreement between simulated and experimental data was obtained. In the experiments, the filament's strength was modified qualitatively using current compliance variation. On the other hand, the dependence of t_{set} on the external bias has been shown in multiple publications and, yet, lack to make connections with the t_{r} [58–60].

The goal of this work is to develop a deeper understanding of the underlying physical processes involved in the relaxation dynamics of diffusive memristors, in particular for the reference system Ag/HfO_2/Pt. The unique approach is to link the voltage and time dependence of filament formation in the SET event to the relaxation time required for filament self-dissolution. For this purpose, reproducible diffusive memristor cells will be fabricated from Ag/HfO_2/Pt as cross-point structures with a few micrometers in size. Atomic layer deposition (ALD) will enable high quality and pin-hole-free thin oxide films that conformally cover the Pt counter electrode (CE). The oxide thickness will be varied between 2 and 5 nm. The influence of the material choice will be studied using SiO_2 thin films instead of HfO_2, and replacing the CE by TiN and W. These high work function materials are more widely used in CMOS technology than Pt. Effects of material variations will be studied based on the main switching characteristics of diffusive memristors including the electroforming and threshold switching behaviors. In addition, the comprehensive study includes an in-depth analysis of the SET switching kinetics and the relaxation dynamics and their correlation using the Ag/HfO_2/Pt devices as a reference system. Therefore, switching and relaxation behavior are characterized for various HfO_2 film thicknesses, device area, and additional circuitry elements such as a series resistor. The findings of this work will be supported by numerical and analytical simulations under the consideration of the device structure and material properties used in this study. In total, this work aims to establish a comprehensive physical understanding of the dependence of t_{set} and t_{r} on circuit design and programming conditions. To its end, this knowledge will be used to propose a design strategy for a diffusive memristor device with predictable and tunable t_{set} and t_{r} for various applications.

To elucidate these points in a clear and organized way, this thesis is structured as follows: In Chapter 2, the fundamentals and principles of emerging memristive devices including non-volatile ECM cells and diffusive memristors are described. In addition, a dynamic compact model that has been successfully applied to explain the dynamics of AgI-based, SiO_2-based, and GeS-based ECM cells (called JART ECM v1 [61]) is introduced in this chapter. Furthermore, a brief overview of the properties of the materials used in this work is given. Chapter 3 deals with the deposition and analysis of the HfO_2 and SiO_2 thin films and different metals used in this work, where the principles of thin film deposition methods including ALD and physical vapor deposition (PVD), specifically sputtering, process optimization as well as the analysis techniques of the grown layers, device fabrication, and electrical characterization methods are explained. Chapter 4 presents the experimental results on the threshold switching characteristics of Ag/HfO_2- and Ag/SiO_2-based diffusive memristor cells, including the forming behavior. The main part of this work which is dedicated to the SET kinetics and relaxation dynamics of Ag/HfO_2/Pt- and Ag/SiO_2/Pt-based diffusive memristors is presented in Chapter 5 and 6, respectively. Furthermore, a modified model of the JART ECM, which is introduced in Chapter 2 is used to analyze the experimentally observed SET kinetics behavior of diffusive memristors. The influence of CE on the SET kinetics of Ag/HfO_2/Pt-based diffusive memristor devices, including the electrocatalytic activity of the metals and the role of native oxides at the switching layer/CE interface is discussed. Additionally, the impact of a series resistor on the SET kinetics and relaxation behavior of Ag/HfO_2/Pt-based diffusive memristor devices is investigated in Chapter 5 and 6, respectively. Furthermore, the role of parasitic capacitance is discussed. The correlation between SET and relaxation processes, including the tradeoff between t_{set} and t_{r} with respect to the programming scheme is dealt with in Chapter 7. In addition, based on the findings of Chapter 5 and 6, different physical mechanisms of silver filament growth are discussed in this chapter. In Chapter 8 design rules of diffusive memristors for emerging applications and a proof-of-concept demonstration are given. A summary of the findings of this work and an outlook for further directions is given in the final Chapter 9.

Chapter 2

Fundamentals

Fundamentals of memristive devices are described in Section 2.1. Section 2.2 presents the working principle of ECM-type memristive cells. The electronic transport mechanism and the SET kinetics of ECM cells is discussed in Section 2.3. A compact model for the SET kinetics of ECM cells (developed by Menzel et al. [62]) is also introduced in this section. Diffusive memristors are introduced in Section 2.4. Furthermore, an overview of different applications of diffusive memristors is given. Finally, in Section 2.5, a comprehensive view of the material properties of oxides that are used in this work is given.

2.1 Fundamentals of Memristive Devices

Memristive devices can generally be classified into three groups, as presented in Figure 2.1, based on magnetic effects, electrostatic effects, and atomic configuration effects [63]. Magnetic tunnel junctions (MTJ) exhibit a phenomenon called tunnel magnetoresistance, in which the probability of electrons tunneling through the junction depends on the direction of the magnetization [64, 65]. This phenomenon is used to develop magnetic RAM (MRAM) [66] and spin-transfer torque MRAM (STT-MRAM) [67]. The electrostatic effect can originate from ferroelectric polarization or from electron trapping-detrapping mechanism, which involves the movement of electrons into and out of traps in the material. Both processes affect the resistance of the material, leading to the development of various memristive devices such as ferroelectric tunneling junction (FTJ) [68], ferroelectric diode [69], Memflash [70], and multiferrioc tunnel junction (MFTJ) [71]. There are four types of memristive devices that are based on atomic configurations: (i) those using mechanical switches such as nano-electrochemical memories (NEM) [72], (ii) those using organic molecules [73], (iii) those using crystallographic phases such as phase change memories (PCM) [74], and (iv) those using the movement of ions to induce redox effects [75]. The last category, which is based on redox effects, can be further divided into thermochemical memory (TCM), valence change memory (VCM), and ECM.

TCM cells are made up of two inert metal electrodes and an insulating layer. The insulating layer exhibits a high and low resistance when being in its most oxidized and reduced states, respectively. As a result, upon the application of voltage, the resistance can be modulated due to local Joule heating and redox reactions leading to the formation of a conductive filament. Such mechanism can be observed for example in NiO-based TCM cells. For further details in TCM, the reader is referred to ref. [76].

VCMs use the valence change of a metal cation in a resistance switching metal oxide matrix to control the resistance of the memory cell. A VCM cell typically consists of two metals (one chemically active and one inert) and a transition metal oxide (TMO) layer. The chemically active metal electrode acts as an oxygen exchange layer (OEL) and generates defects in the TMO layer, such as oxygen vacancies, when a positive voltage is applied. The resistance of the VCM cell is controlled by the arrangement of these defects, which can form a filamentary path of oxygen-deficient TMO material. This path can be opened or closed, resulting in LRS or HRS respectively. Detailed information on VCMs can be found in ref. [63].

ECM cells are made up of an ion-conducting and electronically insulating layer sandwiched between an electrochemically AE such as Ag or Cu and an inert CE [77, 78]. The switching between the HRS and LRS is, therefore, based on the formation and dissolution of a metallic conductive filament within the insulating layer due to the movement of active metal ions such as Ag^{+} and $Cu^{+(2+)}$. The complete process is explained in more detail in the next section.

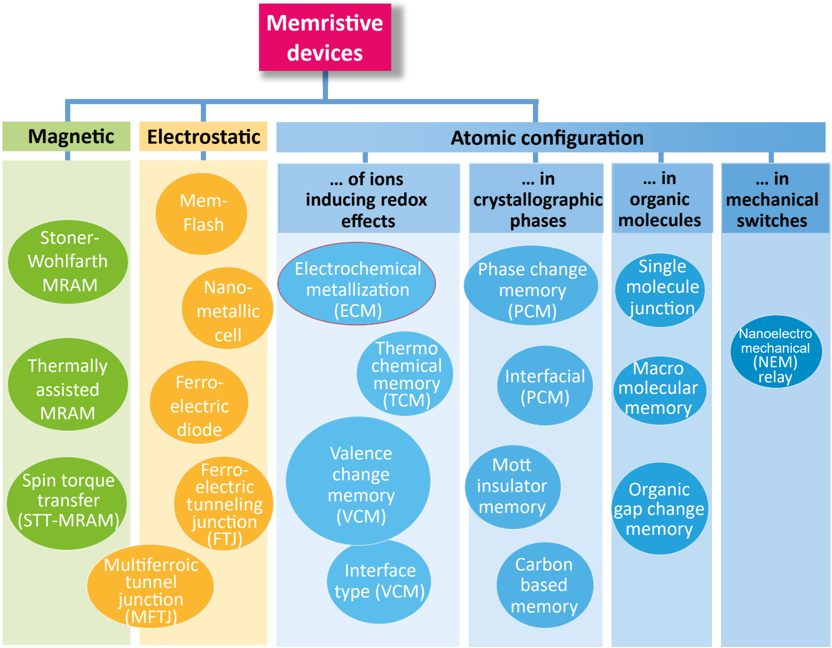
Memristive devices
Magnetic
Electrostatic
Atomic configuration
... of ions inducing redox effects
... in crystallographic phases
... in organic molecules
... in mechanical switches
Stoner-Wohlfarth MRAM
Thermally assisted MRAM
Spin torque transfer (STT-MRAM)
Mem-Flash
Nano-metallic cell
Ferro-electric diode
Ferro-electric tunneling junction (FTJ)
Multiferroic tunnel junction (MFTJ)
Electrochemical metallization (ECM)
Thermo chemical memory (TCM)
Valence change memory (VCM)
Interface type (VCM)
Phase change memory (PCM)
Interfacial (PCM)
Mott insulator memory
Carbon based memory
Single molecule junction
Macro molecular memory
Organic gap change memory
Nanoelectro mechanical (NEM) relay

Figure 2.1: Emerging memristive devices taxonomy. The ECM cell, which is the main focus of this thesis, is highlighted by a red circle. Redrawn with permission from [63].

2.2 Principle of Electrochemical Metallization (ECM) Cells

The insulating layer in ECM cells can cover a variety of materials, including pure ion electrolytes such as AgI [79], mixed ion-electron conductors (MIECs) such as Ge_xSe_{1-x} [80, 81], and insulators such as SiO_2 [82, 83], Ta_2O_5 [84], and HfO_2 [85, 86]. For the AE, on the other hand, pure metals such as Ag, Cu, Te, and Ni or alloys of Ag and Cu containing materials such as AgTe, AgCu, CuTe can be used [54, 87, 88]. Finally, the CE can be Pt, Ir, W, TiN, or Au [89–91]. Figure 2.2 schematically shows the basic operation principle of a non-volatile ECM cell along with a typical current-voltage characteristic using a quasi-static triangular voltage signal.

Initially, the cell is in the HRS which could have a resistance of GΩ up to TΩ, depending on the type of electrolyte material used (Figure 2.2Ⓐ). Upon the application of a sufficiently high enough positive voltage to the AE, the following physiochemical

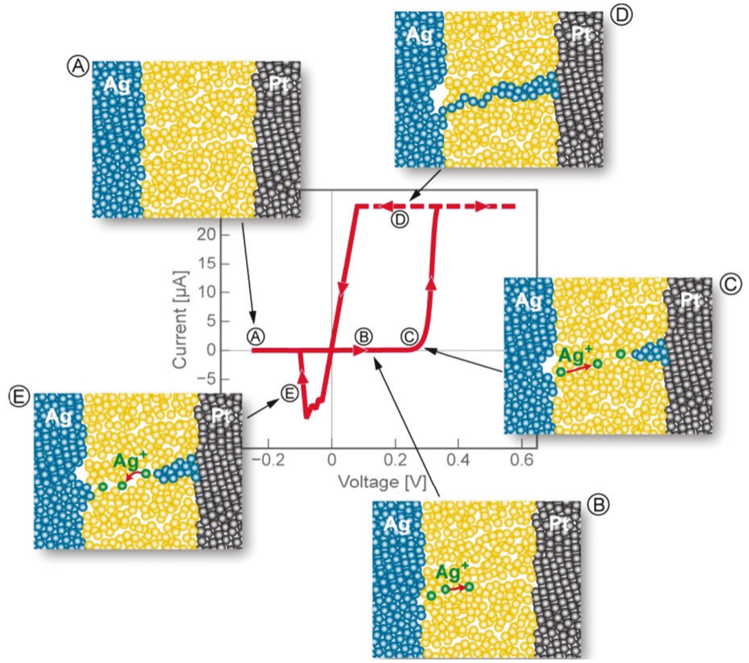
Ⓐ
Ag
Pt
Ⓓ
Ag
Pt
Ⓒ
Ag
Pt
Ag+
Ⓔ
Ag
Pt
Ag+
Ⓑ
Ag
Pt
Ag+
Current [µA]
20
15
10
5
0
−5
Voltage [V]
−0.2
0
0.2
0.4
0.6
Ⓐ
Ⓑ
Ⓒ
Ⓓ
Ⓔ

Figure 2.2: Typical operating mechanism of an ECM cell. Adapted with permission from [77].

processes are involved in the cell's SET operation:

(i) anodic dissolution of the AE metal M according to the reaction

$$\mathrm{M} \longrightarrow \mathrm{M}^{z+} + z\mathrm{e}^{-}$$

where M^{z+} represents the metal cations in the solid electrolyte;

(ii) migration of the M^{z+} cations across the electrolyte due to the high electric field (Figure 2.2Ⓑ);

(iii) reduction of metal ions M^{z+} to their elemental form and deposition on the surface of the CE (Figure 2.2Ⓒ) according to the following reaction

$$\mathrm{M}^{z+} + z\mathrm{e}^{-} \longrightarrow \mathrm{M}$$

As more and more metal M is deposited at the CE surface (Figure 2.2Ⓒ), a metallic conductive filament can be formed inside the electrolyte and bridges the two electrodes electrically (Figure 2.2Ⓓ). This leads to an abrupt jump in resistance to the LRS (ON state) at a specific SET voltage V_{SET}. The electrical connection through the conductive filament can be achieved by either a tunneling gap or galvanic contact, depending on the device structure and operational current range. The LRS is maintained as long as the conductive filament is present between the two electrodes. To RESET the cell to the HRS, a sufficient voltage of opposite polarity must be applied. This causes the filament to rupture (Figure 2.2Ⓔ) and the cell to return to its initial, non-conductive state (Figure 2.2Ⓔ) at a certain RESET voltage V_{RESET}.

Here it is worth noting that a first switching cycle called "electroforming," or simply "forming," is required at a higher voltage of V_{form} than V_{SET} for electrolyte films that do not contain cations of the electrochemically active metal during or after fabrication. This process is typically necessary for electrolytes that are made up of solid-state oxide films such as SiO_2 or HfO_2. During this process, mobile M ions are incorporated into the electrolyte matrix. During subsequent cycles, much less voltage is sufficient to utilize a reproducible resistive switching due to the growth channel established during the forming process that may act as an easy transport channel for active metal ions and an easy growth path for the filament.

There are two important considerations in designing ECM cells: the ion transport or diffusion path. These transport paths could arise from structural inhomogeneities due to short-range structural defects, density differences, or local chemical deviations in the composition of the electrolyte film. These inhomogeneities may be present initially due to deposition methods, interaction with the environment, strain effects, or may arise during electrochemical measurements [93, 94]. Second, due to charge neutrality requirements, the anodic reaction should be supported by a counter-reaction at the CE [83, 91]. The possible counter-reaction process could be a reduction of M^{z+} at the CE surface, through an escape of the trapped electron, or other reaction processes such as reduction of moisture [95]. This is determined by the fundamental properties of the materials used as electrolytes, electrode materials, and the electrochemical reaction rates at the interfaces.

Chalcogenides containing active metals represent a special case. The added active metal such as Ag or Cu reacts with the chalcogen within the compound to create mobile cations, thus no need for counter-reaction from the CE surface during the switching [91]. Since the mobility of the cations is quite high and the activation

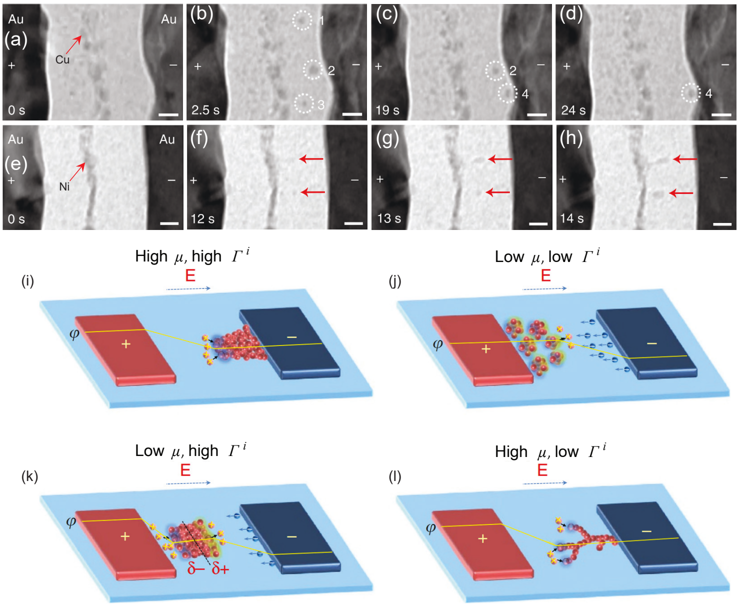

Figure 2.3: Different filament growth mechanisms in diffusive memristors. Reproduced with permission from [92].

energies are low due to the open structure of the amorphous chalcogenides, cations can diffuse fast. However, for oxide systems where Ag and Cu ions are foreign species to the host electrolyte matrix, to initiate the $M \longrightarrow M^{z+} + ze^{-}$ reaction at the AE/electrolyte interface, a counter-reaction at the CE/electrolyte interface must take place. For oxide-based ECM cells it is suggested by Valov et al. that this counter-reaction is supported by the reduction of moisture at the CE [95]. Moisture can be incorporated during fabrication or from the air through the side of electrodes. However, once the forming has taken place and active metal ions reached and reduced at the CE surface, the active metal redox couple reaction can also be used as a CE reaction for further switching cycles.

Furthermore, once nanoscale inclusions such as clusters of active metal are formed within the electrolyte, they dynamically change their shape, size, and position upon the application of electric field. These dynamic behaviors are mainly governed by kinetic factors such as redox rates (Γ^{i}) of cluster i and ion mobility (μ). This leads to different filament growth modes and structures (Figure 2.3a-h). Based on the two factors μ, which is an electrolyte property, and Γ^{i} which accounts for the electrode/electrolyte interfaces, Yang et al. introduced four different classes of systems which can be distinguished as follows [92]:

1. Both Γ^i and μ are high and homogeneous throughout the solid electrolyte film (Figure 2.3i). Thin films from classical solid electrolyte materials (e.g. Ag_2S and AgI) with non-polarizable electrode reactions fall in this category. In such systems ions can reach the CE without agglomerating and nucleating within the electrolyte. Thus the filament growth is initiated at CE and proceeds towards the AE, leading to an inverted cone-shaped filament.

2. Low Γ^i and low and inhomogeneous μ (Figure 2.3j). The ions can pile up within the matrix, reach nucleation conditions, and start growth within the electrolyte, thus further filament growth takes place by means of cluster displacement through repeated splitting and merging processes. Due to the low reaction rates and low ion mobility, these processes are strongly influenced by inhomogeneities inside the electrolyte. Furthermore, predicting the behavior of the system in this category will not be easy as the inhomogeneities are statistically generated. The typical representative material for this category is filament growth in amorphous Si.

3. High Γ^i and low μ (Figure 2.3k). For these systems, nucleation can also occur within the electrolyte matrix and the particle dynamics will be determined from the distances and interactions between the nuclei.

4. Low Γ^i and high μ (Figure 2.3l). Here nucleation occurs at the CE surface due to the fast μ, however, due to the low Γ^i, ion supply is limited. As a result, reduction occurs predominantly at the edges where the electric field strength is high. This leads to a branched filament growth towards the AE.

So far material properties are discussed. Another important factor in the switching of ECM cells is the cation transport and electrode reaction mechanisms under electric field. This will be discussed in detail in the next section. Furthermore, an ECM compact model called Jülich Aachen Research Alliance - JART ECM v1 [61] developed by Menzel et al. [62] will also be introduced.

2.3 Charge Carrier Transport Mechanisms and SET Kinetics of ECM Cells

As discussed in the previous section, the switching in ECM cells involves the transport of active metal cations in the electrolyte film, step (ii), and electrode reactions both at the AE/electrolyte and CE/electrolyte interfaces, steps (i) and (iii), and electrocrystallization or nucleation, step (iii). Assuming that M^{z+} is the only mobile ionic species during the switching process, the ion transport will occur by migration of the cations in the electrolyte matrix. This process can be described by the model of Mott-Gurney for an electric field driven and thermally activated ion hopping process and the corresponding current density can be calculated by [62, 96]:

$$j_{\mathrm{hop}} = 2zecaf \exp\left(-\frac{\Delta G_{\mathrm{hop}}}{k_{\mathrm{B}}T}\right) \sinh\left(\frac{aze}{2k_{\mathrm{B}}T}E\right) \tag{2.1}$$

where z is the ion charge number, e the electron charge, c the concentration of cations M^{z+}, f the attempt frequency, ΔG_{hop} the hopping barrier, k_{B} the Boltzmann constant, T the absolute temperature in Kelvin, and a the hopping distance, which is in the range of interatomic distances.

The electric field strength E, which is the driving force for ion migration, is related to the potential drop across the electrolyte and its thickness by $E = \eta_{\mathrm{hop}}/x$, where η_{hop} is the hopping overpotential and the state variable x describes the tunneling gap between the growing filament and the electrode. For electric fields $E >> 2k_{\mathrm{B}}T/aze$ the ion transport depends exponentially on the electric field, in contrast, for low electric fields $E << 2k_{\mathrm{B}}T/aze$ the dependence becomes linear.

The electron transfer reaction at the electrode/electrolyte interfaces during the anodic oxidation (step (i)) and cathodic reduction (step (ii)) can be mathematically described by the Butler-Volmer equation [62]:

$$j_{\mathrm{et}} = j_{0,\mathrm{et}} \left[\exp\left(\frac{(1-\alpha)\,ze}{k_{\mathrm{B}}T}\eta_{\mathrm{et}}\right) - \exp\left(\frac{\alpha ze}{k_{\mathrm{B}}T}\eta_{\mathrm{et}}\right)\right] \tag{2.2}$$

and the exchange current density $j_{0,\mathrm{et}}$ is given by:

$$j_{0,\mathrm{et}} = zeck_{0,\mathrm{et}} \exp\left(-\frac{\Delta G_{\mathrm{et}}}{k_{\mathrm{B}}T}\right) \tag{2.3}$$

Here, α is the charge transfer coefficient, η_{et} the electron transfer overpotential, ΔG_{et} the electron transfer activation energy, and $k_{0,\mathrm{et}}$ the rate constant.

The first and the second exponential terms in eqn. 2.2 represent the oxidation and the reduction processes, respectively.

Finally, the full filament formation includes the nucleation and growth processes (step (iii)). The formation of a metallic phase on a foreign surface starts with nucleation, which could start on the CE surface or within the electrolyte material, depending on the particular material (Figure 2.3) and experimental conditions. The formed nucleus needs to have a specific number of metal atoms N_{c} to form a critical cluster size for further growth. This depends on the applied voltage and, as a result, the nucleation contributes to the increase in reaction overpotential. Accordingly, the nucleation time can be described by the following equation [62]:

$$t_{\mathrm{nuc}} = t_{0,\mathrm{nuc}} \exp\left(\frac{\Delta G_{\mathrm{nuc}}}{k_{\mathrm{B}}T}\right) \exp\left(-\frac{(N_{\mathrm{c}} + \alpha_{\mathrm{nuc}})\, ze}{k_{\mathrm{B}}T} \eta_{\mathrm{nuc}}\right) \tag{2.4}$$

where $t_{0,\mathrm{nuc}}$ is a prefactor, ΔG_{nuc} the nucleation overpotential, and α_{nuc} the charge transfer coefficient during nucleation.

Assuming the state variable x describes the tunneling gap between the growing filament and the electrode, the growth can be modeled by the change in the tunneling gap and can be mathematically expressed using Faraday's law [62, 97]:

$$\frac{\delta x}{\delta t} = -\frac{m_{\mathrm{Me}}}{ze\rho_{\mathrm{m,Me}}} j_{\mathrm{ion}} \tag{2.5}$$

Here, m_{Me} is the atomic mass of the deposited metal and $\rho_{\mathrm{m,Me}}$ its density.

Compact model for the SET kinetics of ECM cells

The JART ECM model is a physics-based fully numerical compact model developed by using the above set of equations to successfully simulate the behavior of ECM cells.

All SET kinetics simulations performed in this thesis are based on this model. An illustration of the electrochemical processes during SET switching and the respective equivalent circuit diagram used in the model are shown in Figure A.1. The simulation is performed in two steps: nucleation and growth. First, the nucleation time is calculated by using eqn. 2.4. Once nucleation takes place, growth starts at time t_{nuc}. Then the growth is modeled by the change in the tunneling gap as explained above using Faraday's law (eqn. 2.3). The current density j_{ion} is calculated from the hopping current (eqn. 2.1) and the Butler-Volmer equation (eqn. 2.2).

At the initial stage of filament formation, the electronic current is negligible. However, as the filament grows and the gap x decreases, the electron tunneling current becomes significant and this can be represented by Simmon's equation as [62, 98]:

$$I_{\mathrm{Tu}} = C\frac{3\sqrt{2m_{\mathrm{eff}}\Delta W_0}}{2x}\left(-\frac{e}{h}\right)^2 \exp\left(-\frac{4\pi x}{h}\sqrt{2m_{\mathrm{eff}}\Delta W_0}\right) A_{\mathrm{fil}} V_{\mathrm{Tu}} \tag{2.6}$$

Here, m_{eff} denotes the electron effective mass, ΔW_0 the tunneling barrier height, h Planck's constant, A_{fi} the area of the filament, and V_{Tu} the voltage over the tunneling barrier. C is a fitting parameter with a given value of 2.7 [62]. Based on the equivalent circuit diagram, the tunneling voltage is given by $V_{\mathrm{Tu}} = \eta_{\mathrm{ac}} - \eta_{\mathrm{fil}} + \eta_{\mathrm{hop}}$ and by using Kirchhoff's law, the cell voltage can be calculated by

$$V_{\mathrm{cell}} = I_{\mathrm{cell}}\left(R_{\mathrm{el}} + R_{\mathrm{s}} + \rho_{\mathrm{fil}}\left(L - x\right)/A_{\mathrm{fil}}\right) + V_{\mathrm{Tu}} \tag{2.7}$$

Here, R_{s} is an optional series resistor and R_{el} ($R_{\mathrm{el,ac}}$ + $R_{\mathrm{el,in}}$) is the total electrode resistance. The filament resistance R_{fil} can be calculated by $\rho_{\mathrm{fil}}\left(L - x\right)/A_{\mathrm{fil}}$. For further information on the model the reader is referred to the thesis of Stephan Menzel [99] and reference [62].

There are two versions of this model available: one is a fully numerical simulation model, and the other is a simplified analytical model. Both versions produce comparable results, and this has been verified (Appendix A). Both models are implemented to explain mainly the SET kinetics of diffusive memristors. The numerical simulation data were provided by Rana Walied Ahmad, a Ph.D. student at PGI 7. For simplicity and in the interest of saving computing time, the majority of simulation data in this thesis were obtained using the analytical model.

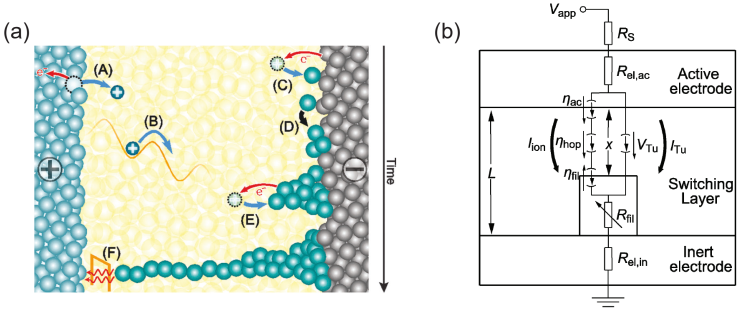

Figure 2.4: Illustration of the electrochemical processes during SET switching and the respective equivalent circuit diagram. Taken from [62].

2.4 Diffusive Memristors

In this section, diffusive memristor will be introduced. Diffusive memristors are ECM-type resistive switching cells with volatile behavior, meaning that their programmed state (LRS) after a successful SET process cannot be kept after the applied voltage is removed [100]. The volatile and non-volatile nature of ECMs is determined by the lifetime of the conductive filament that is formed during the SET process. In standard non-volatile ECM, the filament formed during SET is stable and a RESET process is needed to bring the cell back to HRS [101, 102]. On the other hand, diffusive memristor cells have unstable filaments, i.e. a much shorter lifetime in the range of nanoseconds to a few seconds, and the transition from LRS to HRS is achieved through a spontaneous self-rupture of the filament, which is called relaxation process [57]. The time it takes for such a relaxation process is referred to as relaxation time. A schematic of a typical diffusive memristor cell with a threshold-type switching characteristic is depicted in Figure 2.5.

The nature of the filament has been investigated by several researchers by using physical characterization techniques such as microscopy imaging. Hsiung et al. showed the formation of a chain-like filament composed of Ag nanoparticles in a planar Pt/TiO_2/Ag cell that is formed at a low compliance current of 1 nA and explained their observation using the Rayleigh instability theorem [55]. For increased programming compliance current of 100 µA, for example, Sun et al. observed a continuous conductive filament in a Pt/SiO_2/Ag cell while observing similar discontinuous chain-like filament for low compliance current of 5 and 10 nA, and thus suggesting the switching is due to modulation of the tunneling barrier by either ion migration between neighboring

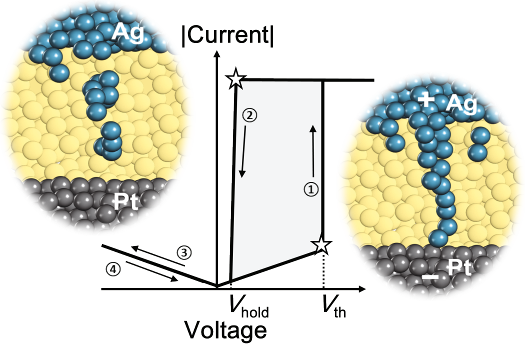

Figure 2.5: Schematic diagram illustrating the threshold switching phenomenon in diffusive memristors.

nanoparticles or charge trapping/detrapping [56]. The driving force for the self-relaxation behavior can originate from surface energy minimization or surface tension effects [55, 57, 103], thermo-diffusion [104], mechanical stress [93], steric repulsion effect [52], or a combination of some, depending on the nature of the filament and the surrounding switching matrix. In 2014 Sun et al. demonstrated that the surface energy of Ag clusters is sufficient to alter the shape of sub-10-nanometer Ag nanoparticles through surface diffusion when subjected to mechanical pressure [105]. This supports the hypothesis that surface energy minimization plays a role in the volatility of diffusive memristors as theoretically predicted by Hurk et al. [106] and Guzman et al. [107, 108].

One of the most revealing experimental studies on the switching mechanism of diffusive memristor was reported by Wang et al. in 2016 [109]. In this work, the authors performed an in situ high resolution transmission electron microscopy (HRTEM) investigation using a planar Au/SiO_xN_y:Ag/Au device. By applying a constant voltage in situ, the authors observed the formation of a thin wire-like filament and an abrupt jump in the current (Figure 2.6a-e). After the removal of the external voltage, the long and thin filament spontaneously transformed into clusters of particles with an almost circular shape in projection (Figure 2.6f-h). This demonstrates the role of interfacial energy minimization as the driving force for the relaxation process in diffusive memristors. Here, it is worth mentioning that it is possible to change an ECM cell switching behavior from volatile to non-volatile or vice versa by properly designing the device stack, for instance by adjusting the thickness of the switching

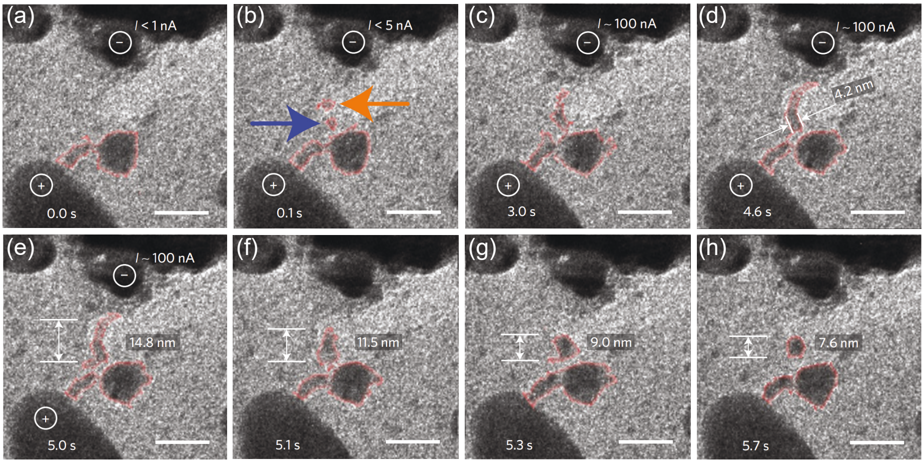

Figure 2.6: In situ TEM observation of the (a)-(f) filament formation and (f)-(h) filament relaxation in diffusive memristors upon the application and removal of external bias, respectively. The scale bar is 20 nm. Redrawn with permission from [109].

film or by controlling the programming voltage/current amplitude during forming and/or switching. Li et al. demonstrated both volatile and non-volatile switching in the same ECM device with a material stack of Cu/GeTe/Al_2O_3/Pt [110]. The authors showed that when a thin Al_2O_3 (3 nm) is used the cell exhibited a non-volatile behavior, however, when the Al_2O_3 thickness increased ($>$ 5 nm) the cell switched in volatile fashion. Such transitions between two switching types are explained by the formation of a filament with different morphologies for the two systems. Furthermore, Sun et al. [56] and Chae et al. [111] also observed both volatile and non-volatile behaviors by using Ag/SiO_2/Pt and Ag/TiO_2/Pt stacks, respectively. They observed that by increasing the programming current, the behavior of the cell transitioned from volatile to non-volatile. They attributed this observation to the different conductive filament morphologies that were present in the cell. They found that in volatile mode, the filament consisted of isolated Ag nanocrystals, while in non-volatile mode, the filament was composed of continuous Ag nanocrystals.

In addition to microscopical studies and electrical characterizations, many research groups have attempted to formulate theoretical models to mathematically represent the switching mechanism in diffusive memristors. Ambrogio et al. suggested that mechanical compressive stress induced by filament growth could impact ion hopping in two migration directions, leading to switching asymmetry and even spontaneous

filament dissolution [93]. Hsiung et al. proposed that structural instability might be the cause of the volatility, by comparing the total free energy of a rod filament under perturbation to that of a chain of spheres in the framework of Rayleigh instability [55]. Wang et al. proposed a model which links electrical, nanomechanical, and heat degrees of freedom and with this, they could interpret experimentally observed properties of diffusive memristors [109]. The filament formation is modeled as field-induced and Joule heating-assisted breakup of larger clusters. This process results in the continuous elongation of the clusters, leading to the formation of a conductive channel. On the other hand, the rupture of the filament is thought to occur by the breaking up of the filament in order to reduce the interfacial energy. This is modeled under the framework of the Gibbs–Thomson effect, which states that the curvature of a phase boundary is related to the interfacial energy.
Recently, a molecular dynamics (MD) simulation performed by Wang et al. confirmed the spontaneous breakdown of a continuous nanoscale Ag filament inside an oxide matrix without additional external forces [57]. They proposed a universal surface-limited self-diffusion mechanism for the rupture of the conductive filament during the relaxation process. This is schematically depicted in Figure 2.7, which shows surface diffusion controlled initial stage filament rupture (Figure 2.7a-b) followed by a post-lifetime evolution of the filament clusters governed by Ostwald ripening (Figure 2.7c). The filament lifetime is related to the size as follows [57]:

$$\tau_\mathrm{r} = \frac{4{r_\mathrm{o}}^4}{B} \tag{2.8}$$

where

$$B = \frac{D_\mathrm{s}\gamma\delta^4}{kT} \tag{2.9}$$

Here, B is a material sensitive parameter that strongly depends on the type of the filament atom. r_0 defines the filament diameter and it is understood as the size of the filament at the weakest part. Furthermore, D_s is the surface diffusion coefficient, γ is the surface energy, δ is the interatomic distance, k is Boltzmann's constant, and T is the temperature.
According to this model, $t_\mathrm{r}(=\tau_\mathrm{r})$ should strongly depend on the filament size r_0 and follow Herring's scaling law [113]: $t_\mathrm{r} \propto r_\mathrm{o}^4$. Furthermore, by using this model the

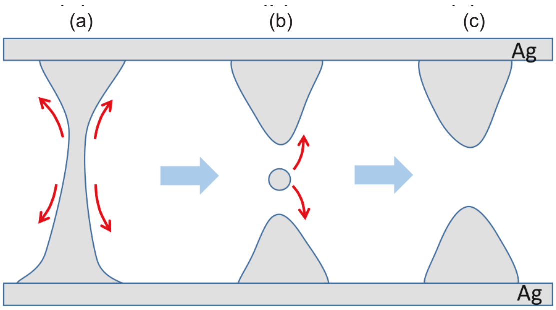

Figure 2.7: (a)-(b) Surface diffusion controlled initial stage of filament rupture. (c) Post-lifetime evolution of the filament particle through Ostwald ripening mechanism [112]. Adapted from [57].

authors were able to successfully fit various previously reported results on Ag- and Cu-based ECM cells [57].

As pointed out in Chapter 1, diffusive memristors have been proposed for use in various applications including as a selector device in crossbar arrays to mitigate the sneak path currents issue [36], as atom-switch integrated with metal oxide semiconductor field effect transistor (MOSFET) to achieve a steep sub-threshold slope [114], and for TRNG by exploiting the stochasticity of the SET event [39]. Recently, triggered by the unique thresholding and temporal behavior, diffusive memristors are being exploited extensively for application in NC areas. For example, in their research, Wang et al. employed a SiO_xN_y:Ag-based diffusive memristor to mimic neuronal functionalities in their fully memristive neural networks and to perform various tasks such as pattern recognition [34]. The diffusive memristor-based neuron carries out signal processing by integrating inputs received from the synapses and generating an output signal. Furthermore, diffusive memristors have been used for realizing short-term synaptic plasticity (STP) [109, 115], short-term plasticity to long-term plasticity (LTP) transition [115, 116], and spike-timing-dependent plasticity (STDP) [109, 117]. Wang et al. demonstrated short-term facilitation and depression on a Pt/SiO_xN_y:Ag/Pt-based diffusive memristor cell depending on the frequency of the input stimulation [109]. They found that high-frequency stimulation increases conductance, while low-frequency stimulation causes a slower increase in conductance, or even a decrease in conductance starting from the same initial conductance.

2.5 Material Properties

In the following, a short overview of the materials used to build the stacks investigated in this work is given.

2.5.1 Metals

In this thesis the following metals are used for the fabrication of diffusive memristor cells: Platinum (Pt), Silver (Ag), Tungsten (W), and Titanium Nitride (TiN). Furthermore, all metals in this thesis are deposited by sputtering technique.

Pt is a transition metal with the atomic number 78 and has a face-centered-cubic (FCC) crystal structure with a lattice parameter of 0.392 nm [118]. It is a highly valued metal for its electronic properties and its electronic structure is characterized by the presence of 5d and 6s electrons in its outermost electron shell. Pt is an inert metal and has a low specific resistivity of $1.0 \cdot 10^{-7}\ \Omega\,\mathrm{m}$ [119] at room temperature and a specific heat capacity of 26 $\mathrm{Jmol^{-1}K^{-1}}$ [119]. Its high electrical conductivity and high catalytic activity make it an excellent material for use as electrical wiring and capping material and in catalytic applications. Pt has a work function of 5.3 eV [120].

Ag is a relatively soft transition metal with an atomic number of 47 and has also an FCC crystal structure with a lattice parameter of 0.406 nm. It has an atomic radius of 172 pm. With resistivity of $1.7 \cdot 10^{-8}\,\Omega\,\mathrm{m}$ [62] and thermal conductivity of 429 $\mathrm{W/m \cdot K}$, at room temperature [121], Ag has the highest known electrical and thermal conductivity of all metals, making it a useful material for electronic applications. It also has high diffusivity and can undergo redox reaction upon electric field, making it ideal for constructing redox based resistive switches. Ag thin film has a work function of 4.28 eV in its polycrystalline state [122, 123], but it varies for different crystal faces such as 4.64 eV, 4.52 eV and 4.74 eV for the (100), (110), and (111) faces, respectively [124].

W is a rare metal with an atomic number of 74. It has a body-centered-cubic (BCC) crystal structure with $a = 0.316$ nm and a nearest neighbor distance of 0.273 nm. W can form a group of oxides like $\mathrm{WO_x}$, where x can vary between 2 and 3 [125]. It is widely used in the semiconductor industry as metal connects, mainly due to its fairly inertness to wet chemical attack, readily etched in fluorine plasma, and its good conformality during the chemical vapor deposition (CVD) process. Furthermore, W has a specific heat capacity of 24.34 $\mathrm{Jmol^{-1}K^{-1}}$ [126] and resistivity of $5.44 \cdot 10^{-8}\,\Omega\,\mathrm{m}$ [127] at room temperature, and has a work function of 4.54 eV in its polycrystalline state [128].

Finally, TiN belongs to a class of compounds commonly called oxynitrides with the general formula $\mathrm{Ti_nN_mO_p}$. It has a rock salt, such as in sodium chloride (NaCl), like a cubic structure with a lattice constant of 0.4241 nm. TiN is well known for its oxidation resistance behavior, which is attributed to the formation of a native oxide or oxynitride layer that partially covers its surface upon exposure to an oxidant environment, hence used as a coating material. Polycrystalline TiN has a resistivity ranging from $1.0 \cdot 10^{-6}$ to $4.0 \cdot 10^{-7}\,\Omega\,\mathrm{m}$ [129, 130], however, values up to $1.4 \cdot 10^{-7}\,\Omega\,\mathrm{m}$ have been reported for single crystalline TiN [131]. Furthermore, TiN has a work function in the range of $4.30 - 4.65$ eV [132]. TiN is a CMOS-compatible metal and is among the materials used for electrical connections in the micro-electronic industry.

2.5.2 Oxides

$\mathrm{HfO_2}$

$\mathrm{HfO_2}$ is a high-k material with a dielectric constant between 18 and 25 [133–136]. In addition, $\mathrm{HfO_2}$ forms a stable interface to $\mathrm{Si/SiO_2}$ and is therefore a prominent material for use in CMOS-technology. $\mathrm{HfO_2}$ crystallizes into the cubic, tetragonal, monoclinic, or orthorhombic phase. Under normal pressure, only the tetragonal ($> 1750\,^{\circ}\mathrm{C}$) and the monoclinic phase ($< 1750\,^{\circ}\mathrm{C}$) are reported in bulk-$\mathrm{HfO_2}$ [137].

The lattice distances of the monoclinc phase are 5.116 Å, 5.172 Å and 5.295 Å [138]. It has a melting temperature of 2758 °C. $\mathrm{HfO_2}$ has a bandgap that depends on the crystallinity and the phase of the material. For polycrytalline and amorphous $\mathrm{HfO_2}$, 5.80 eV and 5.62 eV have been reported, respectively [139]. Simulations reveal that the bandgap of crystalline $\mathrm{HfO_2}$ differs for each phase: the bandgap of monoclinic $\mathrm{HfO_2}$ has been calculated to 5.75 eV, in contrast to 5.60 eV (cubic) and 5.95 eV (tetragonal) [140]. The electron affinity is determined to be 2.50 eV and 2.90 eV for polycrytalline and amorphous $\mathrm{HfO_2}$, respectively [141, 142]. Furthermore, different effective masses have been reported for $\mathrm{HfO_2}$, ranging from $0.1\,\mathrm{m_e}$ [143] up to $2.0\,\mathrm{m_e}$ [144].

$\mathrm{HfO_2}$ in the monoclinic phase has a specific resistivity of $1.0 \cdot 10^{8}\,\Omega\,\mathrm{m}$ [145]. The specific heat capacity and thermal conductivity are $60\,\mathrm{J\,mol^{-1}\,K^{-1}}$ and $1.1\,\mathrm{W\,m^{-1}\,K^{-1}}$, respectively [119]. $\mathrm{HfO_2}$ is deposited using ALD in this work.

SiO_2

SiO_2 is a compound that plays an important role in modern technology. Its unique properties make it a common material in electronic devices. It is abundant in nature and can exist in either a crystalline or amorphous form. Crystalline SiO_2 (c-SiO_2), also known as quartz, is a highly ordered structure that is composed of repeating SiO_4 tetrahedrons and has a very high melting point of around 1700°C [146] and high thermal stability and a band gap of 9.0 eV [147]. On the other hand, amorphous SiO_2 (a-SiO_2) has a dielectric constant of 3.9 eV [148] and a band gap of close to 9.0 eV [149], similar to that of c-SiO_2. Thin films of a-SiO_2 are commonly employed in microelectronic systems for various purposes, such as serving as a dielectric in capacitors and transistors, as an isolation layer for various elements, and as a structural or sacrificial layer in different micro-fabrication processes.

Additionally, a-SiO_2 have a reported electron affinity a-SiO_2 of $0.8\,\mathrm{eV}$ [150] and an effective electron mass of $0.84\,\mathrm{m_e}$ [89]. The resistivity of high quality a-SiO_2 ranges between 10^{13}–$10^{14}\,\Omega\,\mathrm{m}$ [148]. Further, the specific heat capacity and thermal conductivity are reported to be $43.5\,\mathrm{J\,mol^{-1}\,K^{-1}}$ [151] and $1.31\,\mathrm{W\,m^{-1}\,K^{-1}}$ [152], respectively. Thanks to the well-understood properties, a-SiO_2 is one of the well-studied candidates of oxide materials in the research field of resistive switching. In this work, the SiO_2 film is deposited using ALD.

Chapter 3

Experimental methods

This chapter will introduce the thin film deposition methods, device fabrication, and the various physical and electrical characterization techniques used in this work. In Section 3.1, the principle and the benefits of ALD and PVD methods will be discussed. Specifically, the sputter deposition technique, which is the method employed to grow the metal films used in this work, will be the focus. Section 3.2 deals with the methods used for thin film characterization. Section 3.3 gives details on the tools used to characterize the quality of the different thin films and device fabrication processes. Furthermore, a final overview of all fabricated and tested samples will also be given in this section. Section 3.4 provides an overview of the electrical setups used for the device characterization.

3.1 Thin Film Deposition

3.1.1 Atomic Layer Deposition (ALD)

ALD is a thin film deposition technique that is used to deposit thin layers of material onto a substrate. This technique is applied in a variety of applications, including semiconductor manufacturing, energy storage, and biomedical applications. The basic principle of ALD lies in the sequential, self-limiting surface reactions to deposit thin films of material onto a substrate. This is achieved by using precursors, which are typically gaseous or liquid compounds that are introduced into a chamber containing the substrate. ALD is a special type of the chemical vapor deposition (CVD) method where gaseous reactants also known as precursors, are sequentially introduced into the reaction chamber, resulting in the formation of the desired material through chemical surface reactions [153, 154]. In contrast, in a standard CVD process, the reactants are introduced simultaneously into the chamber and react in the gas phase near the substrate.

One of the key advantages of ALD is its ability to deposit very thin, conformal films with excellent control over thickness and composition, meaning that the deposition follows the surface contours so that there is the same thickness of the deposited material over the whole surface regardless of surface roughness, topography, or defects. This is because the reactions that take place during the ALD process are self-limiting and stop when all of the reactive sites on the substrate surface have been covered. This allows the growth of ultrathin dense layers with thicknesses below 1 nm and conformal films in 3D structures, such as pinholes and trenches, with high aspect ratios, making it well-suited for use in DRAM and 3D NAND technologies [155].

The ALD process is simple and can be explained as follows, as depicted schematically in Figure 3.1. In the first step, the first precursor gas, (Precursor A) is introduced and it will attach to all the surfaces as a monolayer in a process called chemisorption (Figure 3.1, I). This process stops when all available surface sites are occupied and saturation is achieved. In step two, the excess gas, including the residual precursor and reaction byproducts, is removed in a process often referred to as purging with the help of an inert gas, usually Ar gas (Figure 3.1, II). In the third step, a second gas (Precursor B) is introduced which also condenses and is chemisorbed on top of the first layer. The first and second precursors then undergo a reaction or decomposition to convert them into the desired material (Figure 3.1, III). Finally, the residual precursor and reaction byproducts are again purged (Figure 3.1, IV). This sequence can be repeated as many times as needed to achieve the desired film thickness.

In a typical ALD process of metal oxide deposition, Precursor A serves as a metal source and Precursor B serves as a source for oxygen as a co-reactant. The oxygen source could be water vapor, oxygen plasma, or ozone.

Therefore, the total thickness of an ALD-grown layer only depends on the number of ALD cycles or repetitions, thus, the growth rate is defined as growth per cycle (GPC) and should be constant. However, this is not to say that the deposition process does not have deviations. Several parameters require optimization to ensure a constant GPC and a balance between high-quality film and efficiency. For example, make sure enough precursor material is present to react with all surface sites and that there is enough time between the precursor dose and precursor purge to allow reactions to occur. Additionally, the purge time must be long enough to remove all residuals from

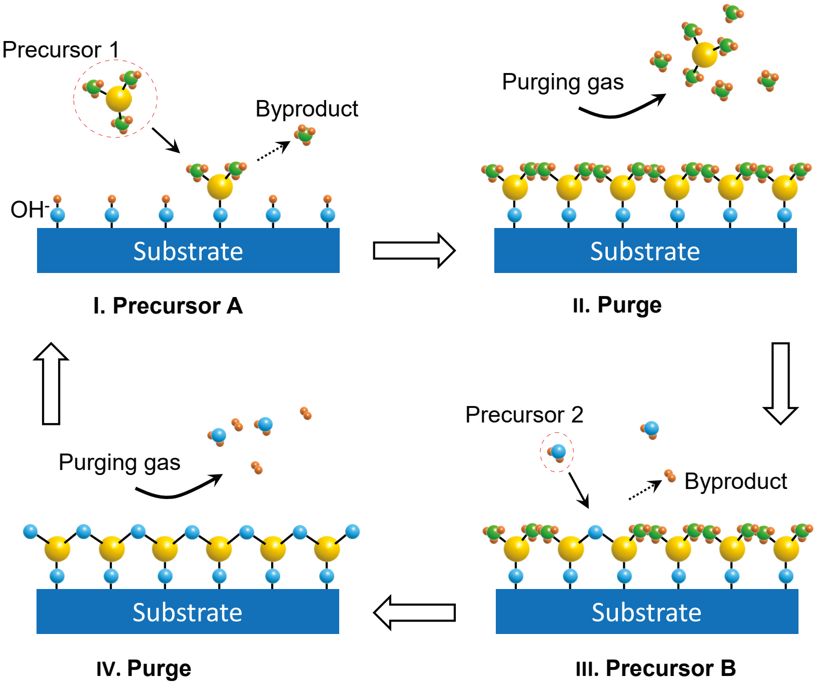
Precursor 1
Byproduct
OH-
Substrate
I. Precursor A
Purging gas
Substrate
II. Purge
Precursor 2
Byproduct
Substrate
III. Precursor B
Purging gas
Substrate
IV. Purge

Figure 3.1: Exemplary schematic diagram of an ALD cycle from a metal Precursor A (metal) and Precursor B (water vapor). I: Precursor material is introduced into the chamber, where a sample with an OH-terminated surface is placed. The precursor reacts with these groups and leaves behind byproducts. II: After the purge, the remaining precursor and the byproduct are purged, so that only chemisorbed precursor molecules stay. III: Water vapor is introduced in the chamber and reacts with the surface, producing a new OH-terminated surface. IV: After the second purge, a metal oxide layer has been grown and growth is continued with step I.

the chamber. Too long precursor dose time and too long purge time will be a waste of material and time, respectively. Thus, finding the right balance of these times is crucial for achieving a stable and reproducible ALD process.

Deposition (heater stage) temperature is another key factor for the ALD process. The temperature can be used to aid the thermal decomposition of the gases applied, thus making substrate temperature an important control parameter. If the substrate temperature is too low, it can slow down or even prevent chemical reactions and decrease the GPC due to the lack of thermal energy. However, if the surface coverage is maintained at a low temperature, the condensation of precursor material on the

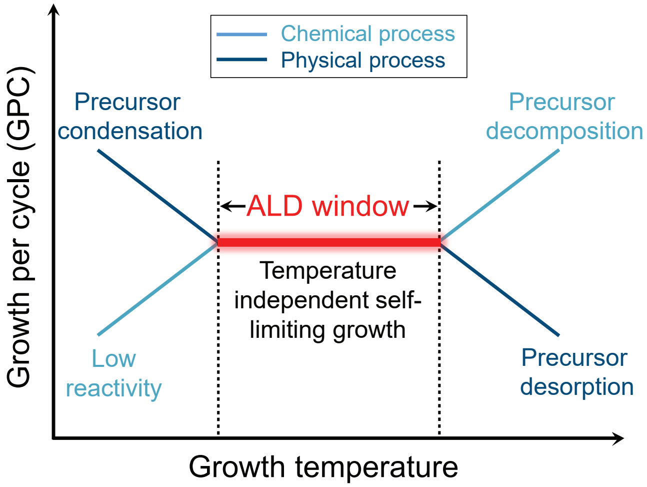
Chemical process
Physical process
Precursor condensation
Precursor decomposition
ALD window
Temperature independent self-limiting growth
Low reactivity
Precursor desorption
Growth per cycle (GPC)
Growth temperature

Figure 3.2: Schematic diagram of the temperature-dependent growth per cycle (GPC) of a typical ALD process. If the temperature is too low, the GPC can decrease as no chemical reactions take place due to the lack of thermal energy. On the other side, the precursor material might condense on the sample surface, leading to an increased GPC. If the temperature is too high, precursor material might decompose onto or desorb from the surface, leading to an increase or decrease in GPC, respectively. Redrawn from [156].

surface can increase GPC. On the other hand, if the temperature is too high, precursor material may decompose, leading to an increase in GPC, or desorb from the surface, resulting in a decrease in GPC. In both cases of low or high temperatures, non-ideal ALD growth can occur, leading to poor-quality layers and difficulty in controlling thickness. Therefore, the goal is to operate the ALD process within a temperature range known as the "ALD window", where ideal growth and temperature-independent GPC occur. This is depicted in Figure 3.2. An ideal ALD process is always a self-limiting [157].

In this thesis, metal oxide films of HfO_2 and SiO_2 are grown by using plasma-enhanced ALD (PE-ALD). These processes require two distinct precursors: one for the metal source and another (co-reactant) for the oxygen source. The selection of appropriate precursors is another crucial aspect of establishing a successful ALD process. The precursor must be reactive at the growth temperature, but also thermally stable to prevent decomposition. Additionally, it should have high volatility for easy transport and distribution in the ALD chamber and be reactive with surface sites. Furthermore, it is important to consider any potential byproducts or residuals, as well as cost. The ALD tool, the precursors and co-reactants, and the recipes used in this work are described in the following section.

Remote plasma FlexAL™ ALD system

The ALD system used in this work is the FlexAL™ by *Oxford Instruments.* This tool is part of the Nanocluster of Forchungszentrum Jülich GmbH. The system consists of a load-lock and main chamber which are separated by a gate valve (shutter). The picture of the tool and the schematics of the cross-section of the main chamber are shown in Figure 3.3. A cabinet that can accommodate 6 precursors is fitted to the tool, allowing the installation of different precursor materials at the same time. During the process, the precursors are delivered to the chamber in the vapor phase from the heated bubbler container via heated lines. For metal sources of high vapor pressure, the metal source vapor is directly extracted from the heated canister. However, for metal sources of lower vapor pressure, bubbling with Ar gas in this case, is used to help reduce the surface energy so that more molecules can enter the gas phase. Different gas lines, including nitrogen, oxygen, hydrogen, ammonia, and argon, are connected to the system to be used as a co-reactant.

As mentioned above, the chamber and load-lock are separated by a gate valve and samples can be transferred to the main chamber via the load-lock. This helps to prevent the ALD chamber from any contamination from outside. The load-lock is connected to an Edwards turbo pump and can be pumped down to a pressure of about 10^{-9} mbar. Furthermore, prior to loading to the main chamber, samples are heated at a temperature of 150 °C for 30 minutes inside the load-lock via a lamp heater to remove any surface contaminants from the wafer.

The ALD used in this work has a remote plasma configuration. That means the plasma ignition zone is located far above the substrate surface. This prevents electron and ion interaction with the surface, thus helping to reduce any plasma-induced damage to the sample. A schematic of the remote plasma configuration is depicted in Fig 3.3b.

HfO_2 and SiO_2 ALD processes

The depositions of HfO_2 and SiO_2 are conducted using the metal-organic precursors tetrakis(ethylmethylamino)hafnium (TEMAH, $Hf(NCH_3C_2H_5)_4$) and bis(t-butylamino)silane

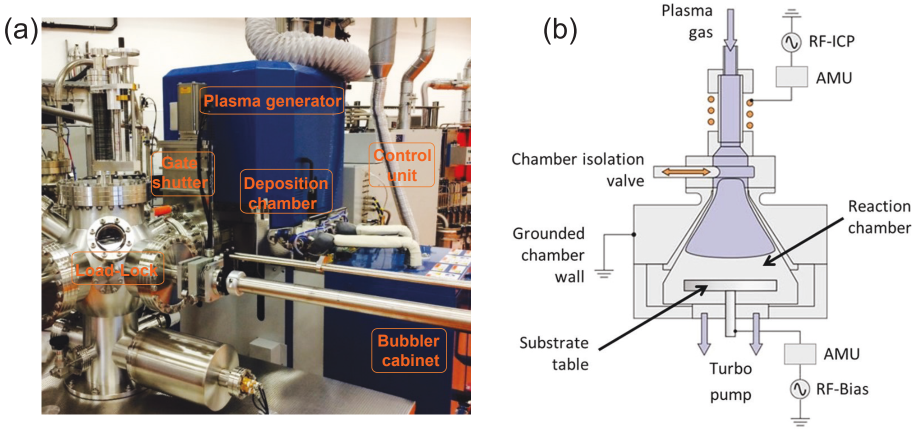
(a)
Plasma generator
Gate shutter
Deposition chamber
Control unit
Load Lock
Bubbler cabinet
(b)
Plasma gas
RF-ICP
AMU
Chamber isolation valve
Reaction chamber
Grounded chamber wall
Substrate table
Turbo pump
AMU
RF-Bias

Figure 3.3: Left: Photo of the FlexAL™ALD system. Right: Cross-section of the ALD chamber, modified from [158].

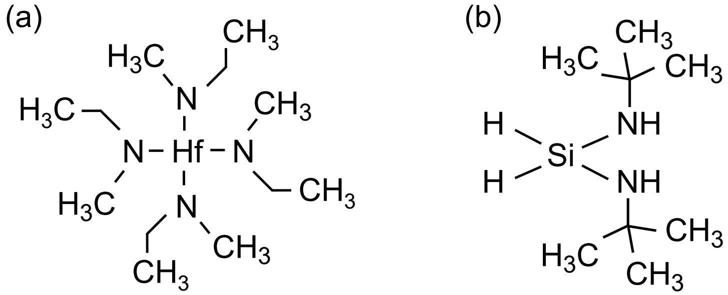

Figure 3.4: Planar chemical representations of the ALD metal sources used in this work: (a) TEMAH and (b) BTBAS.

(BTBAS, $SiH_2(NHC_4H_9)_2$), respectively. Two-dimensional representations of the precursors are depicted in Figure 3.4. For the HfO_2 process, the TEMAH bubbler temperature is set at 70 °C, and the TEMAH is bubbled by Ar. On the other hand, the BTBAS is heated at a much lower temperature of 35 °C. The substrate is heated at 250 °C during both processes. Note that the growth temperature here refers to the heater temperature and the actual temperature at the surface of the sample could likely be lower. An oxygen plasma provided by a radio frequency remote plasma generator is used as an oxidizing agent both for the HfO_2 and SiO_2 processes.

Graphical sketches of the process flow for both metal-oxide depositions are shown in

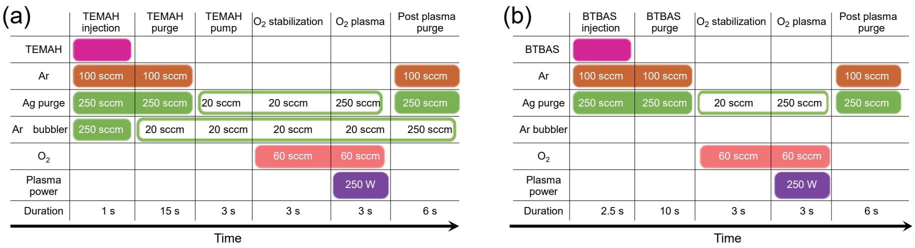
(a)
TEMAH injection
TEMAH purge
TEMAH pump
O2 stabilization
O2 plasma
Post plasma purge
TEMAH
Ar
100 sccm
100 sccm
100 sccm
Ag purge
250 sccm
250 sccm
20 sccm
20 sccm
250 sccm
250 sccm
Ar bubbler
250 sccm
20 sccm
20 sccm
20 sccm
20 sccm
250 sccm
O2
60 sccm
60 sccm
Plasma power
250 W
Duration
1 s
15 s
3 s
3 s
3 s
6 s
Time
(b)
BTBAS injection
BTBAS purge
O2 stabilization
O2 plasma
Post plasma purge
BTBAS
Ar
100 sccm
100 sccm
100 sccm
Ag purge
250 sccm
250 sccm
20 sccm
250 sccm
250 sccm
Ar bubbler
O2
60 sccm
60 sccm
Plasma power
250 W
Duration
2.5 s
10 s
3 s
3 s
6 s
Time

Figure 3.5: Sketch of the ALD processes for PE-ALD (a) HfO_2 and (b) SiO_2.

Figure 3.5. First, the carrier Ar gas is injected into the heated precursor container, while Ar is also supplied through the direct and purge lines to the chamber. These gas flows are maintained during the surface reaction and the following precursor purge step. Then, all the valves are closed for a duration of 3 s as a precursor pump time. This is added to address the sticky nature of the metal precursor, and during this time the exhaust pump removes any metal precursor and byproducts from the chamber. Afterward, an oxygen stabilization step is performed to enable a stable oxygen plasma in the short pulse time of 3 s. During the subsequent plasma step, the surface layer is oxidized and the byproducts of the reaction as well as the remaining oxygen gas are purged from the chamber during the final step of the cycle. The recipes shown in Figure 3.5 result in a growth of 0.100 and 0.116 nm per cycle for the HfO_2 and SiO_2 films, respectively.

3.1.2 Physical Vapor Deposition (PVD)

A PVD technique is used to deposit all metal layers in this work. Different films of Ag, Pt, W, TiN, and Ti (adhesion) are used in the fabrication of devices within this thesis. Sputter deposition, one of the most common types of PVD method, is used to deposit these metal layers. In the following section, the principle of sputter deposition, the type of sputter tool used in this work, and the recipes for all deposited films will be introduced.

Sputter deposition

Sputtering is a technique of ejection of atoms by the bombardment of a solid target by energetic ions, as a result of collisions between the incident energetic ions with surface atoms. The basic principle of the sputter deposition process is sketched in Figure 3.6.

The target material and the substrate wafer are mounted opposite to each other in a high–vacuum (HV) chamber that is filled with a sputtering gas, which is often Ar gas. The target can be powered by direct current (DC) for electrically conductive targets, radio frequency (RF) mainly for non-conductive targets, or a combination of the two. Since sputtering is a purely physical process, deposition of a compound layer is done either from a single compound target, through co–sputtering from multiple targets, or it must be done through the addition of a reactive gas to the plasma, i.e. reactive sputtering.

In DC sputtering a constant voltage is applied to the target while the substrate is grounded. By applying a high negative voltage to the target, positively charged ions are attracted and accelerated, due to the electric field, toward the target. Then the energetic ions bombard the target with sufficient energy to initiate sputtering, ejecting near–surface target atoms [159]. The ejected atoms traverse toward the substrate and deposit on the surface of the substrate wafer. Sputter yield, the measure of the removal rate of surface target atoms, is defined as a ratio between the number of sputter-ejected atoms and the number of incident ions and it depends on the surface binding energy of the target atom species, the relative masses of the ionized gas atoms and target atoms, the ion kinetic energy, and the incident angle of the impact. On the other hand, in the case of RF sputtering, the cathodic target is coupled to an RF generator which accelerates electrons and argon ions in both directions. At the standard frequency (13.56 MHz) or multiples thereof the mobility of free electrons is much faster in the ionized gas compared to the Ar ions, and as a result, a negative DC bias with respect to the anodic substrate is generated. Due to this, the Ar ions are accelerated toward the cathode and impact into the target which results in sputtering. RF sputtering is ideal for non-conductive targets as the static charging of the target material, which hinders a stable plasma, can be avoided. To further increase the deposition rate, magnetron sputtering could be used for both DC and RF sputtering processes. This is achieved by putting a permanent magnet behind the target, which contributes a magnetic field close to the target surface. This forces electrons close to the surface to follow a circular trajectory, and as a result, the electrons are kept in the vicinity of the target surface for a longer time, thus leading to more ionization of the Ar gas and enhanced sputter rate.

Two different sputter tools were used during the fabrication of samples in this work: *Scienta Omicron* sputter system and Univex 450 C sputter tool by *Oerlikon Leybold*. The *Scienta Omicron* is an off–axis sputter tool and it is located at Nanocluster. This

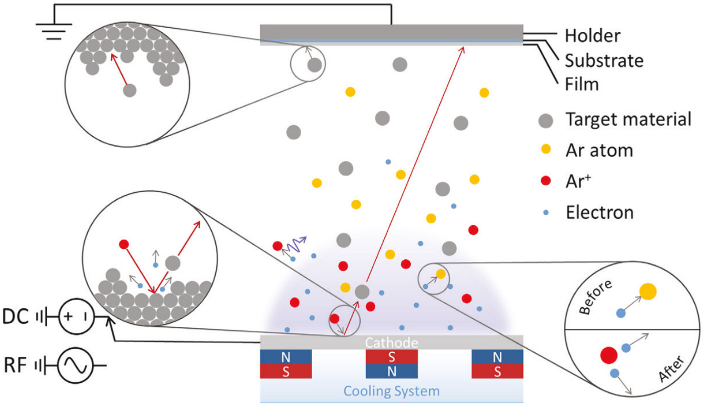

Figure 3.6: Basics of sputter process. Adapted from [160].

tool is equipped with a chamber that offers a very low base pressure of 10^{-10} mbar and a load-lock with a vacuum pressure that can reach 10^{-8} mbar (Figure 3.7a). Films of Pt, W, and TiN together with the 5 nm thick Ti adhesion layer were deposited as a bottom electrode (BE) by using this tool. The sputter parameters for the deposition of bottom metal layers are shown in Table 3.1. On the other hand, the Univex 450 C sputter tool is an on-axis system and it is located at the Peter Grünberg Institute (PGI 7) in the Forschungszentrum Jülich GmbH. One of the advantages of this tool is that it has six independent deposition chambers with a central load-lock and a central transfer chamber with a vacuum and an automated robot arm. This is schematically depicted in Figure 3.7b. Multiple target materials can be mounted individually at every deposition chamber, thus allowing sequential deposition of different materials without breaking the vacuum. Furthermore, all chambers, including the load-lock and central transfer chamber, are equipped with separate pump systems and a programmable logic controller (PLC). This provides a platform for a fully automated process with a programmable and recipe-controlled process sequence. The Ag and the Pt capping layer in all samples used in this work are deposited by using this tool. Detailed sputter parameters for the deposition of top metal layers are presented in Table 3.2.

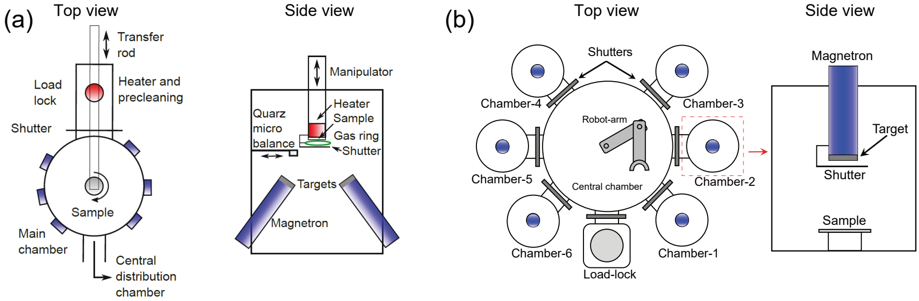
(a)
Top view
Transfer rod
Load lock
Heater and precleaning
Shutter
Sample
Main chamber
Central distribution chamber
Side view
Manipulator
Quarz micro balance
Heater
Sample
Gas ring
Shutter
Targets
Magnetron
(b)
Top view
Shutters
Chamber-4
Chamber-3
Robot-arm
Chamber-5
Chamber-2
Central chamber
Chamber-6
Chamber-1
Load-lock
Side view
Magnetron
Target
Shutter
Sample

Figure 3.7: Top and side views of (a) the Omicron off-axis sputter tool and (b) the Univex 450 C on-axis sputter tool. Picture in (a) is adapted from [161].

Table 3.1: Sputter parameters for the bottom metal layer fabrication in the Omicron system.

Parameter	Ti adhesion	Pt BE	TiN BE	W BE
Sputter type	RF	DC	RF	RF
Sputter power (W)	300	100	100	300
Ar flow (sccm)	30	30	30	30
Target tilt (°)	47	45.8	53	51
Manipulator height (cm)	132	132	132	132
Process pressure (mbar)	0.028	0.055	0.028	0.027
Deposition time (s)	100	300	5775	867
Substrate rotation (rpm)	12	12	12	12
Substrate heater temperature (°C)	RT	RT	RT	RT

Table 3.2: Sputter parameters for the top metal layer fabrication in the Univex 450 C system.

Parameter	Ag active electrode	Pt capping layer
Sputter type	DC	DC
Sputter power (W)	288	359
Ar flow (sccm)	60	60
Process pressure (mbar)	1.2	2.4
Deposition time (s)	6	9
Deposition rate (nm/s)	3.3	2.2
Process temperature (°C)	RT	RT

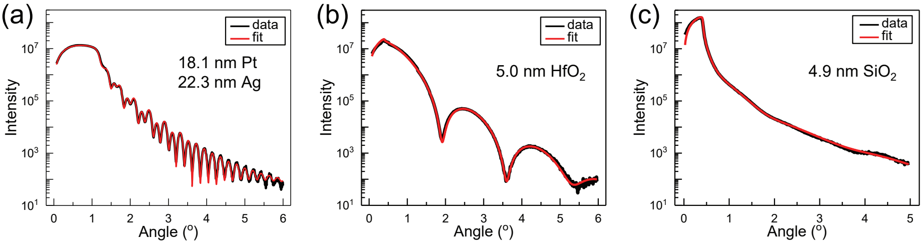

Figure 3.8: X-ray reflectivity measurements of different layers. (a) Sputter deposited Ag metal film on SiO_2 substrate. (b) ALD grown HfO_2 film on SiO_2 substrate. (c) ALD grown SiO_2 film on Si substrate.

3.2 Thin Film Analysis

In order to optimize the ALD and sputter processes, the grown films have to be analyzed from various viewpoints. Among others, thickness, homogeneity, stoichiometry, roughness, and density of the grown films are some of the important parameters to be characterized. Accordingly, the layer thickness and density of the films were analyzed by using X-Ray Reflectivity (XRR) measurement. XRR is the most common and accurate method used to determine the layer thickness and density of thin films. Detailed information on XRR can be found in [162]. Figure 3.8 presents representative XRR measurements performed on a sputter-deposited Ag metal with Pt capping and HfO_2 and SiO_2 ALD films. A Bruker D8 A25 system by *Bruker* was used to carry out the measurements and the fitting was done via open-source software GenX [163]. All the films used in this work are characterized individually in a similar manner.

Furthermore, the roughness and morphology of the different layers were checked by using Atomic Force Microscopy (AFM). The tool used in this work is the Easyscan 2 AFM by *Nanosurf GmbH* and further data visualization and analysis were done by the open source software *Gwyddion* [164]. As oxide films of only a few nm thick are used as a switching layer, the quality and roughness of the underneath metal electrode should be optimized. Figure 3.9 depicts AFM images of the sputter-grown BEs of Pt, TiN, and W with an acceptable roughness of well below 1 nm.

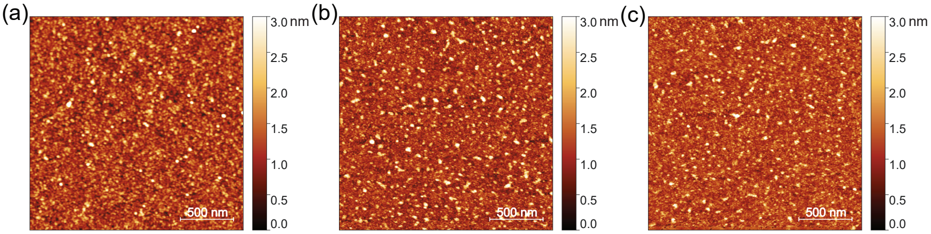

Figure 3.9: Atomic force microscopy images of the sputter grown bottom electrode of (a) Pt, (b) TiN, and (c) W.

3.3 Device Fabrication

In this work, mainly two types of metal-insulator-metal (MIM) device structures are fabricated and investigated. (1) Micro-crossbar devices, where the BEs and TEs are structured into lines, and the active device area is defined by the crossing of the two lines. In this structure the active device size ranges from 2 µm x 2 µm to 20 µm x 20 µm. (2) Nano-plug type devices, where the oxide switching layer is sandwiched between the bottom and top electrodes via nano-holes. This structure offers device sizes as small as 40 nm x 40 nm. The main part of this work is done on the micro-sized crossbar devices and the nano-plug type devices are fabricated to investigate the scalability of diffusive memristors into nano scales. Details of the device fabrication steps for both structures will be discussed in this section.

3.3.1 Crossbar Devices

For all devices in this study, thermally oxidized (430 nm SiO_2) Si substrates are used (a). The full device fabrication steps are schematically depicted in Figure 3.10. Starting with the SiO_2 substrate, thin layers of 5 nm Ti followed by 25 nm Pt are sputter deposited as BE (b). The Ti layer is introduced for better adhesion between the Pt metal electrode and substrate. Afterward, the wafers are coated with a protective resist (AZ 5214E) and diced into 1 inch x 1 inch sized samples. The diced samples are then cleaned in an ultrasonic bath using acetone (twice for 3 min) and isopropanol (3 min) to remove the protective resist.

The next step is the patterning of the BEs by using optical lithography technique (c). For that, samples with the size of 1 inch x 1 inch were spin-coated (4000 RPM for 30 s) with the photoresist AZ 5214E and subsequently dried on a hotplate for

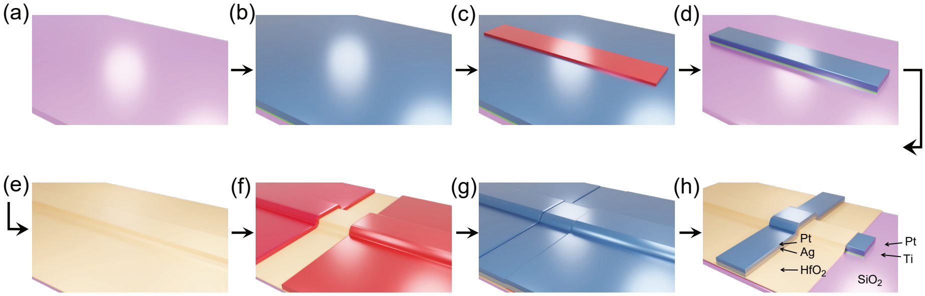

Figure 3.10: Fabrication steps of a typical micro crossbar device.

5 min at 90 °C. Then samples were exposed to UV-light in a mask aligner *MA6* by *Suess micro Tec GmbH* for 25 s with an intensity of 2.2 mW cm^{-2}. The development is subsequently done at room temperature in AZ 326 MIF developer for 90 s and is stopped with deionized water. Then after drying with nitrogen gas, the Pt and Ti layers in the uncovered part of the samples are etched by using an *Ionfab 300 Plus* reactive ion beam etching (RIBE) tool manufactured by *Oxford Instruments* (d). Finally, the residual resist is stripped in a hot (80 °C) dimethyl sulfoxide (DMSO) for 3 h. Subsequently, swabbing is performed in acetone at room temperature, purged in isopropanol, and dried with nitrogen. To further guarantee the removal of any resist residuals, the samples were further cleaned for 10 min under 200 sccm oxygen flow at a power of 600 W in a Tepla 300 Plasma Asher.

Afterward, oxide layers are deposited onto the samples using ALD according to the processes discussed in section 3.1.1 (e). After the ALD process, the samples are transferred to the lithography room for TE pattering. Unlike the BEs where etching is used to structure the patterns, TEs are structured by a liftoff process. For that, the photoresist AZ 5214E with an image reversal process is used (f). After coating and pre-baking, the samples are exposed for 10 s using the same mask aligner tool. Afterwards, a post-bake is performed for 1 min at 120 °C. The development is performed in a similar way as the BEs. Next, the samples are transferred to the Univex 450 C sputter tool and the Ag active and Pt capping layers are deposited as TEs (g). Finally, metals sputtered outside of the desired TE structure are lifted off by putting the samples in acetone overnight followed by rinsing in isopropanol and nitrogen drying. Note that during the ALD process, all the sample areas including the BE pads are covered by oxide film. Thus, one more lithography step is needed to open the BE contact pads. This is done by further lithography step with an image reversal process and subsequent etching by RIBE. The final device has a stack of Pt / HfO_2 / Ag / Pt and Pt / SiO_2 / Ag / Pt at the crosspoint (h). Samples with different CEs of TiN and W are processed in a similar way. More details on the fabrication recipe can be found in Appendix B.1.

Due to the production discontinuity of the AZ 5214E photoresist by the manufacturer [165], some of the samples are fabricated by using different resists of AZ MIR 701 (positive resist) for BEs patterning and AZ nLOF 2020 (negative resist) for TEs pattering and BE contact pad openings. However, the main fabrication steps stay the same. Details of the fabrication process are described in Appendix B.2.

3.3.2 Nano Plug Devices

For industrial-relevant applications, device sizes are in the range of several to ten nanometers. In order to demonstrate the behavior of the discussed stacks for devices in the nanometer regime, resistive switching devices are integrated into nanometer-sized structures. For this integration process, patterning by electron beam lithography (EBL) is utilized. The process is described in the following:

Starting with a 5 nm Ti and 25 nm Pt film sputtered on a thermally oxidized silicon wafer, the samples are spin-coated (4000 rpm, 1 min) with an e-beam resist of AZ nLOF 2020, and subsequently soft-baked for 3 min at 90 °C on a hotplate. The AZ nLOF 2020 resist is thinned with AZ EBR with the proportion of 1:2 in order to achieve a thin resist film. Then, resist is patterned by exposure to an e-beam with an acceleration voltage of 100 kV and a dose of $75\,\mu C\,cm^{-2}$. The e-beam writing machine (Raith EBPG 5200 EBL system) is located in the Helmholtz Nano Facility (HNF) and it is operated by Dr. Stefan Trellenkamp and Dr. Florian Lentz. For detailed information on EBL, the reader is referred to ref. [166]. After the e-beam writing, a post-exposure bake (PEB) is done at 110 °C for 1 min to achieve a cross-linking of the resist. Finally, the resist is developed using AZ 726 MIF at room temperature for 60 s, and BEs are structured by RIBE etching and subsequent residual resist cleaning in DMSO and isopropanol followed by a further treatment in the Tepla 300 Plasma Asher, as explained above for the crossbar structures.

Once the BEs are structured the samples are transferred to the ALD and a 20 nm SiO_2 film is grown on top as an isolation layer. In the subsequent step, nano-sized holes are formed in order to define the "active" device area. For that, samples are spin-coated with another e-beam resist CSAR AR 6200.04 (4000 rpm, 45 s) and

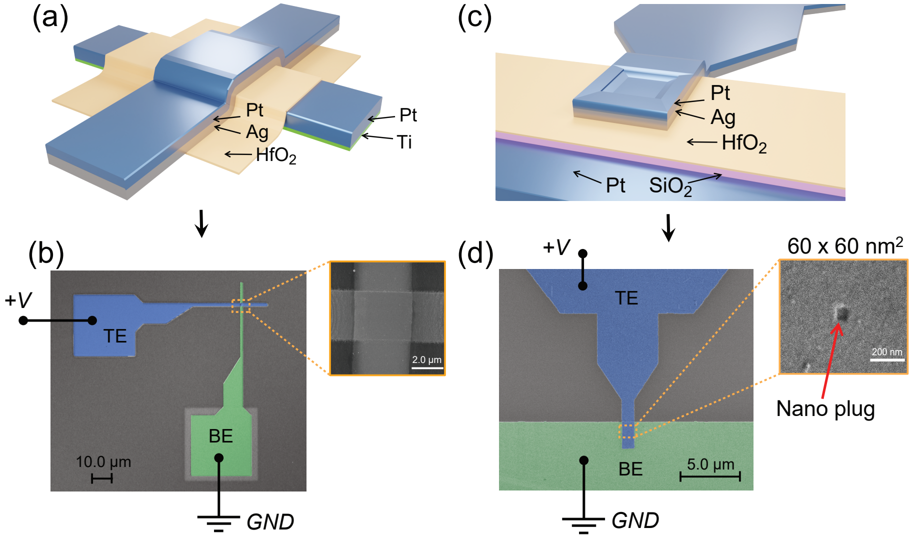

Figure 3.11: Final structures of the fabricated devices: (a) Schematic and (b) optical microscopy image of the micro crossbar device with an inset of scanning electron microscopy (SEM) image of the junction between the top and bottom electrodes. (c) Schematic and (d) SEM image of the nano plug device. The 60 nm x 60 nm nano plug is shown in the inset.

soft-baked at 150 °C for 1 min. Exposure is done with the same parameters as for the BEs. Afterwards, it is developed and stopped with AR600-55 (1 min) and isopropanol (30 s), respectively. Nano-holes are then formed by etching the SiO$_2$ film using RIBE. Residual resist is then removed by AR 600-71 stripper followed by cleaning in acetone and isopropanol and drying by nitrogen gas. In the following step, a 3 nm HfO$_2$ layer is grown using PE-ALD as a switching layer for the diffusive memristor cells. The TEs are structured by one more e-beam step using CSAR, sputter deposition of Ag and Pt layers, and a subsequent lift-off process. Finally, the BEs are opened by e-beam writing using AZ nLOF 2020 accompanied by etching. The full fabrication process steps are depicted in Appendix B.3.

3.3.3 Samples Used in This Work

As already mentioned the samples used in this work are built of HfO$_2$ or SiO$_2$ as switching layers, Pt, TiN, or W as a BE, and Ag as the active layer. A Pt capping

Table 3.3: Layer stacks of the devices investigated in this work. Stacks labeled with a star (*) are films deposited by using the Omicron sputtering tool. Nano-plug structured samples are shown in bold.

Sample	BE	HfO_2	SiO_2	Active layer	Capping
HO2P|Pt	30 nm Pt	2 nm	x	20 nm Ag	20 nm Pt
HO3P|Pt	30 nm Pt	3 nm	x	20 nm Ag	20 nm Pt
HO5P|Pt	30 nm Pt	5 nm	x	20 nm Ag	20 nm Pt
HO7P|Pt	30 nm Pt	7 nm	x	20 nm Ag	20 nm Pt
HO10P|Pt	30 nm Pt	10 nm	x	20 nm Ag	20 nm Pt
HO3P|Pt	30 nm Pt*	3 nm	x	20 nm Ag	20 nm Pt
HO3P|TiN	[20 nm TiN|10 nmPt]*	3 nm	x	20 nm Ag	20 nm Pt
HO3P|W	[20 nm W|10 nmPt]*	3 nm	x	20 nm Ag	20 nm Pt
SO3P|Pt	30 nm Pt	x	3 nm	20 nm Ag	20 nm Pt
SO5P|Pt	30 nm Pt	x	5 nm	20 nm Ag	20 nm Pt
HO3P|Pt	**30 nm Pt**	**3 nm**	**x**	**20 nm Ag**	**20 nm Pt**

layer is used for all samples. For easier reading, the stacks are referred to with the following nomenclature: HOxP|Me or SOxP|Me where x stands for the oxide thickness in nm, P refers to the plasma process of the ALD, and Me for the BE metal. HO and SO refer to the HfO_2 and SiO_2 layers, respectively. The Ag and Pt top layers are not mentioned in the nomenclature as they are the same for all samples. The layer stack of all devices investigated in this work is listed in Table 3.3.

3.4 Electrical Measurements

For the electrical characterization of the devices, different measurement setups are used. Two types of measurement setups are used in this work: continuous current-voltage (I-V) measurements (quasi-static) and pulsed voltage measurements at short timescales. This section introduces the measurement setups utilized to characterize the devices in this work. A Matlab code that was self-written is used to carry out various experimental data analyses, such as extracting forming, hold, and threshold voltages, and determining both the SET and relaxation times.

Quasi-static I-V hysteresis

Agilent B1500A Semiconductor Parameter Analyzer is used to conduct I-V sweep measurements. This tool is equipped with different modules [167]. By using the

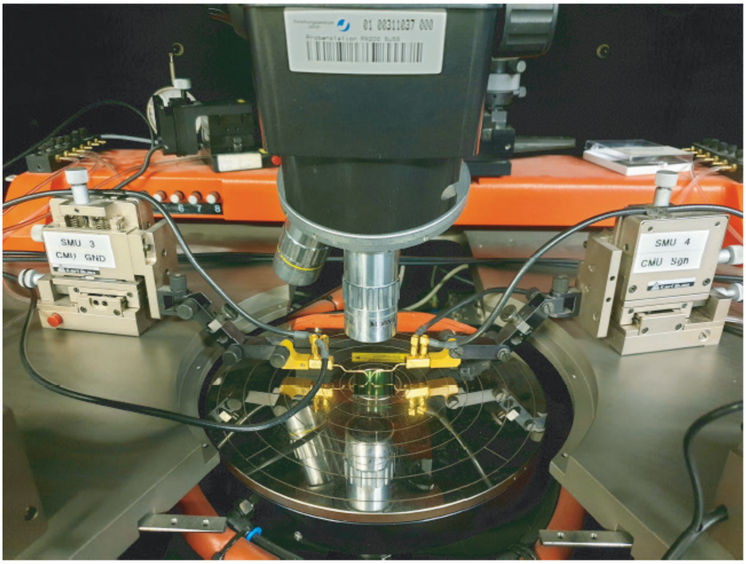

Figure 3.12: Photo of the Suess MicroTec PA-200 semi-automatic table.

source measure units (SMU) and the ground units (GNDU) of the tool a standard current-voltage analysis can be done. With the installed default program *Easy Expert* Software, the measurement parameters such as start/stop voltage, step width, current resolution, and compliance can be controlled. Additionally, capacitance measurements can also be performed in this tool thanks to the installed capacitance measurement unit (CMU) module. Furthermore, the tool provides a minimum current and voltage resolution of down to 5 fA and 0.5 µV, respectively.

One of the advantages of this tool is that it is combined with a Karl Suess Microtec PA-200 semiautomatic prober, allowing automatic measurements of multiple samples. The electronically controllable table can move in all three dimensions with an accuracy of 0.5 µm and can rotate up to an angle range of 6 ° [167] for better alignment. Different masks can be loaded into the system by using a *ProberBench* software and communication to the easy expert software is achieved via GPIB. Furthermore, the prober is connected to an *ATT (Advanced Temperature Test Systems GmbH)* heating unit, allowing high-temperature measurements up to 200 °C. The semiautomatic probe station is shown in Figure 3.12.

Another useful feature of this setup is the active compliance current function. Memristive devices are sensitive to high currents. During the activation of the current compliance mode the SMU basically switches from voltage to current sourcing as soon as the preset maximum current is reached, thus preventing device damage from large current overshoots. However, due to a certain delay (several milliseconds) of the SMU to react and switch to the current sourcing mode, devices can be exposed to higher currents. Nevertheless, this is an intrinsic issue of SMUs and all the electroforming and threshold switching experiments are performed using this setup. However, since electroforming requires higher voltage compared to threshold switching, the compliance currents during the forming step are kept very low (as low as 10 nA) to prevent the device from extremely high current in the event of an overshoot. The ideal case would be to use an active element such as a transistor to limit the current, however, this is outside of the scope of this work and is not considered.

Transient Pulse Measurement

Short pulse experiments are performed by using a Tektronix Keithley 4200-SCS semiconductor characterization tool. This tool is equipped with 4225 Pulse Measurement Units (PMUs) and 4225-RPM Remote Amplifier/Switch modules and an integrated oscilloscope card with a maximum bandwidth of 1 GHz. The 4225 PMUs offer two voltage ranges of ±10 V and ±40 V. The ±10 V range, which is of interest in this work, has two measurement current ranges of 10 mA and 200 mA. However, by using the 4225-RPM pre-amplifiers, detection of currents down to the nA range is possible [168]. The PMUs have a minimum and maximum sweep rate of 0.724 $\mathrm{kV\,s^{-1}}$ and 1 $\mathrm{GV\,s^{-1}}$, respectively, making it possible to study the sweep rate dependence behavior of the fabricated device. The minimum duration of a segment is 20 ns, thus pulse duration down to 60 ns can be applied with the rise and fall times of 20 ns. However, due to the time and precision tradeoff, the minimum detectable current scales inversely with the length of pulse used. Therefore, one has to follow the recommended minimum timing parameters for each current range [169]. A Cascade Microtech MPS150 probe station equipped with a Motic PSM-1000 microscope and manually operated DPP220 probe manipulators is used to probe the samples (Figure 3.13).

One more thing that has to be considered in fast pulse measurements is the RC-time. A schematic of the measurement setup is shown in Figure 3.14a. The parasitic capacitance of the cables and Device Under Test (DUT) in combination with series resistance can lead to significant charging and discharging currents, with an additional RC-time, as a response to fast voltage changes. This is shown in Figure 3.14b, where charging and discharging peaks are visible (red curve). Here, the transient curve is

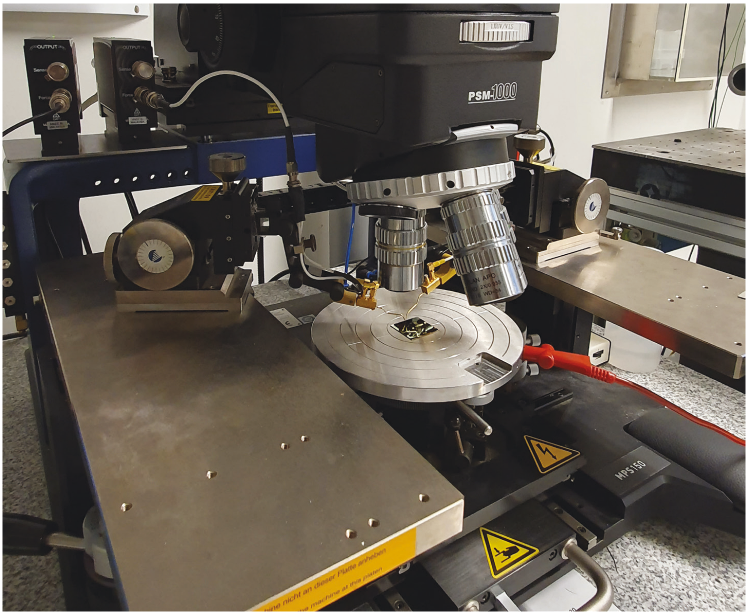

Figure 3.13: Photo of the Keithley 4200-SCS measurement setup.

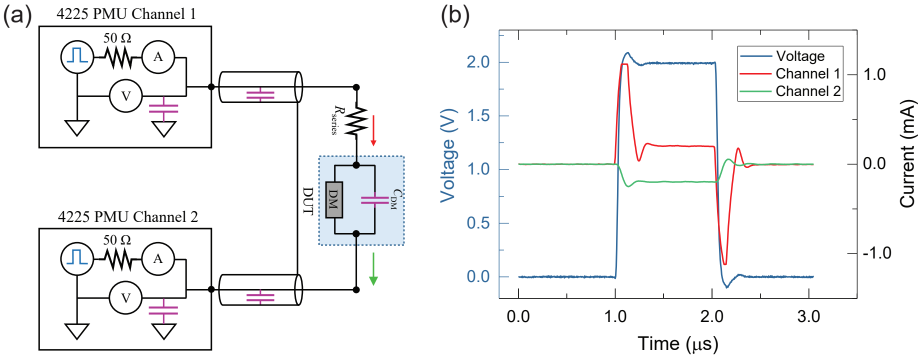

Figure 3.14: (a) Circuitry schematics of the Keithley 4200-SCS measurement setup. (b) A typical transient curve of V-t (blue curve) and I-t (red and green curves) recorded from the setup under a programming voltage of 2.0 V and pulse width of 1 µs, with a series resistor of 100 kΩ connected between the two probe tips.

acquired by connecting 100 kΩ resistor between the two probe tips with the absence of the DUT, thus the observed RC-effect is solely from the measurement setup alone. However, the current from channel 2 (green curve) does not contain the charging and discharging peaks as the current is read passively without any applied voltage to channel 2, instead, the signal gets inverted by the amplifier. Since all the transients curves are recorded during the measurement, the current signal from channel 2 is used by reversing the inversion for all the measurements performed in this setup for this work.

The Keithley system is controlled by using a custom LUA script, via GPIB Control, which gives higher flexibility to write and run complex measurement procedures. Furthermore, for all measurements, the input signal is applied to the Pt/Ag TE while the Pt BE is grounded. A custom-built tungsten probe tip with an SMD (surface-mounted device) resistor with different values is used to limit the current during the measurements.

Chapter 4

Threshold Switching in Diffusive Memristors

This chapter summarizes the switching behavior, including the electroforming and threshold switching, of the different diffusive memristors. The type and thickness of the oxide film, device area, programming conditions such as sweep rate, and the type of CE are some of the most important parameters that influence the performance of diffusive memristors. These are independently analyzed and discussed in this chapter. In Section 4.1, the *I*-*V* characteristics of Ag/HfO_2/Pt-based diffusive memristor are presented. The forming process (Section 4.1.1) and threshold switching (Section 4.1.2) for each device stack are analyzed with respect to oxide film thickness and device area. In addition, the influence of sweep rate is discussed (Section 4.1.4). Furthermore, the influence of CE on the switching behavior of the diffusive memristor is included in Section 4.1.5. Section 4.2 addresses the switching characteristics of Ag/SiO_2/Pt diffusive memristors. The initial forming process (Section 4.2.1) and the threshold switching behavior (Section 4.2.2) are discussed thoroughly. Finally, a comparison between the Ag/SiO_2/Pt and Ag/HfO_2/Pt diffusive memristors followed by a summary is given in Section 4.3.

4.1 Threshold Switching in Ag/HfO_2/Pt Cells

4.1.1 Initial Forming Behavior

Figure 4.1 shows a typical initial forming curve (black curve) of the HO3P|Pt device with an active device size of 3 µm^2. The fabricated device initially exhibits an

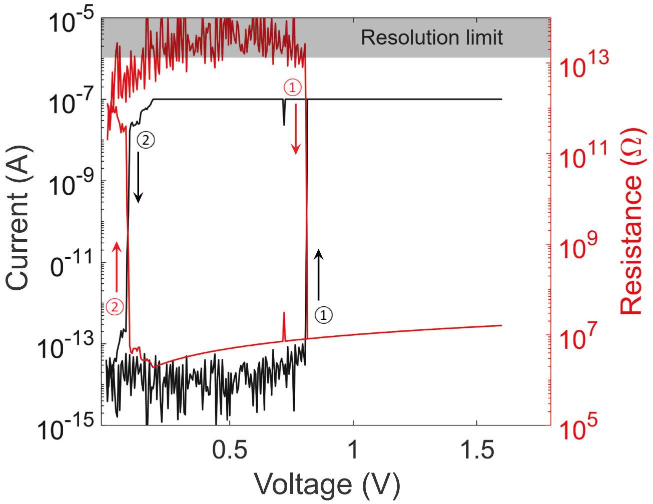

Figure 4.1: Typical forming curve of the HO3P|Pt device. The current response is plotted in black while the calculated resistance of the cell is plotted in red. Current compliance of 100 nA was used to limit current overshoot.

extremely low leakage current below 10 fA and as the bias voltage increases the current abruptly jumps to the low resistive state which is limited by a compliance current of 100 nA ①, at about 0.8 V, spanning orders of magnitude change in current. During the reverse voltage sweep, the current returns back to the initial highly resistive state close to 0 V ②. The abrupt rise and fall of current is a typical phenomenon for ECM-type devices. In addition to the current, the resistance of the device during the switching is plotted against voltage as shown by the red curve. It can be seen that the resistance in the highly resistive state is above 10 TΩ. It should be noted that the initial current, and thus the resistance, at low voltages are below the resolution limit of the measurement setup and the values given are for reference only.

Area and thickness dependence of the forming process

A cumulative distribution function (CDF) plot of the forming voltages for a minimum of 54 devices of different size and for two thicknesses of the HfO_2 layer are shown in Figure 4.2. As can be seen, the forming voltage nicely scales with the area for both HO3P|Pt and HO5P|Pt devices. For the HO3P|Pt device, the forming voltage decreased from a mean value of 1.15 V to 0.9 V when the device area is increased from 3 μm^2 to 220 μm^2. On the other hand, for the HO5P|Pt device, the forming

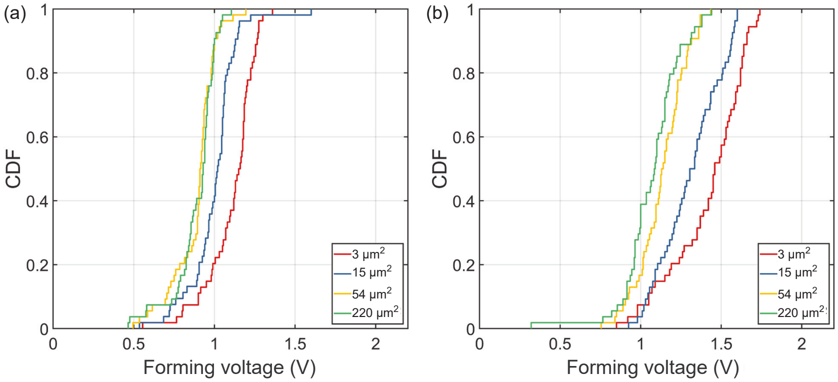

Figure 4.2: CDF plot of the forming voltage for (a) HO3P|Pt and (b) HO5P|Pt devices for various device areas. A constant sweep rate of 100 mV/s was used during the measurement.

voltage decreased from 1.6 V for the small device area of 3 µm^2 to 1.1 V for the 220 µm^2 device area. This is in line with the area dependence of the forming process in ECM cells [170]. Furthermore, one can notice that the forming voltage for the HO3P|Pt with device area of 3 µm^2 in Figure 4.2a (∼ 1.15 V) is higher than the one shown in Figure 4.1 (∼ 0.8 V). This difference is due to the forming methods used in the two cases. For Figure 4.1 the forming was performed in "auto-range" mode. This mode is ideal for resolving currents as low as about 10 fA. However, it has a drawback: in this operation mode, the current range is adjusted automatically to the measured current for optimal precision. The current integration time is very long at low currents and this interferes with the sweep rate of the I-V measurement especially at low currents. On the other hand, measurement data for Figure 4.2 are collected in a fixed current range mode and the sweep rate is constant throughout the I-V measurement. Switching in ECM cells is sweep rate dependent (this will be discussed in Section 4.1.4) and the difference arises from this.

Looking at the impact of film thickness, a clear trend between the forming voltage and the thickness of HfO$_2$ can be observed from Figure 4.2 which is further analyzed in Figure 4.3. Representative forming curves for three devices of HO2P|Pt, HO3P|Pt, and HO5P|Pt with a different HfO$_2$ thickness of 2 nm, 3 nm, and 5 nm, respectively, measured on devices with an area of 3 µm^2 are presented in Figure 4.3a. CDF plots of data collected from 53 individual cells for each device size are shown in Figure 4.3b. The results indicate that the forming voltage increases as the HfO$_2$ thickness increases,

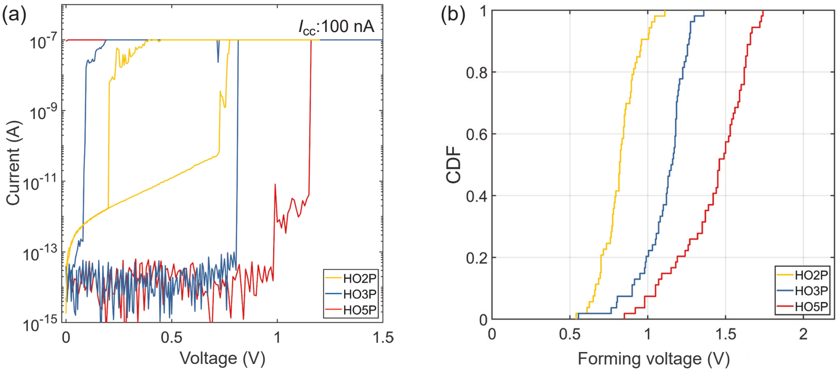

Figure 4.3: (a) Representative forming curves of the HO2P|Pt, HO3P|Pt, and HO5P|Pt devices for the small device area of 3 µm^2. Forming was performed in auto-range mode. (b) CDF plot of the forming voltage for the three devices of 3 µm^2 size. A constant sweep rate of 100 mV/s was used during the measurement in (b).

suggesting that thicker layers require higher forming voltages. This observation is consistent with the field dependence of electroforming in ECM cells. Furthermore, as can be seen in Figure 4.3a, the initial leakage current for the HO2P|Pt device is higher compared to the HO3P|Pt and HO5P|Pt devices. This is due to the higher tunneling current contribution in the very thin 2 nm HfO_2 layer. Once again, the difference between the mean forming voltage for the three devices in Figure 4.3a and 4.3b are different because the forming measurements in Figure 4.3a were performed in auto-range mode for better HRS current resolution.

4.1.2 Threshold Switching

Once the devices are successfully formed, they exhibit a threshold-type volatile switching at a much lower voltage of V_{th} than the forming voltage. This is mainly due to the switching occurring along the preformed conduction paths. As shown in Figure 4.4, the fabricated HO3P|Pt device exhibits a volatile threshold switching characteristic for a wide range of compliance currents (I_{CC}) up to 1 mA with features such as ultra-low leakage current of below 100 fA, low V_{th} of $\sim$ 0.2 V. Low leakage current and low V_{th} are the key attractive properties of diffusive memristors for energy-efficient applications. Further increase of the current leads to non-volatile switching or sometimes to irreversible breakdown of the switching matrix. The volatility yield is generally inversely proportional to the value of I_{CC}. This is because a higher current

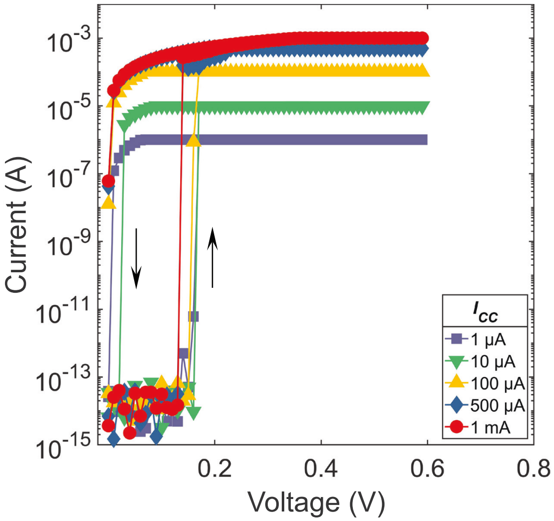

Figure 4.4: I-V characteristics of HO3P|Pt cells under various device compliance currents (I_{CC}) showing volatile behavior up to 1 mA. Reproduced with permission from [1].

means higher temperature within the system (Joule heating) which significantly contributes to the formation of larger filaments that can no longer rupture in very short time scales.

Figure 4.5 shows threshold switching for the HO2P|Pt, HO3P|Pt, and HO5P|Pt devices with the HfO$_2$ thickness of 2, 3, and 5 nm, respectively. Uniform and repeatable threshold switching characteristics can be observed for all devices. For a better comparison, CDF plots of the V_{h} and V_{th} collected from 10 devices and 100 cycles each are shown for all three devices in Figure 4.6. A cycle-to-cycle (c2c) and device-to-device (d2d) good distribution of the V_{h} and V_{th} can be observed for all devices. Note that the V_{th}, with a mean value of ~ 0.2 V, seem to be more or less the same for all devices, although the switching in diffusive memristors is strongly field dependent and thickness variation should result in a change in the V_{th}. The reasons for this will be discussed in detail in Section 4.1.4.

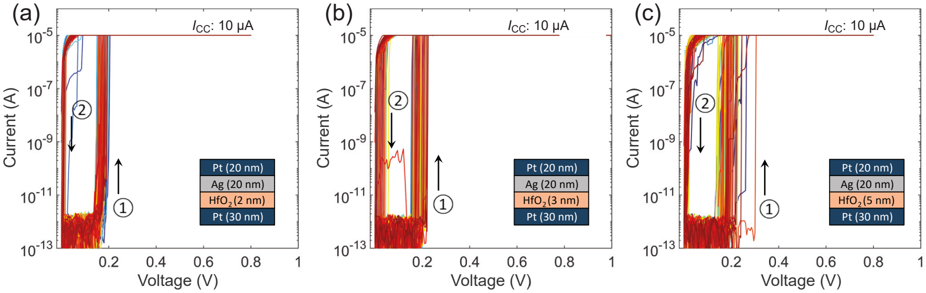

Figure 4.5: I-V sweeps of the (a) HO2P|Pt (b) HO3P|Pt and (c) HO5P|Pt devices of 3 µm^2 size measured under a compliance current (I_{CC}) of 10 µA.

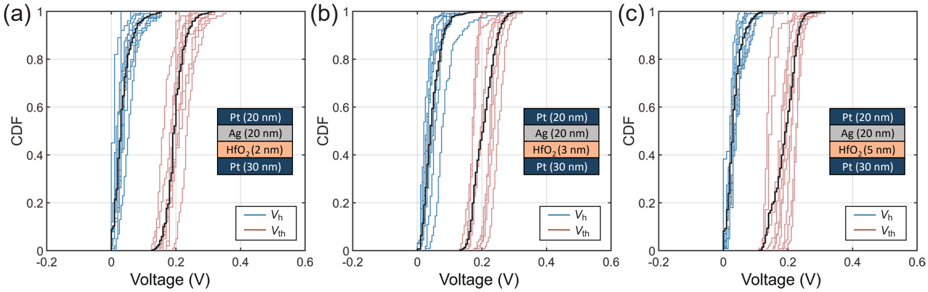

Figure 4.6: CDF plot of (a) HO2P|Pt, (b) HO3P|Pt and (c) HO5P|Pt. Data are collected from 10 devices and 100 cycles each at a constant sweep rate of 100 mV/s.

Threshold switching mechanism of diffusive memristors

As described in Chapter 2, the switching in diffusive memristors happens through the formation and rupture of the conductive Ag filament within the switching layer. Therefore, the electrical connection between the two electrodes can be achieved (i) through a galvanic contact (by a fully connected filament) or (ii) through a tunneling gap between the filament tip and the respective metal electrode. Which way is dominant depends on the device structure and the operational current range. To illustrate this, the diffusive memristors were switched by varying the I_{CC} level ranging from 100 nA to 100 µA. Then the conductance of the device in the LRS, right before transitioning to HRS, is calculated as a function of voltage. The results are shown in Figure 4.7. At lower I_{CC} of 100 nA and 1 µA (Figure 4.7a and 4.7b), the conductance is given as $G << 1 \cdot G_0$ (Figure 4.7e and 4.7f). This means that the current transport is due to the tunneling of carriers through a small tunneling gap between the filament tip and metal electrode. This is illustrated in Figure 4.7i and j for I_{CC} of 100 nA and 1µA, respectively. G_0 defines the single atom conductance calculated as $G_0 = (2e^2)/h \approx 77.5$ µS ≈ 12.9 kΩ^{-1} [171], where e is the electron charge and h Planck's contact. However, at an increased I_{CC} of 10 µA (Figure 4.7c), a quantum conductance plaque of $1.4 \cdot G_0$, which is greater than a single point conductance, can be observed (Figure 4.7g). This indicates the formation of a galvanic contact between the conductive filament and the metallic electrode. When the I_{CC} is further increased to 100µA a higher conductance of $6{\cdot}G_0$ can be seen (Figure 4.7d). A schematic plot of the conduction for I_{CC} of 10µA and 100µA is given in Figure 4.7k and 4.7l, respectively.

Note that in the schematics plots in Figure 4.7i-l, the electrodes on both sides have the same color. This is done intentionally in order to avoid making any conclusion regarding the direction of the filament growth. In spite of many efforts made to understand the switching mechanism using microscopy studies, key aspects of the filament formation such as the nucleation site and nature of the filament remain largely unknown [33, 56, 172–174]. The small size of the filament and its very fast relaxation process makes it challenging to conduct a thorough physical analysis. Nonetheless, a qualitative conclusion can be drawn from electrical measurements in conjunction with electron microscopy observations.

In this regard, there are two primary questions to address:

(i) Which direction the filament retracts and

(ii) How much of the conductive filament ruptures during the relaxation process?

As the filament's weakest point is where it breaks, answering the first question could indicate which direction the filament is growing. Usually, but not always, the thinnest part of the filament is located where it was last closed. To elucidate this, the directionality of the switching is investigated with respect to voltage polarity. For this, the device was biased toward both positive and negative directions with varying I_{CC} under two different cases. Case I: the device was formed at low I_{CC} of 100 nA to ensure it did not run to the non-volatile switching mode (Figure 4.8a). Case II: the device was first formed at low I_{CC} of 100 nA and then switched at higher I_{CC} of 500 µA to drive it to the non-volatile state. Then a negative voltage was applied to the Ag electrode to bring the device back to the HRS (Figure 4.8c). Note that, a direct run into a non-volatile state can be achieved by performing the forming at higher I_{CC}. However, this will lead to irreversible switching. Afterward, both devices

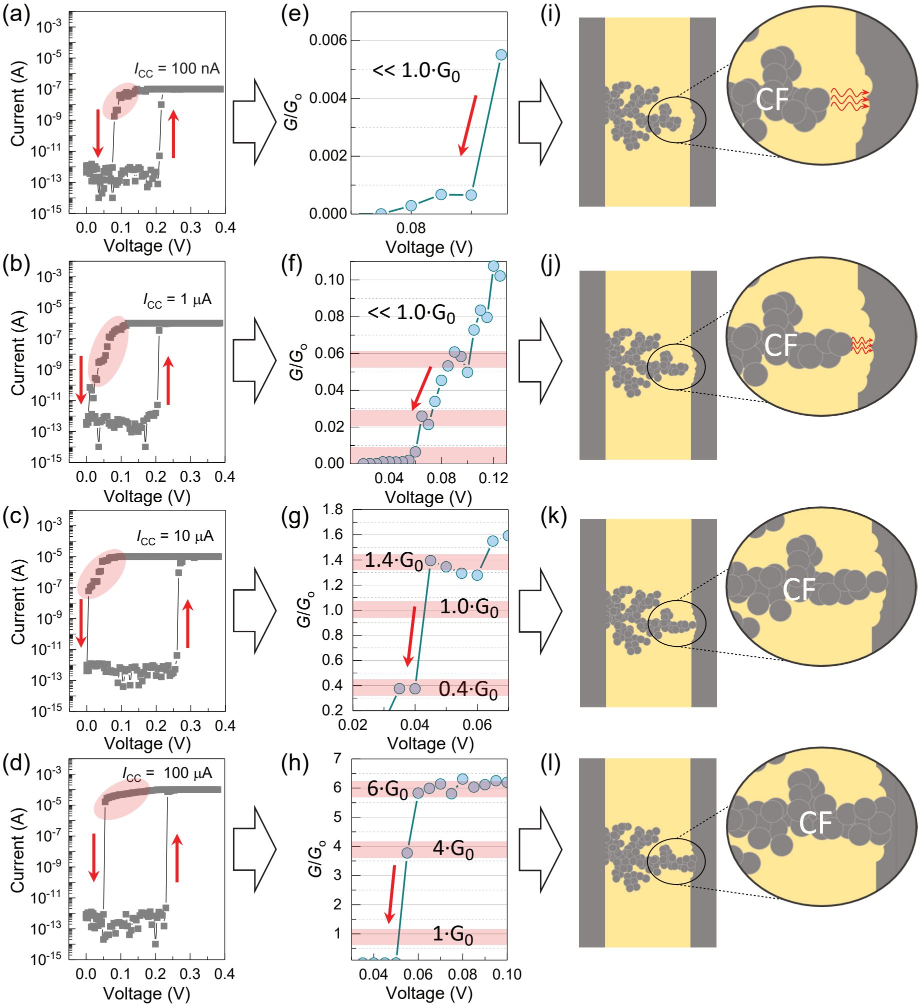

Figure 4.7: (a)-(d) Sweep measurement under different compliance currents and (e)-(h) the corresponding calculated conductance curves as a function of voltage. (i)-(l) A schematic plot showing the filament evolution under various compliance currents. A constant sweep rate of 100 mV/s was used during all measurements. Reproduced with permission from [1].

(Case I and II) were switched in both voltage polarities in a volatile manner. The results are illustrated in Figure 4.8b and d. In the first case, volatile switching is only observed in the positively biased direction, and the device remains in the HRS when

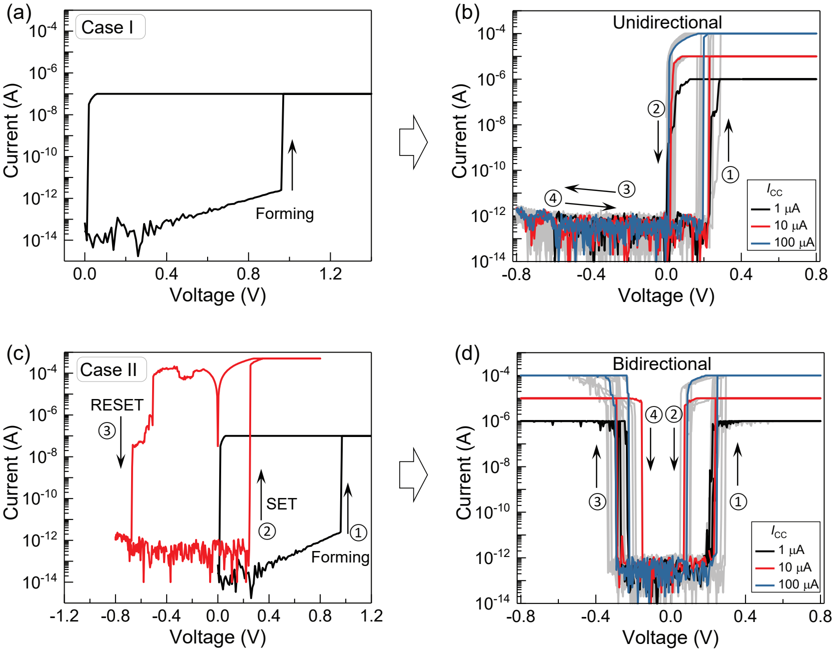

Figure 4.8: (a) Forming curve of HO3P|Pt device and (b) the subsequent switching, showing a unidirectional threshold switching behavior. (c) SET and RESET curves of HO3P|Pt achieved at higher compliance current after first forming at low compliance current and (d) the corresponding bidirectional threshold switching. Redrawn with permission from [1].

biased in the negative direction (Figure 4.8b). From this, it can be inferred that the conductive filament retracts from the Pt CE during the self-relaxation process. As a result, no switching is observed in the negative direction, since there is no Ag^+ ion supply from the Pt electrode side. However, in the second case, the device displays volatile switching in both positive and negative directions (Figure 4.8d). This suggests the presence of a residual Ag (cluster) on the surface of the Pt CE, which acts as a local Ag^+ ion source when a positive bias is applied to the Pt electrode. Therefore, for controlled volatile switching, the thin filament retracts at the CE. This conclusion is consistent with previous TEM observations of filament breakage at the filament/inert electrode interface [175]. Schematic depictions of the possible switching mechanism for Case I and Case II are presented in Figure 4.9a and 4.9b, respectively.

To answer the second question, which is how much of the filament retracts from the

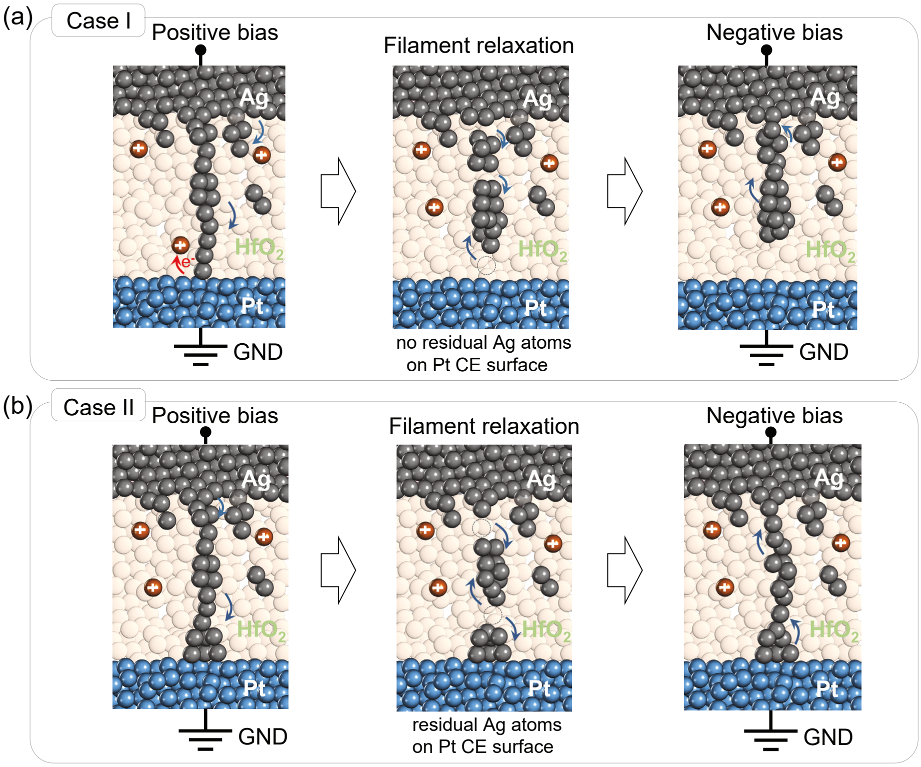
(a)
Case I
Positive bias
Filament relaxation
Negative bias
Ag
Ag
Ag
e-
HfO2
HfO2
HfO2
Pt
Pt
Pt
GND
no residual Ag atoms
on Pt CE surface
GND
(b)
Case II
Positive bias
Filament relaxation
Negative bias
Ag
Ag
Ag
HfO2
HfO2
HfO2
Pt
Pt
Pt
GND
residual Ag atoms
on Pt CE surface
GND

Figure 4.9: A schematic representation of a possible switching mechanism under (a) Case I and (b) Case II. Redrawn with permission from [1].

electrodes during relaxation, an analysis of the currents in the HRS is conducted. In non-volatile ECM cells, the current in the HRS state after the forming process is often higher than that of the pristine device due to incomplete filament rupture during the RESET process, leaving behind a residual filament seed at the oxide/electrode interface [176–178]. However, diffusive memristors exhibit very low leakage currents, similar to that of the pristine device, even after forming and repeated cycling. This is likely due to a significant portion of the conductive filament retracting from the electrodes to maintain the ultra-low current, considering the very thin HfO_2 layer thickness of 3 nm. To test this hypothesis, the tunneling current density through the device was calculated using the Simmons formula [179]:

Table 4.1: Parameters used for the Simmons fitting.

parameter	value
ϕ_1	2.2 eV
ϕ_2	2.8 eV
d_0	5 nm
$l(=L)$	3 nm
m^*	$0.5\,m_e$

$$J = J_0 \left[\bar{\Phi} \cdot \exp\left(-\alpha \cdot \bar{\Phi}^{\frac{1}{2}}\right) - \left(\bar{\Phi} + qV\right) \cdot \exp\left(-\alpha \cdot \left(\bar{\Phi} + qV\right)^{\frac{1}{2}}\right)\right] \tag{4.1}$$

with

$$J_0 = \frac{q}{2\pi h l^2} \tag{4.2}$$

and

$$\alpha = \frac{4\pi l}{h} \cdot \left(2m^*\right)^2 \tag{4.3}$$

here $\bar{\Phi}$ $(= \frac{\phi_1+\phi_1}{2})$ is the mean barrier height, q is the electron charge, h is the Planck's constant, l is the effective barrier width (in this case the thickness), and m^* is the effective mass. For details on the calculations, the reader is referred to Alexander Hardtdegen's dissertation [180].

Figure 4.10a shows the fit of the measurement data of the HO3P|Pt device during the forming cycle for different device areas. From this parameters such as ϕ_1 and ϕ_2 are extracted and later used to perform the calculations in Figure 4.10b. The calculation was done by taking into account contributions from the whole device area with a fixed gap of 3 nm and through the residual filament by varying the tunneling gap x accordingly. In order to accommodate the highest possible tunneling current contribution, a sizeable residual filament diameter d_0 of 5 nm was presumed, which is large compared to the 3 nm thick film. Parameters used in the fit are given in Table 4.1. The results show that a tunneling gap of at least 2.0 nm is required to maintain a leakage current of the measured data (shown in black symbols). This indicates that the conductive filament almost completely transforms into clusters by disconnecting from the electrode(s) during the relaxation process.

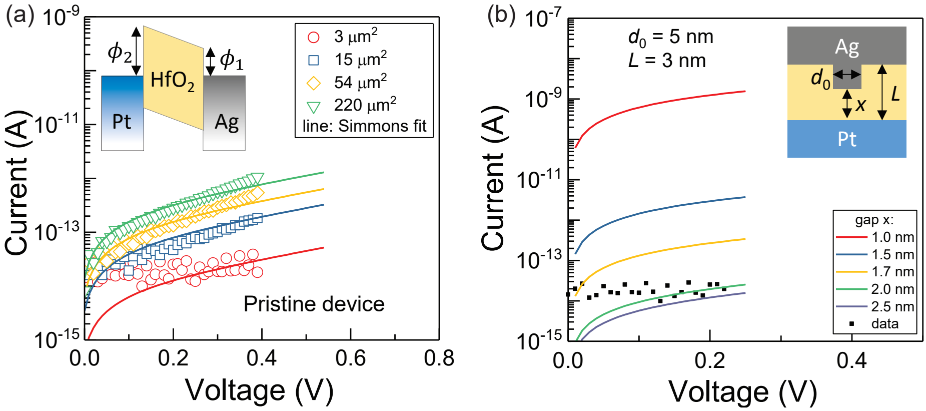

Figure 4.10: (a) Simmons fitting of the leakage current of pristine devices for various cell sizes. (b) Tunneling currents are calculated using the Simmons model under various tunneling gaps. Reproduced with permission from [1].

4.1.3 Device Scalability

One of the significant advantages of filamentary-type memristor devices is their potential for scalability to sub 10x nm in dimension [181–183]. This allows for the development of more compact and efficient devices for memory and NC applications. Furthermore, it enables higher-density integration, which results in increased computational power, reduced energy consumption, and improved performance at reduced manufacturing cost.

Diffusive memristors, which belong to the filamentary-type device category, also show promise for being reduced in size to very small dimensions. Many research groups have successfully produced properly functioning diffusive memristor cells at the nanometer scale [36, 52, 170, 184]. Even though the oxide layer is only 3 nm thick, the work presented in this thesis was conducted using micro-scale crossbar cells. To demonstrate the potential for scaling down diffusive memristors, plug-type structures were used to create cells as small as 40 nm in dimension. The fabrication step of nano-plug type devices is presented in Chapter 3, Section 3.3.2.

Figure 4.11a displays an optical microscopy image of a single cell, which clearly shows the top and bottom contacts. A schematic cross-sectional view of the red-colored line in the microscopy image is shown in the bottom panel. A typical forming curve for the 40 nm x 40 nm device, as well as a CDF of the forming voltage collected from 50 cells for the 40 nm x 40 nm and 100 nm x 100 nm devices, is shown in Figure 4.11b

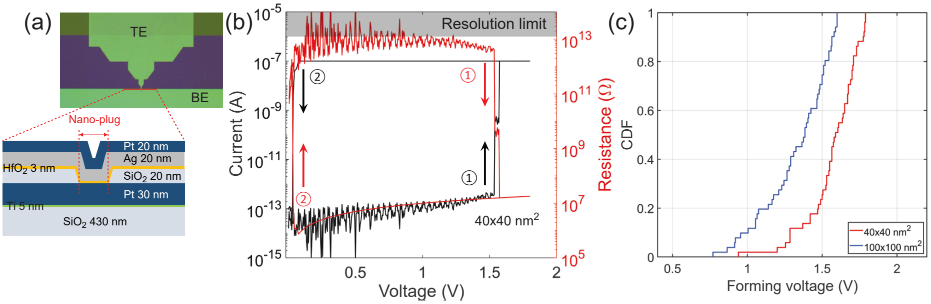

Figure 4.11: (a) Top panel: optical microscopy image of the nano-structured plug-type device. Bottom panel: a schematic cross-sectional view of the red-colored line in the top panel. (b) Typical forming curve of the HO3P|Pt plug-type device with cell dimension of 40 nm x 40 nm. The current response is plotted in black while the calculated resistance of the cell is plotted in red. (c) CDF plot of the forming voltage collected from 50 cells each for 40 nm x 40 nm and 100 nm x 100 nm devices. A current compliance of 100 nA was used during the measurement to prevent current overshoot.

and c, respectively. Except for the forming voltage increase, which is expected since the forming voltage is dependent on the cell size, both devices demonstrate similar behavior as the micro crossbar cells, with decreased leakage currents of below 10 fA (resistance of above 10 TΩ).

A plot of the threshold switching characteristics for the 40 nm x 40 nm and 100 nm x 100 nm devices is shown in Figure 4.12. Both devices show good volatile characteristics with leakage current well below the resolution limit of the setup. Unlike the forming voltage, the V_{th}, which is approximately 0.2 V, remains similar to that of the micro crossbar devices. This, again, is due to the filamentary nature of the switching process, which occurs in a small confined area after the forming process is completed.

To sum up, thanks to the filamentary behavior of the switching process, diffusive memristors can be scaled to a few tens of nanometers in dimension. This has been demonstrated by fabricating a functional device with a size down to 40 nm x 40 nm.

4.1.4 Influence of the Sweep Rate on Threshold Voltage

The sweep rate ($\nu\,[V/s]$), which defines the increase of the applied voltage signal in a defined time, is among the factors that affect the switching process of ECM cells [52, 94, 170, 185]. In particular, since the switching is field-driven, it is expected that ν influences the V_{th}. In this section, the effect of ν on the V_{th} will be discussed.

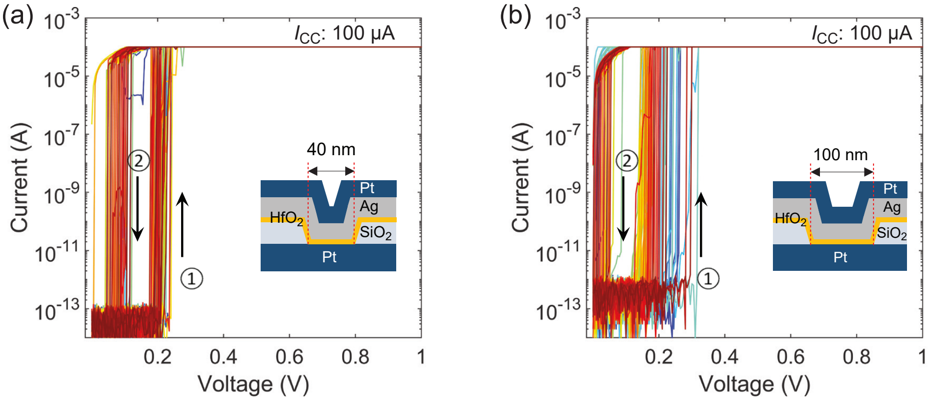

Figure 4.12: Representative I-V curves for the plug-type HO3P|Pt devices with cell size of (a) 40 nm x 40 nm and (b) 100 nm x 100 nm measured under a current compliance of 100 µA.

A triangular pulse with pulse amplitude of V_p and pulse width t_p is used for the study. An exemplary plot of the time-resolved voltage and current signal is plotted in Figure 4.13. The V_p is fixed at 3.0 V for all measurements while t_p is varied from 3 µs to 3 ms, resulting in a variation of the sweep rate of four orders of magnitude. ν is calculated as V_p/t_p with a unit of V/s. The experiment is performed on three devices with different HfO_2 thicknesses of 2, 3, and 5 nm. 100 measurements were performed for each V_p and t_p combination and V_{th} is extracted from the successful switching events. In Figure 4.14, the distribution of V_{th} is plotted for different t_p for all devices. Here, V_{th} acquired from a DC sweep measurement (0.1 V/s) is added to the plot for comparison. From the figure, it can be noticed that there are few data points for the HO5P|Pt device. This is because the reliability of volatility for thick films is generally less compared to thin films, as higher forming voltage is required during the first step, which could lead to oversized filament formations that make the device susceptible to non-volatility. This problem is exacerbated during the sweep rate experiment, where a V_p of 3.0 V is needed to achieve the desired ν. Nevertheless, a quantitative comparison can still be made using the data points that were successfully obtained.

For all devices, an increase of V_{th} can be seen as t_p becomes shorter. This is more clear in a box plot of V_{th} against the log function of ν in Figure 4.15. The mean V_{th} values for the different devices as a function of ν is presented in Figure 4.16a. Furthermore, to probe whether device area has any influence on the V_{th} of diffusive memristors, additional measurements were conducted and compared for different device areas of 3

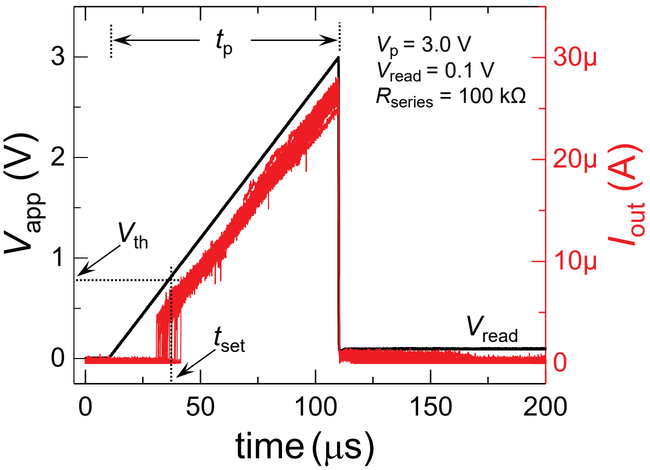

Figure 4.13: An exemplary time-resolved triangular pulse scheme used to estimate threshold voltage (V_{th}) at different sweep rates ($\nu = V_p/t_p$). The plot is made of data obtained from the HO2P|Pt cell. A 100 kΩ resistor was used in series to protect the device from damage.

µm^2 and 220 µm^2 on the HO3P|Pt device. The result is shown in Figure 4.16b. From Figure 4.15 and 4.16, the following conclusions can be drawn:

(i) V_{th} increases exponentially with ν in a V_{th} - log(ν) plot. For instance, an increase of 8 orders of magnitude in ν results in an increase of V_{th} from around 0.2 V to 1.5 V for HO2P|Pt, from 0.2 V to 2.12 V for HO3P|Pt, and from 0.2 V to 2.14 V for HO5P|Pt devices.

(ii) The effect of ν on the change in V_{th} is thickness dependent. This is because (1) the switching is field dependent, for example, a thicker film means a lower effective electric field, and (2) a longer filament has to grow in thicker films in order to bridge the gap between the electrodes.

(iii) The dependence of V_{th} on thickness and ν at lower ν ($<$ 100 V/s) is almost negligible. This is also evidenced by the similar V_{th} observed for devices with different HfO$_2$ thickness (see Figure 4.6). This could be due to the small change in V_{th} for low ν (rf. exponential dependence of V_{th} on ν) that is within the variation of the V_{th}, as pointed out by Schindler et al. [185].

(iv) Device area has no discernible impact on V_{th} throughout the entire ν range.

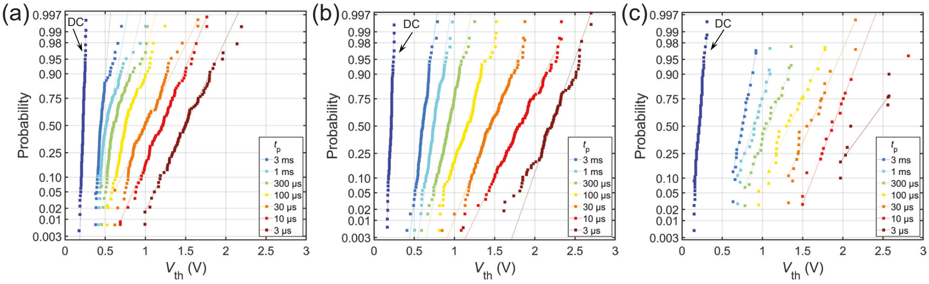

Figure 4.14: Distribution of threshold voltage (V_{th}) with different pulse width (t_{p}) at a pulse voltage (V_{p}) of 3.0 V for (a) HO2P|Pt, (b)HO3P, and (c) HO5P|Pt devices. V_{th} collected from a DC sweep measurement is added for comparison.

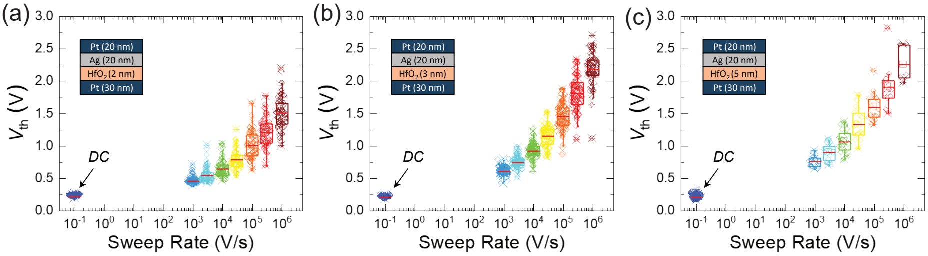

Figure 4.15: Dependence of threshold voltage (V_{th}) on the sweep rate (ν) for (a)HO2P|Pt, (b) HO3P|Pt, and (c) HO5P|Pt devices. The mean of the data is shown in red bar.

This is consistent with the fact that these are filamentary devices. This means that, once the electroforming is performed and a preferred conduction path is established, the subsequent switching cycles are due to the rupture and reformation of the preformed conductive filament, hence, the device area will have no effect on the switching.

4.1.5 Influence of Counter Electrode on Device Performance

In this section, the influence of CE in the switching of diffusive memristors will be discussed. In the context of ECM cells, the CE material is of significant importance in the switching process, owing to its impact on the reactions taking place at the CE/electrolyte interface [89, 91]. The electrocatalytic activity of the CE material, in terms of its ability to facilitate reduction-oxidation reactions, plays a determining role

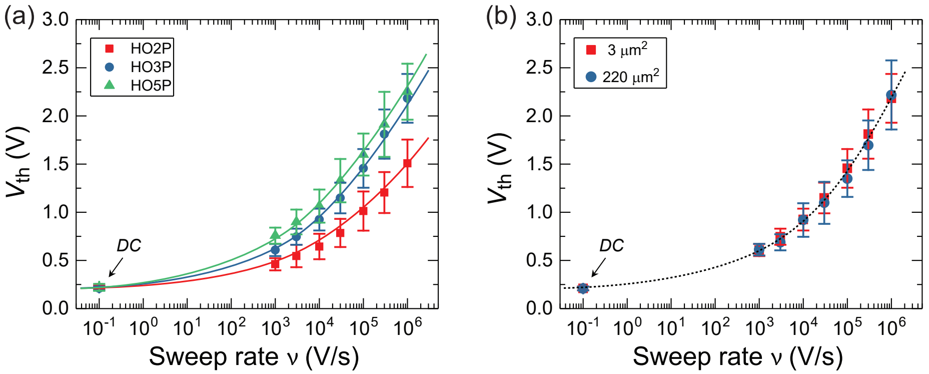

Figure 4.16: (a) Oxide thickness dependence of the threshold voltage (V_{th}) as plotted against sweep rate (ν) for the 3 μm^2 device. (b) Area dependence of V_{th} as a function of ν measured for the HO3P|Pt device. The lines in both plots are for eye guidance only and do not represent any physical fitting.

in controlling the concentration of metal ions in the electrolyte, thereby influencing the kinetics of the switching [91, 94]. Previous studies have indicated that materials with higher electrocatalytic activity lead to faster switching [89, 95].

To investigate the influence of CE materials on the switching process of diffusive memristors, inert Pt metal and two non-noble metals, namely, W and TiN, which are commonly employed in semiconductor technology, were used as the CE in Ag/HfO$_2$/CE-based diffusive memristor cells. This study aims to achieve two main objectives: (i) gain a better understanding of the impact of CE materials on the switching process of diffusive memristors and (ii) engineer and optimize the device towards materials that are widely used in industry and are compatible with CMOS technology, such as TiN and W. First, the oxidation behavior of the employed CE metals (i.e. Pt, TiN, and W) will be investigated. Then, the threshold switching of HO3P|Pt, HO3P|TiN, and HO3P|W devices will be discussed.

Surface oxidation of counter electrodes

As non-noble metals, TiN and W are prone to surface oxidation when exposed to an oxygen-containing environment [186, 187]. Unlike noble metals such as Au and Pt, these metals lack sufficient chemical stability, leading to the formation of an oxide surface layer. The TiN and W CEs are exposed to an oxygen atmosphere during the vacuum breaking for the patterning and structuring process, and to oxygen radicals during the oxygen plasma step of the HfO_2 ALD process, which makes the formation of an oxide layer inevitable. Limitation of surface oxidation may be achieved by in situ sample transfer between deposition systems by modifying the process flows; however, oxidation at the HfO_2/W (or HfO_2/TiN) interface cannot be completely avoided. Therefore, it is imperative to consider interfacial metal oxide layers when evaluating the performance of ECM devices made from an oxide electrolyte layer and a non-noble CE.

In order to gain a better understanding of the interfacial oxide formation and properties of the CE materials, X-ray photo spectroscopy (XPS) analysis was conducted on samples of these materials both with and without the HfO_2 layer. As a surface-sensitive technique, XPS helps to identify and quantify chemical elements in a sample, as well as determine their local valence states, thereby aiding in the characterization of surface and interfacial oxide layers and their potential impact on device performance. For detailed information on the theory of XPS, the reader is referred to ref. [188].

To conduct the measurements, a VersaProbe 5000 by *Physical Electronics* was utilized, which generates monochromatic X-rays from an Al Kα source with an excitation energy of 1486.6 eV. The low-power mode with a 25 W power output and an X-ray spot diameter of roughly 100 µm was utilized. Electron neutralization was carried out with a neutralizer emission of 20 µA current and a neutralizer bias of 1.37 eV to account for charging effects. Survey scans were carried out with a pass energy of 187 eV, while core-level scans were performed with a pass energy of 23.5 eV. The binding energies were adjusted for electrical charge effects by using the C 1 s peak as a reference, which was set to 285 eV. For XPS core-level analyses, a Shirley function was employed for background subtraction, followed by data fitting using Gaussian-Lorentzian profiles for oxide components and Lorentzian-asymmetric profiles for metallic components.

Figure 4.17 presents the results of the XPS analysis. From the Pt 4f core level signal of the HO3P|Pt sample (Figure 4.17a), it can be deduced that the Pt layer up to the HfO_2/Pt interface is pure Pt metal, as only the Pt^0 doublet is present and there are no indications of additional valence states. This is consistent with Pt metal oxidation behavior. Additionally, the Hf 4f core level signal in Figure 4.17b can be successfully simulated only by the Hf^{4+} doublet peak, indicating that the chemical composition of the entire layer is pure HfO_2.

For the TiN and W CEs, XPS analysis was performed on two different samples. The first set of samples was the pure TiN and W surfaces after exposure to air, while the second set was the HfO_2/TiN and HfO_2/W interfaces, which were obtained after the

HfO_2 layer was grown by PE-ALD on the TiN and W CEs, respectively. This enabled a comparison of the properties of the pure surfaces to those of the HfO_2 interfaces. Figure 4.17c shows the Ti 4f core level spectrum for the TiN film after exposure to air, indicating contributions from TiN and Ti^{4+} attributed to the formation of a TiO_2 surface layer when the TiN film was exposed to air. The contribution from Ti^{3+} and Ti^{2+} were disregarded due to overlapping peaks with TiN, however, it is expected that the TiO_x is not stoichiometric TiO_2 but with contributions from Ti^{3+} and Ti^{2+}. For the HfO_2/TiN sample (Figure 4.17d), the Ti^{4+} doublet intensity is further increased compared to the TiN signal, indicating a thicker TiO_2 interface layer after the HfO_2 PE-ALD process compared to the surface oxide formed when the TiN film was exposed to air. The XPS analysis performed on the W CE after exposure to air showed additional components in the W 4f core level spectrum, identified as originating from W^{4+} and W^{6+}, indicating the formation of a WO_2/WO_3 surface layer (Figure 4.17e). The presence of a WO_2 component suggests the presence of an oxygen gradient when traversing from the WO_3 surface layer to the W film. The W 4f core level spectrum for the HfO_2/W sample also shows peaks from W^{6+}, indicating the presence of a WO_x interface layer between the W metal CE and the HfO_2 electrolyte layer (Figure 4.17f). However, it was difficult to accurately fit the WO_2 peaks due to their overlap with the Hf 5p core level of the HfO_2 layer. The native surface oxides formed after exposure of the CEs to air were found to be only several nm in thickness, as confirmed by XPS analysis of a sputter-cleaned TiN surface and an oxidized W surface analyzed with a take-off angle of $\theta = 15°$ to target the bulk of the film. Metallic phases of TiN (Figure 4.17g) and W (Figure 4.17h) were more pronounced in these measurements, indicating that the native oxide layer is only present at the surface of the CEs and does not extend into the bulk of the material. The thickness of 2 to 3 nm was identified for the native oxide layers using XRR measurements, which is a typical value for native oxides on metals [189].

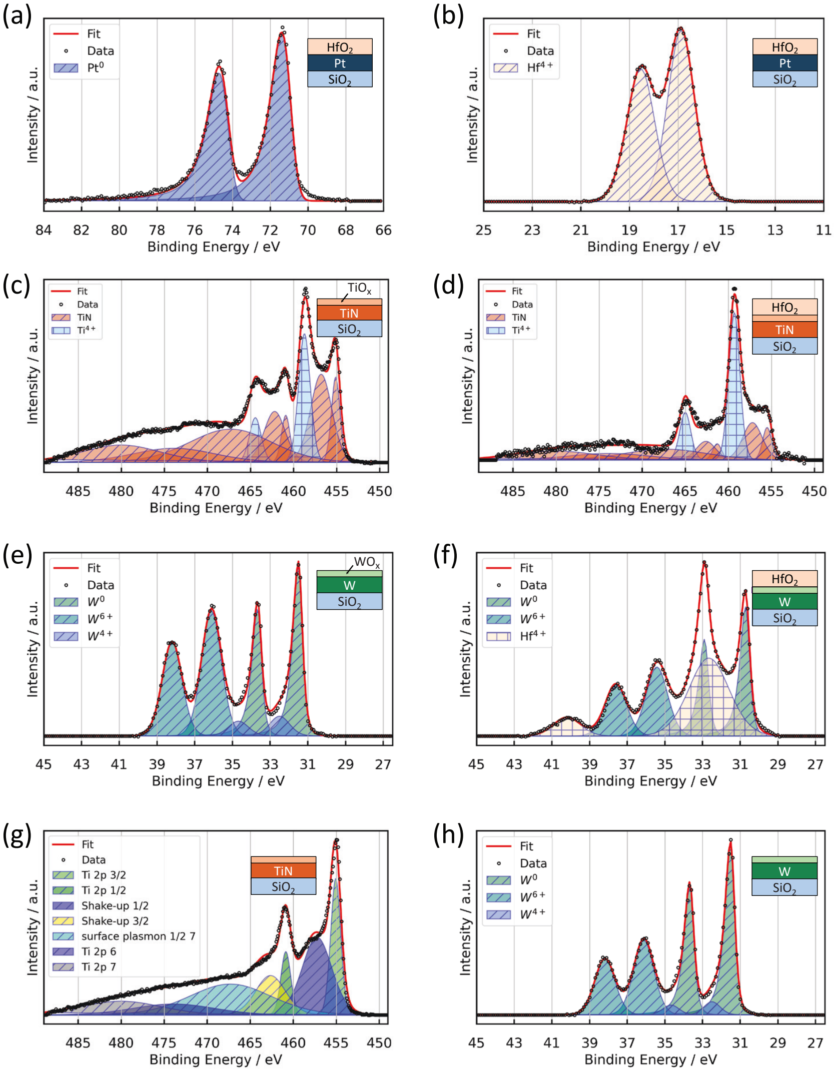

Figure 4.17: XPS analyses of CE metal surfaces and interfaces with and without an HfO_2 layer on top. (a) Pt 4f core level spectra for a Pt film after exposure to air. (b) Hf 4f core level spectra for a Pt film with a 3 nm HfO_2 layer on top. (c) Ti 4f core level spectra for a TiN film after exposure to air. (d) Ti 4f core level spectra for a TiN film after deposition of 3 nm HfO_2. (e) W 4f core level spectra for a W film after exposure to air. (f) W 4f core level spectra for a W film after deposition of 3 nm HfO_2. (g) XPS analysis of an in situ sputter-cleaned TiN CE surface. (h) XPS analysis of a pure W film under a take-off angle of 15° targeting the bulk of the film. Except (h), all measurements were conducted under a take-off angle of 45°. Reproduced with permission from [3].

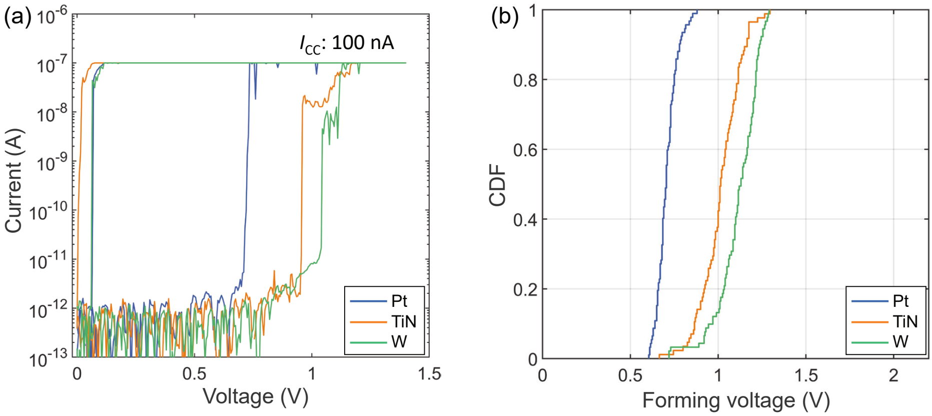

Figure 4.18: (a) Representative I-V curves of the electroforming of Ag/3 nm HfO$_2$/CE devices for the three different CE materials. (b) Statistical distribution of the forming voltage collected from 96 cells for the three different devices. A compliance current of 100 nA and a sweep rate of 62.5 mV/s were used for the measurements. Reproduced with permission from [3].

Electroforming under different counter electrodes

In Figure 4.18a, representative forming curves of the diffusive memristor cells made from different CEs are displayed. These curves indicate that all three types of devices exhibit a very low initial leakage current. Figure 4.18b shows the statistical distribution of forming voltage for each device type, based on the measurements of 96 cells. The forming voltage required for the Ag/HfO$_2$/Pt device is lower than for the Ag/HfO$_2$/TiN and Ag/HfO$_2$/W devices, and the spread of forming voltage is narrower for the devices with Pt CE compared to the ones with TiN and W electrodes. This trend can be explained by considering the formation of an interfacial oxide layer, as described in Section 4.1.5 and confirmed by XPS and XRR analyses. The thickness of the insulating electrolyte layer is a crucial factor during the electroforming process, as it determines the electric field applied to the dielectric. Therefore, a thicker oxide layer will require a higher voltage for the conductive filament to form. Note that, the forming voltage for the Ag/HfO$_2$/Pt shown in Figure 4.18a is lower than the one shown in Figure 4.1. This difference can be attributed to two reasons: Firstly, the device area is different for the two (8 µm^2 vs 3 µm^2). Secondly, the methods used to deposit the Pt metal films were different, which can have an impact on the resulting forming voltage (see 3.3.3).

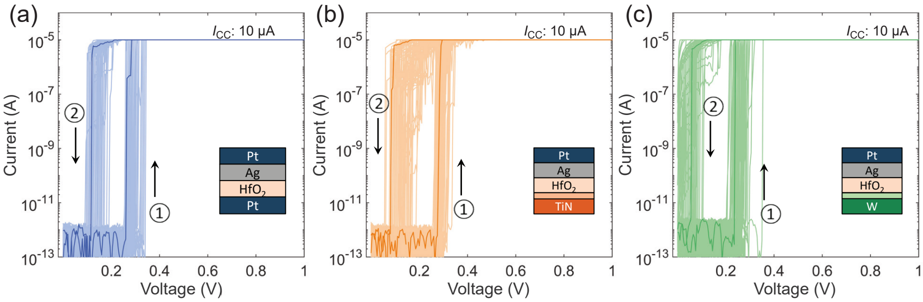

Figure 4.19: Typical threshold I-V curves for (a) HO3P|Pt, (b) HO3P|TiN, and (c) HO3P|W devices. The TiO_x and WO_x interfacial oxides are shown with light orange and light green colors, respectively. A sweep rate of 62.5 mV/s was used for the measurements. Reproduced with permission from [3].

Threshold switching under different counter electrodes

The threshold switching behavior of the Pt, TiN, and W CE devices are presented in Figure 4.19. It can be seen that the three devices exhibit similar threshold switching behavior, switching to LRS at a V_{th} of approximately 0.2-0.3 V. This suggests that these devices have comparable switching characteristics once the forming process has been completed.

For better comparison, data were collected from 8 random devices from each of the three samples and switched for 100 cycles. The results are shown in Figure 4.20. As can be seen, the c2c and d2d variation both in V_h and V_{th} values differs for the three types of diffusive memristors. Devices with Pt CE exhibit the least deviation in both c2c and d2d, with only a small spread in the switching behavior (Figure 4.20a). Conversely, devices with TiN CE exhibit moderate c2c variation for most devices, but a few outliers display much higher variation (Figure 4.20b). Devices with W CE also exhibit stable switching behavior, but the spread in the c2c and d2d variation is larger than for the other two types of devices (Figure 4.20c). The difference in the variation can be attributed to the presence of an inhomogeneous switching layer in devices with TiN and W CE, which includes a metal oxide interfacial layer in addition to the 3 nm HfO_2 electrolyte layer. Furthermore, the increased total thickness of the insulating layer, which is accompanied by an increased forming voltage, can lead to more variation in the switching behavior.

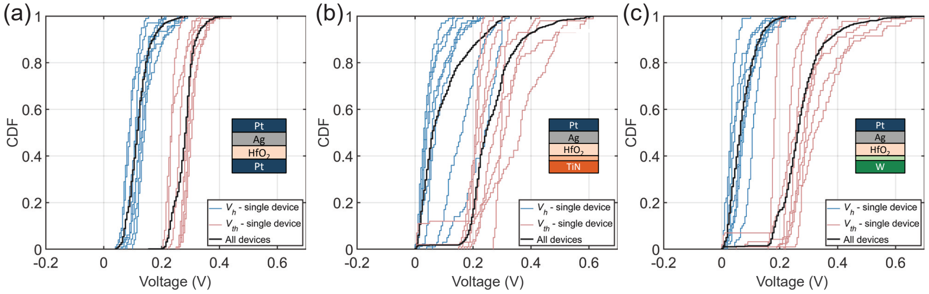

Figure 4.20: Statistical distribution of the hold voltage (V_h) and threshold voltage (V_th) collected from 8 devices and 100 cycles each for (a) HO3P|Pt, (b) HO3P|TiN, and (c) HO3P|W devices. Reproduced with permission from [3].

4.2 Threshold Switching in Ag/SiO$_2$/Pt Cell

4.2.1 Initial Forming Behavior

Similar to that of the HO3P|Pt, the SO3P|Pt device also exhibits an extremely low initial leakage current, as shown in Figure 4.21. Both the SiO$_2$ and HfO$_2$ films are grown by ALD and have a low defect density, thus showing highly insulating behavior in the pristine state. A leakage current below 10 fA (resistance of above 10 TΩ) and a moderate forming voltage of about 0.9 V (in auto-range mode) can be observed (Figure 4.21). Similar to the HfO$_2$, the initial current, and thus resistance, at low voltages is below the resolution limit of the measurement setup and the value given is for reference only.

Area dependence of the forming process

Distributions of the forming voltage of the SO3P|Pt and SO5P|Pt devices collected from four different device areas are shown in Figure 4.22. Device areas ranging from 3 μm^2 to 220 μm^2 were measured and analyzed. Two observations can be made from Figure 4.22: (i) the forming voltage increases as the SiO$_2$ thickness increases and (ii) the forming voltage decreases as the device area increases. The thickness dependence of the forming voltage can be justified by the strong field dependence of the switching process in ECM cells. For thicker films, the effective field strength is lower compared to thin films, thus requiring higher voltage to switch.

On the other hand, it is well known that defects are important for the switching as

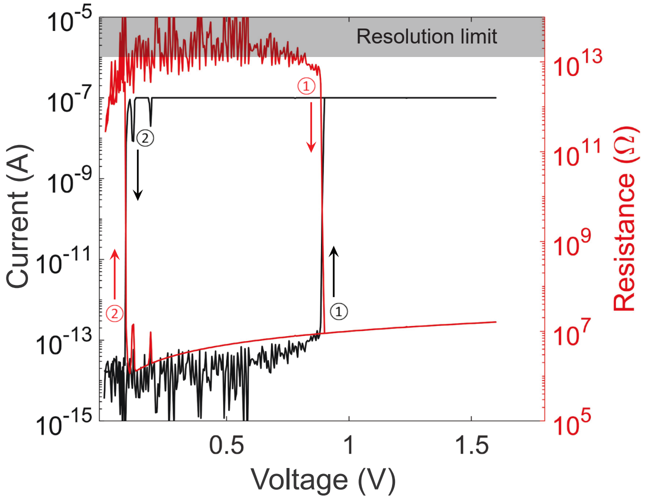

Figure 4.21: Initial forming characteristics of SO3P|Pt device. The current response is plotted in black while the calculated resistance of the cell is plotted in red. Current compliance of 100 nA was used to limit current overshoot.

they can be used as a diffusion path for electrons and/or mobile ions. Furthermore, oxide materials usually contain defects, and their concentration scales with the area. That means devices with large areas have more defects and, thus, require less voltage to form a diffusion path and switch. Thus, the observed area dependence of the forming voltage is consistent with this.

4.2.2 Threshold Switching

Once the devices are successfully formed, they exhibit a threshold type volatile switching at a much lower voltage of V_{th} than the forming voltage. This is mainly due to the switching taking place through preformed conduction paths. An exemplary I-V curve of a threshold switching measured on the SO3P|Pt device is given in Figure 4.23a. An abrupt and volatile switching with clear rising ① at a certain V_{th} and falling ② at a specific V_{h} can be seen for repeated cycles. A distribution of the V_{h} (blue) and V_{th} (red) collected from 10 devices and 100 cycles each is presented in Figure 4.23b. Both V_{h} and V_{th} have a good distribution both in terms of c2c and d2d variations, except for two devices that showed stuck-on behavior for a few cycles as indicated by the zero V_{th}.

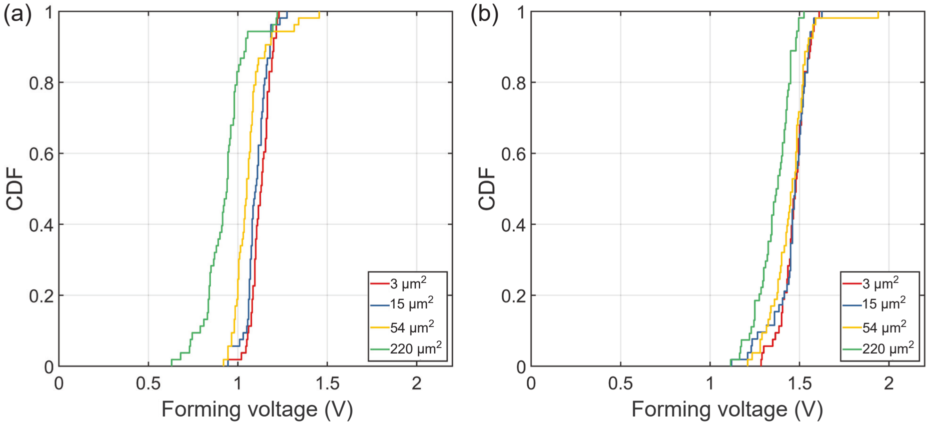

Figure 4.22: CDF plot of the forming voltage of (a) SO3P|Pt and (b) SO5P|Pt devices for varied device areas. A constant sweep rate of 100 mV/s was used during the measurement

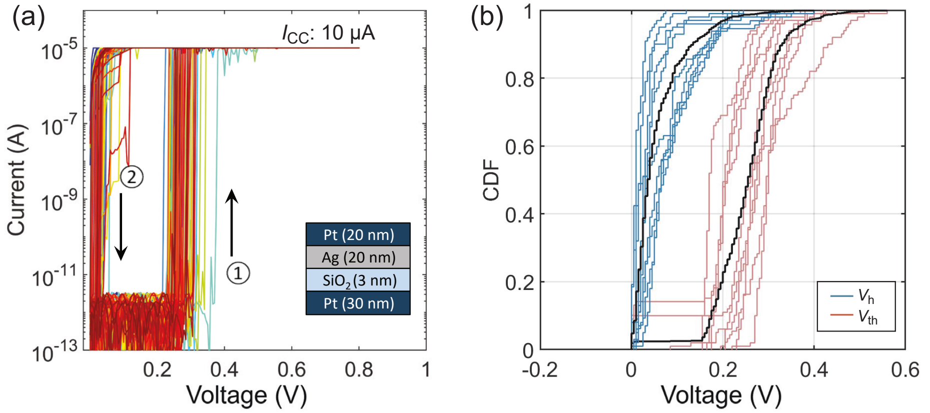

Figure 4.23: I-V sweep of the SO3P|Pt device measured under a compliance current (I_{CC}) of 10 μA. (b) Statistical distribution of the hold (V_h) and threshold (V_{th}) voltages collected from 10 devices and 100 cycles each.

4.3 Comparison and Summary

Both the SiO_2- and HfO_2-based devices exhibit comparable behavior, with similar threshold switching characteristics and threshold voltage, as discussed in this chapter. However, the SiO_2-based device has a slightly higher forming voltage compared to the

HfO_2-based device. This could be due to a higher migration barrier for Ag^+ ion in SiO_2 compared to HfO_2. Another notable difference between the two devices is the distribution of the hold and threshold voltages. The HfO_2-based device demonstrated a tighter c2c and d2d distribution compared to the SiO_2-based device.

In summary, HfO_2- and SiO_2-based diffusive memristors were fabricated and electrically characterized. The two devices showed comparable switching characteristics with volatile switching achieved in both. Overall, the HfO_2-based device showed good thresholding characteristics with a reasonable forming voltage and switching variability. Further in-depth comparison between the two cells will be provided in Chapter 5 and 6.

Chapter 5

SET Kinetics of Diffusive Memristors

This chapter focuses on the kinetics of diffusive memristors by using two oxide systems, HfO_2 and SiO_2, as switching matrices. Section 5.1 explores the kinetics of HfO_2-based diffusive memristors, including investigating the impact of voltage on the SET kinetics (Section 5.1.1), the impact of a series resistor on the SET kinetics of HfO_2-based diffusive memristors (Section 5.1.2), and the influence of CE on the SET kinetics (Section 5.1.3). For comparison, the SET kinetics of SiO_2-based diffusive memristors will be discussed in Section 5.2. Finally, the chapter concludes with a comparison and summary of the two oxide systems.

5.1 SET Kinetics of HfO_2-based Diffusive Memristor

Generally speaking, fast programming times are one of the primary goals for improving the performance of emerging memristor-based technologies. However, for diffusive memristors, how fast the device should switch depends on the target application, which will be discussed in Chapter 8. The switching kinetics in diffusive memristors include both the SET and relaxation processes. This section will discuss the SET kinetics of the fabricated HfO_2- and SiO_2-based diffusive memristors.

Terminologies

This section introduces some technical terms that will be used in the following discussion. Specifically, the terms "SET time" and "relaxation time" are defined, and the pulse scheme used during the measurement is shown in Figure 5.1. A temporal response of the device is first extracted from the current response in the time domain

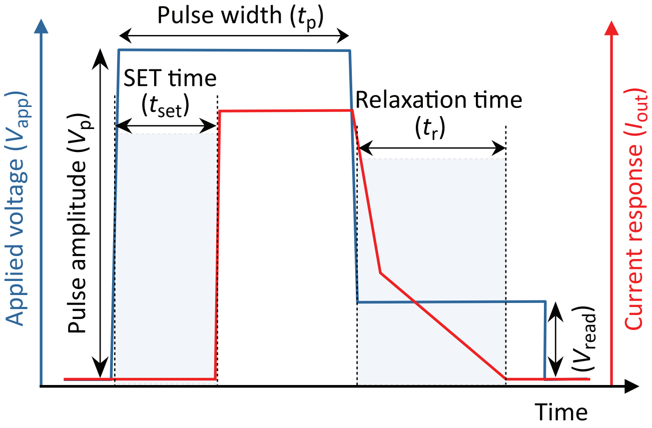

Figure 5.1: Various terminologies and the definitions of SET time (t_{set}) and relaxation time (t_{r}) from a temporal response measurement in the time domain. The applied voltage (V_{app}) and output current signal (I_{out}) are shown in blue and red colors, respectively. Reproduced with permission from [1].

upon a voltage pulse with amplitude V_{p} and pulse width t_{p}. The SET time (t_{set}) is the duration between the maximum edge of V_{p} and the onset of the output current rise I_{out}. On the other hand, the relaxation time (t_{r}) is the time between the points where the voltage drops to the monitor voltage (V_{read}) and where I_{out} fully relaxes back to the initial state. It is worth noting that the initial current of the device, which is in the range of fA, cannot be measured during the pulse measurement due to the resolution limit of the setup. Therefore, a cutoff current of 100-200 nA, depending on the noise level of the different current ranges, is used as a reference for full relaxation. The relaxation dynamics will be discussed in Chapter 6.

5.1.1 Impact of Voltage on the SET Kinetics

The exponential dependence of t_{set} with V_{p} for ECMs has been shown in multiple publications [60, 190]. Many of these reports solely assume nucleation energy as a limiting factor for the switching speed. However, other processes such as ion migration can also significantly affect filament growth dynamics and hence the switching kinetics [62, 175, 191]. Additionally, previous studies have not extensively investigated the SET kinetics of diffusive memristors based on large statistical data sets. To better understand the physical processes involved in both nucleation and filament growth, a thorough analysis of the switching kinetics was conducted by collecting a large data

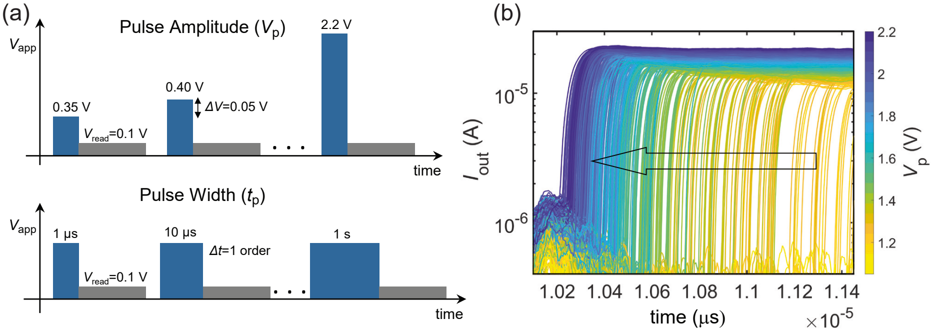

Figure 5.2: (a) Schematics of the programming pulse schemes used for the kinetics study. (b) Typical I_{out}–t curves recorded during the SET event measurement of the device under different V_p.

set from multiple combinations of voltage pulse V_p and t_p.

To carry out this analysis, the devices in the HRS were subjected to defined voltage pulses with V_p ranging from 0.35 V to 2.20 V and t_p ranging from 1 µs to 1 s (Figure 5.2a). The corresponding t_{set} was then extracted from the transient current response, as defined in Figure 5.1. Data from unsuccessful switching events and/or those switched within the rising edge of the pulse are excluded from the analysis. Exemplary I_{out}–t curves for varied V_p are shown in Figure 5.2b.

Figure 5.3 illustrates the experimental results of t_{set} plotted semi-logarithmically against V_p for the HO3P|Pt device. The graph shows that t_{set} decreases exponentially with increasing V_p. At low voltages, switching takes longer to be triggered, but a slight increase in V_p dramatically reduces t_{set}. As V_p is further increased, the corresponding decrease in t_{set} continuously flattens out and appears to approach saturation at higher V_p. Similar observations have been reported for AgI-based [62] and SiO$_2$-based [89] non-volatile ECMs.

To gain further insights into the physical processes that limit the switching speed, a simulation was conducted based on the compact model presented in Section 2.3. Figure 5.4a shows the simulation results as a straight line along with the experimental data, with the parameters used to fit the data presented in Table 5.1. Three different rate-determining processes were identified at different voltage regimes: (I) nucleation-limited, (II) electron-transfer-limited, and (III) mixed (electron-transfer and ion migration) limited. The steepest slope can be observed at voltages below 0.6 V in regime I, which is classified as the nucleation-limited regime. Subsequently, a flatter

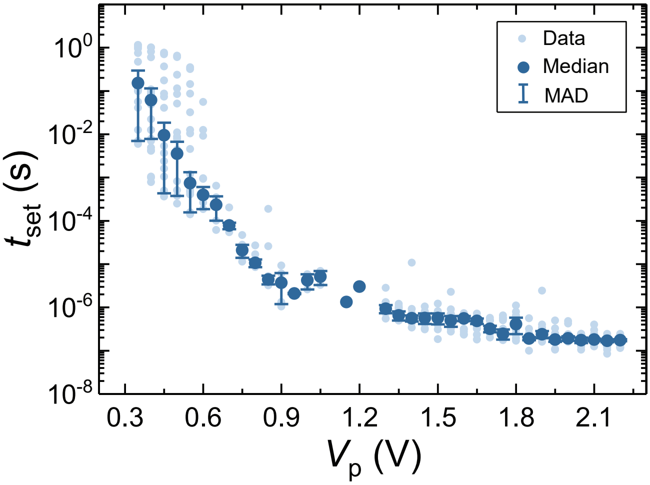

Figure 5.3: SET switching kinetics of HO3P|Pt device. The median values and median absolute deviation (MAD) of the experimental data are displayed using cool black circles and vertical lines, respectively. A series resistor of 100 kΩ was used during the measurement. Reproduced with permission from [1].

slope is observed in regime II between 0.6 V and 1.5 V, where the electron-transfer reaction is the rate-limiting process. Above 1.5 V, regime III with a mixed electron-transfer and ion hopping limited process is visible, with minor voltage dependence on t_{set}.

It is evident from Figure 5.4a that the experimental results in the electron transfer region do not match the simulation curve, with the experimental data showing a much steeper drop in t_{set} compared to the simulation. For the simulation, a constant filament radius (r_{fil}) was assumed regardless of the voltage amplitude. That means a fixed radius number is inserted as an input parameter prior to starting the simulation. For example, r_{fil} value of 1 nm was used for the fit in Figure 5.4a. However, previous kinetic Monte Carlo (KMC) simulations suggest that the metal filament undergoes a structural change from a bulkier to a more fragile appearance as the switching voltage is increased [192]. This change can be explained by a shift from predominantly isotropic to field-driven anisotropic growth at low and high pulse amplitudes, respectively.

To investigate this further, a simulation was conducted using different r_{fil} ranging from 0.15 nm to 3.0 nm, with a single SET kinetics curve still being voltage-independent. The outcomes are shown in Figure 5.4b. The results demonstrate that the filament

Table 5.1: Parameters used for the simulation of SET kinetics.

Parameter	Value	Unit	Parameter	Value	Unit
T	298	K	ΔG_{et}	0.62	eV
z	1	-	α_{et}	0.3	-
m_{r}	$0.15m_0$	-	$k_{0,\mathrm{et}}$	$2 \cdot 10^3$	$\mathrm{m\,s^{-1}}$
f	$1 \cdot 10^{13}$	Hz	ΔG_{hop}	0.21	eV
c_{ion}	$3 \cdot 10^{28}$	m^3	a	0.25	nm
ρ_{Ag}	$1.7 \cdot 10^{-28}$	Ωm	L	3	nm
ΔW_0	2.7	eV	A_{fil}	3.14	nm^2
N_{c}	1	-	A_{is}	3.14	nm^2
ΔG_{nuc}	0.84	eV	A_{ac}	314.16	nm^2
α_{nuc}	0.25	-	R_{el}	1.11	mΩ
$t_{0,\mathrm{nuc}}$	$2 \cdot 10^{-7}$	s	R_{series}	100	kΩ

radius has a significant impact on t_{set}, particularly in the electron transfer region (II). The experimental data also crosses along different r_{fil}, suggesting that different filament sizes may be expected at different voltage regimes. This is consistent with the KMC simulation predictions. Furthermore, the assumption of different filament sizes better fits the experimentally determined SET kinetics values. In particular, Figure 5.4b predicts that the filament radius decreases from approximately 3.0 nm to 0.15 nm as the voltage pulse increases from around 0.5 V to 1.0 V, respectively. Furthermore, data points below 0.15 nm indicate successful SET events that do not lead to galvanic contact. The different possible conduction mechanisms in diffusive memristors are explained in Section 4.1.2. Further discussion on the voltage-dependent filament growth mechanism will be presented in Chapter 7.

5.1.2 Impact of a Series Resistor on the SET Kinetics

Successful implementation of diffusive memristors in complex circuits, whether for storage or neuromorphic computation, requires predictable and controllable threshold and relaxation behaviors, particularly when integrating diffusive memristors into larger circuitry. For instance, in a one-selector one-resistor (1S1R) configuration, the diffusive memristor-based access device is linked in series with the neighboring memory cell, which can be in the HRS or various resistance states in the LRS depending on how the memory cell is previously programmed. This makes the memory cell effectively behave as a series resistor (R_{series}) toward the diffusive memristor cell. Previous studies have demonstrated that R_{series} can significantly impact the switching performance of

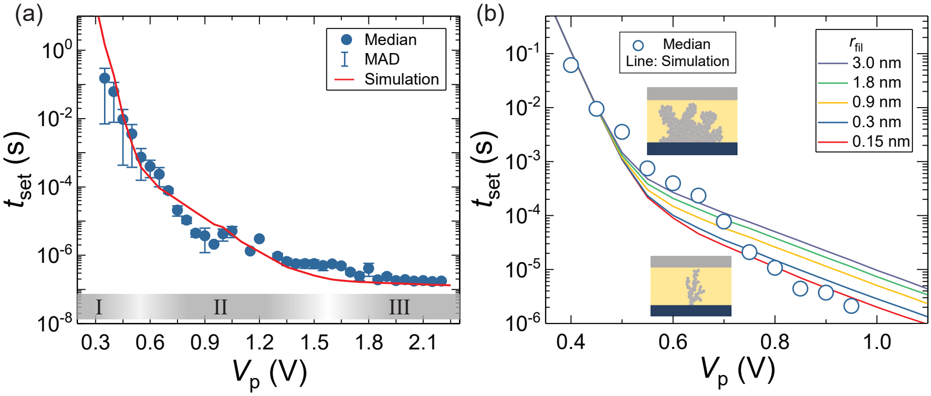

Figure 5.4: (a) Fitting of the median of the experimental data by using numerical simulation. A filament radius of 1 nm is assumed for the simulation. (b) Experimental and simulated SET time for different filament radii ranging from 0.15 to 3 nm as a function of pulse voltage. Reproduced with permission from [1].

non-volatile memristive devices [193–195]. Therefore, comprehending the influence of R_{series} on the switching kinetics of diffusive memristors is equally important.

This section presents the impact of R_{series} on the SET kinetics of diffusive memristors using the HO3P|Pt device. Four distinct SMD resistors with values of 50 kΩ, 100 kΩ, 560 kΩ, and 1000 kΩ were connected in series with the diffusive memristor device. The SMD resistors (COMP-CARD®-System, *OVA Electronik GmbH*) were introduced through a custom-built tungsten probe tip.

Figure 5.5a displays a DC sweep test carried out on a diffusive memristor connected to various series resistors, revealing varying current levels for the diffusive memristor in LRS for each resistor, as anticipated. Nevertheless, the V_{th} remains constant for all resistances. This is reasonable because the initial resistance of the diffusive memristor is much higher than that of the series resistors employed, resulting in all voltage drops on the diffusive memristor. As a result, the V_{th} stays unaffected. Figure 5.5b illustrates a pulse test carried out with a fixed V_{p} of 1.6 V and different series resistances, revealing different current values for the LRS. The pink rectangle in Figure 5.5b marks the area that is shown in magnified form in Figure 5.5c. The current axis in Figure 5.5c is presented on a logarithmic scale to enhance visibility. As can be seen in the figure, the current spike at the beginning of the current rise grows as R_{series} increases. This outcome is caused by the RC-effect, which will be elaborated on in the subsequent section. Furthermore, t_{set} appears to increase as the series resistance value increases.

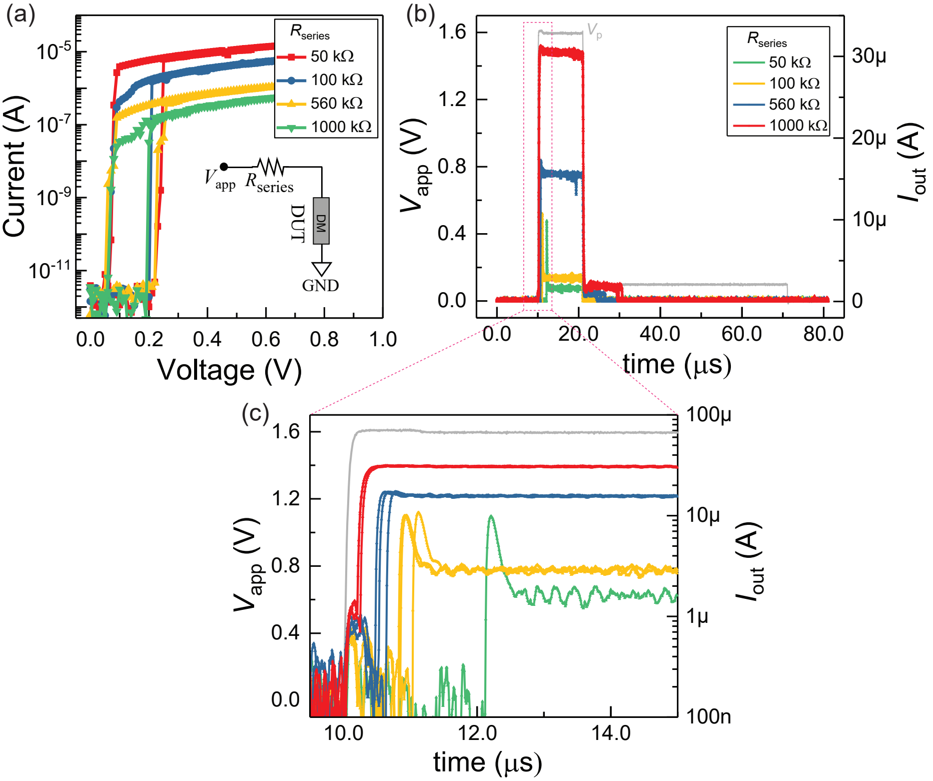

Figure 5.5: (a) I-V sweep measurements performed on HO3P|Pt device with different series resistances. Inset shows the electrical connection during the measurement. (b) The transient current measurement under different series resistance. (c) Magnified image of the box with the pink broken line in (b). The applied voltage (V_{app}) is shown in gray color.

Data were collected from various V_p and t_p combinations, and the corresponding t_{set} values were extracted from the transient current response. Figure 5.6 depicts semi-logarithmic plots of t_{set} against V_p for different R_{series} values, revealing an expected exponential decay of t_{set} with respect to V_p for all R_{series}. All data are collected from one cell one after the other in order to have a better comparison. Figure 5.7a displays the median values of t_{set} for each R_{series}. It can be seen that at low voltages, no change in the SET kinetics is observed for all R_{series} values. However, for voltages higher than 1.0 V, the t_{set} values show differences with varying R_{series}. The t_{set} values increase by approximately two orders of magnitude, from around 30 ns to 1.3 μs, as the R_{series}

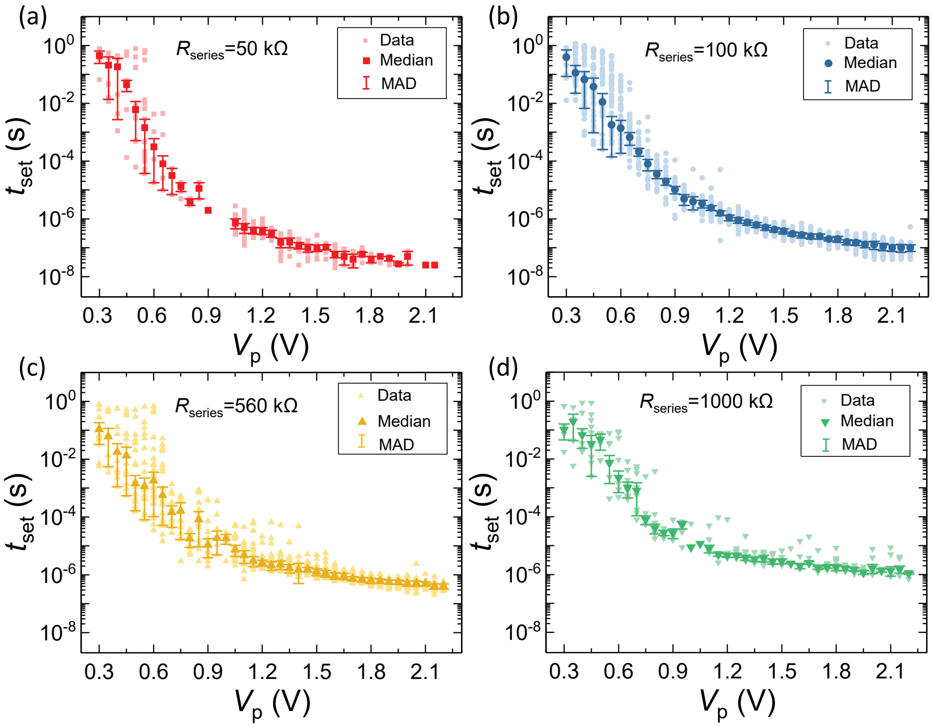

Figure 5.6: SET switching kinetics of HO3P|Pt cell in series with different resistors of (a) 50 kΩ, (b) 100 kΩ, (c) 560 kΩ, and (d) 1000 kΩ. The median values and median absolute deviations (MAD) of the experimental data are displayed using color-filled symbols and vertical lines, respectively. Reproduced with permission from [2].

value changes from 50 kΩ to 1000 kΩ.

Typically, a series resistor affects the switching performance of memristive devices by functioning as a voltage divider element [193]. This becomes significant when the series resistor's value is not considerably different from the resistance of the memristive device. However, the diffusive memristor studied in this thesis has an extremely high resistance in the HRS (in the TΩ range, Figure 5.8a) compared to the largest R_{series} used (1000 kΩ). Therefore, R_{series} should not have a significant impact on the t_{set}. This assessment is valid for $V_{\mathrm{p}} < 0.9$ V, but it does not hold for $V_{\mathrm{p}} > 1.0$ V. Therefore, other factors must be taken into consideration. One possible factor is the RC-time effect, which is evident from the different current spike heights and widths for various R_{series} values in Figure 5.5c. For this, t_{set} values at the saturation regions were plotted

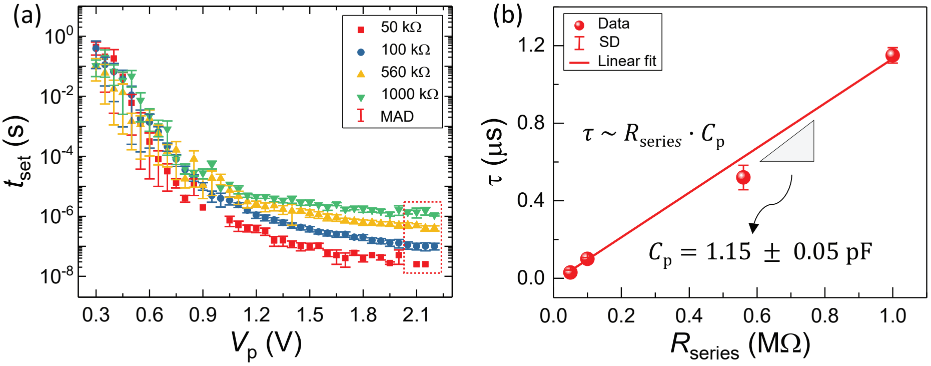

Figure 5.7: (a) A plot of the median values of t_{set} as a function of V_{p} for the different series resistors. (b) The mean of t_{set} taken from the red box marked region in (a) plotted against R_{series} to extract C_{p}. Reproduced with permission from [2].

against R_{series} (Figure 5.7b). Assuming that the t_{set} values in the flat region (> 2.0 V) represent an RC-time constant τ, the slope of a linearly fitted τ-R_{series} plot provides the total parasitic capacitance (C_{p}) of the entire system using a simple equation $\tau = R_{\text{series}} \cdot C_{\text{p}}$. From the data in Figure 5.7b, a C_{p} value of 1.15 ± 0.05 pF is obtained.

The observed RC-time that affects the switching performance of the diffusive memristor may result from the parasitic capacitance of the memristor cell and/or the measurement setup (rf. Section 3.4). A memristive cell is essentially a parallel plate capacitor with a thin oxide material functioning as a dielectric layer. In the case of the diffusive memristor cell with extremely high resistance in the HRS, it initially behaves as an ideal capacitor (Figure 5.8b). To investigate this, a capacitance-voltage (C-V) measurement was conducted on the diffusive memristor cell at 100 kHz and a capacitance value of approximately 0.17 pF was determined. This value corresponds to a mean dielectric permittivity of the amorphous HfO$_2$ layer of approximately 19, which is consistent with reported values ranging from 18 to 25 [133–136], and an equivalent oxide thickness (EOT) of 0.6 nm for a 3 nm HfO$_2$ dielectric layer [134, 196]. The remaining parasitic capacitance can be attributed to the measurement setup and all electrical connections.

Hence, the observed limitation of the SET time is not an intrinsic physical property of the switching device stack but is rather due to the charging time of the collective capacitance of the diffusive memristor and measurement setup environment. To confirm this assumption, a simulation was conducted that accounted for the RC-time effect. The RC-time effect was introduced into the simulation by considering a time

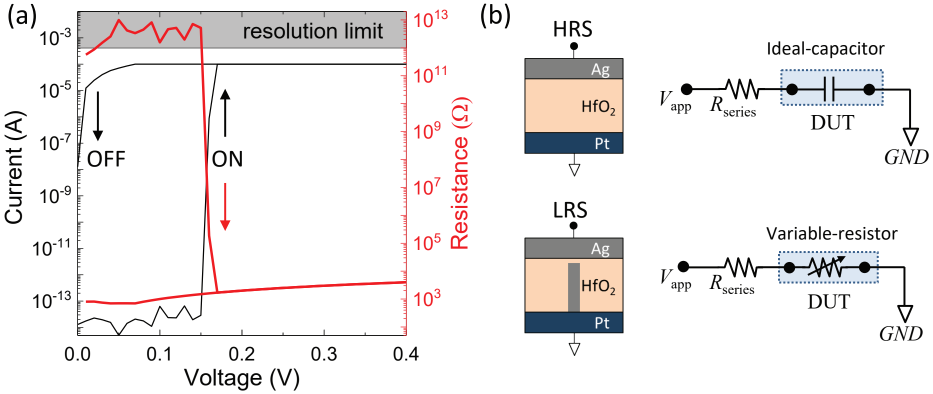

Figure 5.8: (a) A sweep I-V and resistance-voltage (R-V) plot of a HO3P|Pt cell. (b) Schematic drawings showing the capacitive and resistive behavior of the device for the HRS and LRS, respectively. Reproduced with permission from [2].

constant defined by ($R_{\text{series}}\cdot$ 1.15 pF) and varying R_{series}. As depicted in Figure 5.9a, the simulation results closely match the experimental data. The same parameters used in Table 1 were utilized in the simulation, except for the R_{series}, which was modified to match the RC-time. It is worth noting that the capacitance effect can be reduced, and faster SET times can be accomplished by minimizing the parasitic capacitance of the measurement setup and scaling the device area further. This is demonstrated by the simulation data in Figure 5.9b. Assuming a C_{p} of only 1 fF, the influence of the R_{series} on t_{set} becomes negligible, and rapid SET events with t_{set} in the range of a few nanoseconds could be attained.

5.1.3 Influence of Counter Electrode on the SET Kinetics

Electrocatalytic activity

The CE is a crucial component in the switching process, as it supplies the electrons needed for the reduction reaction and charge compensation at the CE/electrolyte interface [91, 94]. Additionally, the catalytic activity of the CE towards the water redox process determines the concentration of active ions within the switching layer, which in turn impacts the switching kinetics of the cell [89, 91]. For instance, electrodes with higher electrocatalytic activity facilitate faster switching, while those with lower electrocatalytic activity significantly hinder the switching speed. This is because the CE material affects the reaction rate and supply of hydroxyl ions, which act as

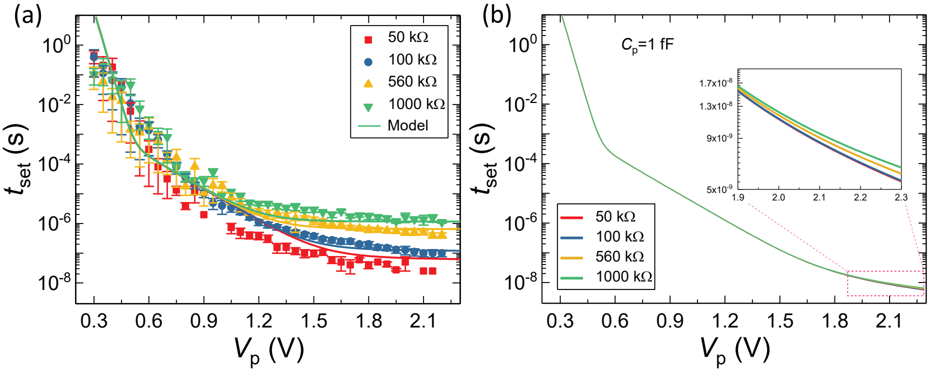

Figure 5.9: (a) Simulation of the SET kinetics when an RC-time constant of the circuit is considered with C_p=1.15 pF. (b) Simulation data was obtained with C_p of 1 fF, showing faster switching times and negligible differences between the R_{series} values. Inset shows a magnified image of the pink box in (b). Reproduced with permission from [2].

counter charges and maintain electroneutrality during the anodic oxidation of the active electrode.

Moreover, different metals exhibit varying levels of attraction towards oxygen, whereby metals with a high affinity for oxygen tend to create a native oxide layer on the surface of the CE. This could potentially reduce the electrocatalytic activity of the CE and ultimately slow down the switching kinetics. For more details on the role of electrocatalytic activity in the switching process of memristive systems, the reader is referred to the Ph.D. thesis of Stefan Tappertzhofen [197] and ref. [91, 95].

SET kinetics under various counter electrodes

To explore the impact of CEs on the diffusive memristor kinetics, the SET times of devices featuring different CEs, namely Pt, TiN, and W, were analyzed. The data was collected from different combinations of V_p and t_p and the corresponding t_{set} values were extracted from the transient current response, using the same methodology as in the previous section. Figure 5.10 illustrates the results obtained. It is evident from the data that t_{set} decreases exponentially with increasing V_p for all devices. The highly non-linear nature of t_{set} observed in all cases is consistent with the SET kinetics of ECM cells.

Further analysis of the median of the data, as shown in Figure 5.10d, reveals differences between the devices featuring different CEs, depending on the voltage regime. At low voltages, where nucleation limits the overall process, all three devices display negligible differences in their SET kinetics. This finding is in agreement with the results obtained from I-V sweeps that fall into this range of low voltage amplitude and long pulse duration (rf. Section 4.1.5). However, when V_p surpasses 0.6 V and reaches the electron-transfer limited and mixed regimes (i.e. when the process is limited by both electron transfer and ion migration), the SET time curves for the various CE materials begin to diverge. Among the devices tested, the HO3P|Pt device exhibits a sharper decline in SET time, followed by HO3P|TiN and HO3P|W devices. The observed differences are explained as follows.

Aside from the catalytic activity of the pure CE material, the interfacial oxide between the HfO_2 electrolyte and the metal CE is also a significant factor to consider. As discussed earlier and demonstrated in Section 4.1.5, non-noble metals tend to form native oxides. In addition to impacting the catalytic activity of the metal by creating a passivation layer, the native oxide also adds to the thickness of the switching layer. If devices with relatively thick electrolyte layers are being switched, the effect of a few additional nanometers of oxide interfacial layer may not be significant. However, in this scenario, where the interfacial oxide layers are nearly as thick as the HfO_2 electrolyte layer, potential impacts should be considered. Although research on the effect of electrolyte thickness on the switching kinetics of diffusive memristors is very scarce, one could argue that the electric field driving the switching process may be reduced for thicker films due to the larger distance between the two conducting electrodes. However, the effect of insulating layer thickness on SET kinetics is very small. For instance, a simulation performed by using the compact model has shown that doubling the thickness of the electrolyte only results in a twofold increase in t_set. Hence, this factor alone cannot entirely account for the significant differences observed in the SET kinetics between the HO3P|Pt and HO3P|TiN or HO3P|W devices, which are nearly ten times apart.

Moreover, when considering only the catalytic activity of the CE, it is expected that the devices with Pt and TiN CE would exhibit similar kinetics behavior, as reported in a previous study by Luebben et al. which involved ECM cells with a 10 nm SiO_2 switching layer [89]. However, in contrast to this, the results obtained from thin 3 nm HfO_2-based ECM cells clearly indicate a difference in the SET kinetics of Pt and TiN, suggesting that additional factors such as the interfacial oxide layer must be taken into account.

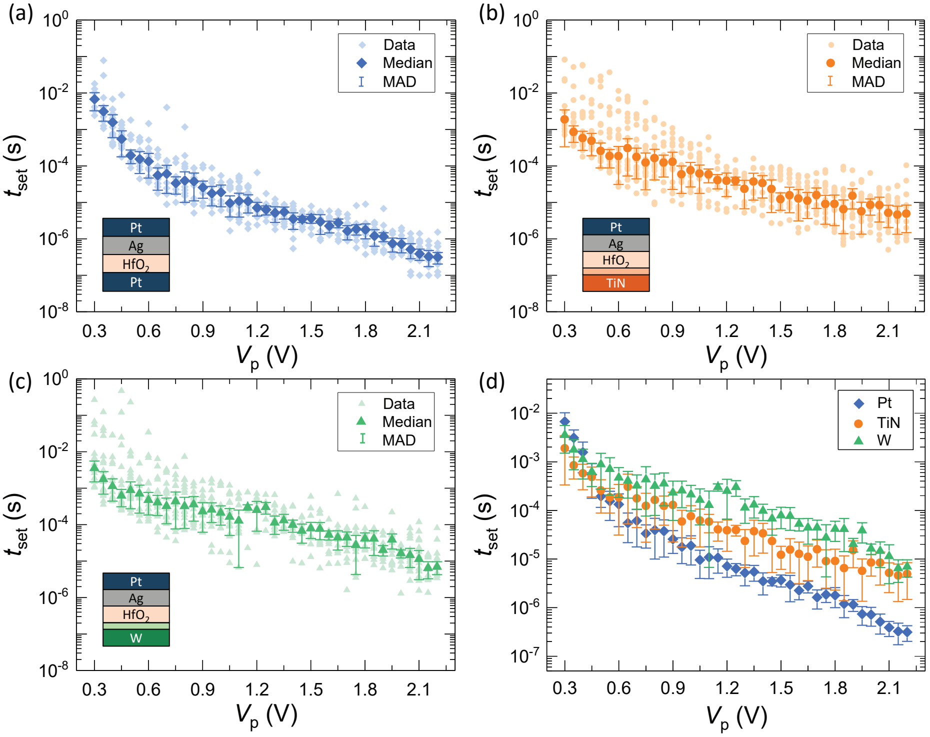

Figure 5.10: SET switching kinetics of (a) HO3P|Pt, (b) HO3P|TiN, and (c) HO3P|W. (d) A median of t_{set} plotted against V_{p} for the three devices. The median values and median absolute deviations (MAD) of the experimental data are displayed using color-filled symbols and vertical lines, respectively. The TiO$_x$ and WO$_x$ interfacial oxides are shown with light orange and light green colors, respectively. A 100 kΩ series resistor was used during the measurements. Reproduced with permission from [3].

Therefore, both the catalytic activity of the CE material itself and the formation of an interfacial oxide layer at the CE/electrolyte interface should be considered. One possible explanation for this is that the additional interfacial TiO$_x$ and WO$_x$ layers acts as an additional barrier for Ag$^+$ ion migration and may also impact the counter-reaction at the CE by forming a passivation layer and reducing the catalytic activity, which in turn alters the concentration of dissolved Ag$^+$ ions in the electrolyte when compared to a clean HfO$_2$/TiN and HfO$_2$/W interfaces [91]. As explained above, the formation of an interfacial oxide layer can lead to an increase in electrolyte thickness as well as a change in the catalytic activity of the CEs. However, discriminating between the contributions of each factor would require further investigation, which is not included in this thesis.

In summary, a CE material has a clear influence on the switching behavior of diffusive memristors. This has been shown experimentally by analyzing the SET kinetics of HfO_2 based diffusive memristor under different CE material. The observed differences are explained by taking into account the interfacial oxide formation at the CE/electrolyte interface and the catalytic activity of the CE material.

5.2 SET Kinetics of SiO_2-based Diffusive Memristor

Another oxide material commonly used in memristive devices is SiO_2. Thin films of SiO_2 allow ions to diffuse within the inert matrix at a reasonable speed. Various researchers have reported on ECM switching in SiO_2, including SET kinetics studies, using Ag or Cu as active electrode [34, 82, 89, 170]. From a materials perspective, factors such as the diffusivity of the active material into the electrolyte and the ionic conductivity of the electrolyte are known to influence the switching behavior of ECM cells. Although both HfO_2 and SiO_2 have been shown to exhibit good ECM characteristics as non-volatile ECM and diffusive memristors, their kinetics may differ due to the different ionic conductivity and/or the tendency to allow ionic diffusion. Moreover, the barrier heights of the AE/electrolyte and CE/electrolyte interfaces may differ, which can affect the electron transfer reaction.

Therefore, the SET kinetics of SiO_2-based diffusive memristor was investigated using a similar programming scheme as shown in Figure 5.2. The experimental results of the SET kinetics curve for the SO3P|Pt device are presented in Figure 5.11a. In addition, Figure 5.11b displays simulation data alongside the median of the experimental data. The parameters used to conduct the simulation are listed in Table 5.2. The results indicate that t_{set} decreases exponentially, which is comparable to the behavior of HfO_2-based devices. However, the magnitude of the decay differs from that of the HfO_2-based cell. A detailed comparison between the two systems will be presented in the following section.

As discussed in Chapter 2, the switching of ECM cells involves multiple distinct steps, including the ionization and incorporation of Ag^+, migration of Ag^+, reduction of Ag^+, and nucleation and growth of Ag clusters. The extent to which the switching layer affects these processes can vary, sometimes having a weaker influence and other times a stronger influence. One important role of the switching layer is in

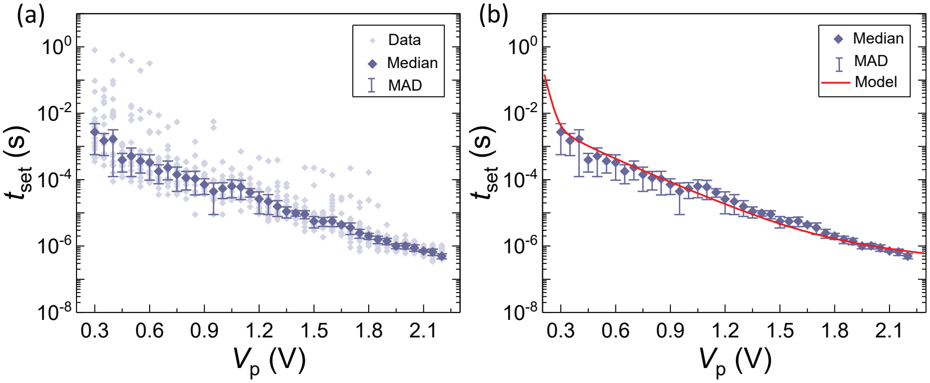

Figure 5.11: SET switching kinetics of SO3P|Pt device. (a) Experimental data and (b) Simulation curve together with the experimental data. The median values and median absolute deviation (MAD) of the experimental data are displayed using dark blue-gray symbols and vertical lines, respectively. A series resistor of 100 kΩ was used during the measurement.

facilitating the diffusion of the active material. This diffusion can occur through interstitial sites, substitutions, or defects such as grain boundaries, vacancies, and voids. The preferred diffusion path is determined by the specific material system and the associated migration barriers.

According to Patel et al., in the Ag/SiO$_2$ system, Ag species in SiO$_2$ prefer to propagate through defects and voids rather than dense areas, as it requires overcoming higher migration barriers [198]. Additionally, the authors noted that oxygen vacancies facilitate reduction and nucleation processes. Specifically, a mobile Ag$^+$ binds to an oxygen vacancy to form an [Ag/V$_o$]$^+$ complex, which then traps an electron and reduces to [Ag/V$_o$]^0, serving as a nucleation site for further clustering of Ag and filament formation. These processes are energetically favored in the Ag/SiO$_2$ system.

The density of defects, therefore, plays an important role in the switching process, which ultimately influences the kinetics. In this particular case, the SiO$_2$ film is grown by using ALD and has a lower defect density which limits the mobility of Ag$^+$ in the densely packed SiO$_2$. Nucleation typically only requires a few Ag atoms to agglomerate, sometimes even just one, so the density of defects or oxygen vacancies does not have a significant impact on nucleation. However, other processes that impede filament growth, such as ion mobility, are severely affected, leading to hindered switching kinetics.

Table 5.2: Parameters used to simulate SET kinetics of SO3P|Pt device.

Parameter	Value	Unit	Parameter	Value	Unit
T	298	K	ΔG_{et}	0.55	eV
z	1	-	α_{et}	0.84	-
m_{r}	$0.84m_0$	-	$k_{0,\mathrm{et}}$	$1 \cdot 10^2$	$\mathrm{m\,s^{-1}}$
f	$1 \cdot 10^{13}$	Hz	ΔG_{hop}	0.3	eV
c_{ion}	$8 \cdot 10^{27}$	$\mathrm{m^3}$	a	0.3	nm
ρ_{Ag}	$1.7 \cdot 10^{-28}$	Ωm	L	3	nm
ΔW_0	2.7	eV	A_{fil}	3.14	$\mathrm{nm^2}$
N_{c}	1	-	A_{is}	3.14	$\mathrm{nm^2}$
ΔG_{nuc}	0.7	eV	A_{ac}	314.16	$\mathrm{nm^2}$
α_{nuc}	0.32	-	R_{el}	1.11	mΩ
$t_{0,\mathrm{nuc}}$	$1 \cdot 10^{-8}$	s	R_{series}	100	kΩ

Furthermore, due to the energetically favored binding of $\mathrm{Ag^+}$ ions and oxygen vacancies and subsequent reduction by trapping electrons, the filament is formed by the continuous movement of Ag clusters. This could result in a rather homogeneous and bulky filament formation, which can have an impact on the relaxation process as well.

5.3 Comparison and Summary

Both $\mathrm{HfO_2}$ and $\mathrm{SiO_2}$ offer suitable conditions for fabricating diffusive memristors, as demonstrated by the various characterizations in this thesis. Nevertheless, variations in their SET kinetics are observable. Figure 5.12 depicts a direct comparison of the SET kinetics of HO3P|Pt and SO3P|Pt devices. Based on the figure, the following conclusions can be drawn:

(i) Both devices show voltage-dependent exponential decay of t_{set}, which is attributed to the field-dominated and accelerated switching process.

(ii) The two devices exhibit different nucleation behaviors. The SO3P|Pt device has a lower nucleation barrier (0.70 eV) compared to HO3P|Pt (0.84 eV), leading to faster nucleation in SO3P|Pt and rendering the nucleation regime almost invisible in the experimental data. This outcome also implies that nucleation does not always initiate from the CE surface; otherwise, the two devices would have similar nucleation behaviors since they share similar CE. This observation is consistent with the findings of Patel et al. [198], where they argued that the nucleation in $\mathrm{Ag/SiO_2}$ system happens within the oxide.

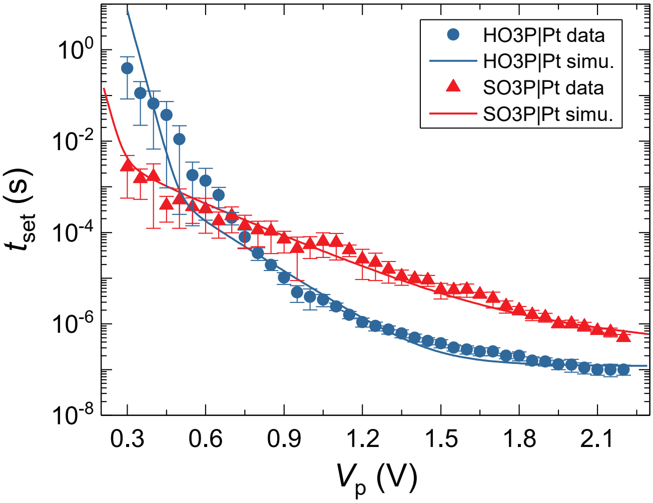

Figure 5.12: Direct comparison of the SET kinetics of HO3P|Pt and SO3P|Pt devices. The scatter plot is the median of the experimental data and the line is the fitting from the model.

(iii) The SET time for the HO3P|Pt device decreases more sharply than SO3P|Pt. Additionally, the SO3P|Pt device is almost two orders of magnitude slower than the HO3P|Pt device above 0.95 V. This could be due to the higher ion-migration barrier and ion-hopping distance in the SiO_2 system than in the HfO_2, leading to prolonged filament formation.

(iv) Unlike in the HO3P|Pt device, there is no observed correlation between filament radius and t_{set} for the SO3P|Pt device, indicating that filament formation and size are comparable regardless of the voltage applied. This, again, is consistent with the assumption of a homogeneous and bulky filament formation due to the continuous movement of clusters (see Section 5.2). This will be further discussed in Chapter 6 and 7, as the outcome will have significance for the relaxation behavior.

Chapter 6

Relaxation Behavior of Diffusive Memristors

In this chapter, a comprehensive analysis of the relaxation dynamics studies conducted in this thesis is presented. The relaxation process in diffusive memristors is influenced by various factors, which will be discussed in detail. Section 6.1 will focus on the relaxation dynamics of HfO_2-based diffusive memristors. The discussion will cover the impact of programming scheme (Section 6.1.1), series resistor (Section 6.1.3), and sweep rate (Section 6.1.4) on the relaxation dynamics, and highlight the key findings, including the relationship between filament morphology and relaxation behavior. Additionally, the role of residual voltage drop on filament growth and morphology will be examined. In Section 6.2, the relaxation dynamics of SiO_2-based devices will be presented and discussed. Finally, a comparison and summary of the HfO_2- and SiO_2-based devices will be provided in Section 6.3.

6.1 Relaxation Dynamics of HfO_2-based Cells

6.1.1 Impact of Programming Scheme on Relaxation Behavior

The duration of the relaxation process, as well as the t_r, is affected by the size and shape of the conductive filament created during the SET process. A larger and stronger filament typically takes more time to rupture, whereas a thinner and weaker filament ruptures faster. Filament formation occurs in two stages: nucleation and growth. Initially, during the early stages of filament formation, multiple filament seeds may form due to the randomness of the nucleation process. However, due to the strong

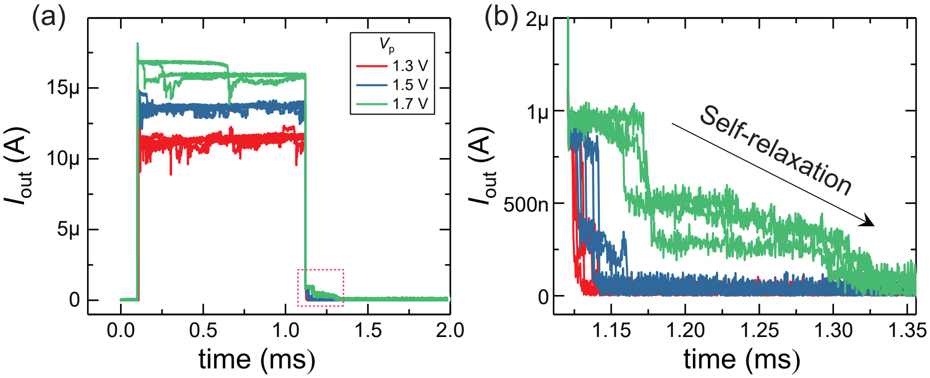

Figure 6.1: (a) Typical current response, I_{out}-t, under programming pulses V_{p}/ t_{p} of 1.3 V, 1.5 V, and 1.7 V/ 1 ms followed by a 0.1 V monitoring voltage. (b) Magnified plot of the pink marked region in (a), showing the different relaxation times for different V_{p}. R_{series} of 100 kΩ was used during the measurement. Reproduced with permission from [1].

field dependence of the switching behavior, only one "winning" filament continues to evolve during the growth process and electrically connects the two electrodes [198]. As a result, the relaxation time is determined by the strength of this filament.

Furthermore, the strength of the filament is determined by the programming conditions during the SET process. Unlike the SET kinetics, where t_{set} is determined at the closing of the filament, t_{r} is dependent on the final size of the filament. This implies that not only does V_{p} control t_{r}, but t_{p} also plays a role since the growth of a conductive filament can continue throughout the entire pulse duration. To investigate the impact of programming conditions on the relaxation process, programming pulses with varying V_{p} and t_{p} were applied, and the corresponding t_{r} was measured. The measurement setup is depicted in Figure 5.2a in Chapter 5. Figure 6.1 illustrates a representative relaxation behavior of the HO3P|Pt device under three different V_{p} values [36, 60, 109].

The outcomes are displayed in Figure 6.2. The results show an exponential relationship between t_{r} and V_{p} when various programming conditions were applied to the device in a defined HRS. As V_{p} increased step-wise from 0.6 V to 1.7 V, t_{r} increased by approximately two orders of magnitude, with t_{p} remaining fixed between 10 μs and 10 ms (as shown in Figure 6.2a). On the other hand, increasing t_{p} shifted the linear $\log(t_{\mathrm{r}})$ - V_{p} dependencies upwards in time without any significant change in the slope.

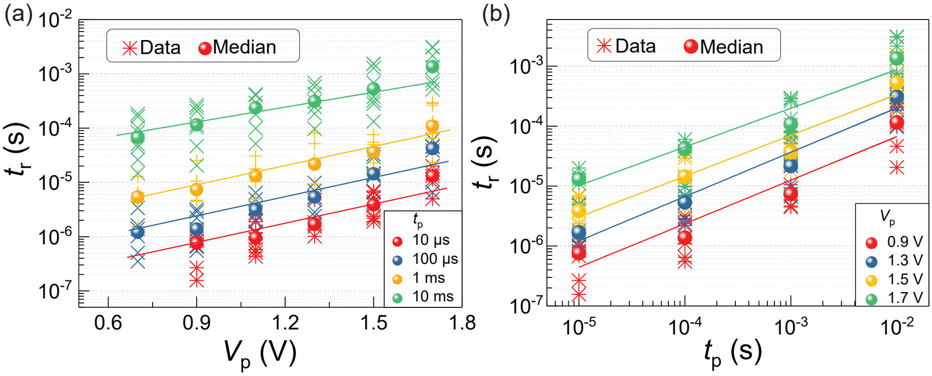

Figure 6.2: (a) The statistical analysis of t_r as a function of (a) V_p and (b) t_p collected from 10 measurements for each V_p/ t_p combination. Reproduced with permission from [1].

The observed polynomial relationship between t_r and t_p is illustrated in Figure 6.2b. Similar trends have been reported for various types of oxide-based diffusive memristors [36, 60, 109]. It is important to note that while the duration of the pulse t_p has no significant effect on the SET kinetics, which is not surprising, it can significantly impact t_r, as shown in Figure 6.2. Hence, a crucial query arises: How can a constant pulse voltage V_p, which corresponds to a particular SET time t_set for closing the conductive filament, result in relaxation times t_r that vary significantly simply by increasing the pulse duration t_p? To further explore this, the transient signals during switching were thoroughly analyzed, along with the experimental setup used to collect the data. The underlying reason was identified in the voltage divider built by the chosen R_series and the device in LRS. This will be discussed in detail in the following section.

6.1.2 Origin of the Relaxation Time Dependence on Programming Pulse Width

The relaxation time reflects the strength of the filament formed during the programming stage, which can be expressed in terms of cell resistance. The resistance of the cell after programming is mainly determined by the amplitude and duration of the programming voltage, while the R_series reduces the voltage drop across the diffusive memristor cell (V_dm) during the SET process until it reaches a minimum voltage (V_min)

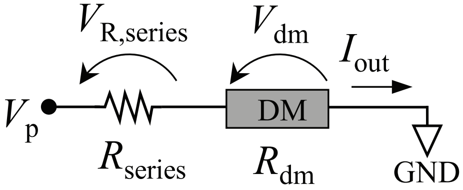

Figure 6.3: A schematic representation of the voltage divider effect between the diffusive memristor R_{dm} and the series resistor R_{series}.

at which the driving force for resistance reduction becomes zero. V_{min} is linked to the kinetics of the device and can be traced from the SET kinetics curve's asymptotic line at low voltage, which is equivalent to the V_{th} of the diffusive memristor from DC sweep measurement in the range of approximately 0.10 V - 0.15 V. Below V_{min}, the device does not switch regardless of the measurement time. However, for $V_{\text{dm}} > V_{\text{min}}$, the resistance of the diffusive memristor cell (R_{dm}) will continue to decrease until V_{dm} reaches V_{min}.

Therefore, R_{dm} in LRS was extracted and the corresponding V_{dm} was calculated, for a given V_{p}, thanks to the full transient signal recorded during the measurement. A schematic depiction of the voltage divider effect between the diffusive memristor and the series resistor is shown in Figure 6.3. The output current (I_{out}) during the SET process for a given V_{p} and t_{p} can be expressed using Kirchhoff's current law:

$$I_{\text{out}} = \frac{V_{\text{p}}}{R_{\text{total}}} = \frac{V_{\text{p}}}{R_{\text{series}} + R_{\text{dm}}} \tag{6.1}$$

Rearranging eqn. 6.1 yields an expression for the cell resistance R_{dm} as a function of V_{p}, I_{out}, and R_{series}, which are all known, as follow:

$$R_{\text{dm}} = \left(\frac{V_{\text{p}}}{I_{\text{out}}}\right) - R_{\text{series}} \tag{6.2}$$

The results for the calculated R_{dm} values are shown in Figure 6.4a. It can be seen that R_{dm} slowly decreases with time under constant V_{p}. Resistance values extracted at the beginning and end of t_{p} show R_{dm} reduction of on average 40 to 50 percent for all V_{p} values. Part of the I_{out} signal at the beginning of t_{p} is excluded from the analysis due to the current spike from parasitic capacitance discharging, which does not represent

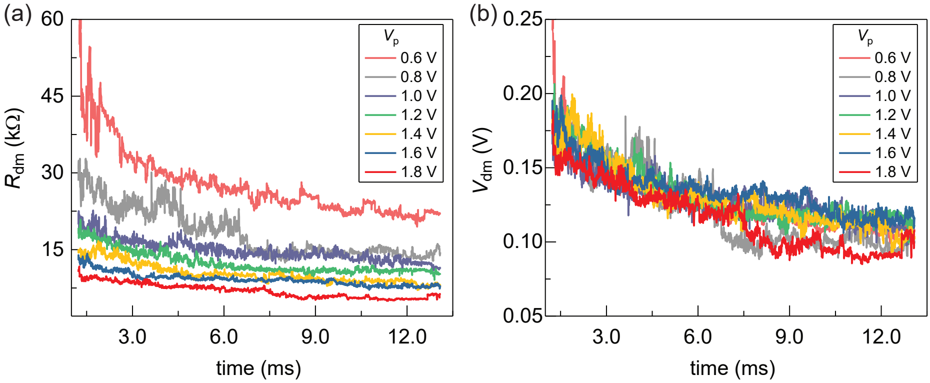

Figure 6.4: (a) Calculated resistance of the diffusive memristor (R_{dm}) and (b) the corresponding voltage drop (V_{dm}) during the bias duration for various V_{p}. Reproduced with permission from [1].

the device resistance. Thus, the reduction in resistance from the filament closer to the end of t_{p} could be even higher. Furthermore, from eqn. 6.2, V_{dm} can be calculated as:

$$V_{\mathrm{dm}} = \left(\frac{R_{\mathrm{dm}}}{R_{\mathrm{series}} + R_{\mathrm{dm}}} \right) * V_{\mathrm{p}} \tag{6.3}$$

The calculated V_{dm} is plotted as a function of time for various V_{p} in Figure 6.4b. Based on the results, it was found that there was a remaining voltage drop of approximately 0.15 V to 0.20 V throughout the duration of the pulse. This analysis leads to the conclusion that, when the diffusive memristor is switched to the LRS, a minor residual voltage drop, equivalent to a fraction of the pulse voltage, is adequate to sustain the growth of the filament during the SET operation.

6.1.3 Impact of Series Resistor on the Relaxation Dynamics

When a resistor is placed in series with a diffusive memristor, it can function as a current limiter and/or a voltage divider, as discussed earlier. While the current limiter functionality is mainly activated in the ON-state of the diffusive memristor, the voltage divider effect could be triggered at any state of the cell. The extent of its impact is determined by the value of R_{series} in relation to the resistance of the diffusive memristor cell. Consequently, it is crucial to investigate the influence of R_{series} on the relaxation process and establish any correlation between the two in

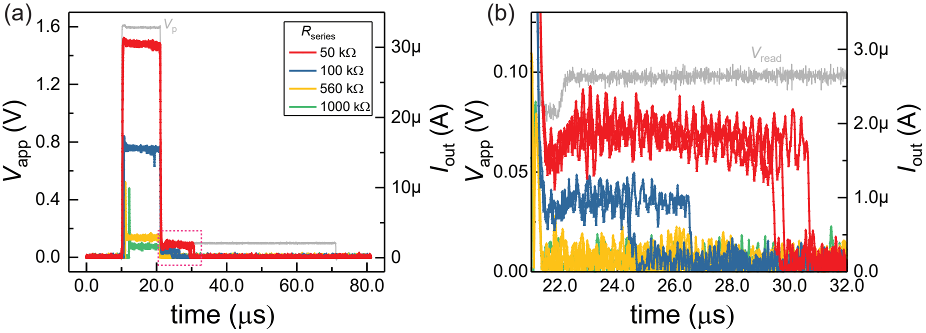

Figure 6.5: (a) Transient measurement under different series resistance of 50 kΩ, 100 kΩ, 560 kΩ, and 1000 kΩ at a fixed V_p/ t_p of 1.6 V/ 10 µs. (b) A magnified image of the pink box marked region in (a) shows the effect of different series resistors on the relaxation time.

order to further enhance the understanding and control of the relaxation dynamics of diffusive memristors.

To examine this, the relaxation times were obtained and analyzed from the same transient measurements utilized for the SET kinetics study in Chapter 5, Section 5.1.2. Only data indicating successful switching events and current relaxation to the HRS within the read (monitoring) pulse duration were considered for the analysis of t_r. Exemplary graphs of t_r versus *time* for various R_{series} of 50 kΩ, 100 kΩ, 560 kΩ, and 1000 kΩ measured at a constant V_p of 1.6 V are displayed in Figure 6.5. As shown in Figure 6.5b, t_r decreases as the R_{series} value increases.

To probe deeper into the influence of R_{series} on t_r, relaxation times with different R_{series} values and for three values of t_p were extracted in the same manner and are presented in Figure 6.6. The graphs in Figure 6.6 reveal three dependencies: (i) t_r significantly decreases with increasing R_{series}, traversing from top to bottom, (ii) t_r increases with increasing V_p, and (iii) the slope in the log(t_r) - V_p plot varies with changing R_{series}, traversing from top to bottom for every t_p.

For a better illustration, Figure 6.7 shows the median t_r of the data in Figure 6.6 plotted against V_p for all R_{series} and a fixed t_p. Based on this figure, the above three observations are discussed in detail as follows:

(i) A change in R_{series} by a factor of 20 (from 50 kΩ to 1000 kΩ) results in a decrease of t_r by more than a factor of ten for a given V_p. For t_p of 10 µs, values obtained at V_p of 1.1 V and 2.1 V yield a t_r decrease from around 4 µs to 300

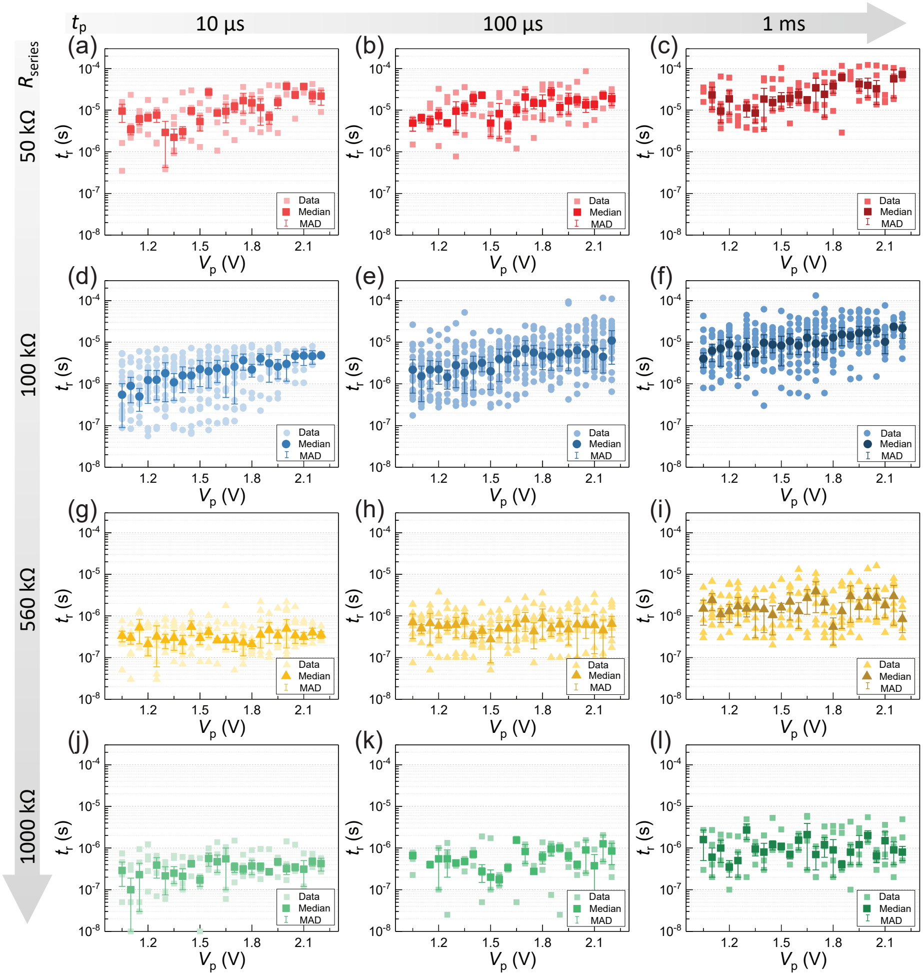

Figure 6.6: Relaxation time plot of t_r as a function of V_p with different R_series of (a)-(c) 50 kΩ, (d)-(f) 100 kΩ, (g)-(i) 560 kΩ, and (j)-(l) 1000 kΩ and t_p of 10 µs, 100 µs, and 1 ms (left to right). The median values and median absolute deviations (MAD) of the experimental data are displayed using color-filled symbols and vertical lines, respectively. Reproduced with permission from [2].

ns and from 20 µs to 400 ns, respectively. For t_p of 100 µs, the t_r decreases from 5 µs to 400 ns and from 25 µs to 600 ns, respectively, while for t_p of 1 ms, the t_r decreases from 10 µs to 700 ns and from 70 µs to 900 ns, respectively.

(ii) All plots exhibit a clear linear increase of $\log(t_\mathrm{r})$ as V_p increases. This finding is

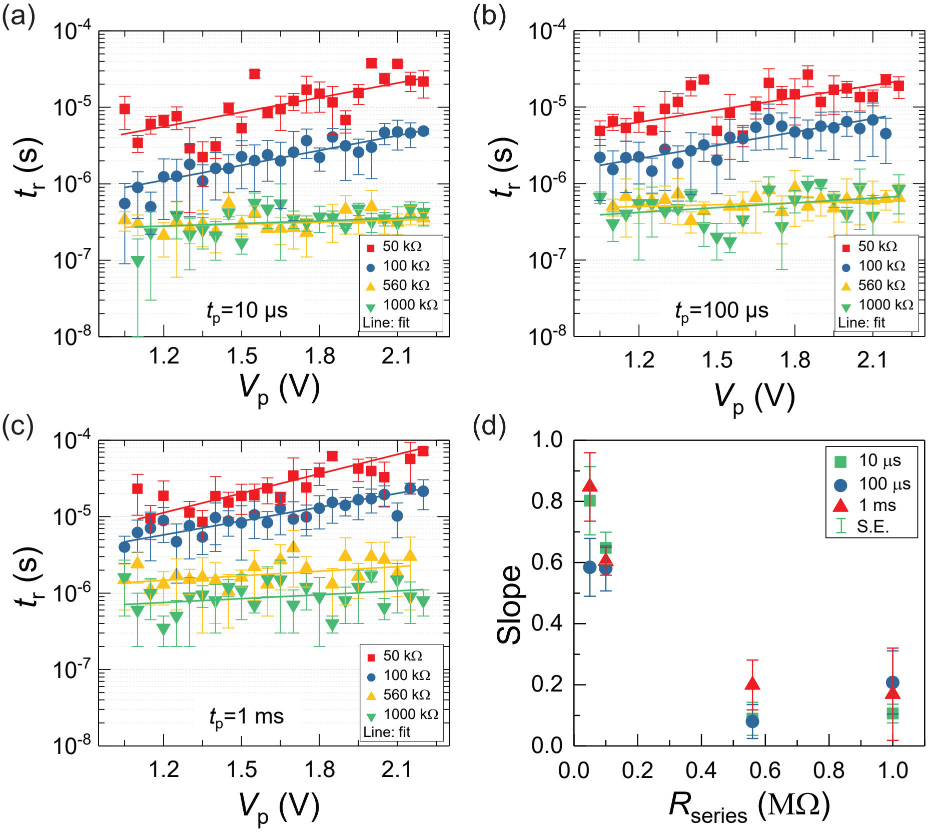

Figure 6.7: Median t_r for different R_{series} plotted against V_p for t_p of (a) 10 μs, (b) 100 μs, (c) 1 ms. Median absolute deviation (MAD) is represented using vertical lines. (d) Slopes extracted from (a)-(c) and plotted as a function of R_{series} for various t_p. The standard error (S.E.) is shown as vertical lines. Reproduced with permission from [2].

unexpected since t_r is typically determined by filament size and instability. Based on the physical mechanisms contributing to filament growth, a decrease in t_r is anticipated as V_p increases. At low voltages, nucleation dominates the process and results in a homogeneous growth and a bulky filament. As voltage increases, the filament shape becomes relatively thick and dendritic type and then wire-like as the regimes controlled by electron-transfer and mixed (electron-transfer and ion-migration) are approached. In other words, as V_p increases, filament size continues to decrease. The next chapter will provide a detailed discussion of the various voltage-dependent filament formation mechanisms. Consequently, the relaxation process should speed up as V_p increases. In contrast, Figure 6.7 demonstrates that t_r increases as voltage increases, with the rate of increase also dependent on R_series. This finding aligns with previous reports on the relaxation behavior of diffusive memristors, which have also observed a rise in relaxation time with increasing voltage [36, 170]. However, this apparent contradiction with the predictions from physics-based simulations can be explained by the influence of series resistance and residual voltage drop. In Figure 6.6, the relaxation times were determined following the application of a defined voltage pulse of V_p and a fixed t_p. However, this means that after the filament closure, the device in LRS remains exposed to a portion of the applied voltage for the remaining pulse time (t_p - t_set). Therefore, any prolongation of t_r resulting from further filament growth is a consequence not only of V_p but also t_p. This observation is not unexpected given the strong dependence of t_r on t_p. The residual voltage drop V_dm (a small fraction of V_p) is a function of the resistance of the device in LRS and the R_series.

(iii) The slope in the log(t_r) - V_p relationship decreases with increasing R_series. This highlights that the relaxation behavior of a diffusive memristor device depends on the SET programming conditions, V_p and t_p (in relation to the SET kinetics), and R_series in line with the diffusive memristor.

Accordingly, the cell resistance R_dm and respective voltage drop V_dm were calculated from the total resistance in the LRS by using eqn. 6.2 and 6.3, respectively. The total resistance (R_total) extracted from the transient curves of the current signals in the LRS is plotted as a function of R_series, as shown in Figure 6.8. The device resistance R_dm calculated by using eqn. 6.2 plotted against V_p for t_p of 1 ms is depicted in Figure 6.9a. It is important to mention that both R_dm and V_dm of the cell are also affected by the pulse duration t_p, as shown in Figure 6.4. However, to simplify the analysis, data with a fixed t_p of 1 ms is used. From the result, two trends can be observed: (i) there is an inverse correlation between R_dm and V_p as R_dm decreases with increasing V_p, and (ii) R_dm increases when the R_series value increases.

Furthermore, the voltage across the cell V_dm at a given t_p calculated from eqn. 6.3 is shown in Figure 6.9b as a function of V_p for the different R_series. The plot suggests that V_dm varies with R_series. As previously discussed, the residual voltage drop across the cell following the SET process also contributes to reducing the device resistance,

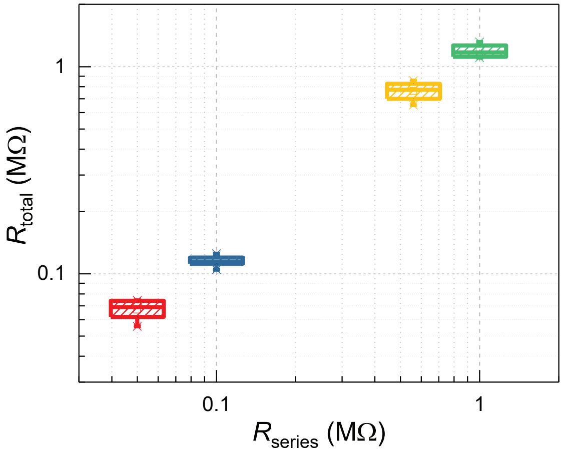

Figure 6.8: (a) Total resistance R_{total} calculated from the output current I_{out} of the transient curve in the LRS plotted as a function of R_{series} for a pulse amplitude V_{p} of 1.4 V. Reproduced with permission from [2].

thereby causing an increase in the filament size during the pulse duration. The degree of change in device resistance is influenced by the magnitude of the residual voltage drop, V_{dm}. This, to some extent, accounts for the different slopes observed for different R_{series} values in the log(t_{r}) - V_{p} plot (Figure 6.7).

Based on Figure 6.7c, it can be observed that the relaxation time is dependent on V_{p}, with significantly steeper slopes for R_{series} values of 50 kΩ and 100 kΩ, while the slopes for R_{series} values of 560 kΩ and 1000 kΩ are relatively flat and less dependent on V_{p}. This raises the question of why there is such a large difference in slopes between the relatively small and large series resistances. Furthermore, while the V_{dm} of the cell is almost constant for all V_{p} values within the same R_{series}, a strong dependence of t_{r} on V_{p} can be seen for the 50 kΩ and 100 kΩ series resistors. These are addressed as follows:

- Conduction mechanism consideration: The conduction in diffusive memristors can occur either through galvanic contact with the full filament closing between the electrodes or through tunnel-gap type, where the current is mainly due to electron tunneling between the filament tip and the opposing electrode (see Section 4.1.2). Based on the calculated cell resistances in Figure 6.9a, it can be concluded that diffusive memristors programmed with R_{series} of 560 kΩ and 1000 kΩ are of gap-type nature, as the calculated R_{dm} is higher than the

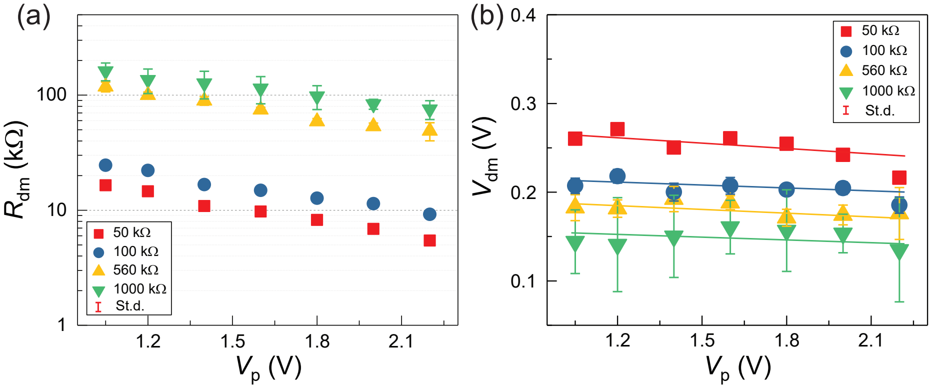

Figure 6.9: Calculated (a) cell resistance R_{dm} and (b) voltage drop across the cell V_{dm} plotted as against V_{p} for different R_{series} values at a fixed t_{p} of 1 ms. The lines in (b) are a guide to the eye. Reproduced with permission from [2].

single atom resistance of 12.9 kΩ, indicating that full filament closing was not achieved. Note that for large series resistances, the voltage divider effect occurs much earlier, as the cell resistance approaches the value of the R_{series} early, and most of the applied voltage drops on the R_{series}, reducing the cell voltage V_{dm} close to V_{min}. As a result, no significant filament growth is expected after SET, regardless of the pulse amplitude and duration. Therefore, the filament ruptures quickly, and the relaxation becomes fast and almost independent of V_{p}. The conductance of the diffusive memristors with R_{series} of 50 kΩ and 100 kΩ, on the other hand, indicates a fully closed filament and galvanic contact-type electrical conduction ($R_{\mathrm{dm}} < 12.9$ kΩ). Once the filament is closed, a small residual voltage is enough to maintain further growth of the filament. This explains the longer t_{r} of the diffusive memristors connected to a 50 kΩ and 100 kΩ series resistor and addresses the large differences in slope observed between the relatively small and large series resistances.

- Non-linearity of the SET kinetics: Looking at the data for the 50 kΩ and 100 kΩ, while the voltage drop across the cell within the same R_{series} is almost constant for all voltages (Figure 6.9b), the magnitude and changing rate (slope) of t_{r} are different for different V_{p} and the two series resistances, respectively. This is originated from the high non-linearity of the SET kinetics where the filament closing time t_{set} decreases exponentially with voltage as is indicated by the steep slope in the log(t_{set})-V plot (see Figure 5.3). To put this differently, a slight increase in V_{p} leads to a significant decrease in t_{set}, which means that for a fixed pulse duration of t_{p}, the shorter the t_{set} (or the higher the V_{p}), the longer the excess pulse duration after the filament closes. This means that the size of filaments formed at different voltages depends not only on the electric field strength (V_{p}) but also on the excess pulse time (t_{p} - t_{set}) for a given V_{p}, particularly for closed filaments. However, the effect of this excess pulse duration is determined by the residual voltage drop V_{dm}, which is smaller for the R_{series} of 100 kΩ (0.18 V - 0.21 V) than for the R_{series} of 50 kΩ (0.23 V - 0.27 V). Therefore, the influence of V_{dm} on filament growth is slightly more pronounced for the latter case, and the device with R_{series} of 50 kΩ has a steeper slope and higher t_{r} compared to the device with R_{series} of 100 kΩ. Note that, V_{dm} is calculated close to the end of t_{p} and the values could be higher at the closing of the filament.

In conclusion, the relaxation time in a diffusive memristor is influenced not only by the voltage V_{p}, but also by the duration of the pulse t_{p}. This is because of the voltage drop that remains on the cell after the SET event begins. To control this effect and the corresponding t_{r}, a series resistor can be utilized. It is important to note that the experimentally observed relationship between t_{r} and V_{p} or t_{r} and t_{p} cannot be interpreted as a direct dependence since both variables have an impact. Rather, it is a combination of the two. Further details on this will be provided in Chapter 7.

6.1.4 Impact of Sweep Rate on the Relaxation Dynamics

The influence of ν on the V_{th} of diffusive memristors is discussed in Chapter 4. From the analysis, an exponential rise of V_{th} is observed in the V_{th}-log(ν) plot. In this section, the effect of ν on t_{r} is discussed.

To analyze this, t_{r} data were extracted from the same data set used in Figure 4.14. Before the extraction, noisy data were smoothed by a length of 20 using Gaussian-weighted moving average in order to avoid false detection of t_{r} due to noise in the measurement data. This is shown in Figure 6.10. The plot in Figure 6.10a shows the triangular pulse with a fixed V_{p} of 3 V and a duration of t_{p} followed by a monitoring voltage of 0.1 V to trace the t_{r} together with the output current. The output current is plotted logarithmically in Figure 6.10b, with the original and smoothed data on top of each other.

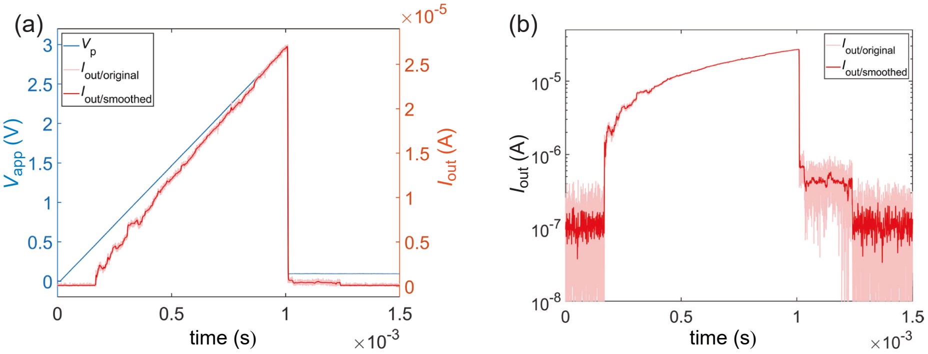

Figure 6.10: (a) The triangular pulses scheme used to analyze the influence of sweep rate on the relaxation time. The voltage pulse V_{p} is given in blue and the output current I_{out} in red. (b) A $\log(I_{\mathrm{out}})$ - t plot of the data in (a) showing the original and smoothed data using Gaussian-weighted filter.

The relaxation time was measured for two devices, HO2P|Pt and HO3P|Pt, by sweeping the voltage at different rates ranging from 1 kV/s to 1 MV/s. This was achieved by using a fixed V_{p} of 3 V and varying the t_{p} ranging from 3 ms to 3 µs. The collected relaxation times were then plotted against ν for the HO2P|Pt and HO3P|Pt devices in Figure 6.11a and 6.11b, respectively. The following observations can be drawn from the median plot in Figure 6.11c.

(i) Relaxation time decreases as ν increases. This can be attributed to the fact that at higher ν (i.e. shorter t_{p}), the device is exposed to voltage stress for a shorter time. As a result, thinner filaments may be formed due to the reduced extra pulsing time, effectively suppressing further growth of the filament after closing.

(ii) The HO2P|Pt device exhibits a much faster relaxation than the HO3P|Pt device, suggesting that devices with thinner HfO_2 layers have a shorter relaxation time. This can be explained by the higher vertical electric field enhancement in thin films compared to thick films [199]. For a fixed applied voltage of V_{p}, an addition of a single cation/atom into the growing filament reduces the effective gap between the filament and the corresponding electrode, resulting in an increase in the vertical electric field from $E = \frac{V_{\mathrm{p}}}{t_{\mathrm{ox}}}$ to $E = \frac{V_{\mathrm{p}}}{t_{\mathrm{ox}}-d_{\mathrm{o}}}$ (where t_{ox} is the oxide film thickness and d_{o} the size of the cation/atom). However, this electric field change is much more significant in thin films than in thicker films. Since the filament growth rate is exponentially dependent on the electric field, a more pronounced positive feedback process of filament growth occurs in thin films [199]. As a result, the formation of thin, chain-like filaments is enhanced in thinner oxide films, leading to faster relaxation.

(iii) The HO3P|Pt device shows a higher rate of decrease in t_r compared to the HO2P|Pt device, as indicated by the slope of the two lines in Figure 6.11c. At a ν of 1 kV/s, there is almost a two-order of magnitude difference in t_r between the two devices, while at a ν of 1 MV/s, there is less than one-order of magnitude difference. At low ν, the formation and growth of filaments require a low voltage, as confirmed by the ν dependence of V_{th} experiment in Chapter 4 (see Section 4.1.4). This means that both devices are exposed to an extra pulse of t_p-t_{set}, which could contribute to further increasing the filament size. However, as discussed in (ii), thin oxides tend to form thinner filaments due to the positive feedback from the vertical electric field enhancement. Thus, the effect of ν is reduced for thin films. On the other hand, at higher ν, the t_{set} where the device turns to LRS is close to t_p, and the effect of excessive pulse is drastically reduced. This is illustrated in Figure 6.12, which shows representative curves of a measurement performed under t_p of 3 ms and 3 µs. Note the x-axis scale, which is a difference of three orders of magnitude, further emphasizing the influence of the excess pulse the device is subjected to. Consequently, both devices exhibit faster relaxation at higher ν due to the formation of thin filaments.

To summarize, ν affects the t_r of diffusive memristors by influencing the size and morphology of the filament. When ν is low, the filament grows relatively thick, resulting in a longer relaxation time, whereas a high ν results in a thinner filament and a faster relaxation process. The variation in filament size is linked to the voltage regime at which the device turns on, as well as the excessive pulsing associated with it. Additionally, in very thin oxide films, the impact of the ν is reduced due to the significant enhancement of the vertical field in thin films compared to thicker ones.

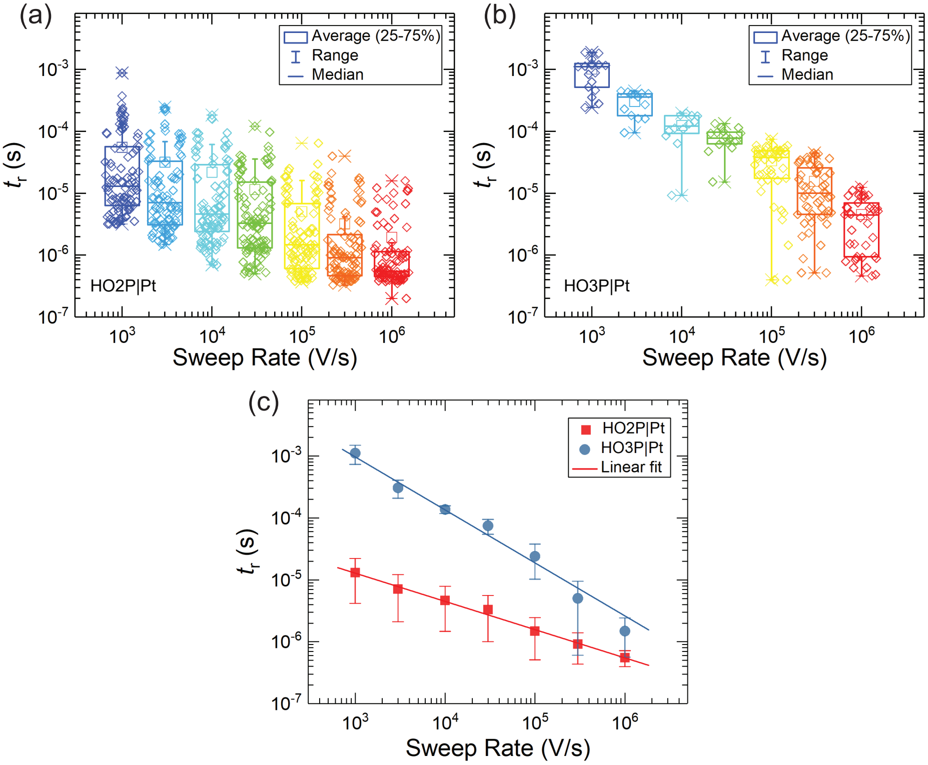

Figure 6.11: Relaxation time t_{r} plotted as a function of sweep rate ν for (a) HO2P|Pt and (b) HO3P|Pt devices. (c) The median of t_{r} for the two devices is plotted against ν. The error bar in (c) is the median absolute deviation (MAD) of the measured data.

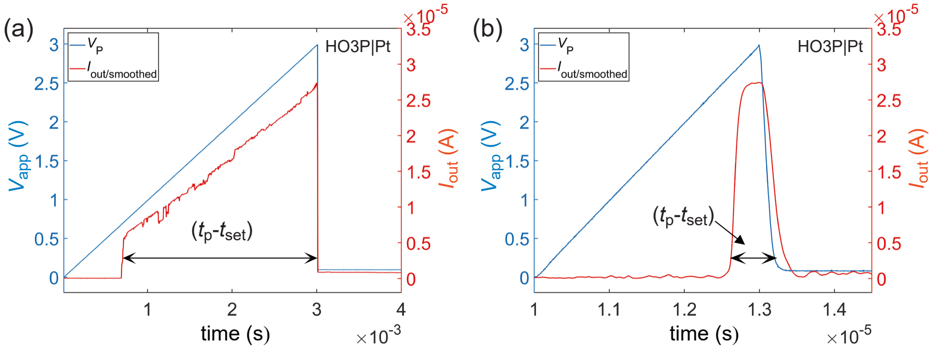

Figure 6.12: (a) An output current I_{out} from a triangular pulse scheme plotted for HO3P|Pt device measured under t_{p} of (a) 3 ms (b) 3 µs. The excessive pulse is shown as t_{p}-t_{set}.

6.2 Relaxation Dynamics of Ag/SiO_2-based Cells

6.2.1 Impact of Programming Scheme on Relaxation Behavior

This section will cover the analysis of the relaxation behavior of diffusive memristors based on SiO_2. The investigation will focus solely on the SO3P|Pt cell, with the aim of contrasting the results with those obtained from HfO_2-based systems. Readers interested in learning more about the use of SiO_2 in ECM cells, particularly in relation to non-volatile memory, are encouraged to refer to references [82, 200–203].

Figure 6.13 displays a plot depicting t_r against V_p, with different values of t_p. The data is extracted from the same transient curves used to analyze the SET kinetics, as seen in Figure 5.11. It is worth noting that there are no data points provided for a t_p value of 1 µs. This is due to the fact that, as demonstrated by the SET kinetics curve in Figure 5.11, the device does not undergo switching at a t_p of 1 µs within the relevant voltage ranges. From Figure 6.13, the following observations can be made:

- No significant correlation between t_r and V_p can be observed for all t_p values. The median curve shown in Figure 6.13c indicates that t_r remains nearly constant across the entire V_p range. This suggests that the filaments formed at all voltages possess comparable size and morphology. This is consistent with the SET kinetics behavior of the SO3P|Pt devices (see Figure 5.11,) which reveals a very weak influence of V_p on the filament radius.

- Looking at the dependence of t_r on t_p, a slight increase in t_r can be observed with increasing t_p. For instance, when examining V_p values ranging from 1.2 V to 1.5 V, an increase in t_p from 10 µs to 1 ms - a two-order of magnitude increase - results in an increase in t_r of approximately one order of magnitude.

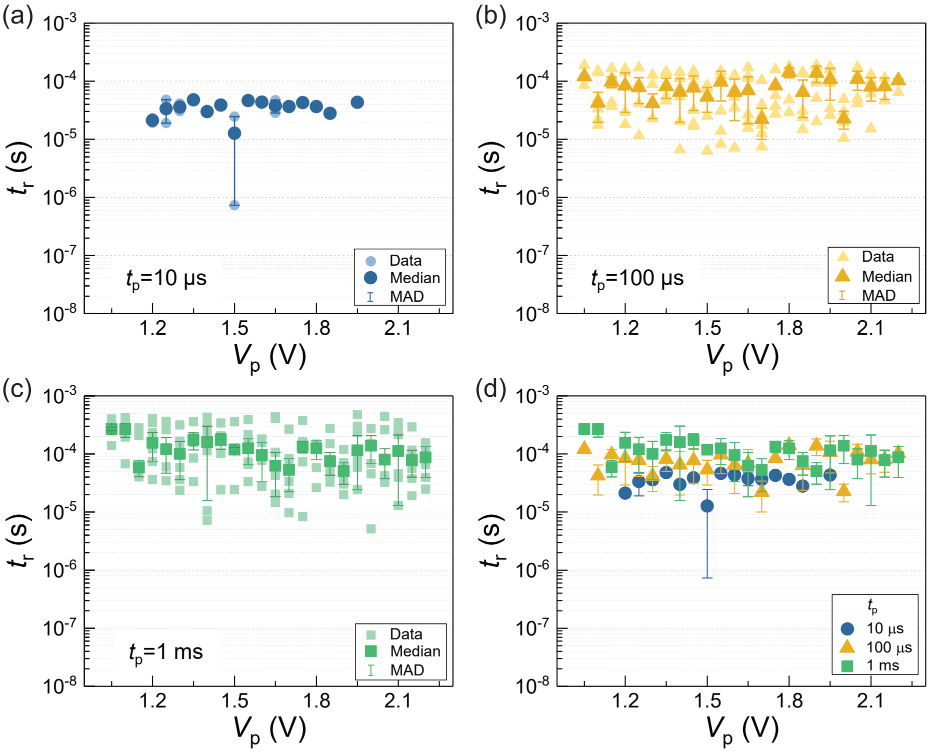

Figure 6.13: Relaxation time plotted as a function of V_p for various t_p of (a) 10 µs, (b) 100 µs, and (c) 1 ms. (d) Median of t_r as a function of V_p. The median values and median absolute deviations (MAD) of the experimental data are displayed using color-filled symbols and vertical lines, respectively. A 100 kΩ resistor was used during the measurements.

6.3 Comparison and Summary

In summary, the relaxation behavior of diffusive memristors is determined by the strength of the filament formed during the SET process. This can be modulated by using various programming schemes. Furthermore, in addition to the programming scheme, the type of the system also impacts the filament morphology as the switching layer affects the migration of the mobile ion. This has been shown by fabricating diffusive memristors from HfO_2 and SiO_2 films. As discussed in this chapter, the HfO_2 system provides more flexibility in tuning the t_r by using different programming schemes compared to the SiO_2 system. This is shown in Figure 6.14 of the direct

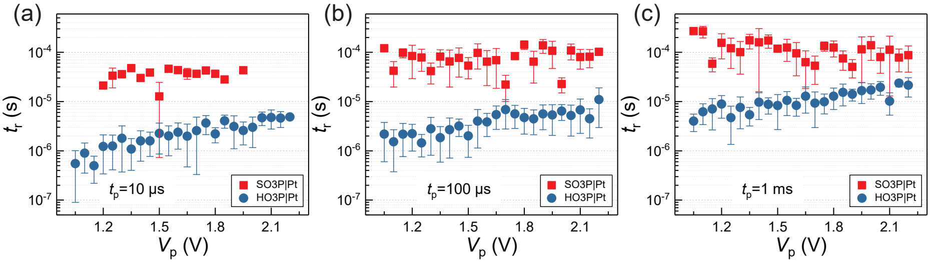

Figure 6.14: Relaxation dynamics of HO3P|Pt and SO3P|Pt devices. The median of t_r is plotted against V_p for various pulse durations of (a) 10 µs, (b) 100 µs, and (c) 1 ms.

comparison of t_r for the two oxide systems with HO3P|Pt and SO3P|Pt given in blue and red colors, respectively.

The differences are explained by the distinct ways in which filaments form, influenced by variables such as the amplitude and duration of the programming voltage, as well as the densities of defects in the switching layer, which impact the movement of the active metal ion. In the case of the SiO_2 system, the movement of Ag^+ ions, the reduction of Ag^+ ions, nucleation of Ag, and clustering of Ag atoms occur through defects like oxygen vacancies and voids. Since ALD-grown films have a low concentration of defects, the mobility of Ag^+ ions is limited, thus, there is a homogeneous growth of filaments facilitated by the movement of these clusters. It is worth mentioning that, the mobility of Ag^+ ions in the SiO_2 system can be improved by introducing more defects. This can be done by using a different growth method, for example by using sputtered or evaporated SiO_2 [92], or intentionally generating defects like oxygen vacancies by first applying a positive bias to the Pt electrode, as demonstrated in ref. [54]. Consequently, better controllability of the filament formation, and hence, tunable t_r could be achieved in the Ag/SiO_2 system.

Chapter 7

Correlation between the SET Kinetics and Relaxation Behavior

In this chapter, a correlation between the SET and relaxation processes in diffusive memristors will be formulated based on the results shown in Chapter 5 and 6. The interdependence between the two is given in Section 7.1. In Section 7.2, the different filament growth mechanisms are discussed. Furthermore, Section 7.3 presents the implications of the findings, including the impact of series resistors, on device operations.

7.1 Interdependence of SET and Relaxation Processes

The results of the SET kinetics (Chapter 5) and relaxation behavior (Chapter 6), reveal a trade-off between t_{set} and t_{r}, depending on the programming conditions. Figure 7.1 illustrates this relationship, showing that while t_{set} decreases exponentially as the programming voltage increases, t_{r} increases substantially with voltage increase (Figure 7.1a). This means that increasing V_{p} can result in a shorter t_{set}, but at the cost of a longer relaxation process. However, t_{p} has no effect on t_{set}, as it only defines the delay time between the voltage pulse starting and the abrupt rise in current, as long as t_{p} is greater than or equal to t_{set} for a given value of V_{p}. This is represented by the horizontal line in Figure 7.1b. On the other hand, a linear correlation is observed between $\log(t_{\mathrm{r}})$ and $\log(t_{\mathrm{p}})$ in Figure 7.1b. Here, the plots illustrate the dependence on V_{p} at a fixed t_{p} and the dependence of t_{p} at a fixed V_{p}.

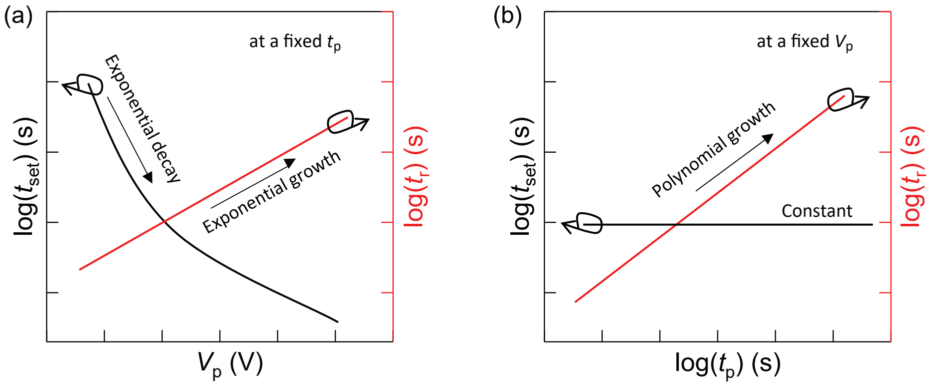

Figure 7.1: Schematic depiction of (a) the dependence of t_{set} and t_{r} on V_{p} at a fixed t_{p} and (b) the dependence of t_{set} and t_{r} on t_{p} at a fixed V_{p}. Reproduced with permission from [1].

The relationship between t_{set} and t_{r} as a function of V_{p} and t_{p} is summarized in a heat map presented in Figure 7.2. The stars on the heat map indicate the measurement data points for t_{r}. The color code used in the heat map represents the experimental data, while values outside of the measurement range are extrapolated based on the fittings of the measurement data. Moreover, additional t_{r} data collected from various reports on Ag-based volatile ECM cells are shown for comparison. The trend of t_{r} versus V_{p} and t_{p} behavior in the data collected from other reports is quite similar to the findings of this study. Furthermore, the broken line in Figure 5c represents the SET kinetics curve of t_{set}-V_{p}, which separates the HRS regime from the successful SET events. For the successful SET events, the relaxation behavior of the filament and the corresponding t_{r} depends on both V_{p} and t_{p}. For instance, increasing t_{p} from 10 µs to 10 ms, i.e. moving upward in Figure 7.2, results in a significant change in t_{r}, spanning several orders of magnitude.

The relationship between the SET and relaxation process, which is depicted in Figure 7.2, provides a more profound comprehension of the $\log(t_{\mathrm{r}})$-V_{p} and $\log(t_{\mathrm{r}})$-$\log(t_{\mathrm{p}})$ behavior shown in Chapter 6, Figure 6.2a and 6.2b, respectively. Previous studies, such as those cited in references [36, 60, 109], have noted similar trends. Experimental results have demonstrated that for a given V_{p}, the pulse duration t_{p} can alter t_{r} by several orders of magnitude. Similarly, for a fixed t_{p}, the programming voltage V_{p} changes the relaxation time exponentially. These observations have previously been interpreted simply as a change in the strength of the metallic filament. However, by

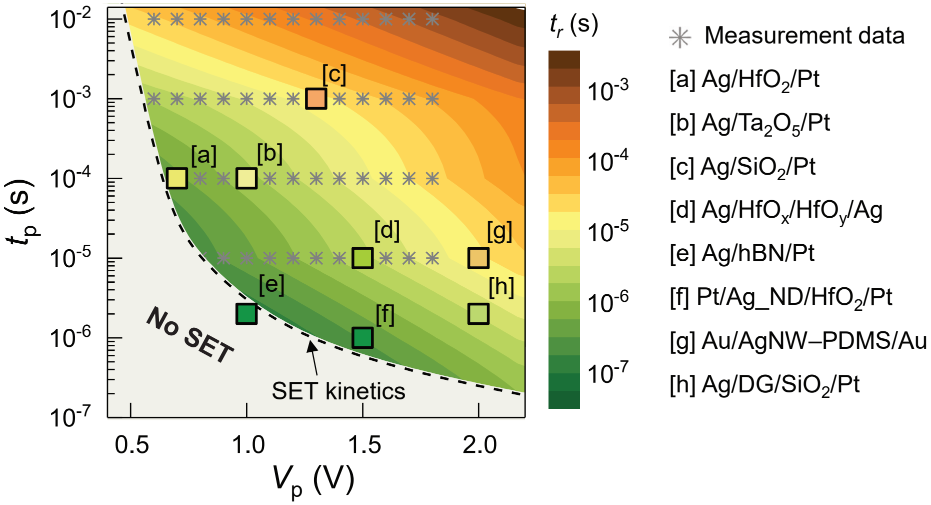

Figure 7.2: A heat map of the combination of the SET kinetics (broken line) and relaxation dynamics showing several orders of magnitude change in relaxation time t_r over a certain range of V_p and t_p. The SET kinetics curve is a representative fitting curve of the experimental data. The color-coded relaxation time is plotted based on experimental data (represented by stars) and an extrapolation from the fitting of the experimentally obtained data. Letter assigned boxes are t_r data collected from various publications of [35, 60, 174, 190, 204–207]. Reproduced with permission from [1].

taking into account the SET and relaxation behaviors together, it is now apparent that a more detailed description of the filament's growth process is necessary to fully comprehend the complex correlation displayed in Figure 7.2.

7.2 Filament Evolution During SET Process and Relaxation Behavior

As previously discussed, the size of the filament is a critical determinant of t_r in diffusive memristors, and therefore, the filament growth process is a crucial point of focus. Recent TEM observations have revealed clusters comprising the active Ag or Cu element, with diffusive memristor models often attributing the self-diffusion process to surface energy minimization or surface tension. As pointed out in Chapter 2, Section 2.4, MD simulations have further supported this notion by demonstrating the spontaneous breakdown of a continuous nanoscale Ag filament within an oxide matrix, without any external forces. The MD simulation model also reasonably replicated the experimentally observed relaxation times in various Ag- and Cu-based volatile ECM cells. In this model, the lifetime of the filament, i.e., t_r in diffusive memristors, is linked to the size of the filament at the weakest point, following Herring's scaling law, i.e., $t_\mathrm{r} \propto {r_\mathrm{o}}^4$ (see eqn. 2.8). As can be seen in Figure 7.2, t_r modulation of more than four-orders of magnitude is achieved from a combined influence of V_p and t_p. According to Herring's scaling law, such a change in t_r would require an alteration in the filament radius by one order of magnitude. Note that the on-state current is limited by the series resistor of 100 kΩ during the measurement. As V_p increases from 0.6 V to 1.8 V, the on-state current only rises from around 6 µA to about 18 µA. While the maximum current passing through the cell can affect t_r, this level of current should not significantly contribute to filament growth or result in a significant change in the filament's radius. For instance, Covi et al. observed a t_r change of less than 5x when increasing the I_CC from 9 µA to 20 µA [170]. Hence, the size and shape of the filament are mainly determined by the kinetically limiting process and corresponding biasing conditions, such as voltage and duration.

In total, the voltage-dependent filament size has a noticeable impact on the SET kinetics of diffusive memristors, especially in the electron transfer regime (see Figure 5.4). Although this effect is not as strong as the power of four law for the relaxation time ($t_\mathrm{r} \propto {r_\mathrm{o}}^4$), the two variables ($V_\mathrm{p}$ and t_p) together have significant consequences for the programming regime of diffusive memristors. Additionally, it is important to note that the size of the filament determined during the fitting process only represents the initial size at the onset of the switching event, and may not be the final size since the influence of t_p is not considered. The overall process during the switching is schematically depicted in Figure7.3a. The impact of different biasing conditions on the formation of the filament and, subsequently, on the SET and relaxation processes can be explained as follows:

- At lower voltage regimes (in this case < 0.6 V) nucleation is the rate-limiting process. This means that neither electron-transfer nor ion-migration are rate limiting, thus, there are enough Ag^+ ions available for filament formation. As a result, a homogeneous growth and a relatively bulky filament are expected (Figure 7.3b). The rupture of this takes a long time. Note that, a longer time is needed for the SET process at low voltages. Therefore, both the SET and relaxation processes take longer in the low voltage regime, where nucleation is the rate-limiting step for the SET event.

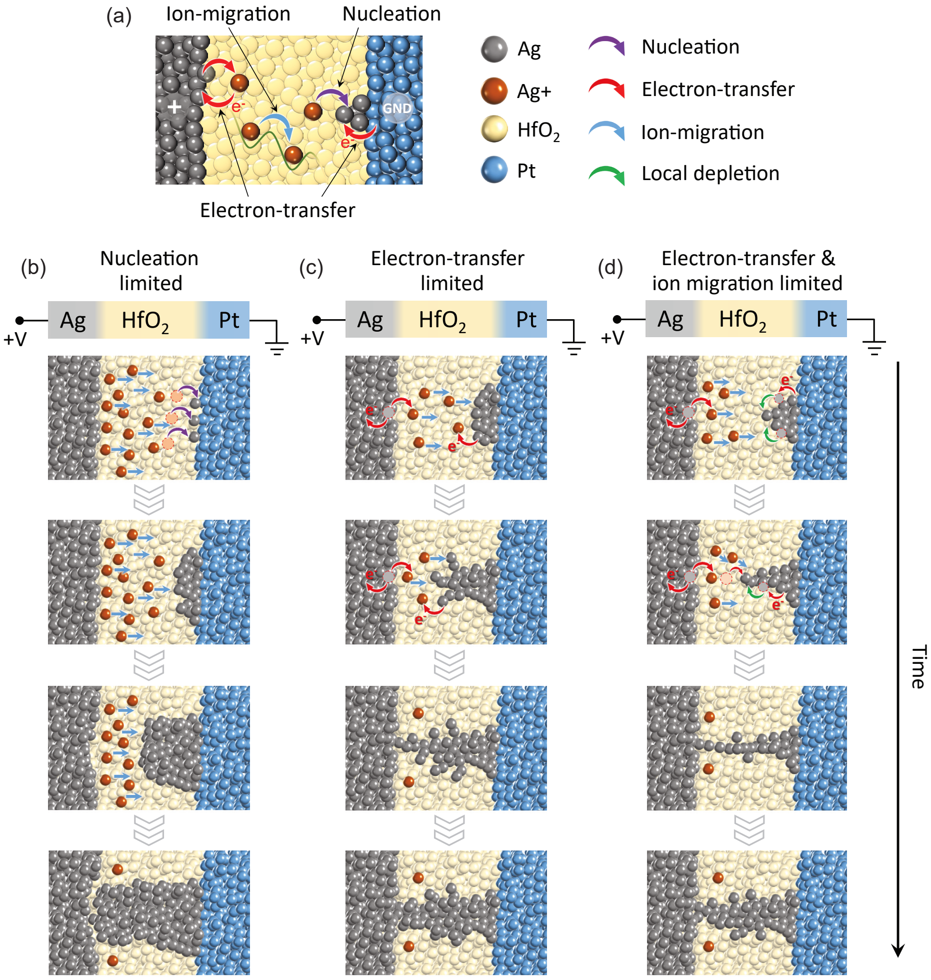
(a)
Ion-migration
Nucleation
+
e-
GND
e-
Electron-transfer
Ag
Ag+
HfO_2
Pt
Nucleation
Electron-transfer
Ion-migration
Local depletion
(b)
Nucleation limited
(c)
Electron-transfer limited
(d)
Electron-transfer & ion migration limited
Ag
HfO_2
Pt
+V
Time

Figure 7.3: Voltage-dependent filament growth mechanisms. (a) Definitions of the three different rate-limiting processes. Filament growth mechanisms as a function of time in the (b) nucleation-limited regime, (c) electron-transfer limited regime, and (d) mixed (electron-transfer and ion-migration) limited regimes. Reproduced with permission from [1].

- In the intermediate voltage regimes, the growth rate of the filament during SET is limited by electron transfer. As a result, the rates of Ag^+ ion generation and reduction are the same. Thus, linear growth of a dendritic-shaped filament is expected. The final size of the filament depends on the total pulse duration

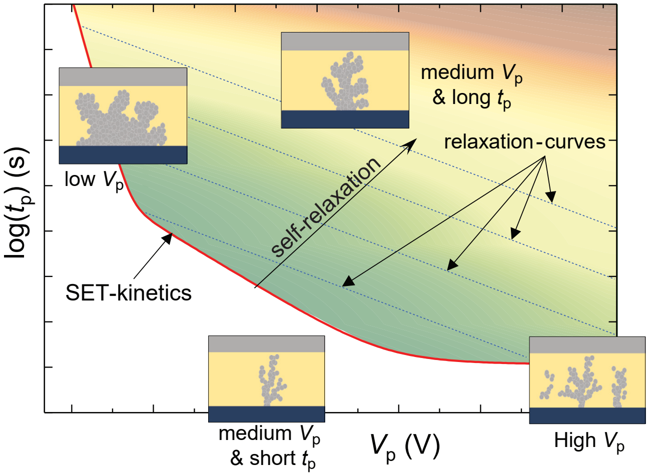

Figure 7.4: Schematic representation of the filament morphology at different combinations of V_p and t_p. Reproduced with permission from [1].

t_p (Figure 7.3c). If a short t_p is used, just enough to cause a successful SET event, a thin filament can be formed, and ultimately shorter t_r can be achieved. However, if longer than necessary pulses are used, the excess time after the switching contributes to further growth of the filament, causing an increase in t_r.

- In the medium-high voltage region, ion migration also becomes a limiting factor, and the supply of Ag^+ ions is limited due to the migration barrier. As a result, local depletion of Ag^+ ions takes place and this creates an electric field enhancement in this region, causing self-acceleration of the filament growth. This leads to a more anisotropic filament growth, resulting in a thin dendritic filament structure (Figure 7.3d). However, due to the self-acceleration and field enhancement effect, filament formation is much faster, and any extra time beyond t_set will contribute to the further growth of the filament. This prolongs the relaxation process and thus t_r.
- Further increasing the voltage will lead to extremely fast and uncontrolled filament formation, possibly resulting in excessive loading of Ag^+ ions into the matrix due to the very high electric field. This can modify the chemical potential of the matrix surrounding the filament, causing an extended relaxation process and long t_r.

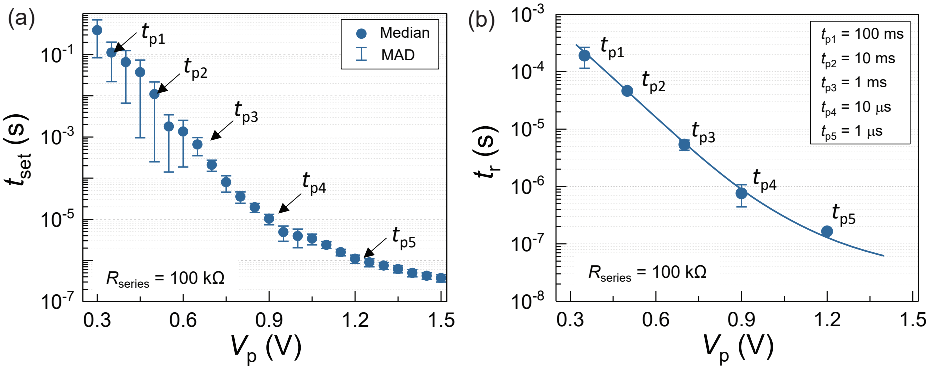

Figure 7.5: (a) SET kinetics data and the selection of different pulse duration t_p along the SET kinetics curve. (b) A plot of tr against V_p for different pulse durations defined in (a), displaying the exponential decay of t_r with V_p when short pulses that are long enough to close the filament are used. The solid line in (b) is a guide to the eye and does not represent any physical fitting. Reproduced with permission from [2].

A schematic representation of the voltage-dependent filament growth together with the SET kinetics and relaxation dynamics is shown in Figure 7.4. Based on the plot, it can be inferred that if the effect of t_p is to be avoided, shorter t_r should be anticipated as V_p increases. In order to assess this t_r values were extracted at different V_p and t_p combinations that are close to the SET kinetics curve, as shown in Figure 7.5a. The outcome is presented in Figure 7.5b. The results show that t_r decreases with increasing V_p, as predicted by the KMC model and the voltage-dependent filament growth mechanism explained earlier. This is a new finding and has not been shown before. One reason is that previous experimental data often showed an increase in t_r with V_p, which was primarily due to the influence of t_p, which was not distinguished from V_p. As explained in Chapter 6, the dependence of t_r on t_p is attributed to the residual voltage drop V_{dm} that causes an extra growth of the filament. However, even when looking at the diffusive memristor cell with the largest R_{series} of 1000 kΩ, where V_{dm} has the least impact, the inverse relationship is not observed (see Figure 6.7). It should be noted that t_p, in this case, is 1 ms, which is much longer than t_{set} of a few tens of ns to µs at high voltage regimes. This means that although the effect of V_{dm} on further growth of the filament is almost negligible, it cannot be completely disregarded as long as $V_{dm} > V_{min}$ holds, particularly when using excessively long pulses ($t_p \gg t_{set}$).

7.3 Series Resistor and its Implications in Device Operation

Depending on the intended application, either fast relaxation or tunability of t_r may be more important. For achieving fast relaxation, it is crucial to avoid an unnecessary excess pulse time ($t_\mathrm{p} \gg t_\mathrm{set}$), as this can lead to further growth after filament closure. There are two methods to achieve this. The first is to use a short pulse that is only long enough to trigger filament closure. As shown in Figure 7.5, short relaxation times can be achieved in a diffusive memristor cell if the device is programmed while fully taking into account its intrinsic SET kinetics. However, implementing such a programming scheme requires constantly adjusting t_p for different V_p due to the highly nonlinear nature of the SET kinetics curve.

A technically more easy solution toward diffusive memristor circuits with fast relaxation times is the usage of a proper R_series. This allows any unwanted residual voltage drop that could cause uncontrolled filament growth to be directed to the resistor. This approach effectively eliminates the need to adjust t_p every time V_p changes, while still enabling fast relaxation. This is nicely shown in Figure 7.6, which provides heat maps of the t_r together with t_set as a function of V_p and t_p for different R_series. For instance, traversing upward at a fixed V_p of 2.0 V, t_r could be tuned by more than four-orders of magnitude with R_series of 50 kΩ, but only by less than one-order of magnitude when R_series of 1000 kΩ is used. As discussed in Chapter 5, the differences in t_set for various R_series in Figure 7.6 are due to RC-time and not due to internal dynamics of the device itself.

Implications on the use of diffusive memristors as a selector

Using diffusive memristors as a selector in a crossbar array can only be done if the SET and relaxation times are short because the memory cells in the array need to be accessed quickly and efficiently. It is especially important for relaxation to be fast so that current does not pass through the unselected cells during operation. However, the existing trade-off between t_set and t_r with respect to V_p and t_p makes it challenging to achieve this goal.

Additionally, as it is revealed in this work, the dependence of t_r on the value of R_series makes things even more complicated because adjacent memory cells in a crossbar array could be in different states. Therefore, to use diffusive memristors as a selector device

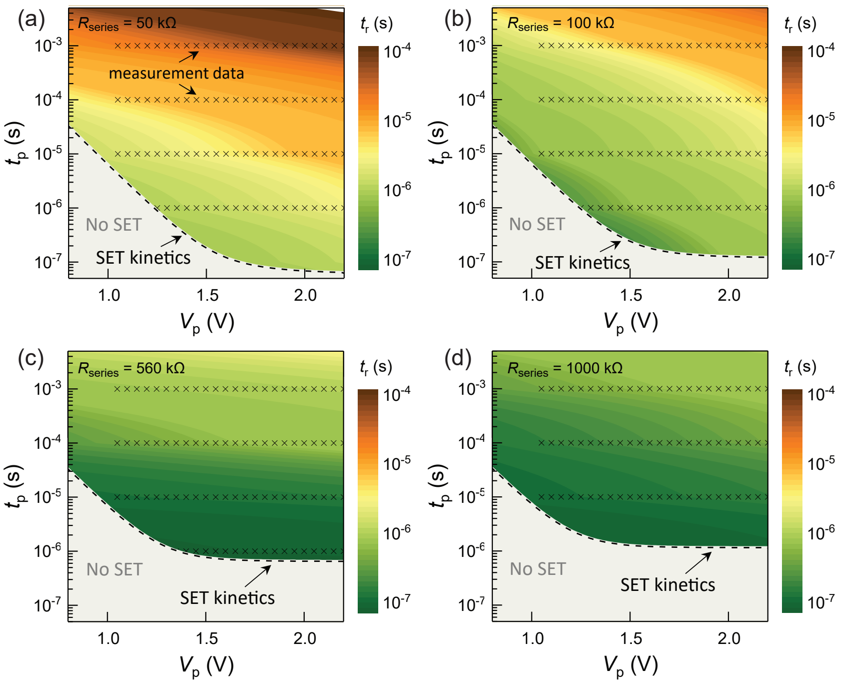

Figure 7.6: A heat map combining the SET kinetics (dashed line) and relaxation dynamics as a function of V_p and t_p for various series resistors R_series of (a) 50 kΩ, (b) 100 kΩ, (c) 560 kΩ, and (d) 1000 kΩ. The SET kinetics curve (dashed line) is a representative fitting curve of experimentally obtained data. The color-coded t_r is plotted based on experimental data (stars) and an extrapolation. Reproduced with permission from [2].

in a crossbar array, new concepts and programming techniques such as distributed programming, two-step read scheme [208], or leveraging the timing or the kinetics of the threshold switching device as shown in Figure 7.5 and/or suggested in the reference [37] must be used.

Implications on the use of diffusive memristors in neuromorphic computing areas

In the context of neuromorphic applications like artificial neurons and eligibility traces, having a fast relaxation is not a crucial requirement. What is more important is the ability to adjust and control t_r. For instance, in a spiking neural network (SNN) where diffusive memristors can potentially be utilized as an integrate-and-fire neuron, the neuron is anticipated to fire continuously upon receiving a voltage pulse train. However, one major challenge is that the diffusive memristor has to return to its initial state during the time interval between voltage pulses so that it is ready for the next integrate-and-fire process.

Therefore, to ensure complete relaxation of the diffusive memristor between voltage pulses, the time interval between pulses needs to be longer than the t_r of the device. As a result, the maximum firing rate is determined by the t_r of the diffusive memristor cell. Thus, finding ways to control the t_r without impacting the t_set is crucial for optimizing these devices for NC applications, given the trade-off between t_r and t_set. On the other hand, the accumulation and spontaneous relaxation behaviors of diffusive memristors are well-suited for tasks like eligibility trace and short-term synapses. Both of these applications rely on the short-term memory of the memristive element to store the activity of post-neuronal elements. Therefore, adjusting the relaxation time may be advantageous depending on the intended purpose of the device in neuromorphic circuits. In this sense, the findings of this work provide insight into the potential of using an internal or external series resistor to adjust the relaxation time of diffusive memristors for applications like artificial neurons and eligibility trace.

Chapter 8

Applications of Diffusive Memristors

The objective of this chapter is to examine the diverse application areas of diffusive memristors. Section 8.1 introduces a generalized design rule that is based on the findings made in this thesis. The subsequent sections will showcase preliminary results obtained from proof-of-concept experiments that demonstrate the potential use of diffusive memristors in various NC applications. These include the use of diffusive memristors as synaptic emulators (Section 8.2) and artificial neurons (Section 8.3). The data presented in this chapter is obtained utilizing the HO3P|Pt device.

8.1 Design Rule of Diffusive Memristors for Emerging Applications

As shown in Chapter 5 and 6, the ability to modulate the SET and relaxation behavior of diffusive memristors by simply modifying the programming schemes provide a possibility to design systems with specific t_{set} and t_{r}, depending on the desired end-use. Furthermore, the use of a series resistor offers additional freedom to tune t_{r} without affecting t_{set}. For example, for selector devices in a cross-point array, considering the trade-off between t_{set} and t_{r}, achieving fast t_{set} and t_{r} could be difficult. In this regard, the use of R_{series} could be beneficial to overcome the trade-off and attain the desired $t_{\mathrm{set}}/t_{\mathrm{r}}$ combinations.

In neuromorphic applications, the relaxation behavior becomes important. For instance, in integrate-and-fire neurons, the device resistance should relax back to the resting state to enable continuous firing during the application of a pulse train. Note that not only threshold switches but also non-volatile memristors such as oxide-based resistive switches, phase change memories, and ferroelectric memories have been proposed and implemented for use as artificial neurons. However, due to the non-volatile nature of those devices, a RESET operation is needed to return the device state back to HRS after every firing event [209–211]. This approach requires additional circuitry for the detection and activation of the RESET operation, making it area and energy-efficient. In this regard, threshold switches offer a unique opportunity for use as neuronal elements as the RESET process can be avoided.

Eligibility trace is another area where diffusive memristors could potentially be used. Thanks to their spontaneous relaxation behavior, they can be used to store the neural activity which then can be used later as additional input for weight updating. However, this process relies on the decay of t_r of the volatile device and a precise prediction of the decay over time [212]. Nonetheless, diffusive memristors could potentially be utilized for such applications. Especially, the dependency and tunability of the relaxation processes based on programming conditions provide a unique opportunity to design diffusive memristors for eligibility tracing applications.

A broad range of applications where diffusive memristor could be utilized is illustrated in Figure 8.1. Controlling t_set and t_r allows for tailoring these devices for specific applications, which is crucial for achieving optimal performance, particularly in NC. However, it is vital to take into account the specific traits of the device, such as its inherent SET kinetics and relaxation behavior, when designing these systems so that they can produce the desired results for the intended application.

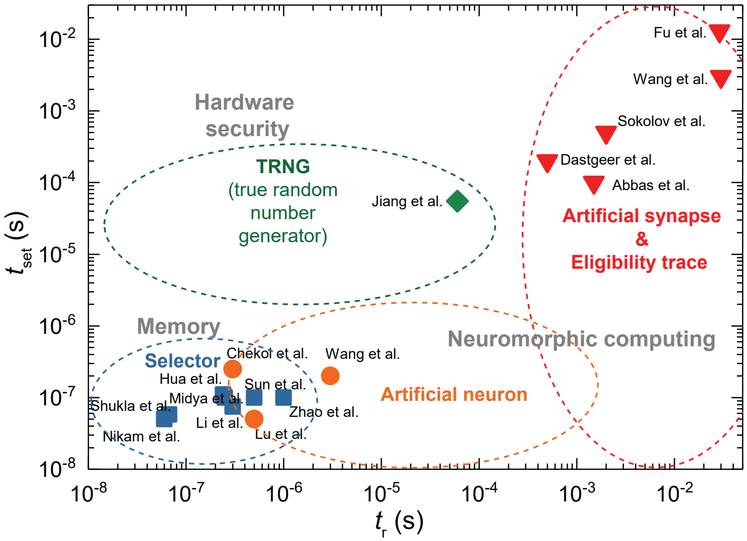

Figure 8.1: Various application areas of diffusive memristors arranged based on exemplary requirements for SET (t_{set}) and relaxation (t_{r}) times. The t_{set} and t_{r} data shown are collected from different references [1, 33, 36, 39, 60, 173, 174, 207, 213–220]. Reproduced with permission from [1].

8.2 Diffusive Memristors as Synaptic Emulators

The distinctive diffusion characteristics of diffusive memristors can be used to mimic the synaptic Ca^{2+} dynamics present in biological synapses [109]. In addition, their simple two-terminal structure provides a significant reduction in footprint, complexity, and energy consumption compared to their CMOS-based counterparts [115, 116, 221].

In general, devices based on ECM have been utilized to display both short-term and long-term synaptic functions [34, 217, 222, 223]. The non-volatile ECM is used for long-term synapse behavior, while the short-term behavior of diffusive memristors is exploited in this particular case. To achieve this, a voltage pulse train was applied to the device with an amplitude of V_{p}, a width of t_{p}, and an inter-pulse interval of t_{int}. Figure 8.2a shows a diagram of the pulse scheme, and Figure 8.2b illustrates a typical current response to a $V_{\text{p}}/\ t_{\text{p}}$ pulse train of 1.0 V/ 10 µs and t_{int} of 20 µs. An increase in conductance can be observed when a short t_{int} is used.

The application of paired pulses to short-term synapses can lead to either an increase or a decrease in postsynaptic responses, depending on the magnitude and frequency

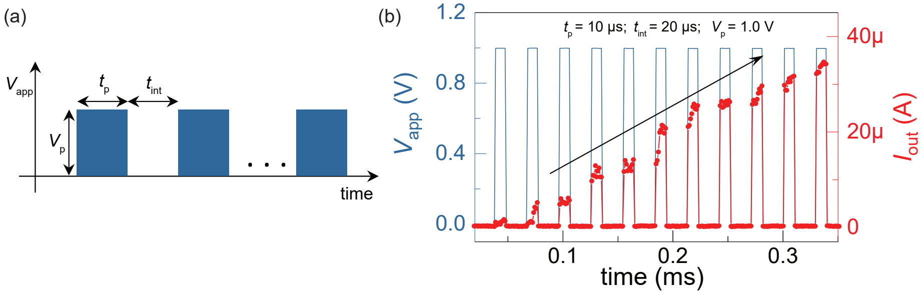

Figure 8.2: (a) Pulse train scheme used for testing synaptic functionality of diffusive memristors, with voltage pulse amplitude V_p, pulse duration t_p, and pulse interval t_int. (b) Typical current response of the device to a V_p/ t_p pulse train of 1.0 V/ 10 µs and t_int of 20 µs. A 10 kΩ series resistor was used to prevent device damage from any possible current overshoot.

of the applied pulses. When there is an increase in conductance, it is called paired-pulse-facilitation (PPF), while a decrease in conductance is referred to as paired-pulse-depression (PPD). This is illustrated in Figure 8.3, where a pulse train is applied to the device with a fixed t_p of 10 µs and varying V_p of 0.6 V, 0.7 V and 0.8 V. Two different intervals t_int of 10 µs and 500 µs were used between the pulses in order to change the frequency of the input pulse. Two main features can be seen in Figure 8.3:

- At high frequency (short t_int of 10 µs), the device conductance shows PPF characteristics, where an increase in the number of pulses leads to an increase in conductance. Conversely, at low frequency (long t_int of 500 µs), the device conductance exhibits PPD characteristics, where an increase in the number of pulses results in a decrease in conductance.

- The change in V_p has two effects: (i) as V_p increases, the incremental rate of current (PPF) and the saturation current for short t_int also increase. (ii) When considering the PPD characteristics with long t_int, increasing V_p results in a lower rate of current reduction, for example, comparing V_p of 0.6 V and 0.8 V.

The switching dynamics of diffusive memristors can explain these phenomena. When a voltage is applied, Ag^+ ions undergo electric field-assisted diffusion, leading to accumulation and ultimately the formation of a metallic filament. Consequently, the current or conductance of the device increases. However, when the voltage is removed, the filament slowly ruptures due to a surface diffusion dominated relaxation process,

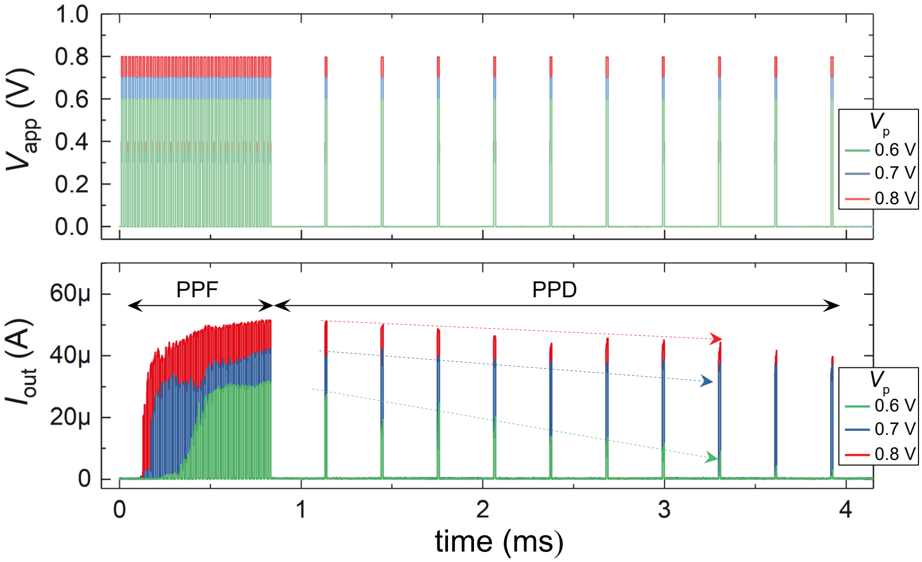

Figure 8.3: PPF and PPD of a HO3P|Pt diffusive memristor under a continuous pulse train with varying V_p of 0.6 V, 0.7 V, and 0.8 V, and two pulse intervals t_{int} of 10 µs and 500 µs, with a fixed t_p of 10 µs.

mainly driven by surface energy minimization. The duration of relaxation depends on the strength of the formed filament, as explained in Chapter 6. A high V_p leads to a longer relaxation process, while a low V_p results in a shorter relaxation process. Hence, when a pulse train with a high V_p and short t_{int} is applied, the accumulation of Ag (i.e., filament growth) is stronger than the removal of Ag from the filament due to relaxation within t_{int}. As a result, the device displays PPF characteristics. On the other hand, if a t_{int} longer than t_r is used, the relaxation process takes precedence over accumulation, resulting in PPD characteristics. However, it is important to note that the device conductance always increases in the presence of a voltage signal. Therefore, the crucial parameters for controlling PPF and PPD behaviors are t_r, which is determined by V_p and t_p, and t_{int}, which regulates the frequency of the pulse train.

To sum up, diffusive memristors possess distinct diffusion qualities that can imitate the synaptic actions of biological equivalents. The crucial factor for obtaining PPF and PPD characteristics is the formation of the filament and its relaxation process, which can be accomplished by modifying the surrounding circuitry and programming conditions.

8.3 Diffusive Memristors as Artificial Neuronal Elements

Short-term dynamics are necessary for both neuronal elements, just like artificial synapses. However, neurons require even shorter time frames in order to maximize the output frequency window. For instance, for use in SNN, an artificial neuron must possess the following characteristics:

- It should exhibit an all-or-nothing spiking behavior.
- The spiking should be threshold-driven, meaning that the neuron will only generate a spiking output if the input signal is above a certain threshold value.
- The neuron should have a refractory period during which it cannot respond to input signals after generating a spiking output.
- The neuron should provide strength-modulated frequency, meaning that a strong input signal will yield a higher spiking frequency and a weak input signal will result in a lower spiking frequency.

Diffusive memristors are well-suited for these requirements because they are volatile and exhibit intrinsic short-term dynamics. This eliminates the need for additional circuitry for RESET operation that is needed for non-volatile memristor-based neurons. When diffusive memristors are connected in series with an external resistance and in parallel with a capacitive load, the resulting circuit can exhibit the functionality of an integrate-and-fire neuron (Figure 8.4). This simple circuitry can be used to mimic biological neurons.

Figure 8.5 illustrates schematics of the equivalent RC-circuits and the operational mechanism. The working mechanism is explained as follows: Initially, the load capacitor (C_{ex}) is charged via the series resistor (R_{ex}) when an input voltage is applied (Figure 8.5a). Once the input potential reaches the membrane potential (V_{mem}) of the diffusive memristor, i.e., the threshold voltage (V_{th}), the device abruptly jumps to the LRS, causing an output spike to be generated (Figure 8.5b). Then, C_{ex} is discharged through the diffusive memristor (as shown in Figure 8.5a). Due to R_{ex}, the V_{mem} cannot be sustained, and as a consequence, the diffusive memristor returns to its initial state. The process repeats itself throughout the pulse duration as the capacitor is recharged, and the cycle continues. Here, the R_{ex} represents the overall resistance of an

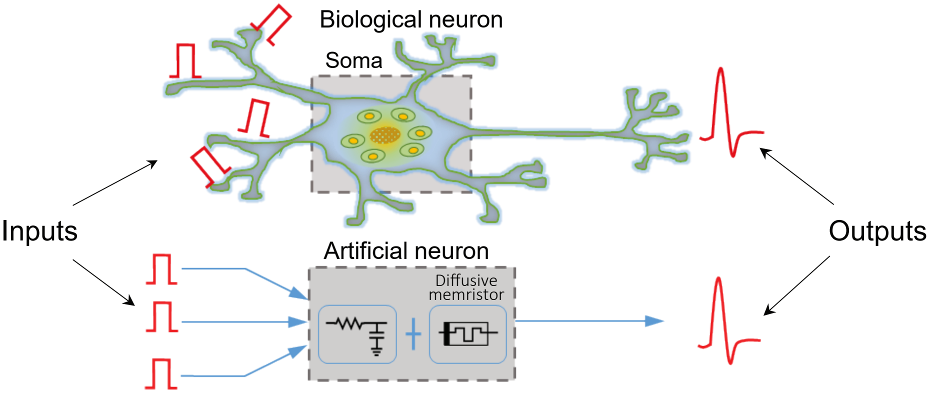

Figure 8.4: Schematic overview of the biological neuron (top) and diffusive memristor-based artificial neuron (bottom).

adjacent memristive array (for example see Figure 1.2a). An exemplary measurement of integrate-and-fire characteristics is shown in Figure 8.5c. To carry out a successful integrate-and-firing operation the following conditions have to be fulfilled:

(i) In order to charge the parallel capacitor, the $R_{\mathrm{ex}}C_{\mathrm{ex}}$-time constant should have a lower value than $R_{\mathrm{HRS}}C_{\mathrm{ex}}$ in the HRS of the diffusive memristor. Conversely, during LRS, the $R_{\mathrm{ex}}C_{\mathrm{ex}}$ constant should have a higher value than $R_{\mathrm{LRS}}C_{\mathrm{ex}}$ to discharge the capacitor. Assuming that C_{ex} is constant, the R_{ex} value for the diffusive memristor should be between R_{LRS} and R_{HRS}.

(ii) The relaxation time t_{r} of the diffusive memristor should be shorter than the RC-time of the circuit in order to modulate the spiking frequency by altering the RC-constant. If t_{r} is longer than the RC-time, the maximum frequency that can be achieved will be limited by t_{r} as the device will not be able to respond during the refractory period.

(iii) To ensure a continuous and uninterrupted firing event, the inter-pulse interval time t_{int} should be greater than t_{r}. Even though the V_{mem} drops immediately after spiking, a small residual voltage may keep on the filament and prolong the relaxation process.

For better characterization, the integrate-and-fire behavior of the device was investigated using different input voltage conditions as well as R_{ex} and C_{ex} values. The

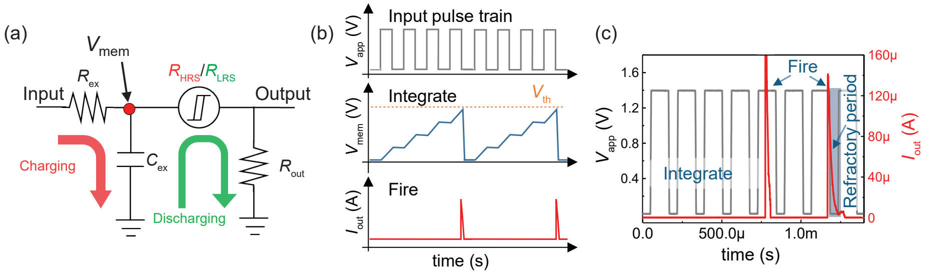

Figure 8.5: (a) Schematics of an equivalent circuit of diffusive memristor-based integrate-and-fire neuron. (b) The operating principle of an integrate-and-fire neuron. (c) Typical integrate-and-fire characteristics of the HO3P|Pt device showing the integration, firing, and refractory period. Redrawn with permission from [4]. Copyright © 2021 IEEE.

pulse scheme used has 100 µs pulse width, 50 µs pulse interval, and 5 µs rising/falling time. The voltage V_p was adjusted between 0.8 V and 1.5 V, while two different R_{ex} values of 50 kΩ and 100 kΩ and three different C_{ex} values of 1 nF, 10 nF, and 22 nF were used. Figure 8.6a illustrates typical spiking patterns resulted from 15 input pulse trains for selected V_p and R_{ex}/C_{ex} combinations. It is apparent from Figure 8.6a that a rise in V_p leads to an increase in spiking frequency. This implies that, like biological neurons, a higher post-synaptic voltage necessitates a shorter time for the post-neuron to spike. Likewise, the spiking frequency of the output can be adjusted by altering the value of the parallel capacitor, which modulates the $R_{ex}C_{ex}$ constant or charging time. Reducing the capacitance value decreases the $R_{ex}C_{ex}$ constant, which in turn results in more frequent output spikes. Similarly, a lower R_{ex} value also reduces the $R_{ex}C_{ex}$ constant, leading to an increase in spiking frequency. Moreover, the number of pulses required to initiate the first fire event decreases with an increase in input voltage amplitude or a decrease in C_{ex}. A plot of spiking data collected from 20 input pulse trains for a fixed R_{ex} of 50 kΩ and various combinations of V_p and R_{ex}/C_{ex} are shown in Figure 8.6b and 8.6c.

It should be emphasized that the pulse width employed in this study is solely for illustrative purposes, and a considerably shorter pulse width coupled with a suitable selection of other parameters can result in a higher spiking frequency. As described in earlier sections, decreasing t_p and increasing V_p, in conjunction with selecting an appropriate R_{ex}, can substantially reduce t_r. This leads to an increase in the spiking rate.

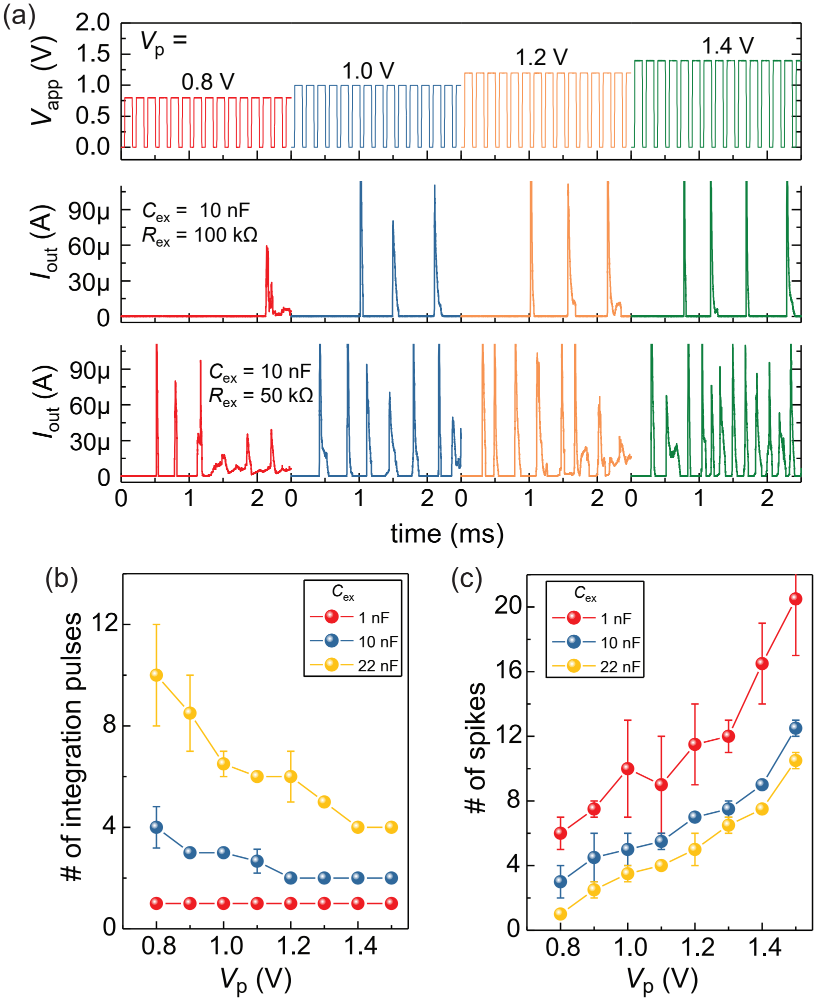

Figure 8.6: Integrate-and-fire characteristics of the device illustrated through different experiments. (a) Continued spiking behavior under various input voltages of V_p, capacitance of C_ex, and series resistance of R_ex. (b) Statistical results of the number of pulses required to trigger the first firing under different V_p amplitudes and C_ex. (c) The number of spikes as a function of V_p and C_ex. The data in (b) and (c) are acquired with a fixed R_ex of 50 kΩ. Published in [4]. Copyright © 2021 IEEE.

In summary, diffusive memristors provide an adjustable relaxation time that can be used for various applications in the emerging field of NC. By using the fabricated Ag/HfO_2/Pt-based device, integrate and fire neuron and artificial synapse functionalities were realized. By altering the amplitude of the input voltage signal, distinct firing rates were obtained. Similarly, manipulation of the input pulse amplitude and/or pulse interval enabled the emulation of synaptic functions such as pulsed-pair-facilitation (PPF) and pulsed-pair-depression (PPD).

Chapter 9

Summary and Outlook

Diffusive memristors made from volatile ECM cells reveal high resistances in the HRS in the range of several Gigaohms and threshold voltages of less than 1 Volt. This makes diffusive memristors interesting for neuromorphic applications such as artificial neurons, artificial synapses, and eligibility traces as well as for hardware security applications and, to some extent, for selectors. Diffusive memristors are characterized by an electrolyte layer that supports the formation and growth of a tiny metal filament under voltage application. If the voltage falls below the hold voltage, the filament ruptures in the matrix due to surface energy minimization. Important for any application of these threshold devices are the time constants of the SET process, t_{set}, and of the relaxation step, t_{r}, but lack of a strong understanding of the switching dynamics hampered their realization.

The goal of this thesis was to investigate the SET kinetics and relaxation dynamics, as well as their interdependence in diffusive memristors. To achieve this, comprehensive device characterization and a detailed analysis of the switching dynamics were performed using Ag/HfO_2- and Ag/SiO_2-based diffusive memristors. In order to optimize the devices, various factors such as film thickness, electrode material, and fabrication conditions were considered. Various CEs, such as Pt, TiN, and W metals, were used to investigate the role of CEs in the switching dynamics, particularly the SET kinetics. Additionally, the behavior of the fabricated cells around other circuitry elements was further investigated by introducing various external resistors in series to the device during the measurement. Both sweep and pulse mode electrical measurements were carried out to gain a deeper understanding of the physical mechanisms that govern the switching in diffusive memristors.

The main results of this investigation are summarized as follows:

(i) From a DC voltage sweep characterizations, it was found that all of the fabricated devices required a one-time forming process at a relatively high voltage. Furthermore, an increase in the forming voltage was observed with respect to oxide film thickness, which was attributed to the electric-field dependence of the switching. Additionally, a decrease in the forming voltage was observed as the device area increased, which could be explained by the higher probability of defect concentration in larger areas that facilitated the forming process. These results are consistent with previous findings. However, the V_{th} at lower sweep rates did not exhibit any dependence on either device area or film thickness. This can be explained by the fact that once the device is formed, successive switching occurs through the retraction and reformation of the preformed filament.

(ii) The SET kinetics study revealed highly non-linear characteristics with an exponential decay of t_{set} with respect to V_{p}. For example, for the HO3P|Pt device connected to an R_{series} of 100 kΩ, t_{set} decreased roughly from 1 s to 100 ns as V_{p} increased from 0.3 V to 2.2 V. Furthermore, three main processes were identified as rate-limiting steps during the SET. These are nucleation, electron-transfer, and mixed electron-transfer and ion-migration at low, intermediate, and high voltage regimes, respectively.

(iii) The relaxation process was found to be strongly influenced by the SET process. The observed strong dependence of t_{r} on the V_{p} is explained by the different filament growth mechanisms. This is due to the different rate-limiting steps during the SET process. At low voltages the growth is dominantly isotropic, resulting in a rather bulky filament, and at higher voltages, the growth becomes field-driven and anisotropic yielding a thin and fragile filament. However, it was found that the final size of the filament is also determined by the pulse duration. If t_{p} that is significantly longer than t_{set} is used at any given V_{p}, the excessive pulse duration is utilized to further growth of the filament, leading to elongation of t_{r}. Thus, the dependence of t_{r} on t_{p} is a result of the residual voltage drop over the device after the filament closing. It was revealed that once the filament is closed, a small residual voltage of a fraction of V_{p} is enough to keep the filament growing.

The different filament growth mechanism analogy suggests that t_{r} should decrease with V_{p}, as the filament size becomes thinner as V_{p} increases. This is quite the opposite of what has been shown in previous reports where a rise of t_{r} as s function V_{p} is reported. This discrepancy is because previous studies did not distinguish the effect of t_{p} from V_{p}. By disentangling the effect of t_{p}, an exponential decrease of t_{r} with V_{p} has been demonstrated in this work for the first time.

(iv) The CE material appeared to have a strong influence on the SET kinetics of diffusive memristors. Non-noble CE materials such as TiN and W tend to form a native oxide either during ambient transfer or during the ALD process of the HfO_2 switching layer. This has been confirmed by the XPS analysis of different stacks with and without the HfO_2 layer. The analysis of the switching kinetics showed that in the low voltage regime, where nucleation is the rate-limiting factor, the differences between different CE materials are minor. However, at higher voltages, where SET kinetics is limited by electron transfer and ion migration, the SET time differs for the different CE materials. Among the materials studied, Pt showed the fastest SET process, followed by TiN and W. This difference can be explained by (1) the different electrocatalytic activity of the different CE metals, which limits the counter-reaction and, thus, the amount of Ag^+ ions available for switching; and (2) the tendency of native oxides to form a passivation layer at the electrolyte/CE interface, inhibiting the redox reaction. The native oxide can also act as an additional diffusion barrier for Ag^+ ions. These features of non-noble metals are often neglected and, therefore, should be considered in the fabrication and characterization of diffusive memristor devices.

(v) Series resistance does not have a significant impact on the SET kinetics of diffusive memristors. The experimentally observed differences in SET time at higher voltages are mainly due to a capacitive charging time of the device and measurement setup rather than an intrinsic device property. This claim is further supported by physics-based device simulation using the JART ECM model. On the other hand, the t_r appears to be significantly affected by the R_series. It is shown that the dependence of relaxation time on the pulse voltage amplitude can be strongly influenced by the magnitude of the R_series. Two main reasons attributed to this are (1) the high non-linearity of the SET kinetics and (2) the contribution of a residual voltage drop over the device in LRS to the further growth and strengthening of the conductive filament. Furthermore, the implications of these findings on device operation and exploiting this to tune the relaxation behavior for use in various applications, like as a synapse and artificial neuron, are suggested. The understanding of the influence of series resistance on the switching kinetics of diffusive memristors can contribute to optimizing their operating conditions and expanding their use as energy-efficient switches in NC areas.

Beyond the scope of this work, there are still various aspects that need to be explored and addressed in the future to advance these devices further toward realization.
As the focus of the thesis was mainly to understand the switching kinetics, the devices are not fully optimized for performance enhancement. Similar to most emerging memristive devices, the forming process is not desired as it leads to higher variability and low yield as a result of the high voltage and current involved. In this regard, further optimization towards electrolyte and active ion source engineering such as utilizing active metal-doped electrolytes, alloyed electrodes like AgTe, CuTe, and AgCu would be beneficial to improve device performance. Previous reports have shown that the use of alloyed electrodes can decrease the amount of Ag^+ ions introduced into the switching electrolyte, which consequently lowers the possibility of filament overgrowth and device failure [59]. Similar benefits can be gained from doping the electrolyte, for example with Ag, as this will reduce the forming voltage significantly.
Unlike in SET kinetics, a physics-based and predictive model is still lacking for the relaxation dynamics of diffusive memristors. Although a comprehensive experimental characterization of diffusive memristors is performed in this work, the development of a model that can also reproduce the relaxation behavior frequently observed in these devices would help to deepen the understanding of relaxation dynamics on the one hand and to efficiently design an optimized system suitable for the target application on the other hand.
Finally, the proof-of-concept demonstrations for the various applications of diffusive memristors shown in this study were measured on stand-alone devices externally connected to other circuit elements. Therefore, the fabrication of diffusive memristors on CMOS chips along with other circuit elements, including drift memristors as synapses, and application demonstrations in monolithically integrated systems will take the realization of these devices in real-time applications a step forward.

Appendix A

Numerical and Analytical JART ECM Models

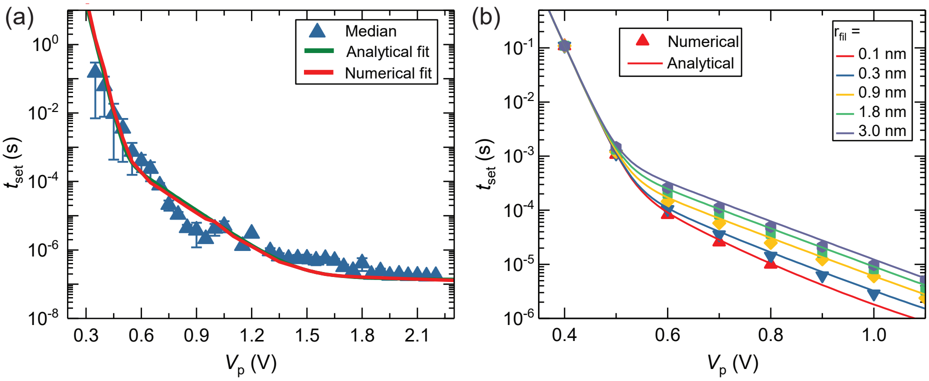

Figure A.1: Comparison of the two versions of the JART ECM model. (a) Numerical and analytical simulation fits of the SET kinetics of the HO3P|Pt device. (b) Numerical and analytical simulations of SET kinetics for various filament radii.

Appendix B

Device Fabrication Protocols

B.1 Micro-crossbar structure fabrication | AZ 5214E resist

Starting substrate: 1 in x 1 in Si/430 nm $\mathbf{SiO_2}$

Step 1: Bottom electrode metal deposition: Sputtering of 5 nm Ti and 25 nm Pt (10 nm Pt and 20 nm of TiN or W for different counter electrodes)

Step 2: Cleaning: 3 minutes of ultrasonic bath in Acetone at power level 3 followed by 3 minutes of ultrasonic bath in isopropyl alcohol at power level 3, drying with N_2 gas

Step 3: Bottom electrode lithography:

- Substrate dehydration at 120 °C for 3 min
- Spincoating of AZ 5214E resist at 4000 rpm for 45 s (≈ 1 µm)
- Resist baking at 90 °C for 5 min
- UV light exposure for 25 s using mask `"Mark_II_Xbar_(BE)"`
- Development in AZ 326 MIF developer for 80 s, stopped in deionized water, drying with N_2 gas

Step 4: RIBE etching using Argon process gas

Step 5: Resist removal by DMSO at 80 °C for minimum of 3 hours, followed by 3 min ultrasonic bath at power level 5. Swabbing in Acetone and optional plasma ashing for 10 min at 600 W

Step 6: Deposition of the switching layers of 3-10 nm HfO_2 or SiO_2 by plasma enhanced ALD

Step 7: Top electrode lithography:

- Spincoating of AZ 5214E resist at 4000 rpm for 45 s (≈ 1 µm)
- Resist pre-exposure baking at 90 °C for 5 min
- UV light exposure for 10 s using mask `"Mark_II_Xbar_(TE)"`
- Resist post-exposure baking at 120 °C for 1 min
- UV light flood exposure for 1 min
- Development in AZ 326 MIF developer for 80 s, stopped in deionized water, drying with N_2 gas

Step 8: Deposition of the top electrode metal layers of 20 nm Ag and 20 nm Pt by sputtering

Step 9: Lift-off by Acetone over night, followed by isopropyl alcohol and deionized water bath and subsequent drying with N_2 gas

Step 10: BE contact pad opening lithography:

- Spincoating of AZ 5214E resist at 4000 rpm for 45 s (≈ 1 µm)
- Resist pre-exposure baking at 90 °C for 5 min
- UV light exposure for 10 s using mask `"Mark_II_Xbar_(BE_open)"`
- Resist post-exposure baking at 120 °C for 1 min
- UV light flood exposure for 1 min
- Development in AZ 326 MIF developer for 80 s, stopped in deionized water, drying with N_2 gas

Step 11: RIBE etching using CF_4 process gas

Step 12: Resist removal using Acetone overnight, followed by isopropyl alcohol and deionized water bath and drying with N_2 gas

B.2 Micro-crossbar structure fabrication | AZ MIR 701 and AZ nLOF 2020 resists

Starting substrate: 1 in x 1 in Si/430 nm SiO_2

Step 1: Bottom electrode metal deposition: Sputtering of 5 nm Ti and 25 nm Pt (10 nm Pt and 20 nm of TiN or W for different counter electrodes)

Step 2: Cleaning: 3 minutes of ultrasonic bath in Acetone at power level 3 followed by 3 minutes of ultrasonic bath in isopropyl alcohol at power level 3, drying with N_2 gas

Step 3: Bottom electrode lithography:

- Substrate dehydration at 120 °C for 3 min
- Spincoating of AZ MIR 701 14cP resist at 4000 rpm for 45 s (≈ 1 µm)
- Resist baking at 90 °C for 90 s
- UV light exposure for 11 sec using mask `"Mark_II_Xbar_(BE)"`
- Resist post-exposure baking at 115 °C for 1 mi
- Development in AZ 726 MIF developer for 60 s, stopped in deionized water, drying with N_2 gas

Step 4: RIBE etching using Argon process gas

Step 5: Resist removal by DMSO at 80 °C for minimum of 3 hours, followed by 3 min ultrasonic bath at power level 5. Swabbing in Acetone and optional plasma ashing for 10 min at 600 W

Step 6: Deposition of the switching layers of 3-10 nm HfO_2 or SiO_2 by plasma enhanced ALD

Step 7: Top electrode lithography:

- Spincoating of AZ nLOF 2020 resist at 4000 rpm for 45 s (≈ 1 µm)
- Resist pre-exposure baking at 110 °C for 1 min
- UV light exposure for 3.4 s using mask `"Mark_II_Xbar_(TE)"`
- Resist post-exposure baking at 110 °C for 1 min

- UV light flood exposure for 1 min
- Development in AZ 326 MIF developer for 60 s, stopped in deionized water, drying with N_2 gas

Step 8: Deposition of the top electrode metal layers of 20 nm Ag and 20 nm Pt by sputtering

Step 9: Lift-off by Acetone over night, followed by isopropyl alcohol and deionized water bath and subsequent drying with N_2 gas

Step 10: BE contact pad opening lithography:

- Spincoating of AZ nLOF 2020 resist at 4000 rpm for 45 s ($\approx$ 1 µm)
- Resist pre-exposure baking at 110 °C for 1 min
- UV light exposure for 3.4 s using mask `"Mark_II_Xbar_(BE_open)"`
- Resist post-exposure baking at 110 °C for 1 min
- UV light flood exposure for 1 min
- Development in AZ 326 MIF developer for 60 s, stopped in deionized water, drying with N_2 gas

Step 11: RIBE etching using CF_4 process gas

Step 12: Resist removal using Acetone overnight, followed by isopropyl alcohol and deionized water bath and drying with N_2 gas

B.3 Nanoplug structure fabrication

Starting substrate: 1 in x 1 in Si/430 nm SiO_2

Step 1: Bottom electrode metal deposition: Sputtering of 5 nm Ti and 25 nm Pt

Step 2: Cleaning: 3 minutes of ultrasonic bath in Acetone at power level 3 followed by 3 minutes of ultrasonic bath in isopropyl alcohol at power level 3, drying with N_2 gas

Step 3: Bottom electrode lithography:

- Substrate dehydration at 120 °C for 3 min
- Spincoating of (1:2) diluted AZ nLof 2020 resist at 4000 rpm for 45 s
- Resist baking at 90 °C for 3 min
- Electron beam exposure at 100 kV using mask `"True_Planar_Device_L1"`
- Post-exposure baking at 110 °C for 3 min
- Development in AZ 726 MIF developer for 1 min, stopped in deionized water, drying with N_2 gas

Step 4: RIBE etching using Argon process gas

Step 5: Resist removal by DMSO at 80 °C for minimum of 3 hours, followed by 3 min ultrasonic bath at power level 5. Swabbing in Acetone and optional plasma ashing

Step 6: Deposition of the insulation layer of 20 nm SiO_2 by plasma enhanced ALD

Step 7: Nano hole lithography:

- Spincoating of CSAR 6200.04 resist at 4000 rpm for 45 s
- Resist baking at 150 °C for 1 min
- Electron beam exposure at 100 kV using mask `"True_Planar_Device_L2"`
- Development in AR 600-55 developer for 1 min, stopped in isopropyl alcohol, drying with N_2 gas

Step 8: RIBE etching using CF_4 process gas

Step 9: Resist removal by AR 600-71 for minimum of 30 min, followed by acetone, isopropyl alcohol and deionized water bath

Step 10: Deposition of the switching layers of 3 nm HfO_2 by plasma enhanced ALD

Step 11: Top electrode lithography:

- Spincoating of CSAR 6200.04 resist at 4000 rpm for 45 s
- Baking of the resist at 150 °C for 1 min
- Electron beam exposure at 100 kV using mask `"True_Planar_Device_L3"`
- Development in AR 600-55 developer for 1 min, stopped in isopropyl alcohol, drying with N_2 gas

Step 12: Deposition of the top electrode metal layers of 10 nm Ti and 20 nm Pt by sputtering

Step 13: Lift-off by AR 600-71 over night, followed by acetone, isopropyl alcohol and deionized water bath

Step 14: Contact pad opening lithography:

- Substrate dehydration at 120 °C for 3 min
- Spincoating of (1:2) diluted AZ nLof 2020 resist at 4000 rpm for 45 s
- Pre-baking of the resist at 90 °C for 3 min
- Electron beam exposure at 100 kV using mask `"True_Planar_Device_L4"`
- Post-exposure baking at 110 °C for 3 min
- Development in AZ 726 MIF developer for 1 min, stopped in deionized water, drying with N_2 gas

Step 15: RIBE etching using CF_4 process gas

Step 16: Resist removal by AR 600-71 for minimum of 30 min, followed by acetone, isopropyl alcohol and deionized water bath and optional swabbing in Acetone

List of Abbreviations

1S1R	one-selector one-resistor
ADC	analog to digital converter
AE	active electrode
AFM	atomic force microscopy
ALD	atomic layer deposition
BCC	body-centered cubic
BTBAS	bis(tertiary-butylamino)silane
c2c	cycle to cycle
CBRAM	conductive bridge random access memory
CDF	cumulative distribution function
CE	counter electrode
CMOS	complementary metal oxide semiconductor
CMU	capacitance measurement unit
CPU	central processing unit
CVD	chemical vapor deposition
d2d	device to device
DAC	digital to analog converter
DC	direct current
DMSO	dimethyl sulfoxide
DRAM	dynamic random access memory
DUT	device under test
EBL	electron beam lithography
ECM	electrochemical metallization
EOT	equivalent oxide thickness
FCC	face centered cubic
FeFET	ferroelectric field effect transistor

FRAM	ferroelectric random access memory
FTJ	ferroelectric tunnel junction
GNDU	ground unit
GPC	growth per cycle
GPIB	general purpose interface bus
HRS	high resistive state
HRTEM	high resolution transmission electron microscopy
HV	high vacuum
IMT	insulator to metal transition
KMC	kinetic Monte Carlo
LRS	low resistive state
LTD	long term depression
LTP	long term potentiation
LTP	long term plasticity
MD	molecular dynamic
MFTJ	multiferrioc tunnel junction
MIEC	mixed ionic electronic conductor
MIM	metal insulator metal
MOSFET	metal-oxide-semiconductor field effect transistor
MRAM	magnetic random access memory
MTJ	magnetic tunnel junction
NEM	nano-electrochemical memory
OEL	oxygen exchange layer
OTS	Ovonic threshold switching
PCM	phase change memory
PCRAM	phase change random access memory
PE-ALD	plasma enhanced-atomic layer deposition
PEB	post exposure bake
PLC	programmable logic controller
PMU	pulse measurement unit
PPD	pulsed pair depression
PPF	pulsed pair potentiation
PVD	physical vapor deposition
RAM	random access memory
ReRAM	resistive random access memory

RF	radio frequency
RIBE	reactive ion beam etching
RPM	rounds per minute
S.E.	standard error
SEM	scanning electron microscopy
SMD	surface mounted device
SMU	source measurement unit
SNN	spiking neural network
STDP	spike-timing-dependent plasticity
STP	short-term synaptic plasticity
STT-MRAM	spin-transfer torque magnetic random access memory
TCM	thermochemical memory
TEMAH	tetrakis(ethylmethylamino)hafnium
TMO	transition metal oxide
TRNG	true random number generator
TSV	through-silicon via
UV	ultraviolet
VCM	valence change memory
XRR	x-ray reflectivity

List of Figures

1.1 (a) Illustration of a neural network consisting of an input layer, hidden layers, and an output layer. (b) Equivalent circuit representation of one layer with a CMOS-based neuron connected to the output side of the layer. (b) is redrawn with permission from [4]. Copyright © 2021 IEEE. 2

1.2 (a) Equivalent circuit illustration of memristive arrays connected to a threshold switching based neuron. (b) Leakage current and threshold voltage of various types of threshold switching devices. Data in (a) are collected from [25–30, 36, 41–54]. (b) is redrawn with permission from [4]. Copyright © 2021 IEEE. 4

2.1 Emerging memristive devices taxonomy. The ECM cell, which is the main focus of this thesis, is highlighted by a red circle. Redrawn with permission from [63]. 9

2.2 Typical operating mechanism of an ECM cell. Adapted with permission from [77]. 10

2.3 Different filament growth mechanisms in diffusive memristors. Reproduced with permission from [92]. 12

2.4 Illustration of the electrochemical processes during SET switching and the respective equivalent circuit diagram. Taken from [62]. 17

2.5 Schematic diagram illustrating the threshold switching phenomenon in diffusive memristors. 18

2.6 In situ TEM observation of the (a)-(f) filament formation and (f)-(h) filament relaxation in diffusive memristors upon the application and removal of external bias, respectively. The scale bar is 20 nm. Redrawn with permission from [109]. 19

2.7 (a)-(b) Surface diffusion controlled initial stage of filament rupture. (c) Post-lifetime evolution of the filament particle through Ostwald ripening mechanism [112]. Adapted from [57]. 21

3.1 Exemplary schematic diagram of an ALD cycle from a metal Precursor A (metal) and Precursor B (water vapor). I: Precursor material is introduced into the chamber, where a sample with an OH-terminated surface is placed. The precursor reacts with these groups and leaves behind byproducts. II: After the purge, the remaining precursor and the byproduct are purged, so that only chemisorbed precursor molecules stay. III: Water vapor is introduced in the chamber and reacts with the surface, producing a new OH-terminated surface. IV: After the second purge, a metal oxide layer has been grown and growth is continued with step I. 27

3.2 Schematic diagram of the temperature-dependent growth per cycle (GPC) of a typical ALD process. If the temperature is too low, the GPC can decrease as no chemical reactions take place due to the lack of thermal energy. On the other side, the precursor material might condense on the sample surface, leading to an increased GPC. If the temperature is too high, precursor material might decompose onto or desorb from the surface, leading to an increase or decrease in GPC, respectively. Redrawn from [156]. 28

3.3 Left: Photo of the FlexAL™ALD system. Right: Cross-section of the ALD chamber, modified from [158]. 30

3.4 Planar chemical representations of the ALD metal sources used in this work: (a) TEMAH and (b) BTBAS. 30

3.5 Sketch of the ALD processes for PE-ALD (a) HfO_2 and (b) SiO_2. . . 31

3.6 Basics of sputter process. Adapted from [160]. 33

3.7 Top and side views of (a) the Omicron off-axis sputter tool and (b) the Univex 450 C on-axis sputter tool. Picture in (a) is adapted from [161]. 34

3.8 X-ray reflectivity measurements of different layers. (a) Sputter deposited Ag metal film on SiO_2 substrate. (b) ALD grown HfO_2 film on SiO_2 substrate. (c) ALD grown SiO_2 film on Si substrate. 35

3.9 Atomic force microscopy images of the sputter grown bottom electrode of (a) Pt, (b) TiN, and (c) W. 36

3.10 Fabrication steps of a typical micro crossbar device. 37

3.11 Final structures of the fabricated devices: (a) Schematic and (b) optical microscopy image of the micro crossbar device with an inset of scanning electron microscopy (SEM) image of the junction between the top and bottom electrodes. (c) Schematic and (d) SEM image of the nano plug device. The 60 nm x 60 nm nano plug is shown in the inset. 39

3.12 Photo of the Suess MicroTec PA-200 semi-automatic table. 41

3.13 Photo of the Keithley 4200-SCS measurement setup. 43

3.14 (a) Circuitry schematics of the Keithley 4200-SCS measurement setup. (b) A typical transient curve of V-t (blue curve) and I-t (red and green curves) recorded from the setup under a programming voltage of 2.0 V and pulse width of 1 µs, with a series resistor of 100 kΩ connected between the two probe tips. 43

4.1 Typical forming curve of the HO3P|Pt device. The current response is plotted in black while the calculated resistance of the cell is plotted in red. Current compliance of 100 nA was used to limit current overshoot. 46

4.2 CDF plot of the forming voltage for (a) HO3P|Pt and (b) HO5P|Pt devices for various device areas. A constant sweep rate of 100 mV/s was used during the measurement. 47

4.3 (a) Representative forming curves of the HO2P|Pt, HO3P|Pt, and HO5P|Pt devices for the small device area of 3 µm^2. Forming was performed in auto-range mode. (b) CDF plot of the forming voltage for the three devices of 3 µm^2 size. A constant sweep rate of 100 mV/s was used during the measurement in (b). 48

4.4 I-V characteristics of HO3P|Pt cells under various device compliance currents (I_{CC}) showing volatile behavior up to 1 mA. Reproduced with permission from [1]. 49

4.5 I-V sweeps of the (a) HO2P|Pt (b) HO3P|Pt and (c) HO5P|Pt devices of 3 µm^2 size measured under a compliance current (I_{CC}) of 10 µA. . 50

4.6 CDF plot of (a) HO2P|Pt, (b) HO3P|Pt and (c) HO5P|Pt. Data are collected from 10 devices and 100 cycles each at a constant sweep rate of 100 mV/s. 50

4.7 (a)-(d) Sweep measurement under different compliance currents and (e)-(h) the corresponding calculated conductance curves as a function of voltage. (i)-(l) A schematic plot showing the filament evolution under various compliance currents. A constant sweep rate of 100 mV/s was used during all measurements. Reproduced with permission from [1]. 52

4.8 (a) Forming curve of HO3P|Pt device and (b) the subsequent switching, showing a unidirectional threshold switching behavior. (c) SET and RESET curves of HO3P|Pt achieved at higher compliance current after first forming at low compliance current and (d) the corresponding bidirectional threshold switching. Redrawn with permission from [1]. 53

4.9 A schematic representation of a possible switching mechanism under (a) Case I and (b) Case II. Redrawn with permission from [1]. 54

4.10 (a) Simmons fitting of the leakage current of pristine devices for various cell sizes. (b) Tunneling currents are calculated using the Simmons model under various tunneling gaps. Reproduced with permission from [1]. 56

4.11 (a) Top panel: optical microscopy image of the nano-structured plug-type device. Bottom panel: a schematic cross-sectional view of the red-colored line in the top panel. (b) Typical forming curve of the HO3P|Pt plug-type device with cell dimension of 40 nm x 40 nm. The current response is plotted in black while the calculated resistance of the cell is plotted in red. (c) CDF plot of the forming voltage collected from 50 cells each for 40 nm x 40 nm and 100 nm x 100 nm devices. A current compliance of 100 nA was used during the measurement to prevent current overshoot. 57

4.12 Representative *I*-*V* curves for the plug-type HO3P|Pt devices with cell size of (a) 40 nm x 40 nm and (b) 100 nm x 100 nm measured under a current compliance of 100 µA. 58

4.13 An exemplary time-resolved triangular pulse scheme used to estimate threshold voltage (V_{th}) at different sweep rates ($\nu = V_{\mathrm{p}}/t_{\mathrm{p}}$). The plot is made of data obtained from the HO2P|Pt cell. A 100 kΩ resistor was used in series to protect the device from damage. 59

4.14 Distribution of threshold voltage (V_{th}) with different pulse width (t_{p}) at a pulse voltage (V_{p}) of 3.0 V for (a) HO2P|Pt, (b)HO3P, and (c) HO5P|Pt devices. V_{th} collected from a DC sweep measurement is added for comparison. 60

4.15 Dependence of threshold voltage (V_{th}) on the sweep rate (ν) for (a)HO2P|Pt, (b) HO3P|Pt, and (c) HO5P|Pt devices. The mean of the data is shown in red bar. 60

4.16 (a) Oxide thickness dependence of the threshold voltage (V_{th}) as plotted against sweep rate (ν) for the 3 µm^2 device. (b) Area dependence of V_{th} as a function of ν measured for the HO3P|Pt device. The lines in both plots are for eye guidance only and do not represent any physical fitting. 61

4.17 XPS analyses of CE metal surfaces and interfaces with and without an HfO_2 layer on top. (a) Pt 4f core level spectra for a Pt film after exposure to air. (b) Hf 4f core level spectra for a Pt film with a 3 nm HfO_2 layer on top. (c) Ti 4f core level spectra for a TiN film after exposure to air. (d) Ti 4f core level spectra for a TiN film after deposition of 3 nm HfO_2. (e) W 4f core level spectra for a W film after exposure to air. (f) W 4f core level spectra for a W film after deposition of 3 nm HfO_2. (g) XPS analysis of an in situ sputter-cleaned TiN CE surface. (h) XPS analysis of a pure W film under a take-off angle of 15° targeting the bulk of the film. Except (h), all measurements were conducted under a take-off angle of 45°. Reproduced with permission from [3]. 64

4.18 (a) Representative I-V curves of the electroforming of Ag/3 nm HfO_2/CE devices for the three different CE materials. (b) Statistical distribution of the forming voltage collected from 96 cells for the three different devices. A compliance current of 100 nA and a sweep rate of 62.5 mV/s were used for the measurements. Reproduced with permission from [3]. 65

4.19 Typical threshold I-V curves for (a) HO3P|Pt, (b) HO3P|TiN, and (c) HO3P|W devices. The TiO_x and WO_x interfacial oxides are shown with light orange and light green colors, respectively. A sweep rate of 62.5 mV/s was used for the measurements. Reproduced with permission from [3]. 66

4.20 Statistical distribution of the hold voltage (V_{h}) and threshold voltage (V_{th}) collected from 8 devices and 100 cycles each for (a) HO3P|Pt, (b) HO3P|TiN, and (c) HO3P|W devices. Reproduced with permission from [3]. 67

4.21 Initial forming characteristics of SO3P|Pt device. The current response is plotted in black while the calculated resistance of the cell is plotted in red. Current compliance of 100 nA was used to limit current overshoot. 68

4.22 CDF plot of the forming voltage of (a) SO3P|Pt and (b) SO5P|Pt devices for varied device areas. A constant sweep rate of 100 mV/s was used during the measurement 69

4.23 I-V sweep of the SO3P|Pt device measured under a compliance current (I_{CC}) of 10 µA. (b) Statistical distribution of the hold (V_{h}) and threshold (V_{th}) voltages collected from 10 devices and 100 cycles each. 69

5.1 Various terminologies and the definitions of SET time (t_{set}) and relaxation time (t_{r}) from a temporal response measurement in the time domain. The applied voltage (V_{app}) and output current signal (I_{out}) are shown in blue and red colors, respectively. Reproduced with permission from [1]. 72

5.2 (a) Schematics of the programming pulse schemes used for the kinetics study. (b) Typical I_{out}–t curves recorded during the SET event measurement of the device under different V_{p}. 73

5.3 SET switching kinetics of HO3P|Pt device. The median values and median absolute deviation (MAD) of the experimental data are displayed using cool black circles and vertical lines, respectively. A series resistor of 100 kΩ was used during the measurement. Reproduced with permission from [1]. 74

5.4 (a) Fitting of the median of the experimental data by using numerical simulation. A filament radius of 1 nm is assumed for the simulation. (b) Experimental and simulated SET time for different filament radii ranging from 0.15 to 3 nm as a function of pulse voltage. Reproduced with permission from [1]. 76

5.5 (a) I-V sweep measurements performed on HO3P|Pt device with different series resistances. Inset shows the electrical connection during the measurement. (b) The transient current measurement under different series resistance. (c) Magnified image of the box with the pink broken line in (b). The applied voltage (V_{app}) is shown in gray color. 77

5.6 SET switching kinetics of HO3P|Pt cell in series with different resistors of (a) 50 kΩ, (b) 100 kΩ, (c) 560 kΩ, and (d) 1000 kΩ. The median values and median absolute deviations (MAD) of the experimental data are displayed using color-filled symbols and vertical lines, respectively. Reproduced with permission from [2]. 78

5.7 (a) A plot of the median values of t_{set} as a function of V_{p} for the different series resistors. (b) The mean of t_{set} taken from the red box marked region in (a) plotted against R_{series} to extract C_{p}. Reproduced with permission from [2]. 79

5.8 (a) A sweep I-V and resistance-voltage (R-V) plot of a HO3P|Pt cell. (b) Schematic drawings showing the capacitive and resistive behavior of the device for the HRS and LRS, respectively. Reproduced with permission from [2]. 80

5.9 (a) Simulation of the SET kinetics when an RC-time constant of the circuit is considered with C_{p}=1.15 pF. (b) Simulation data was obtained with C_{p} of 1 fF, showing faster switching times and negligible differences between the R_{series} values. Inset shows a magnified image of the pink box in (b). Reproduced with permission from [2]. 81

5.10 SET switching kinetics of (a) HO3P|Pt, (b) HO3P|TiN, and (c) HO3P|W. (d) A median of t_{set} plotted against V_{p} for the three devices. The median values and median absolute deviations (MAD) of the experimental data are displayed using color-filled symbols and vertical lines, respectively. The $\mathrm{TiO_x}$ and $\mathrm{WO_x}$ interfacial oxides are shown with light orange and light green colors, respectively. A 100 kΩ series resistor was used during the measurements. Reproduced with permission from [3]. 83

5.11 SET switching kinetics of SO3P|Pt device. (a) Experimental data and (b) Simulation curve together with the experimental data. The median values and median absolute deviation (MAD) of the experimental data are displayed using dark blue-gray symbols and vertical lines, respectively. A series resistor of 100 kΩ was used during the measurement. 85

5.12 Direct comparison of the SET kinetics of HO3P|Pt and SO3P|Pt devices. The scatter plot is the median of the experimental data and the line is the fitting from the model. 87

6.1 (a) Typical current response, I_{out}-t, under programming pulses V_{p}/ t_{p} of 1.3 V, 1.5 V, and 1.7 V/ 1 ms followed by a 0.1 V monitoring voltage. (b) Magnified plot of the pink marked region in (a), showing the different relaxation times for different V_{p}. R_{series} of 100 kΩ was used during the measurement. Reproduced with permission from [1]. 90

6.2 (a) The statistical analysis of t_{r} as a function of (a) V_{p} and (b) t_{p} collected from 10 measurements for each V_{p}/ t_{p} combination. Reproduced with permission from [1]. 91

6.3 A schematic representation of the voltage divider effect between the diffusive memristor R_{dm} and the series resistor R_{series}. 92

6.4 (a) Calculated resistance of the diffusive memristor (R_{dm}) and (b) the corresponding voltage drop (V_{dm}) during the bias duration for various V_{p}. Reproduced with permission from [1]. 93

6.5 (a) Transient measurement under different series resistance of 50 kΩ, 100 kΩ, 560 kΩ, and 1000 kΩ at a fixed V_{p}/ t_{p} of 1.6 V/ 10 µs. (b) A magnified image of the pink box marked region in (a) shows the effect of different series resistors on the relaxation time. 94

6.6 Relaxation time plot of t_{r} as a function of V_{p} with different R_{series} of (a)-(c) 50 kΩ, (d)-(f) 100 kΩ, (g)-(i) 560 kΩ, and (j)-(l) 1000 kΩ and t_{p} of 10 µs, 100 µs, and 1 ms (left to right). The median values and median absolute deviations (MAD) of the experimental data are displayed using color-filled symbols and vertical lines, respectively. Reproduced with permission from [2]. 95

6.7 Median t_{r} for different R_{series} plotted against V_{p} for t_{p} of (a) 10 µs, (b) 100 µs, (c) 1 ms. Median absolute deviation (MAD) is represented using vertical lines. (d) Slopes extracted from (a)-(c) and plotted as a function of R_{series} for various t_{p}. The standard error (S.E.) is shown as vertical lines. Reproduced with permission from [2]. 96

6.8 (a) Total resistance R_{total} calculated from the output current I_{out} of the transient curve in the LRS plotted as a function of R_{series} for a pulse amplitude V_{p} of 1.4 V. Reproduced with permission from [2]. 98

6.9 Calculated (a) cell resistance R_{dm} and (b) voltage drop across the cell V_{dm} plotted as against V_{p} for different R_{series} values at a fixed t_{p} of 1 ms. The lines in (b) are a guide to the eye. Reproduced with permission from [2]. 99

6.10 (a) The triangular pulses scheme used to analyze the influence of sweep rate on the relaxation time. The voltage pulse V_{p} is given in blue and the output current I_{out} in red. (b) A log(I_{out}) - t plot of the data in (a) showing the original and smoothed data using Gaussian-weighted filter. 101

6.11 Relaxation time t_{r} plotted as a function of sweep rate ν for (a) HO2P|Pt and (b) HO3P|Pt devices. (c) The median of t_{r} for the two devices is plotted against ν. The error bar in (c) is the median absolute deviation (MAD) of the measured data. 103

6.12 (a) An output current I_{out} from a triangular pulse scheme plotted for HO3P|Pt device measured under t_{p} of (a) 3 ms (b) 3 µs. The excessive pulse is shown as t_{p}-t_{set}. 104

6.13 Relaxation time plotted as a function of V_{p} for various t_{p} of (a) 10 µs, (b) 100 µs, and (c) 1 ms. (d) Median of t_{r} as a function of V_{p}. The median values and median absolute deviations (MAD) of the experimental data are displayed using color-filled symbols and vertical lines, respectively. A 100 kΩ resistor was used during the measurements. 106

6.14 Relaxation dynamics of HO3P|Pt and SO3P|Pt devices. The median of t_{r} is plotted against V_{p} for various pulse durations of (a) 10 µs, (b) 100 µs, and (c) 1 ms. 107

7.1 Schematic depiction of (a) the dependence of t_{set} and t_{r} on V_{p} at a fixed t_{p} and (b) the dependence of t_{set} and t_{r} on t_{p} at a fixed V_{p}. Reproduced with permission from [1]. 110

7.2 A heat map of the combination of the SET kinetics (broken line) and relaxation dynamics showing several orders of magnitude change in relaxation time t_r over a certain range of V_p and t_p. The SET kinetics curve is a representative fitting curve of the experimental data. The color-coded relaxation time is plotted based on experimental data (represented by stars) and an extrapolation from the fitting of the experimentally obtained data. Letter assigned boxes are t_r data collected from various publications of [35, 60, 174, 190, 204–207]. Reproduced with permission from [1]. 111

7.3 Voltage-dependent filament growth mechanisms. (a) Definitions of the three different rate-limiting processes. Filament growth mechanisms as a function of time in the (b) nucleation-limited regime, (c) electron-transfer limited regime, and (d) mixed (electron-transfer and ion-migration) limited regimes. Reproduced with permission from [1]. 113

7.4 Schematic representation of the filament morphology at different combinations of V_p and t_p. Reproduced with permission from [1]. 114

7.5 (a) SET kinetics data and the selection of different pulse duration t_p along the SET kinetics curve. (b) A plot of tr against V_p for different pulse durations defined in (a), displaying the exponential decay of t_r with V_p when short pulses that are long enough to close the filament are used. The solid line in (b) is a guide to the eye and does not represent any physical fitting. Reproduced with permission from [2]. 115

7.6 A heat map combining the SET kinetics (dashed line) and relaxation dynamics as a function of V_p and t_p for various series resistors R_series of (a) 50 kΩ, (b) 100 kΩ, (c) 560 kΩ, and (d) 1000 kΩ. The SET kinetics curve (dashed line) is a representative fitting curve of experimentally obtained data. The color-coded t_r is plotted based on experimental data (stars) and an extrapolation. Reproduced with permission from [2].117

8.1 Various application areas of diffusive memristors arranged based on exemplary requirements for SET (t_set) and relaxation (t_r) times. The t_set and t_r data shown are collected from different references [1, 33, 36, 39, 60, 173, 174, 207, 213–220]. Reproduced with permission from [1]. 121

8.2 (a) Pulse train scheme used for testing synaptic functionality of diffusive memristors, with voltage pulse amplitude V_{p}, pulse duration t_{p}, and pulse interval t_{int}. (b) Typical current response of the device to a V_{p}/ t_{p} pulse train of 1.0 V/ 10 µs and t_{int} of 20 µs. A 10 kΩ series resistor was used to prevent device damage from any possible current overshoot. 122
8.3 PPF and PPD of a HO3P|Pt diffusive memristor under a continuous pulse train with varying V_{p} of 0.6 V, 0.7 V, and 0.8 V, and two pulse intervals t_{int} of 10 µs and 500 µs, with a fixed t_{p} of 10 µs. 123
8.4 Schematic overview of the biological neuron (top) and diffusive memristor-based artificial neuron (bottom). 125
8.5 (a) Schematics of an equivalent circuit of diffusive memristor-based integrate-and-fire neuron. (b) The operating principle of an integrate-and-fire neuron. (c) Typical integrate-and-fire characteristics of the HO3P|Pt device showing the integration, firing, and refractory period. Redrawn with permission from [4]. Copyright © 2021 IEEE. 126
8.6 Integrate-and-fire characteristics of the device illustrated through different experiments. (a) Continued spiking behavior under various input voltages of V_{p}, capacitance of C_{ex}, and series resistance of R_{ex}. (b) Statistical results of the number of pulses required to trigger the first firing under different V_{p} amplitudes and C_{ex}. (c) The number of spikes as a function of V_{p} and C_{ex}. The data in (b) and (c) are acquired with a fixed R_{ex} of 50 kΩ. Published in [4]. Copyright © 2021 IEEE. . . . 127

A.1 Comparison of the two versions of the JART ECM model. (a) Numerical and analytical simulation fits of the SET kinetics of the HO3P|Pt device. (b) Numerical and analytical simulations of SET kinetics for various filament radii. 133

List of Tables

3.1 Bottom electrode sputter deposition parameters. 34
3.2 Top electrode sputter deposition parameters. 34
3.3 Layer stacks of the devices investigated in this work. Stacks labeled with a star (*) are films deposited by using the Omicron sputtering tool. Nano-plug structured samples are shown in bold. 40

4.1 Parameters used for the Simmons fitting. 55

5.1 Parameters used for the simulation of SET kinetics. 75
5.2 Parameters used to simulate SET kinetics of SO3P|Pt device. 86

List of Publications

Peer Reviewed Journals

S. A. Chekol, S. Menzel, R. W. Ahmad, R. Waser, and S. Hoffmann-Eifert, *"Effect of the Threshold Kinetics on the Filament Relaxation Behavior of Ag-Based Diffusive Memristors,"* Advanced Functional Materials, **32**, 2111242, 2022, `DOI: 10.1002/adfm.202111242`

S. A. Chekol, S. Menzel, R. Waser, and S. Hoffmann-Eifert, *"Strategies to Control the Relaxation Kinetics of Ag-Based Diffusive Memristors and Implications for Device Operation,"* Advanced Electronic Materials, **8**, 2200549, 2022, `DOI:10.1002/aelm.202200549`

S. A. Chekol, R. Nacke, S. Aussen, and S. Hoffmann-Eifert, *"SET Kinetics of Ag/*HfO_2*-Based Diffusive Memristors under Various Counter-Electrode Materials,"* Micromachines, **14**(3), 571, 2023, `DOI:10.3390/mi14030571`

Conference Proceedings

S. A. Chekol, F. Cüppers, R. Waser, and S. Hoffmann-Eifert, *"An Ag/*HfO_2*/Pt Threshold Switching Device with an Ultra-Low Leakage (*< 10 *fA), High On/Off Ratio (*$> 10^{11}$*), and Low Threshold Voltage (*< 0.2 *V) for Energy-Efficient Neuromorphic Computing,"* Proc. 2021 IEEE 13th International Memory Workshop, 2021, `DOI:10.1109/IMW51353.2021.9439601`

S. A. Chekol and S. Hoffmann-Eifert, *"Controllability of Relaxation Behavior in Ag-based Diffusive Memristors,"* 2023 Device Research Conference (DRC), Santa Barbara, CA, USA, 2023, pp. 1-2, `DOI:10.1109/DRC58590.2023.10186979`

Conference Talks and Posters

S. A. Chekol, R. Waser, S. Hoffmann-Eifert, *"Integrate and Fire Neurons Based on Diffusive Memristors for Spiking Neural Networks,"* 2021 International Conference on Neuromorphic Systems (ICONS), Oak Ridge, Tennessee, USA, July 27-29, 2021 (Best Poster Award)

S. A. Chekol, S. Menzel, R. W. Ahmad, R. Waser, and S. Hoffmann-Eifert, *"Enhanced Performance of Ag/HfO_2/Pt-based Diffusive Threshold Switches for Energy-Efficient Neuromorphic Computing,"* 2021 MRS Fall Meeting, Boston, Massachusetts, USA, December 6-8, 2021

S. A. Chekol, S. Menzel, R. W. Ahmad, R. Waser, and S. Hoffmann-Eifert, *"Correlation between the Threshold Kinetics and Relaxation Behavior of Ag/HfO_2/Pt-based Diffusive Memristors,"* 2022 CIMTEC, 9th Forum on New Materials, Perugia, Italy, June 20-29, 2022

S. A. Chekol, S. Menzel, R. W. Ahmad, R. Waser, and S. Hoffmann-Eifert, *"Switching Kinetics of Ag/HfO_2/Pt-based Diffusive Memristors,"* 2022 The 5th International Conference on Memristive Materials, Devices and Systems, Boston, Massachusetts, USA, November 30 - December 02, 2022

S. A. Chekol, R. Nacke, S. Aussen, and S. Hoffmann-Eifert, *"Effect of the Counter Electrode Material on the SET kinetics of Ag/HfO_2-based Diffusive Memristors,"* 2023 The 65th Electronic Materials Conference EMC, Santa Barbara, California, USA, June 28 - 30, 2023

Bibliography

[1] S. A. Chekol, S. Menzel, R. W. Ahmad, R. Waser, and S. Hoffmann-Eifert. "Effect of the threshold kinetics on the filament relaxation behavior of Ag-Based diffusive memristors". In: *Adv. Funct. Mater.* 32.15 (2022), pp. 2111242/1–11 (cit. on pp. vii, 3, 49, 52–54, 56, 72, 74, 76, 90, 91, 93, 110, 111, 113, 114, 121).

[2] S. A. Chekol, S. Menzel, R. Waser, and S. Hoffmann-Eifert. "Strategies to control the relaxation kinetics of Ag-based diffusive memristors and implications for device operation". In: *Adv. Electron. Mater.* 8.11 (2022), pp. 2200549/1–11 (cit. on pp. vii, 78–81, 95, 96, 98, 99, 115, 117).

[3] S. A. Chekol, R. Nacke, S. Aussen, and S. Hoffmann-Eifert. "SET kinetics of Ag/HfO_2-based diffusive memristors under various counter-electrode materials". In: *Micromachines* 14.13 (2023), p. 571 (cit. on pp. vii, 64–67, 83).

[4] S. A. Chekol, F. Cüppers, R. Waser, and S. Hoffmann-Eifert. "An Ag/HfO_2/Pt threshold switching device with an ultra-low leakage (< 10 fA), High On/Off ratio ($> 10^{11}$), and low threshold voltage (< 0.2 V) for energy-efficient neuromorphic computing". In: *2021 IEEE International Memory Workshop (IMW)*. IEEE International Memory Workshop (IMW), 2021, pp. 1–4 (cit. on pp. vii, 2, 4, 126, 127).

[5] J. von Neumann. *First draft of a report on EDVAC*. Tech. rep. 1945 (cit. on p. 1).

[6] M. A. Zidan, J. P. Strachan, and W. D. Lu. "The future of electronics based on memristive systems". In: *Nat. Electron.* 1 (2018), pp. 22–29 (cit. on p. 1).

[7] C. S. Poon and K. Zhou. "Neuromorphic silicon neurons and large-scale neural networks: challenges and opportunities". In: *Frontiers in Neuroscience* 5 (2011), pp. 108/1– (cit. on p. 1).

[8] SRC. *SRC Decadal Plan.* 2020. URL: `https://www.semiconductors.org/wp-content/uploads/2020/10/Decadal-Plan_Interim-Report.pdf` (cit. on p. 1).

[9] O. Krestinskaya, A. P. James, and L. O. Chua. "Neuromemristive circuits for edge computing: A review". In: *IEEE Transactions on Neural Networks and Learning* 31 (2020), 4–23 (cit. on p. 1).

[10] B. Chen, F. Cai, J. Zhou, W. Ma, P. Sheridan, and W. D. Lu. "Efficient in-memory computing architecture based on crossbar arrays". In: *2015 IEEE International Electron Devices Meeting (IEDM).* 2015 IEEE International Electron Devices Meeting (IEDM), 2015, pp. 17.5.1–17.5.4 (cit. on p. 1).

[11] A. Mehonic and A. J. Kenyon. "Brain-inspired computing needs a master plan". In: *Nature* 604.7905 (2022), pp. 255–260 (cit. on p. 1).

[12] G. W. Burr, M. J. Brightsky, A. Sebastian, H. Cheng, J. Wu, S. Kim, N. E. Sosa, N. Papandreou, H. Lung, H. Pozidis, E. Eleftheriou, and C. H. Lam. "Recent progress in phase-change memory technology". In: *IEEE J. Emerging Sel. Top. Circuits Syst.* 6.2 (2016), pp. 146–162 (cit. on p. 2).

[13] M. Wimmer and M. Salinga. "The gradual nature of threshold switching". In: *New Journal of Physics* 16 (2014), p. 113044 (cit. on p. 2).

[14] M. Salinga, B. Kersting, I. Ronneberger, V. P. Jonnalagadda, X. T. Vu, M. L. Gallo, I. Giannopoulos, O. Cojocaru-Mirédin, R. Mazzarello, and A. Sebastian. "Monatomic phase change memory". In: *Nat. Mater.* (2018), p. 1 (cit. on p. 2).

[15] S. Bhatti, R. Sbiaa, A. Hirohata, H. Ohno, S. Fukami, and S. N. Piramanayagam. "Spintronics based random access memory: A review". In: *Mater. Today* 20.9 (2017), pp. 530–548 (cit. on p. 2).

[16] C. C. Xu, Y. Zheng, D. Niu, X. Zhu, S. H. Kang, and Y. Xie. "Impact of write pulse and process variation on 22 nm FinFET-based STT-RAM design: A device-architecture co-optimization approach". In: *IEEE Trans. Multi-Scale Comput. Syst.* 1 (2015), pp. 195–206 (cit. on p. 2).

[17] R. Waser, R. Dittmann, G. Staikov, and K. Szot. "Redox-based resistive switching memories - Nanoionic mechanisms, prospects, and challenges". In: *Adv. Mater.* 21.25-26 (2009), pp. 2632–2663 (cit. on p. 2).

[18] H. Akinaga and H. Shima. "Resistive random access memory (ReRAM) based on metal oxides". In: *Proc. IEEE* 98.12 (2010), pp. 2237–2251 (cit. on p. 2).

[19] M. H. Park, Y. H. L. andT. Mikolajick, U. Schroeder, and C. S. Hwang. "Review and perspective on ferroelectric HfO_2-based thin films for memory applications". In: *MRS Communications* (2018), pp. 1–14 (cit. on p. 2).

[20] G. Walters, A. Shekhawat, N. G. Rudawski, S. Moghaddam, and T. Nishida. "Tiered deposition of sub-5 nm ferroelectric $Hf_{1-x}Zr_xO_2$ films on metal and semiconductor substrates". In: *Appl. Phys. Lett.* 112 (2018), p. 192901 (cit. on p. 2).

[21] W. Wan, R. Kubendran, C. Schaefer, S. B. Eryilmaz, W. Zhang, D. Wu, S. Deiss, P. Raina, H. Qian, B. Gao, S. Joshi, H. Wu, H. P. Wong, and G. Cauwenberghs. "A compute-in-memory chip based on resistive random-access memory". In: *Nature* 608.7923 (2022), pp. 504–512 (cit. on p. 2).

[22] G. Indiveri, B. Linares-Barranco, T. Hamilton, A. van Schaik, R. Etienne-Cummings, T. Delbruck, S. Liu, P. Dudek, P. Haefliger, S. Renaud, J. Schemmel, G. Cauwenberghs, J. Arthur, K. Hynna, F. Folowosele, S. SAÏGHI, T. Serrano-Gotarredona, J. Wijekoon, Y. Wang, and K. Boahen. "Neuromorphic silicon neuron circuits". In: *Frontiers in Neuroscience* 5 (2011), p. 73 (cit. on p. 2).

[23] J. H. B. Wijekoon and P. Dudek. "Compact silicon neuron circuit with spiking and bursting behaviour". In: (2008). DOI: `10.1016/j.neunet.2007.12.037` (cit. on p. 2).

[24] M. Mahowald and R. Douglas. "A silicon neuron". In: *Nature* 354 (1991), 515–518 (cit. on p. 2).

[25] B. Govoreanu, G. L. Donadio, K. Opsomer, W. Devulder, V. V. Afanas'ev, T. Witters, S. Clima, N. S. Avasarala, A. Redolfi, S. Kundu, O. Richard, D. Tsvetanova, G. Pourtois, C. Detavemier, L. Goux, and G. S. Kar. "Thermally stable integrated Se-based OTS selectors with $>$20 MA/cm^2 current drive, $> 3{\cdot}10^3$ half-bias nonlinearity, tunable threshold voltage and excellent endurance". In: *2017 Symposium on VLSI Technology*. 2017, T92–T93 (cit. on pp. 3, 4).

[26] S. A. Chekol, J. Yoo, J. Park, J. Song, C. Sung, and H. Hwang. "A C-Te-based binary OTS device exhibiting excellent performance and high thermal stability for selector application". In: *Nanotechnology* 29.34 (2018), pp. 345202/1–6 (cit. on pp. 3, 4).

[27] Y. Koo, K. Baek, and H. Hwang. "Te-based amorphous binary OTS device with excellent selector characteristics for x-point memory applications". In: *Te-based amorphous binary OTS device with excellent selector characteristics for x-point memory applications.* 2016, pp. 1–2 (cit. on pp. 3, 4).

[28] H. Y. Cheng, W. C. Chien, I. T. Kuo, E. K. Lai, Y. Zhu, J. L. Jordan-Sweet, A. Ray, F. Carta, F. M. Lee, P. H. Tseng, M. H. Lee, Y. Y. Lin, W. Kim, R. Bruce, C. W. Yeh, C. H. Yang, M. BrightSky, and H. L. Lung. "An ultra high endurance and thermally stable selector based on TeAsGeSiSe chalcogenides compatible with BEOL IC Integration for cross-point PCM". In: *2017 IEEE International Electron Devices Meeting (IEDM).* IEEE, 2017, pp. 2.2.1–2.2.4 (cit. on pp. 3, 4).

[29] J. A. J. Rupp, R. Waser, and D. J. Wouters. "Threshold switching in amorphous Cr-doped vanadium oxide for new crossbar selector". In: *2016 IEEE 8th International Memory Workshop (IMW).* Ed. by IEEE. Institut für Werkstoffe der Elektrotechnik II (IWE II) RWTH Aachen. IEEE Xplore, 2016, p. 4 (cit. on pp. 3, 4).

[30] J. Woo, P. Wang, and S. Yu. "Integrated crossbar array with resistive synapses and oscillation neurons". In: *IEEE Electron Device Lett.* 40.8 (2019), pp. 1313–1316 (cit. on pp. 3, 4).

[31] E. Cha, J. Park, J. Woo, D. Lee, A. Prakash, and H. Hwang. "Comprehensive scaling study of NbO_2 insulator-metal-transition selector for cross point array application". In: *Appl. Phys. Lett.* 108.15 (2016), pp. 153502/1–3 (cit. on p. 3).

[32] J. Song, J. Woo, J. Yoo, S. A. Chekol, S. Lim, C. Sung, and H. Hwang. "Effects of liner thickness on the reliability of AgTe/TiO_2-based threshold switching devices". In: *IEEE Trans. Electron Devices* 64.11 (2017), pp. 4763–4767 (cit. on p. 3).

[33] Z. Wang, S. Joshi, S. E. Savel'ev, H. Jiang, R. Midya, P. Lin, M. Hu, N. Ge, J. P. Strachan, Z. Li, Q. Wu, M. Barne, G. Li, H. L. Xin, R. S. Williams, Q. Xia, and J. J. Yang. "Memristors with diffusive dynamics as synaptic emulators for neuromorphic computing". In: *Nat. Mater.* 16 (2017), pp. 101–108 (cit. on pp. 3, 51, 121).

[34] Z. Wang et al. “Fully memristive neural networks for pattern classification with unsupervised learning”. In: *Nature Electronics* 1.2 (2018), pp. 137–145 (cit. on pp. 3, 21, 84, 121).

[35] M. Wang, W. Wang, W. R. Leow, C. Wan, G. Chen, Y. Zeng, J. Yu, Y. Liu, P. Cai, H. Wang, D. Ielmini, and X. Chen. “Enhancing the matrix addressing of flexible sensory arrays by a highly nonlinear threshold switch”. In: *Advanced Materials* 30.33 (2018), pp. 1802516/1– (cit. on pp. 3, 111).

[36] R. Midya, Z. Wang, J. Zhang, S. E. Savel’ev, C. Li, M. Rao, M. H. Jang, S. Joshi, H. Jiang, P. Lin, K. Norris, N. Ge, Q. Wu, M. Barnell, Z. Li, H. L. Xin, R. S. Williams, Q. Xia, and J. J. Yang. “Anatomy of Ag/Hafnia-based selectors with 10^{10} nonlinearity”. In: *Adv. Mater.* (2017) (cit. on pp. 3, 4, 21, 56, 90, 91, 97, 110, 121).

[37] M. Rao, W. Song, F. Kiani, S. Asapu, Y. Zhuo, R. Midya, N. Upadhyay, Q. Wu, M. Barnell, P. Lin, C. Li, Z. Wang, Q. Xia, and J. J. Yang. “Timing Selector: Using transient switching dynamics to solve the sneak Path issue of crossbar arrays”. In: *Small Sci.* (2021) (cit. on pp. 3, 117).

[38] Y. Zhuo, R. Midya, W. Song, Z. Wang, S. Asapu, M. Rao, P. Lin, H. Jiang, Q. Xia, R. S. Williams, and J. J. Yang. “A dynamical compact model of diffusive and drift memristors for neuromorphic computing”. In: *Adv. Electron. Mater.* (2021) (cit. on p. 3).

[39] H. Jiang, D. Belkin, S. E. Savel’ev, S. Lin, Z. Wang, Y. Li, S. Joshi, R. Midya, C. Li, M. Rao, M. Barnell, Q. Wu, J. J. Yang, and Q. Xia. “A novel true random number generator based on a stochastic diffusive memristor”. In: *Nature Communications* 8 (2017), pp. 882/1– (cit. on pp. 3, 21, 121).

[40] Y.-F. Lu, H.-Y. Li, Y. Li, L.-H. Li, T.-Q. Wan, L. Yang, W.-B. Zuo, K.-H. Xue, and X.-S. Miao. “A high-performance Ag/TiN/HfO_x/HfO_y/HfO_x/Pt diffusive memristor for calibration-free true random number generator”. In: *Adv. Electron. Mater.* 8.2200202 (2022) (cit. on p. 3).

[41] S. Li, X. Liu, S. K. Nandi, D. K. Venkatachalam, and R. G. Elliman. “Coupling dynamics of Nb/Nb_2O_5 relaxation oscillators”. In: *Nanotechnology* 28 (2017), p. 125201 (cit. on p. 4).

[42] X. Liu, S. Li, S. K. Nandi, D. K. Venkatachalam, and R. G. Elliman. “Threshold switching and electrical self-oscillation in niobium oxide films”. In: *J. Appl. Phys.* 120.12 (2016), pp. 124102/1–10 (cit. on p. 4).

[43] D. Lee, M. Kwak, K. Moon, W. Choi, J. Park, J. Yoo, J. Song, S. Lim, C. Sung, W. Banerjee, and H. Hwang. “Various threshold switching devices for integrate and fire neuron Applications”. In: *Adv. Electron. Mater.* 5.9 (2019), pp. 1800866/1–7 (cit. on p. 4).

[44] Y. Koo and H. Hwang. “$\mathrm{Zn}_{1-x}\mathrm{Te}_x$ Ovonic threshold switching device performance and its correlation to material parameters”. In: *Sci Rep* 8 (2018), pp. 11822/1–7 (cit. on p. 4).

[45] S. Jia, H. Li, T. Gotoh, C. Longeaud, B. Zhang, J. Lyu, S. Lv, M. Zhu, Z. Song, Q. Liu, J. Robertson, and M. Liu. “Ultrahigh drive current and large selectivity in GeS selector”. In: *Nat. Commun.* 11.1 (2020), pp. 4636/1–9 (cit. on p. 4).

[46] A. Velea, K. Opsomer, W. Devulder, J. Dumortier, J. Fan, C. Detavernier, M. Jurczak, and B. Govoreanu. “Te-based chalcogenide materials for selector applications”. In: *Scientific Reports* 7.8103 (2017), pp. 1–12 (cit. on p. 4).

[47] A. Verdy, G. Navarro, M. Bernard, P. Noe, C. Licitra, G. Bourgeois, J. Garrione, M. C. Cyrille, V. Sousa, and E. Nowak. “High temperature stability and performance analysis of N-doped Ge-Se-Sb based OTS selector devices”. In: *10th IEEE International Memory Workshop (IMW), Kyoto, JAPAN.* 2018 IEEE 10th International Memory Workshop (IMW), 2018, pp. 85–88 (cit. on p. 4).

[48] N. S. Avasarala, G. L. Donadio, T. Witters, K. Opsomer, B. Govoreanu, A. Fantini, S. Clima, H. Oh, S. Kundu, W. Devulder, M. H. van der Veen, J. V. Houdt, M. Heyns, L. Goux, and G. S. Kar. “Half-threshold bias I_{off} reduction down to nA range of thermally and electrically stable high-performance integrated OTS selector, obtained by Se enrichment and N-doping of thin GeSe layers”. In: *38th IEEE Symposium on VLSI Technology, Honolulu, HI.* 2018 IEEE Symposium On VlSI Technology, 2018, pp. 209–210 (cit. on p. 4).

[49] H. Y. Cheng, W. C. Chien, I. T. Kuo, C. W. Yeh, L. Gignac, W. Kim, E. K. Lai, Y. F. Lin, R. L. Bruce, C. Lavoie, C. Cheng, A. Ray, F. M. Lee, F. Carta, C. H. Yang, M. H. Lee, H. Y. Ho, and M. B. andH. L. Lung. “Ultra-high endurance and low I_{OFF} selector based on AsSeGe chalcogenides for wide memory window

3D stackable crosspoint memory”. In: *2018 IEEE International Electron Devices Meeting (IEDM).* 2018, pp. 37.3.1–37.3.4 (cit. on p. 4).

[50] W. Chen, H. J. Barnaby, and M. N. Kozicki. “Volatile and non-volatile switching in Cu-SiO_2 programmable metallization cells”. In: *IEEE Electron Device Lett.* 37.5 (2016), pp. 580–583 (cit. on p. 4).

[51] X. Zhang, W. Wang, Q. Liu, X. Zhao, J. Wei, R. Cao, Z. Yao, X. Zhu, F. Zhang, H. Lv, S. Long, and M. Liu. “An artificial neuron based on a threshold switching memristor”. In: *IEEE Electron Device Lett.* 39.2 (2018), pp. 308–311 (cit. on p. 4).

[52] J. Song, J. Woo, A. Prakash, D. Lee, and H. Hwang. “Threshold selector with high selectivity and steep slope for cross-Point memory array”. In: *IEEE Electron Device Lett.* 36.7 (2015), pp. 681–683 (cit. on pp. 4, 18, 56, 57).

[53] Q. Hua, H. Wu, B. Gao, Q. Zhang, W. Wu, Y. Li, X. Wang, W. Hu, and H. Qian. “Low-voltage oscillatory neurons for memristor-based neuromorphic systems”. In: *Glob. Chall.* 3.11 (2019), pp. 1900015/1–6 (cit. on p. 4).

[54] W. Banerjee, I. V. Karpov, A. Agrawa, S. Kim, S. L. andSangmin Lee, D. Lee, and H. Hwang. “Highly-stable ($<$ 3% fluctuation) Ag-based threshold switch with extreme-low OFF current of 0.1 pA, extreme-high selectivity of 10^9 and high endurance of 10^9 cycles”. In: *2020 IEEE International Electron Devices Meeting (IEDM).* IEEE, 2020, pp. 28.4.1–28.4.4 (cit. on pp. 4, 9, 107).

[55] C. P. Hsiung, H. W. Liao, J. Y. Gan, T. B. Wu, J. C. Hwang, F. Chen, and M. J. Tsai. “Formation and instability of silver nanofilament in Ag-based programmable metallization cells”. In: *Acs Nano* 4.9 (2010), pp. 5414–5420 (cit. on pp. 4, 17, 18, 20).

[56] H. Sun, Q. Liu, C. Li, S. Long, H. Lv, C. Bi, Z. Huo, L. Li, and M. Liu. “Direct observation of conversion between threshold switching and memory switching induced by conductive filament morphology”. In: *Adv. Funct. Mater.* 24.36 (2014), pp. 5679–5686 (cit. on pp. 4, 18, 19, 51).

[57] W. Wang, M. Wang, E. Ambrosi, A. Bricalli, M. Laudato, Z. Sun, X. Chen, and D. Ielmini. “Surface diffusion-limited lifetime of silver and copper nanofilaments in resistive switching devices”. In: *Nature Communications* (2019), p. 9 (cit. on pp. 4, 17, 18, 20, 21).

[58] T. Liu, M. Verma, Y. Kang, and M. Orlowski. “Volatile resistive switching in Cu/TaO$_x$/delta-Cu/Pt devices”. In: *Appl. Phys. Lett.* 101.7 (2012), p. 073510 (cit. on p. 4).

[59] J. Yoo, J. Song, and H. Hwang. “Effect of cation amount in the electrolyte on characteristics of Ag/TiO$_2$ based threshold switching devices”. In: *Nanotechnology* 29.36 (2018), pp. 365707/1–5 (cit. on pp. 4, 132).

[60] Y. Li, J. Tang, B. Gao, W. Sun, Q. Hua, W. Zhang, X. Li, W. Zhang, H. Qian, and H. Wu. “High-uniformity threshold switching HfO$_2$-based selectors with patterned Ag nanodots”. In: *Advanced Science* 7.22 (2020), pp. 2002251/1– (cit. on pp. 4, 72, 90, 91, 110, 111, 121).

[61] JART. *Juelich Aachen Resistive Switching Tools (JART).* Tech. rep. 2019 (cit. on pp. 5, 13).

[62] S. Menzel, S. Tappertzhofen, R. Waser, and I. Valov. “Switching kinetics of electrochemical metallization memory cells”. In: *PCCP* 15.18 (2013), pp. 6945–6952 (cit. on pp. 7, 13–17, 22, 72, 73).

[63] R. Dittmann, S. Menzel, and R. Waser. “Nanoionic memristive phenomena in metal oxides: the valence change mechanism”. In: *Adv. Phys.* (2022) (cit. on pp. 7–9).

[64] J. S. Moodera, L. R. Kinder, T. M. Wong, and R. Meservey. “Large magnetoresistance at room-temperature in ferromagnetic thin-film tunnel-junctions”. In: *Phys. Rev. Lett.* 74.16 (1995), pp. 3273–3276 (cit. on p. 7).

[65] T. Miyazaki and N. Tezuka. “Giant magnetic tunneling effect in Fe/Al$_2$O$_3$/Fe junction”. In: *J. Magn. Magn. Mater.* 139.3 (1995), pp. L231–L234 (cit. on p. 7).

[66] K. Inomata. “Present and future of magnetic RAM technology”. In: *IEICE Trans. Electron.* E84C.6 (2001), pp. 740–746 (cit. on p. 7).

[67] B. Dieny, R. Sousa, J.-P. Nozieres, O. Redon, and I. L. Prejbeanu. “Magnetic randon access memories”. In: *Nanoelectronics and Information Technology (3rd ed.)* Ed. by R. Waser. Wiley-VCH, 2012, pp. 655–668 (cit. on p. 7).

[68] E. T. Breyer, H. Mulaosmanovic, T. Mikolajick, and S. Slesazeck. “Perspective on ferroelectric, hafnium oxide based transistors for digital beyond von-Neumann computing”. In: *Appl. Phys. Lett.* 118.5 (2021), pp. 50501/1– (cit. on p. 7).

[69] P. W. M. Blom, R. M. Wolf, J. F. M. Cillessen, and M. P. C. M. Krijn. “Ferroelectric Schottky diode”. In: *Phys. Rev. Lett.* 73.15 (1994), pp. 2107–10 (cit. on p. 7).

[70] M. Ziegler, M. Oberlaender, D. Schroeder, W. H. Krautschneider, and H. Kohlstedt. “Memristive operation mode of floating gate transistors: A two-terminal MemFlash-cell”. In: *Appl. Phys. Lett.* 101 (2012), p. 263504 (cit. on p. 7).

[71] R. Guo, W. Lin, X. Yan, T. Venkatesan, and J. Chen. “Ferroic tunnel junctions and their application in neuromorphic networks”. In: *Applied Physics Reviews* 7.1 (2020), pp. 11304/1– (cit. on p. 7).

[72] K. Akarvardar and H.-S. P. Wong. “Nanomechnical Logic Gates”. In: *Nanoelectronics and Information Technology (3rd ed.)* Ed. by R. Waser. Wiley-VCH, 2012 (cit. on p. 8).

[73] S. Goswami, S. P. Rath, D. Thompson, S. Hedstrom, M. Annamalai, R. Pramanick, B. R. Ilic, S. Sarkar, S. Hooda, C. A. Nijhuis, J. Martin, R. S. Williams, S. Goswami, and T. Venkatesan. “Charge disproportionate molecular redox for discrete memristive and memcapacitive switching”. In: *Nat. Nanotechnol.* 15.5 (2020), 380–389 (cit. on p. 8).

[74] S. Raoux and M. Wuttig. “Information storage based on phase change materials”. In: *Nanoelectronics and Information Technology (3rd ed.)* Ed. by R. Waser. Wiley-VCH, 2012, pp. 669–682 (cit. on p. 8).

[75] R. Waser, R. Bruchhaus, and S. Menzel. “Redox-based resistive switching memories”. In: *Nanoelectronics and Information Technology (3rd ed.)* Ed. by R. Waser. Wiley-VCH, 2012, pp. 683–710 (cit. on p. 8).

[76] D. Ielmini, R. Bruchhaus, and R. Waser. “Thermochemical resistive switching: materials, mechanisms, and scaling projections”. In: *Phase Transit.* 84.7 (2011), pp. 570–602 (cit. on p. 8).

[77] I. Valov, R. Waser, J. R. Jameson, and M. N. Kozicki. “Electrochemical metallization memories-fundamentals, applications, prospects”. In: *Nanotechnology* 22.25 (2011), pp. 254003/1–22 (cit. on pp. 8, 10).

[78] W. Lu, D. S. Jeong, M. Kozicki, and R. Waser. “Electrochemical metallization cells-blending nanoionics into nanoelectronics?” In: *MRS Bulletin* 37.2 (2012), pp. 124–130 (cit. on p. 8).

[79] I. Valov, I. Sapezanskaia, A. Nayak, T. Tsuruoka, T. Bredow, T. Hasegawa, G. Staikov, M. Aono, and R. Waser. “Atomically controlled electrochemical nucleation at superionic solid electrolyte surfaces”. In: *Nat. Mater.* 11.6 (2012), pp. 530–535 (cit. on p. 9).

[80] R. Soni, P. Meuffels, G. Staikov, R. Weng, C. Kuegeler, A. Petraru, M. Hambe, R. Waser, and H. Kohlstedt. “On the stochastic nature of resistive switching in Cu doped $Ge_{0.3}Se_{0.7}$ based memory devices”. In: *J. Appl. Phys.* 110.5 (2011), pp. 54509/1–10 (cit. on p. 9).

[81] C. Schindler, K. Szot, S. K. anduser, and R. Waser. “Controlled local filament growth and dissolution in Ag-Ge-Se”. In: *Phys. Status Solidi-Rapid Res. Lett.* 2.3 (2008), pp. 129–31 (cit. on p. 9).

[82] M. Lübben, F. Cüppers, J. Mohr, M. von Witzleben, U. Breuer, R. Waser, C. Neumann, and I. Valov. “Design of defect-chemical properties and device performance in memristive systems”. In: *Sci. Adv.* 6.19 (2020), eaaz9079/1–10 (cit. on pp. 9, 84, 105).

[83] S. Tappertzhofen, H. Mündelein, I. Valov, and R. Waser. “Nanoionic transport and electrochemical reactions in resistively switching silicon dioxide”. In: *Nanoscale* 4.10 (2012), pp. 3040–3043 (cit. on pp. 9, 11).

[84] T. Tsuruoka, T. Hasegawa, I. Valov, R. Waser, and M. Aono. “Rate-limiting processes in the fast SET operation of a gapless-type Cu-Ta_2O_5 atomic switch”. In: *AIP Adv.* 3.3 (2013), pp. 32114/1–7 (cit. on p. 9).

[85] M. Haemori, T. Nagata, and T. Chikyow. “Impact of Cu electrode on switching behavior in a Cu/HfO_2/Pt structure and resultant Cu ion diffusion”. In: *Applied Physics Express* 2.6 (2009), pp. 61401/1– (cit. on p. 9).

[86] F. G. Aga, J. Woo, J. Song, J. Park, S. Lim, C. Sung, and H. Hwang. “Controllable quantized conductance for multilevel data storage applications using conductive bridge random access memory”. In: *Nanotechnology* 28.11 (2017), pp. 115707/1–6 (cit. on p. 9).

[87] I. Valov and Y. Yang. “Memristors with alloyed electrodes”. In: *Nat. Nanotechnol.* 15.7 (2020), pp. 510–511 (cit. on p. 9).

[88] H. Yeon, P. Lin, C. Choi, S. H. Tan, Y. Park, D. Lee, J. Lee, F. Xu, B. Gao, H. Wu, H. Qian, Y. Nie, S. Kim, and J. Kim. “Alloying conducting channels for reliable neuromorphic computing”. In: *Nat. Nanotechnol.* 15.7 (2020), pp. 574–579 (cit. on p. 9).

[89] M. Luebben, S. Menzel, S. G. Park, M. Yang, R.Waser, and I. Valov. “SET kinetics of electrochemical metallization cells - influence of counter electrodes in SiO_2/Ag based systems”. In: *Nanotechnology* 28.13 (2017), pp. 135205/1–6 (cit. on pp. 9, 24, 60, 61, 73, 80, 82, 84).

[90] B. Grisafe, M. Jerry, J. A. Smith, and S. Datta. “Performance enhancement of Ag/HfO_2 metal ion threshold switch cross-point selectors”. In: *IEEE Electron Device Lett.* 40.10 (2019), pp. 1602–1605 (cit. on p. 9).

[91] S. Tappertzhofen, R. Waser, and I. Valov. “Impact of counter electrode material on the redox processes in resistive switching memories”. In: *ChemElectroChem* 1 (2014), pp. 1287–1292 (cit. on pp. 9, 11, 60, 61, 80, 81, 83).

[92] Y. Yang, P. Gao, L. Li, X. Pan, S. Tappertzhofen, S. Choi, R. Waser, I. Valov, and W. D. Lu. “Electrochemical dynamics of nanoscale metallic inclusions in dielectrics”. In: *Nat. Commun.* 5 (2014), pp. 4232/1–9 (cit. on pp. 12, 13, 107).

[93] S. Ambrogio, S. Balatti, S. Choi, and D. Ielmini. “Impact of the mechanical stress on switching characteristics of electrochemical resistive memory”. In: *Advanced Materials* 26 (2014), pp. 3885–3892 (cit. on pp. 11, 18, 20).

[94] I. Valov and W. Lu. “Nanoscale electrochemistry using dielectric thin films as solid electrolytes”. In: *Nanoscale* 8.29 (2016), pp. 13828–13837 (cit. on pp. 11, 57, 61, 80).

[95] I. Valov and T. Tsuruoka. “Effects of moisture and redox reactions in VCM and ECM resistive switching memories”. In: *J. Phys. D Appl. Phys.* 51.41 (2018), p. 413001 (cit. on pp. 11, 12, 61, 81).

[96] N. F. Mott and R. W. Gurney. *Electronic processes in ionic crystals.* Oxford Univ. Press, London, U.K., 1948 (cit. on p. 14).

[97] M. Faraday. “Experimental researches in electricity”. In: *Phil. Trans. Roy. Soc. London* 124 (1834), pp. 77–122 (cit. on p. 15).

[98] J. G. Simmons. “Electric tunnel effect between dissimilar electrodes separated by a thin insulating film”. In: *J. Appl. Phys.* 34 (1963), p. 2581 (cit. on p. 16).

[99] S. Menzel. “Modeling and simulation of resistive switching devices”. PhD thesis. 2012 (cit. on p. 16).

[100] Z. Wang, M. Rao, R. Midya, S. Joshi, H. Jiang, P. Lin, W. Song, S. Asapu, Y. Zhuo, C. Li, H. Wu, Q. Xia, and J. J. Yang. “Threshold switching of Ag or Cu in dielectrics: Materials, mechanism, and applications”. In: *Adv. Funct. Mater.* 28.6 (2018), pp. 1704862/1–19 (cit. on p. 17).

[101] W. Banerjee, S. H. Kim, S. Lee, D. Lee, and H. Hwang. “An efficient approach Based on tuned nanoionics to maximize memory characteristics in Ag-based devices”. In: *Advanced Electronic Materials* 7.4 (2021), pp. 2100022/1– (cit. on p. 17).

[102] S. H. Choi, S. O. Park, S. Seo, and S. Choi. “Reliable multilevel memristive neuromorphic devices based on amorphous matrix via quasi-1D filament confinement and buffer layer”. In: *Science Advances* 8.3 (2022), eabj7866/1– (cit. on p. 17).

[103] I. Valov, E. Linn, S. Tappertzhofen, S. Schmelzer, J. v. d. Hurk, F. Lentz, and R. Waser. “Nanobatteries in redox-based resistive switches require extension of memristor theory”. In: *Nature Communications* 4 (2013), p. 1771 (cit. on p. 18).

[104] P. Bousoulas, D. Sakellaropoulos, C. Papakonstantinopoulos, S. Kitsios, C. Arvanitis, E. Bagakis, and D. Tsoukalas. “Investigating the origins of ultra-short relaxation times of silver filaments in forming-free SiO_2-based conductive bridge memristors”. In: *Nanotechnology* 31.45 (2020), p. 454002 (cit. on p. 18).

[105] J. Sun, L. He, Y. C. Lo, T. Xu, H. Bi, L. Sun, Z. Zhang, S. X. Mao, and J. Li. “Liquid-like pseudoelasticity of sub-10-nm crystalline silver particles”. In: *Nat. Mater.* 13.11 (2014), pp. 1007–1012 (cit. on p. 18).

[106] J. van den Hurk, E. Linn, H. Zhang, R. Waser, and I. Valov. “Volatile resistance states in electrochemical metallization cells enabling non-destructive readout of complementary resistive switches”. In: *Nanotechnology* 25.42 (2014), p. 425202 (cit. on p. 18).

[107] D. M. Guzman, N. Onofrio, and A. Strachan. “First principles investigation of copper and silver intercalated molybdenum disulfide”. In: *J. Appl. Phys.* 121.5 (2017), pp. 55703/1–10 (cit. on p. 18).

[108] D. M. Guzman, N. Onofrio, and A. Strachan. "Stability and migration of small copper clusters in amorphous dielectrics". In: *J. Appl. Phys.* 117.19 (2015), pp. 195702/1–8 (cit. on p. 18).

[109] Z. Wang, S. Joshi, S. E. Savel'ev, H. Jiang, R. Midya, P. Lin, M. Hu, N. Ge, J. P. Strachan, Z. Li, Q. Wu, M. Barnell, G.-L. Li, H. L. Xin, R. S. Williams, Q. Xia, and J. J. Yang. "Memristors with diffusive dynamics as synaptic emulators for neuromorphic computing". In: *Nat. Mater.* 16 (2016), pp. 101–108 (cit. on pp. 18–21, 90, 91, 110, 121).

[110] H. Y. Li, X. D. Huang, J. H. Yuan, Y. F. Lu, T. Q. Wan, Y. Li, K. H. Xue, Y. H. He, M. Xu, H. Tong, and X. S. Miao. "Controlled memory and threshold switching behaviors in a heterogeneous memristor for neuromorphic computing". In: *Adv. Electron. Mater.* 6.8 (2020), pp. 2000309/1–11 (cit. on p. 19).

[111] B. G. Chae, J. B. Seol, J. H. Song, K. Baek, S. H. Oh, H. Hwang, and C. G. Park. "Nanometer-scale phase transformation determines threshold and memory switching mechanism". In: *Advanced Materials* 29.30 (2017) (cit. on p. 19).

[112] S. B. Simonsen, I. Chorkendorff, S. Dahl, M. Skoglundh, J. Sehested, and S. Helveg. "Direct observations of oxygen-induced platinum nanoparticle ripening studied by in situ TEM". In: *J. Am. Chem. Soc.* 132.23 (2010), pp. 7968–7975 (cit. on p. 21).

[113] C. Herring. "Effect of change of scale on sintering phenomena". In: *J. Appl. Phys.* 21.4 (1950), pp. 301–303 (cit. on p. 20).

[114] J. Song, J. Park, K. Moon, J. Woo, S. Lim, J. Yoo, D. Lee, and H. Hwang. "Monolithic integration of AgTe/TiO_2 based threshold switching device with TiN liner for steep slope field-effect transistors". In: *2016 IEEE International Electron Devices Meeting (IEDM).* IEEE, 2016, pp. 25.3.1–25.3.4 (cit. on p. 21).

[115] T. Ohno, T. Hasegawa, T. Tsuruoka, K. Terabe, J. K. Gimzewski, and M. Aono. "Short-term plasticity and long-term potentiation mimicked in single inorganic synapses". In: *Nat. Mater.* 10 (2011), pp. 591–595 (cit. on pp. 21, 121).

[116] S. L. Barbera, D. Vuillaume, and F. Alibart. "Filamentary switching: synaptic plasticity through device volatility". In: *ACS Nano* 9.1 (2015), pp. 941–949 (cit. on pp. 21, 121).

[117] S. L. Barbera, A. F. Vincent, D. Vuillaume, D. Querlioz, and F. Alibart. “Interplay of multiple synaptic plasticity features in filamentary memristive devices for neuromorphic computing”. In: *Sci Rep* 6 (2016), pp. 39216/1–11 (cit. on p. 21).

[118] X. Huang, F. Li, Q. Zhou, G. Wu, Y. Huang, L. Wang, B. Liu, and T. Cui. “In situ synchrotron X-ray diffraction with laser-heated diamond anvil cells study of Pt up to 95 GPa and 3150 K”. In: *RSC Adv.* 5.19 (2015), pp. 14603–14609 (cit. on p. 22).

[119] D. R. Lide. *CRC handbook of chemistry and physics.* Vol. 84. CRC press, 2004 (cit. on pp. 22, 23).

[120] C. herring and M. Nichols. “Thermionic emission”. In: *Rev. Mod. Phys.* 21.2 (1949), pp. 185–270 (cit. on p. 22).

[121] C. Y. Ho, R. W. Powell, and P. E. Liley. “Thermal conductivity of the elements: A comprehensive review”. In: *J. Phys. Chem. Ref. Data* 3 (1974), p. 607 (cit. on p. 22).

[122] M. H. Miles and M. A. Thomason. “Periodic variations of overvoltages for water electrolysis in acid solutions from cyclic voltammetric studies”. In: *J. Electrochem. Soc.* 123.10 (1976), pp. 1459–1461 (cit. on p. 22).

[123] A. Hickling and F. Salt. “Studies in hydrogen overvoltage at high current densities. Part VI. The mechanism of hydrogen overvoltage”. In: *Transactions of the Faraday Society* 38 (1942), pp. 474–489 (cit. on p. 22).

[124] A. Dweydari and C. Mee. “Work function measurements on (100) and (110) surfaces of silver”. In: *Phys. Status Solidi A-Appl. Res.* 27.1 (1975), pp. 223–230 (cit. on p. 22).

[125] W. W. Webb, J. T. Norton, and C. Wagner. “Oxidation of tungsten”. In: *Journal of The Electrochemical Society* 103.2 (1956), p. 107. doi: `10.1149/1.2430238`. url: `https://dx.doi.org/10.1149/1.2430238` (cit. on p. 22).

[126] M. Zhao, Z. Zhou, M. Zhong, J. Tan, Y. Lian, and X. Liu. “Thermal shock behavior of fine grained W-Y_2O_3 materials fabricated via two different manufacturing technologies”. In: *J. Nucl. Mater.* 470 (2016), pp. 236–243 (cit. on p. 23).

[127] P. Desai, T. Chu, H. James, and C. Ho. “Electrical-resistivity of selected elements”. In: *J. Phys. Chem. Ref. Data* 13.4 (1984), pp. 1069–1096 (cit. on p. 23).

[128] E. Muller. “Work function of tungsten single crystal planes measured by the field emission microscope”. In: *J. Appl. Phys.* 26.6 (1955), pp. 732–737 (cit. on p. 23).

[129] I. H. Ho, C. W. Chang, Y. L. Chen, W. Y. Chang, T. J. Kuo, Y. J. Lu, S. Gwo, and H. Ahn. “Ultrathin TiN epitaxial films as transparent conductive electrodes”. In: *ACS Appl. Mater. Interfaces* 14.14 (2022), pp. 16839–16845 (cit. on p. 23).

[130] T. Brat, N. Parikh, N. Tsai, A. Sinha, J. Poole, and C. Wickersham. “Characterization of titanium nitride films sputter deposited from a high-purity titanium nitride target”. In: *J. Vac. Sci. Technol. B* 5.6 (1987), pp. 1741–1747 (cit. on p. 23).

[131] R. Chowdhury, R. Vispute, K. Jagannadham, and J. Narayan. “Characteristics of titanium nitride films grown by pulsed laser deposition”. In: *J. Mater. Res.* 11.6 (1996), pp. 1458–1469 (cit. on p. 23).

[132] S. A. Vitale, J. Kedzierski, P. Healey, P. W. Wyatt, and C. L. Keast. “Work-function-tuned TiN metal gate FDSOI transistors for subthreshold operation”. In: *IEEE Trans. Electron Devices* 58.2 (2011), pp. 419–426 (cit. on p. 23).

[133] E. Gusev, E. Cartier, D. Buchanan, M. Gribelyuk, M. Copel, H. Okorn-Schmidt, and C. D’Emic. “Ultrathin high-K metal oxides on silicon: processing, characterization and integration issues”. In: (2001) (cit. on pp. 23, 79).

[134] J. Robertson. “High dielectric constant oxides”. In: *Eur. Phys. J. Appl. Phys* 28 (2004), pp. 265–291 (cit. on pp. 23, 79).

[135] P. K. Park and S. W. Kang. “Enhancement of dielectric constant in HfO_2 thin films by the addition of Al2O3”. In: *Appl. Phys. Lett.* 89.19 (2006), pp. 192905/1–3 (cit. on pp. 23, 79).

[136] Y. Lin, R. Puthenkovilakam, and J. Chang. “Dielectric property and thermal stability of HfO_2 on silicon”. In: *Appl. Phys. Lett.* 81.11 (2002), pp. 2041–2043 (cit. on pp. 23, 79).

[137] C. Zhao, G. Roebben, M. Heyns, and O. van der Biest. "Crystallisation and tetragonal-monoclinic transformation in ZrO_2 and HfO_2 dielectric thin films". In: (2002) (cit. on p. 23).

[138] R. Ruh and P. Corfield. "Crystal structure of monoclinic HfO_2 and a comparison with monoclinic ZrO_2". In: (1969) (cit. on p. 23).

[139] N. Nguyen, A. Davydov, D. Chandler-Horowitz, and M. Frank. "Sub-bandgap defect states in polycrystalline hafnium oxide and their suppression by admixture of silicon". In: *Appl. Phys. Lett.* 87.19 (2005), pp. 192903/1–3 (cit. on p. 23).

[140] K. Xiong, J. Robertson, M. C. Gibson, and S. J. Clark. "Defect energy levels in HfO_2 high-dielectric-constant gate oxide". In: *Appl. Phys. Lett.* 87 (2005), pp. – (cit. on p. 23).

[141] E. Bersch, S. Rangan, R. A. Bartynski, E. Garfunkel, and E. Vescovo. "Band offsets of ultrathin high-k oxide films with Si". In: *Phys. Rev. B: Condens. Matter* 78.8 (2008), p. 085114 (cit. on p. 23).

[142] T. Cook, C. Fulton, W. Mecouch, R. Davis, G. Lucovsky, and R. Nemanich. "Band offset measurements of the GaN (0001)/HfO_2 interface". In: *J. Appl. Phys.* 94.11 (2003), pp. 7155–7158 (cit. on p. 23).

[143] S. Monaghan, P. K. Hurley, K. Cherkaoui, M. A. Negara, and A. Schenk. "Determination of electron effective mass and electron affinity in HfO_2 using MOS and MOSFET structures". In: *Solid-State Electron.* 53.4 (2009), pp. 438–444 (cit. on p. 23).

[144] T. V. Perevalov, V. A. Gritsenko, S. B. Erenburg, A. M. Badalyan, H. Wong, and C. W. Kim. "Atomic and electronic structure of amorphous and crystalline hafnium oxide: X-ray photoelectron spectroscopy and density functional calculations". In: *J. Appl. Phys.* 101.5 (2007), pp. 53704/1–8 (cit. on p. 23).

[145] Z. Wang, H. Yu, X. A. Tran, Z. Fang, J. Wang, and H. Su. "Transport properties of HfO_{2-x} based resistive-switching memories". In: *Phys. Rev. B: Condens. Matter* 85.19 (2012), pp. 195322/1–10 (cit. on p. 23).

[146] E. Ringdalen and M. Tangstad. "Softening and melting of SiO_2, an important parameter for reactions with quartz in Si production". In: *10th International Conference on Molten Slags, Fluxes and Salts, Seattle, WA*. Advances in Molten Slags, Fluxes, and Salts, 2016, pp. 43–51 (cit. on p. 24).

[147] T. A. Khachaturova, V. G. But'ko, and A. A. Gusev. "Electronic structure and properties of two-dimensional silicon dioxide". In: *J. Exp. Theor. Phys. Lett.* 115.1 (2022), pp. 41–44 (cit. on p. 24).

[148] H. Bartzsch, D. Glöß, B. Böcher, P. Frach, and K. Goedicke. "Properties of SiO_2 and Al_2O_3 films for electrical insulation applications deposited by reactive pulse magnetron sputtering". In: *Surf. Coat. Technol.* 174-175 (2003), pp. 774–778 (cit. on p. 24).

[149] T. H. DiStefano and D. E. Eastman. "The band edge of amorphous SiO_2 by photoinjection and photoconductivity measurements". In: *Solid State Comm.* 9 (1971), 2259—2261 (cit. on p. 24).

[150] V. Astasauskas, A. Bellissimo, P. Kuksa, C. Tomastik, H. Kalbe, and W. S. M. Werner. "Optical and electronic properties of amorphous silicon dioxide by single and double electron spectroscopy". In: *J. Electron Spectrosc. Relat. Phenom.* 241 (2020), pp. 146829/1–7 (cit. on p. 24).

[151] S. Andersson and L. Dzhavadov. "Thermal-conductivity and heat-capacity of amorphous SiO_2 - pressure and volume dependence". In: *J. Phys. Condens. Mat.* 4.29 (1992), pp. 6209–6216 (cit. on p. 24).

[152] S. Callard, G. Tallarida, A. Borghesi, and L. Zanotti. "Thermal conductivity of SiO_2 films by scanning thermal microscopy". In: (1999) (cit. on p. 24).

[153] S. M. George. "Atomic layer deposition: An overview". In: *Chem. Rev.* 110.1 (2010), pp. 111–131 (cit. on p. 26).

[154] N. Pinna and M. Knez. "Atomic layer deposition of nanostructured materials". In: ed. by N. P. M. Knez. 1st ed. WILEY-VCH, 2011. Chap. 1 (cit. on p. 26).

[155] M. Bosund, E. M. Salmi, and R. Peltonen. *Atomic layer deposition into ultra-high aspect ratio structures with a stop-flow ALD reactor.* Tech. rep. 2016 (cit. on p. 26).

[156] A. C. P. Perros. "Thermal and plasma-enhanced atomic layer deposition: the study of and employment in various nanotechnology applications". In: *School of Electrical Engineering* (2014) (cit. on p. 28).

[157] R. M. and J. Niinisto. "Chapter 4 Atomic layer deposition, in chemical vapour deposition: Precursors". In: The Royal Society of Chemistry, 2009. Chap. 4, pp. 158–206 (cit. on p. 28).

[158] O. Instruments. *FlexAL ald chamber,* 2019. URL: `https://plasma.oxinst.com/campaigns/technology/` (cit. on p. 30).

[159] J. E. Mahan and A. Vantomme. "A simplified collisional model of sputtering in the linear cascade regime". In: *J. Vac. Sci. Technol. A* 15.4 (1997), pp. 1976–1989 (cit. on p. 32).

[160] L. Cai and F. Zhu. "Toward efficient and stable operation of perovskite solar cells: Impact of sputtered metal oxide interlayers". In: *Nano Select.* 2.8 (2021) (cit. on p. 33).

[161] S. Aussen. "Interfacial oxide formation during atomic layer deposition of oxides on reactive metals for memristor applications". MA thesis. 2017 (cit. on p. 34).

[162] L. G. Parratt. "Surface studies of solids by total reflection of X-rays". In: *Physical Review* 95.2 (1954), pp. 359–369 (cit. on p. 35).

[163] A. Glavic and M. Bjorck. "GenX 3: the latest generation of an established tool". In: *J. Appl. Crystallogr.* 55 (2022), pp. 1063–1071 (cit. on p. 35).

[164] D. Necas and P. Klapetek. "Gwyddion: an open-source software for SPM data analysis". In: *Cent. Eur. J. Phys.* 10.1 (2012), pp. 181–188 (cit. on p. 35).

[165] Microchemicals. *AZ 5214E phase out,* 2021. URL: `https://www.microchemicals.com/micro/PCN_Letter_AZ_5214E_phase_out_20201209.pdf` (cit. on p. 38).

[166] F. Lentz. "Integration of redox-based resistive switching memory devices". PhD thesis. 2014 (cit. on p. 38).

[167] A. Technologies. *Agilent B1500A semiconductor device analyzer users guide.* Ed. by A. Technologies. 6th ed. Agilent Technologies, 2007 (cit. on pp. 40, 41).

[168] Tekteonix. *Using model 4225-RPM Remote Amplifier/Switch to switch automatically between DC I-V, C-V, and pulsed I-V measurements, technical report.* 2016 (cit. on p. 42).

[169] K. I. Inc. *4200-SCS semiconductor characterization system technical data.* No. 2199 2.1.11. Keithley Instruments Inc. 2011 (cit. on p. 42).

[170] E. Covi, W. Wang, Y. H. Lin, M. Farronato, E. Ambrosi, and D. Ielmini. "Switching dynamics of Ag based filamentary volatile resistive switching devices-part I: Experimental characterization". In: *IEEE Trans. Electron Devices* (2021), pp. 1–7 (cit. on pp. 47, 56, 57, 84, 97, 112).

[171] E. Scheer, N. Agrait, J. Cuevas, A. Yeyati, B. Ludoph, A. Martin-Rodero, G. Bollinger, J. van Ruitenbeek, and C. Urbina. “The signature of chemical valence in the electrical conduction through a single-atom contact”. In: *Nature* 394.6689 (1998), pp. 154–157 (cit. on p. 51).

[172] F. Yuan, Z. Zhang, C. Liu, F. Zhou, H. M. Yau, W. Lu, X. Qiu, H.-S. P. Wong, J. Dai, and Y. Chai. “Real-time observation of the electrode-size-dependent evolution dynamics of the conducting filaments in a SiO_2 layer”. In: *ACS Nano* 11.4 (2017), 4097–4104 (cit. on p. 51).

[173] Y. Sun, X. Zhao, C. Song, K. Xu, Y. Xi, J. Yin, Z. Wang, X. Zhou, X. Chen, G. Shi, H. Lv, Q. Liu, F. Zeng, X. Zhong, H. Wu, M. Liu, and F. Pan. “Performance-enhancing selector via symmetrical multilayer design”. In: *Adv. Funct. Mater.* 29.13 (2019), pp. 1808376/1–9 (cit. on pp. 51, 121).

[174] X. Zhao, J. Ma, X. Xiao, Q. Liu, L. Shao, D. Chen, S. Liu, J. Niu, X. Zhang, Y. Wang, R. Cao, W. Wang, Z. Di, H. Lv, S. Long, and M. Liu. “Breaking the current-retention dilemma in cation-based resistive switching devices utilizing graphene with controlled defects”. In: *Adv. Mater.* 30.14 (2018), pp. 1705193/1–9 (cit. on pp. 51, 111, 121).

[175] Y. Yang, P. Gao, S. Gaba, T. Chang, X. Pan, and W. Lu. “Observation of conducting filament growth in nanoscale resistive memories”. In: *Nature Communications* 3 (2012), p. 732 (cit. on pp. 53, 72).

[176] S. Z. Rahaman, S. Maikap, W. S. Chen, H. Y. Lee, F. T. Chen, T. C. Tien, and M. J. Tsai. “Impact of TaO_x nanolayer at the $GeSe_x$/W interface on resistive switching memory performance and investigation of Cu nanofilament”. In: *J. Appl. Phys.* 111.6 (2012), pp. 63710/1– (cit. on p. 54).

[177] D. Kumar, R. Aluguri, U. Chand, and T. Y. Tseng. “Enhancement of resistive switching properties in nitride based CBRAM device by inserting an Al_2O_3 thin layer”. In: *Appl. Phys. Lett.* 110.20 (2017), pp. 203102/1– (cit. on p. 54).

[178] M. Barci, G. Molas, C. Cagli, E. Vianello, M. Bernard, A. Roule, A. Toffoli, J. Cluzel, B. D. Salvo, and L. Perniola. “Bilayer metal-oxide conductive bridge memory technology for improved window margin and reliability”. In: *IEEE J. Electron Devices Soc.* 4.5 (2016), pp. 314–320 (cit. on p. 54).

[179] J. G. Simmons. “Generalized formula for the electric tunnel effect between similar electrodes separated by a thin insulating film”. In: *J. Appl. Phys.* 34 (1963), pp. 1793–1803 (cit. on p. 54).

[180] A. Hardtdegen. “Engineering of HfO_2-based gradual resistive switching devices obtained from atomic layer deposited oxide bilayers”. PhD thesis. 2022 (cit. on p. 55).

[181] X. Sheng, C. E. Graves, S. Kumar, X. Li, B. Buchanan, L. Zheng, S. Lam, C. Li, and J. P. Strachan. “Low-conductance and multilevel CMOS-integrated nanoscale oxide memristors”. In: *Advanced Electronic Materials* (2019), p. 1800876 (cit. on p. 56).

[182] B. Govoreanu et al. “10x10 nm^2 Hf/HfO_x crossbar resistive RAM with excellent performance, reliability and low-energy operation”. In: *2011 IEEE International Electron Devices Meeting (IEDM)*. IEDM Tech. Dig., 2011, pp. 31.6.1–31.6.4 (cit. on p. 56).

[183] J. Park, W. Lee, M. Choe, S. Jung, M. Son, S. Kim, S. Park, J. Shin, D. Lee, M. Siddik, J. Woo, G. Choi, E. Cha, T. Lee, and H. Hwang. “Quantized conductive filament formed by limited cu source in sub-5nm era”. In: *IEDM Techn. Dig.* (2011), p. 3.7.1 (cit. on p. 56).

[184] R. Zhang, H. Jiang, Z. R. Wang, P. Lin, Y. Zhuo, D. Holcomb, D. H. Zhang, J. J. Yang, and Q. Xia. “Nanoscale diffusive memristor crossbars as physical unclonable functions”. In: *Nanoscale* 10.6 (2018), pp. 2721–2726 (cit. on p. 56).

[185] C. Schindler, G. Staikov, and R. Waser. “Electrode kinetics of Cu-SiO_2-based resistive switching cells: Overcoming the voltage-time dilemma of electrochemical metallization memories”. In: *Appl. Phys. Lett.* 94.7 (2009), pp. 072109/1–3 (cit. on pp. 57, 59).

[186] N. Saha and H. Tompkins. “Titanium nitride oxidation chemistry - an X-ray photoelectron-spectroscopy study”. In: *J. Appl. Phys.* 72.7 (1992), pp. 3072–3079 (cit. on p. 61).

[187] G. F. You and J. T. L. Thong. “Thermal oxidation of polycrystalline tungsten nanowire”. In: *J. Appl. Phys.* 108.9 (2010), pp. 94312/1–6 (cit. on p. 61).

[188] P. van der Heide. *X-Ray photoelectron spectroscopy.* 1st ed. Wiley, 2012 (cit. on p. 62).

[189] A. A. Koroleva, M. G. Kozodaev, Y. Y. Lebedinskii, and A. M. Markeev. “Interface engineering for enhancement of the analog properties of W/WO$_{3-x}$ /HfO$_2$/Pd resistance switched structures”. In: *J. Phys. D Appl. Phys.* 54.50 (2021), pp. 504004/1–10 (cit. on p. 63).

[190] J. Yoo, J. Park, J. Song, S. Lim, and H. Hwang. “Field-induced nucleation in threshold switching characteristics of electrochemical metallization devices”. In: *Appl. Phys. Lett.* 111.6 (2017), pp. 63109/1– (cit. on pp. 72, 111).

[191] S. Menzel, U. Böttger, and R. Waser. “Simulation of multilevel switching in electrochemical metallization memory cells”. In: *J. Appl. Phys.* 111.1 (2012), pp. 014501/1–5 (cit. on p. 72).

[192] S. Menzel, P. Kaupmann, and R. Waser. “Understanding filamentary growth in electrochemical metallization memory cells using kinetic Monte Carlo simulations”. In: *Nanoscale* 7.29 (2015), pp. 12673 –12681 (cit. on p. 74).

[193] U. Böttger, M. von Witzleben, V. Havel, K. Fleck, V. Rana, R. Waser, and S. Menzel. “Picosecond multilevel resistive switching in tantalum oxide thin films”. In: *Sci. Rep.* 10.1 (2020), p. 16391 (cit. on pp. 76, 78).

[194] K. M. Kim, J. J. Yang, J. P. Strachan, E. M. Grafals, N. Ge, N. D. Melendez, Z. Li, and R. S. Williams. “Voltage divider effect for the improvement of variability and endurance of TaOx memristor”. In: *Sci Rep* 6 (2016), pp. 20085/1–6 (cit. on p. 76).

[195] A. Hardtdegen, C. L. Torre, F. Cüppers, S. Menzel, R. Waser, and S. Hoffmann-Eifert. “Improved switching stability and the effect of an internal series resistor in HfO$_2$/TiO$_x$ bilayer ReRAM cells”. In: *IEEE Trans. Electron Devices* 65.8 (2018), pp. 3229–3236 (cit. on p. 76).

[196] H. Harris, K. Choi, N. Mehta, A. Chandolu, N. Biswas, G. Kipshidze, S. Nikishin, S. Gangopadhyay, and H. Temkin. “HfO$_2$ gate dielectric with 0.5 nm equivalent oxide thickness”. In: *Appl. Phys. Lett.* 81.6 (2002), pp. 1065–1067 (cit. on p. 79).

[197] S. Tappertzhofen. “Redox and mass transport phenomena in resistively switching thin films”. PhD thesis. 2014 (cit. on p. 81).

[198] K. Patel, J. Cottom, M. Bosman, A. J. Kenyon, and A. L. Shluger. "An oxygen vacancy mediated Ag reduction and nucleation mechanism in SiO RRAM devices". In: *Microelectronics Reliability* 98 (2019), pp. 144–152 (cit. on pp. 85, 87, 90).

[199] H. Zhao, Z. Dong, H. Tian, D. DiMarzi, M. G. Han, L. Zhang, X. Yan, F. Liu, L. Shen, S. J. Han, S. Cronin, W. Wu, J. Tice, J. Guo, and H. Wang. "Atomically thin femtojoule memristive device". In: *Advanced Materials* 29.47 (2017), pp. 1703232/1– (cit. on pp. 101, 102).

[200] S. Tappertzhofen, M. Hempel, I. Valov, and R. Waser. "Proton mobility in SiO_2 thin films and impact of hydrogen and humidity on the resistive switching effect". In: *Mater. Res. Soc. Symp. Proc.* 1330 (2011) (cit. on p. 105).

[201] A. Bricalli, E. Ambrosi, M. Laudato, M. Maestro, and R. R. andDaniele Ielmini. "Resistive switching device technology based on silicon oxide for improved on–off ratio—part II: Select devices". In: *IEEE Trans. Electron Devices* (2018) (cit. on p. 105).

[202] A. B. andElia Ambrosi andMario Laudato andMarcos Maestro andRosana Rodriguez andDaniele Ielmini. "Resistive switching device technology based on silicon oxide for improved on–off ratio—part I: Memory devices". In: *IEEE Trans. Electron Devices* (2018) (cit. on p. 105).

[203] S. R. Nandakumar, M. Minvielle, S. Nagar, and C. D. andBipin Rajendran. "A 250 mV $Cu/SiO_2/W$ memristor with half-integer quantum conductance states". In: *Nano Letters* 16.3 (2016), pp. 1602–1608 (cit. on p. 105).

[204] Y. Wang, Z. Zhang, H. Li, and L. Shi. "Realizing bidirectional threshold switching in $Ag/Ta_2O_5/pt$ diffusive devices for selector applications". In: *Journal of Electronic Materials* 48.1 (2019), pp. 517–525 (cit. on p. 111).

[205] Y. Zhao, C. Fang, X. Zhang, X. Xu, T. Gong, Q. Luo, C. Chen, Q. Liu, H. Lv, Q. Li, F. Zhang, L. Li, and M. Liu. "A compact model for drift and diffusion memristor applied in neuron circuits design". In: *IEEE Trans. Electron Devices* 65.10 (2018), pp. 4290–4296 (cit. on p. 111).

[206] J. Yin, F. Zeng, Q. Wan, Y. Sun, Y. Hu, J. Liu, G. Li, and F. Pan. "Self-modulating interfacial cation migration induced threshold switching in bilayer oxide memristive device". In: *J. Phys. Chem. C* 123.1 (2019), pp. 878–885 (cit. on p. 111).

[207] R. D. Nikam, K. G. Rajput, and H. Hwang. “Single-atom quantum-point contact switch using atomically thin hexagonal boron nitride”. In: *Small* 17.7 (2021), pp. 2006760/1– (cit. on pp. 111, 121).

[208] J. Woo and S. Yu. “Two-step read scheme in one-selector and one-RRAM crossbar-based neural network for improved inference robustness”. In: *IEEE Trans. Electron Devices* 65.12 (2018), pp. 5549–5553 (cit. on p. 117).

[209] S. Lashkare, S. Chouhan, T. Chavan, A. Bhat, P. Kumbhare, and U. Ganguly. “PCMO RRAM for integrate-and-fire neuron in spiking neural networks”. In: *IEEE Electron Device Lett.* 39.4 (2018), pp. 484–487 (cit. on p. 120).

[210] T. Tuma, A. Pantazi, M. L. Gallo, A. Sebastian, and E. Eleftheriou. “Stochastic phase-change neurons”. In: *Nat. Nanotechnol.* (2016) (cit. on p. 120).

[211] Z. Wang, B. Crafton, J. Gomez, R. Xu, A. Luo, Z. Krivokapic, L. Martin, S. Datta, A. Raychowdhury, and A. I. Khan. “Experimental demonstration of ferroelectric spiking neurons for unsupervised clustering”. In: *64th IEEE Annual International Electron Devices Meeting (IEDM), San Francisco, CA*. 2018 IEEE International Electron Devices Meeting (IEDM), 2018 (cit. on p. 120).

[212] Y. Demirag, F. Moro, T. Dalgaty, G. Navarro, C. Frenkel, G. Indiveri, E. Vianello, and M. Payvand. “PCM-trace: Scalable synaptic eligibility traces with resistivity drift of phase-change materials”. In: *IEEE International Symposium on Circuits and Systems (IEEE ISCAS), Daegu, SOUTH KOREA*. 2021 IEEE International Symposium On Circuits and Systems (ISCAS), 2021 (cit. on p. 120).

[213] Q. Hua, H. Wu, B. Gao, M. Zhao, Y. Li, X. Li, X. Hou, M. F. Chang, P. Zhou, and H. Qian. “A threshold switching selector based on highly ordered Ag nanodots for x-point memory applications”. In: *Adv. Sci.* 6.10 (2019), pp. 1900024/1–9 (cit. on p. 121).

[214] N. Shukla, B. Grisafe, R. K. Ghosh, N. Jao, A. Aziz, J. Frougier, M. Jerry, S. Sonde, S. Rouvimov, T. Orlova, S. Gupta, and S. Datta. “Ag/HfO_2 based threshold switch with extreme non-linearity for unipolar cross-point memory and steep-slope phase-FETs”. In: *2016 IEEE International Electron Devices Meeting (IEDM)*. 2016 IEEE International Electron Devices Meeting (IEDM), 2016, pp. 34.6.1–34.6.1 (cit. on p. 121).

[215] Y.-F. Lu, Y. Li, H. Li, T.-Q. Wan, X. Huang, Y.-H. He, and X. Miao. “Low-power artificial neurons based on Ag/TiN/HfAlO$_x$/Pt threshold switching memristor for neuromorphic computing”. In: *IEEE Electron Device Lett.* 41.8 (2020), pp. 1245 –1248 (cit. on p. 121).

[216] K. Wang, Q. Hu, B. Gao, Q. Lin, F. W. Zhuge, D. Y. Zhang, L. Wang, Y. H. He, R. H. Scheicher, H. Tong, and X. S. Miao. “Threshold switching memristor-based stochastic neurons for probabilistic computing”. In: *Materials Horizons* 8.2 (2021), pp. 619–629 (cit. on p. 121).

[217] T. Fu, X. Liu, H. Gao, J. E. Ward, X. Liu, B. Yin, Z. Wang, Y. Zhuo, D. J. F. Walker, J. J. Yang, J. Chen, D. R. Lovley, and J. Yao. “Bioinspired bio-voltage memristors”. In: *Nature Communications* 11.1 (2020), pp. 1861/1– (cit. on p. 121).

[218] A. S. Sokolov, M. Ali, R. Riaz, Y. Abbas, M. J. Ko, and C. Choi. “Silver-adapted diffusive memristor based on organic nitrogen-doped graphene oxide quantum dots (N-GOQDs) for artificial biosynapse applications”. In: *Advanced Functional Materials* 29.18 (2019), pp. 1807504/1– (cit. on p. 121).

[219] G. Dastgeer, H. Abbas, D. Y. Kim, J. Eom, and C. Choi. “Synaptic characteristics of an ultrathin hexagonal boron nitride (h-BN) diffusive memristor”. In: *Physica Status Solidi-Rapid Research Letters* 15.1 (2021), pp. 2000473/1– (cit. on p. 121).

[220] H. Abbas, Y. Abbas, G. Hassan, A. S. Sokolov, Y. R. Jeon, B. Ku, C. J. Kang, and C. Choi. “The coexistence of threshold and memory switching characteristics of ALD HfO$_2$ memristor synaptic arrays for energy-efficient neuromorphic computing”. In: *Nanoscale* 12.26 (2020), pp. 14120–14134 (cit. on p. 121).

[221] P. Yao, H. Wu, B. Gao, S. B. Eryilmaz, X. Huang, W. Zhang, Q. Zhang, N. Deng, L. Shi, H. P. Wong, and H. Qian. “Face classification using electronic synapses”. In: *Nat. Commun.* 8.1 (2017), p. 15199 (cit. on p. 121).

[222] P. Bousoulas, C. Papakonstantinopoulos, S. Kitsios, K. Moustakas, G. C. Sirakoulis, and D. Tsoukalas. “Emulating artificial synaptic plasticity characteristics from SiO$_2$-based conductive bridge memories with Pt nanoparticles”. In: *Micromachines* 12.3 (2021), pp. 306/1–18 (cit. on p. 121).

[223] Z. Zhang, S. Gao, Z. Li, Y. Xu, R. Yang, and X. Miao. “Artificial LIF neuron With bursting behavior based on threshold switching device”. In: *IEEE Transactions on Electron Devices* 70.3 (2023), pp. 1374–1379 (cit. on p. 121).

Schriften des Forschungszentrums Jülich
Reihe Information

Band / Volume 89
Controlling the electrical properties of oxide heterointerfaces through their interface chemistry
M.-A. Rose (2022), vi, 162 pp
ISBN: 978-3-95806-667-0

Band / Volume 90
Modeling and Suppressing Unwanted Parasitic Interactions in Superconducting Circuits
X. Xu (2022), 123, XVIII pp
ISBN: 978-3-95806-671

Band / Volume 91
Activating molecular magnetism by controlled on-surface coordinationI.
Cojocariu (2022), xi, 169 pp
ISBN: 978-3-95806-674-8

Band / Volume 92
Computational study of structural and optical properties of two-dimensional transition-metal dichalcogenides with implanted defects
S. H. Rost (2023), xviii, 198 pp
ISBN: 978-3-95806-682-3

Band / Volume 93
DC and RF characterization of bulk CMOS and FD-SOI devices at cryogenic temperatures with respect to quantum computing applications
A. Artanov (2023), xv, 80, xvii-liii pp
ISBN: 978-3-95806-687-8

Band / Volume 94
HAXPES study of interface and bulk chemistry of ferroelectric HfO_2 capacitors
T. Szyjka (2023), viii, 120 pp
ISBN: 978-3-95806-692-2

Band / Volume 95
A brain inspired sequence learning algorithm and foundations of a memristive hardware implementation
Y. Bouhadjar (2023), xii, 149 pp
ISBN: 978-3-95806-693-9

Band / Volume 96
Characterization and modeling of primate cortical anatomy and activity
A. Morales-Gregorio (2023), ca. 260 pp.
ISBN: 978-3-95806-698-4

Band / Volume 97
Hafnium oxide based memristive devices as functional elements of neuromorphic circuits
F. J. Cüppers (2023), vi, ii, 214 pp
ISBN: 978-3-95806-702-8

Band / Volume 98
Simulation and theory of large-scale cortical networks
A. van Meegen (2023), ca. 250 pp
ISBN: 978-3-95806-708-0

Band / Volume 99
Structure of two-dimensional multilayers and topological superconductors: surfactant mediated growth, intercalation, and doping
Y.-R. Lin (2023), x, 111 pp
ISBN: 978-3-95806-716-5

Band / Volume 100
Frequency mixing magnetic detection for characterization and multiplex detection of superparamagnetic nanoparticles
A. M. Pourshahidi (2023), X, 149 pp
ISBN: 978-3-95806-727-1

Band / Volume 101
Unveiling the relaxation dynamics of Ag/HfO$_2$ based diffusive memristors for use in neuromorphic computing
S. A. Chekol (2023), x, 185 pp
ISBN: 978-3-95806-729-5

Weitere ***Schriften des Verlags im Forschungszentrum Jülich*** unter
http://wwwzb1.fz-juelich.de/verlagextern1/index.asp

Information
Band / Volume 101
ISBN 978-3-95806-729-5

Mitglied der Helmholtz-Gemeinschaft

JÜLICH
Forschungszentrum